Crack propagation on rock mass on the CO2 storage context

Gisèle Suhett Helmer

▶ To cite this version:

Gisèle Suhett Helmer. Crack propagation on rock mass on the CO2 storage context. Materials. Université Paris-Est, 2014. English. NNT : 2014PEST1190 . tel-01722801

HAL Id: tel-01722801
https://pastel.hal.science/tel-01722801

Submitted on 5 Mar 2018

THÈSE

Crack propagation in reservoir rocks in the CO_2 storage context

préparée à

l'École des Ponts et des Chaussées (ENPC)

et au

Bureau des Recherches Géologiques et minières (BRGM)

pour obtenir le grade de

Docteur de L'Université Paris Est

Spécialité : Géotechnique

Rapport provisoire présenté par :

Gisèle Suhett Helmer

Soutenance prévue le 11 décembre 2014 à Champs-sur-Marne devant le jury composé de :

Mme Muriel Gasc-Barbier	CEREMA Toulouse	Rapporteur
M. Vincent Lagneau	École des Mines ParisTech	Rapporteur
M. Ahmad Pouya	École des Pont ParisTech	Examinateur/Président
M. Darius Seyedi	ANDRA	Examinateur
Mme Sylvine Guedon	IFSTTAR	Examinateur
M. Jean Sulem	École des Pont ParisTech	Directeur de Thèse
M. Siavash Ghabezloo	École des Pont ParisTech	Encadrant
M. Jérémy Rhomer	BRGM	Encadrant

Part I – Introduction

In Memoriam of Doralice

Remerciements

Je voudrais remercier à toutes les personnes sans lesquelles ce travail ne serait pas possible. Premièrement à toute l'équipe du CERMES, en donnant spéciale attentions aux secrétaires Armelle Fayol et Rachida, les techniciens du CERMES Emmanuel Delaure et principalement à Baptiste Chabot qui m'a énormément aidé.

Je ne peux pas oublier les techniciens et chercheurs des autres laboratoires qui m'ont donné support pour les essais ou préparations d'échantillons réalisés au sein des leurs institutions comme, le Lami, le LMT-Cachan, l'IFSTTAR, le LMS-Polytechnique, l'EIFER, le BRGM.

Je voudrais remercier mon directeur de thèse M. Sulem, et mes encadrants M. Ghabezloo et M. Rohmer, ainsi que Darius Seyedi pour tout l'aide qu'il m'a apporté.

A tous les collègues et amis des toutes les institutions où cette thèse a été conçu et réalisée. Votre compagnie et votre accueil ont été indispensable.

Je remercie à la Chaire CSTC et l'ANR pour le financement de la thèse.

Je voudrais aussi remercier les deux rapporteurs Mme Gasc et M. Lagneau, ainsi que les autres membres du jury M.Pouya et Mme. Guedon pour avoir participé à la soutenance et pour avoir lu le manuscrit et surtout pour toutes les bonnes remarques faites pour l'améliorer.

Je souhaite également remercier à tous les professeurs qui ont été mes grandes sources d'inspirations pour que je continue la vie académiques : Katia Bicalho, Eric Vuilermet et Euripedes Vargas.

Je ne peux pas oublier de remercier tous les personnels de l'école et de l'université Paris-Est que d'une façon et de l'autre ont permis la construction d'un environnent favorable à la recherche.

Enfin je veux remercier ma famille qui a été le support fondamentale pour que ce travaille se concrétise. Ma chienne Doralice qui a été ma compagnie pendant les nuits que je suis passé en train d'étudier seule. Mes frères qui m'ont toujours traité avec admiration. Ma tante Misma qui a toujours été là pour moi. Mon père que n'a jamais attendu moins de moi et surtout ma mère qui a lutté toute sa vie pour qu'on puisse avoir la meilleure formation scolaire possible. Je vous aime tant que ce ne même pas possible de l'exprimer.

Résumé

Le captage et stockage du CO_2 (CSC) dans les formations géologiques profondes est une solution prometteuse pour réduire les effets indésirables des concentrations atmosphériques du CO_2. Un des aspects les plus importants en vue de l'acceptabilité par le public de cette technologie et son déploiement industriel est la démonstration de la sécurité et de l'intégrité à long terme de ce stockage.

Les formations géologiques étant des milieux très hétérogènes, contiennent très souvent des réseaux de fissures. La réponse hydromécanique de ces milieux fissurés sous l'effet combiné de l'augmentation de la pression interstitielle due à l'injection et des réactions chimiques engendrant la précipitation et la dissolution des différents minéraux est un paramètre clé pour étudier l'intégrité à long terme du stockage. L'effet combiné des variations de contraintes (effectives) et des réactions chimiques peut provoquer l'ouverture, le colmatage et/ou la propagation des fissures préexistantes ou induites.

La ténacité (K_C) est un paramètre de la roche associé à la capacité du matériau à résister à propagation d'une fissure. La propagation d'une fissure existante peut dériver du changement de l'état de contrainte (effet mécanique de l'injection), ou du changement de la ténacité dû à la dégradation de la roche (effet chimique). La connaissance de la ténacité de la roche et son évolution due aux effets chimiques est donc importante pour la modélisation de la propagation des fissures dans le contexte du stockage géologique du CO_2.

Ce travail a deux objectifs principaux :

(1) L'évaluation expérimentale de la dégradation par le CO_2 sur la ténacité d'une roche réservoir (que consiste à comprendre le mécanisme à petite échelle)

(2) L'évaluation de l'intégrité d'un réservoir sous l'injection de CO_2 (que consiste à comprendre le mécanisme à grande échelle).

En ce qui concerne la réalisation du programme expérimental, une phase préliminaire a porté sur le choix de la roche à étudier, le mode de dégradation de la roche et les essais les plus appropriés pour atteindre les objectifs de l'étude. Ainsi, un calcaire (Pierre de Lens) est choisi pour être étudié dans son état sain et après une dégradation par le CO_2. La dégradation de la roche est réalisée dans un autoclave: les échantillons sont placés dans une solution aqueuse saturée en CO_2, sous les conditions de réservoir (température de 60°C et pression de 15 MPa) pendant un temps de dégradation d'un mois.

Plusieurs configurations ont été choisies pour la réalisation des essais mécaniques de ténacité en modes I et II :

- Pour la propagation d'une fissure en mode I (ouverture):

  - l'essai brésilien (BDT),

  - l'essai brésilien avec entaille en demi-lune CCNBD et entaille rectangulaire CCBD,

  - l'essai de flexion trois points sur un échantillon semi-circulaire SCB

- Pour la propagation d'une fissure en mode II (cisaillement dans le plan de la fissure) :

  - l'essai de flexion trois points avec un échantillon semi-circulaire et appuis asymétriques ASCB

  - l'essai brésilien avec entaille inclinée en demi-lune CCNBD et entaille rectangulaire CCBD,

  - l'essai de double cisaillement (PTST) réalisé en cellule triaxiale.

Certains essais mécaniques ont été réalisés en utilisant une technique de corrélation d'images (DIC). Ce dispositif permet d'évaluer la ténacité de la roche à partir des champs de déplacements des échantillons de manière parallèle aux résultats obtenus par les méthodes classiques basées sur l'évaluation des charges de rupture. L'utilisation de la technique de corrélation d'image a été réalisée dans le cadre d'une collaboration avec le Laboratoire de Mécanique et Technologie de l'Ecole Normale Supérieure de Cachan.

Il est important de préciser que tous les essais ont été réalisés avec une roche dans des conditions d'humidité ambiante. Une autre partie de l'étude vise l'analyse de l'effet de la présence d'eau et d'eau saturée en CO_2 lors d'un chargement mécanique sur la propagation des fissures.

En complément de ces essais mécaniques, une caractérisation de la microstructure de la roche et son évolution après la dégradation est réalisée en utilisant des observations au microscope électronique à balayage, ainsi que des mesures de porosimétrie au mercure.

Les résultats expérimentaux ont montré que les valeurs de ténacité en mode I obtenues par les différents types d'essai et analysées par différentes méthodes sont tout à fait concordantes. La technique de corrélation d'image a mis en évidence que la ténacité en mode II ne pouvant pas être évaluée dans les essais de chargement non confiné.

Deux procédures de dégradation ont été menées : (1) les échantillons sont maintenus un mois dans l'eau saturée en CO_2 dans l'autoclave, (2) l'eau de l'autoclave est renouvelée chaque semaine. Dans les deux cas, on a pu constater par des analyses au porosimètre que la porosité de la roche change peu (0,4 %). Ce changement de porosité est similaire à celui obtenu dans des simulations numériques pour un réservoir calcaire sur une période de 10 ans dans la zone loin du puits d'injection (fluide saturé en CO2). Les analyses au MEB montrent une dégradation observable sous la forme du changement de la distribution des porosités avant et après dégradation. La ténacité de la roche n'est pas sensiblement affectée passant de 0,62 à 0,58 MPa.m^{0,5}. On a également étudiée l'effet de la présence de l'eau en réalisant des essais de fracturation avec des échantillons saturés. Celle-ci a une influence plus significative vis-à-vis de la ténacité avec une réduction d'environ 17% par rapport aux échantillons secs. Ce résultat est peu affecté par la présence de CO_2 dans le fluide de saturation.

En ce qui concerne l'analyse en mode II, plusieurs essais ont été réalisés (cellule triaxiale) avec des échantillons soumis à différentes pressions de confinement 5, 10 et 15 MPa. On a pu constater que l'essai PTST permet une bonne évaluation de la ténacité en mode II (de l'ordre de 3 MPa.$m^{0,5}$ pour la Pierre de Lens). Cependant, le mode I est encore présent pour les pressions de confinement de 5 et 10 MPa, et n'est pas toujours inexistant pour une pression de confinement égale à 15 MPa. On a montré, là encore, que l'influence du CO_2 est faible avec une ténacité en mode II passant de 2,96 à 2,77 MPa.$m^{0,5}$. Un autre point important étudié par la simulation numérique concerne l'influence de l'épaisseur de la fissure de l'échantillon qui favorise l'apparition d'un mode mixte. Cette influence diminue avec l'augmentation de la contrainte de confinement.

L'influence de la dégradation de la roche par le CO_2 sur la propagation de fissures a été également étudiée à l'aide d'une modélisation numérique en utilisant le modèle ENDO-HETEROGENE, développé au BRGM (dans le cadre de la thèse de Nicolas Guy (BRGM/ LMT-Cachan) et intégré dans le code de calcul par éléments finis Code-Aster®. Ce modèle est basé sur l'amorçage et la propagation des fissures dans un milieu hétérogène dont la variabilité des paramètres du matériau suit le modèle probabiliste de Weibull à 2 paramètres. On a exploré la possibilité que la dégradation chimique réduit la ténacité de la roche et influence également l'hétérogénéité de la microstructure (défauts pré-existants). Cette hétérogénéité est représentée dans le modèle de Weibull par le paramètre m. Ainsi l'impact des variations de la ténacité K_C de la roche et du paramètre m, dans la plage des données obtenues par l'étude expérimentale sur l'amorçage et la propagation des fissures a été étudié pour une couche sédimentaire en conditions de réservoir. Les résultats de la modélisation montrent que le paramètre de Weibull m influence le nombre et la dimension des fissures, cependant, la taille maximale de la fissure ne varie pas avec m.

Pour remettre ces résultats expérimentaux en contexte avec la roche étudiée, les paramètres de Weibull ont été évalués pour la roche saine et la roche dégradée. On a observé que m varie de 8,55 à 8,52 et σ_0 de 2,8 et 2,2 MPa. Selon les résultats de la simulation numérique cette variation n'est pas suffisante pour changer le réseau des fissures créées après un chargement dans une couche géologique.

Ces résultats montrent que dans le cas d'un réservoir calcaire l'injection de CO_2 n'influe pas significativement ni sur le paramètre ténacité de la roche, ni sur les paramètres probabilistes de la fracturation. Ces résultats correspondent à une période de 10 ans dans une zone du réservoir loin du puits d'injection.

Abstract

The CO_2 capture and storage (CSC) in the deep geological formations is a promising solution to decrease the undesirable effects of the CO_2 concentration in the atmosphere. One of the most important aspects concerning the public acceptability of this technology and its use in the industry is the demonstration of the storage safety and integrity.

The geological formations, being very heterogeneous environments, often have crack networks. The environment hydromechanic response under the combined effect of the pore pressure due to the injection and the chemical reactions that generate precipitation and dissolution of different minerals is a key parameter to study the long term storage integrity. The combined effect of the effective stress variation and the chemical reactions can provoke the opening, the clogging and/or the crack propagation of pre-existent cracks.

The fracture toughness (K_C) is a parameter associated with the ability of the material to resist the crack propagation. The crack propagation can be due the change of the state of stress (mechanical effect of the injection), or the rock fracture toughness change due to the rock degradation (chemical effect). Knowing the rock fracture toughness and its evolution due to the chemical effects it's then, important to the modeling of crack propagation in the geological CO_2 storage context.

The two principal objectives of this work are:

(1) The experimental evaluation of the CO_2 degradation over the reservoir rock fracture toughness (to understand the mechanism in a smaller scale)

(2) The reservoir integrity evaluation due to the CO_2 injection (to understand the mechanism in a bigger scale)

Concerning the experimental program performance, one preliminary phase consists on the choice of the study rock, the degradation mode and the most appropriate laboratory tests to reach the study objectives. Thereby, a limestone (Pierre de Lens) is chosen to be study both in a sound and after being degraded by the CO_2. The rock degradation is made in a autoclave and the samples are placed in a aqueous solution saturated with CO_2, under reservoir conditions (temperature of 60 °C and pressure of 15 MPa) during a degradation time of a month.

Many configurations for the mechanical laboratory test were chosen for testing the fracture toughness of the rock both on mode I and mode II of crack propagation.

To the crack propagation on mode I (opening):

- The Brazilian test (BDT) ;

- The Central Crack Notched Brazilian test (CCNBD -- half-moon crack format) and the Central Crack Brazilian test (CCBD – rectangular crack);

- The semi-circular three point bending test (SCB);

- Pour la propagation d'une fissure en mode II (cisaillement dans le plan de la fissure) :

- The semi-circular three point bending test with asymmetric supports (ASCB);

The Central Crack Notched Brazilian test (CCNBD -- half-moon crack format) and the Central Crack Brazilian test (CCBD – rectangular crack);

- The Punch Through Shear Test (PTST) performed in a triaxial cell.

Some of the mechanical tests will be performed using a digital image correlation technique (DIC). This device allows evaluating the rock fracture toughness from the displacement fields on the samples in parallel to the classic methods based of the rupture load (of peak load). The utilization of the image correlation technique it was made under the monitoring of the LMT-Cachan (Mechanic and Technology laboratory of the Normale Supérieure de Cachan).

It is important to precise that a part of the tests (most of them) were realized on ambient humidity. Another part aim to study crack propagation under the effect of the water presence and the presence of and water with CO_2 dissolved under a mechanical load.

As a complement of the mechanical tests, a microstructure characterization of the rock was made and its evolution before and after degradation was realized using observations in a scanner electron microscope (SEM). It was also made a mercury porosimetry analysis.

The experimental results show that the fracture toughness values for the mode I obtained by the different types of tests and analyzed by the different methods are concordant. The image correlation technique put in evidence the fact that the evaluation for the mode II crack propagation mode can't be evaluated on non confined tests.

Two degradation procedures were carried on : (1) the samples were put in a CO_2 saturated water in an autoclave ; (2) the autoclave water is renewed each week. For each case we could note that the porosity didn't change much (0.4%). This variation is equivalent to the one obtained by numerical simulations for a limestone reservoir for a 10 years period in a zone far from the injection point (zone of CO_2 saturated water). The SEM analyses show an observable degradation due to a variation on the porosity distribution before and after the degradation. The rock fracture toughness it's not much affected by this variation passing from 0.62 to 0.58 $MPa.m^{0,5}$. The effect of water presence being also studied, mechanical tests were performed on saturated samples (submersed). This has a great influence over the fracture toughness parameter with a decrease of 17% (comparing with dry samples).This results it not much affect by the presence of CO_2 on the fluid.

Concerning the analysis on mode II, many tests were made (in a triaxial cell), with samples under different confined pressures (5, 10 and 15 MPa). It was possible to notice that the PTST test allows a great evaluation of the fracture toughness on mode II (3 $MPa.m^{0.5}$ for the Pierre the Lens). Nevertheless, the mode I is still present for the confinement pressure of 5 and 10 MPa and it's not always inexistent for the 15 MPa pressure. It was also shown that the CO_2 influence is not important, with a fracture toughness passing from 2.96 to 2.77 $MPa.m^{0,5}$.Another important point is the numerical modeling concerning the influence of the sample crack thickness that favor the appearance of the mixed mode. Its influence decreases with the increase of the confinement pressure.

The influence of the rock degradation by the crack propagation was also studied by a numerical modeling using the numerical model ENDO-HETEROGENE, developed by the BRGM (in the context of the Nicolas Guy PhD – coordinated both by BRGM and LMT-Cachan) and integrated on the finite elements code – Code-Aster®. Its model is based on the crack initiation and crack propagation in a heterogeneous environment where the material parameters variability follows a two parameters Weibull distribution. It was explored the possibility that the chemical degradation that reduces the fracture toughness will also influence the Weibull parameters changing the heterogeneity of the crack distribution on a microstructure scale (pre-existent defects). Its heterogeneity is represented on the Weibull distribution by the parameter *m*. Thereby the impact of these variations (on the fracture toughness K_c and the parameter *m*) on the range of the data obtained by the experimental study it was study with the aid of the numerical model to analyze the crack initiation and the crack propagation on a sedimentary layer on reservoir conditions. The results show that the parameter *m* can influence the number and the dimensions of the cracks but it does not change the maximum size of the crack.

Putting the experimental results in context with the studied rock, the Weibull parameters were evaluated for the sound and the degraded rock. It was observed that *m* changes from 8.55 to 8.52 and σ_0 from 2.8 to 2.2 MPa (sound and degraded rock respectively). The numerical results show that these variations are not enough to change the crack network created after a load under a geological layer.

This results show that in the case of a limestone reservoir the CO_2 injection won't influence significantly neither the fracture toughness nor the probabilistic parameters. These results correspond to a period of 10 years of injection in a zone far from the injection point.

Table of contents

List of Figures

List of Tables

List of Symbols

Symbol	Unit	Description
		Greek Letters
α	/	Empirical value used on the Heterogeneity factor
α_0	/	Dimensionless parameter CCNBD test – related to a_0
α_1	/	Dimensionless parameter CCNBD test – related to a_1
α_B	/	Dimensionless parameter CCNBD test – related to B
α_S	/	Dimensionless parameter CCNBD test – related to D_s
β	/	Empirical value used on the Heterogeneity factor
β_I	m	For a displacing crack, it is the curve's limit (u_n^2/r) when r tends to zero.
β_{II}	m	For a displacing crack, it is the curve's limit (u_t^2/r) when r tends to zero.
$L\gamma$	J/m²	Surface Energy of the solid
Γ	J	Surface Energy
η	/	Term that depends of the type of analysis -plane stress η=1 - plane strain η=1-ν^2
λ_0	Cracks/m^3	Density of cracks
θ	Degrees	Radial distance of polar plan
κ,		Lamé coefficients
μ, ν		Constants for the determination of Y* (CCNBD test)

v		Poisson constant
π	/	Pi number
Π	J	Total energy
σ_0	Pa	Applied stress tension or Weibull parameter(scale factor σ_0^m/λ_0)
σ_n	Pa	Normal tension
σ_t	Pa	Tangential tension

a	m/m^2	Crack length or crack surface
a_0	m	Internal crack part (CCNBD test)
a_1	m	External crack part (CCNBD test)
B	m	Thickness for the sample
B_1	Pa^2	Brittleness index 1
B_2	/	Brittleness index 2
c	m	Natural defect size for the BDT
D	m	Diameter of the sample
D_s	m	Diameter of the saw used to cut the notch (CCNBD)
e	/	Euler's number
E	Pa	Young's modulus
E'	Pa	Equivalent Young's modulus
E_d	Pa	Dynamic Young's modulus
G	J/m²	Energy Release Rate
G_I; G_{II}; G_{III}	J/m²	Energy Release Rate for crack propagating in mode I, II and III
H	/	Heterogeneity Factor
h_c	m	Dimension of the saw disc that penetrates in the sample.
i	/	Imaginary Unit
$I_s^{(50)}$	Pa	Point load Index corrected by a diameter of 50 mm
K_C	$Pa.\sqrt{m}$	Fracture Toughness
K_I; K_{II}; K_{III}	$Pa.\sqrt{m}$	Stress Intensity Factor for the mode I, II and II
K_{IC}; K_{IIC}; K_{IIIC}	$Pa.\sqrt{m}$	Fracture Toughness for mode I, II and III
L	m	Length of the sample
m		Weibull parameter
N_I; N_{II}	/	Geometry factor for mode I and II(CCBD and CCNBD tests)

P	N/bar; Pa	Force or load /Pressure
pH	/	Hydrogen Potential
Q	m^3/s	Flow
r	m	Radius in a polar plan
R	m	Radius
S_1	m	Distance from the center to the first support
S_2	m	Distance from the center to the second support
T	°C	Temperature
U	J	Internal energy (plastic and elastic)
u_n	m	Normal displacement
u_t	m	Tangential displacement
V_p	m/s	Compression wave velocity
V_s	m/s	Shear wave velocity
W	J	External Work
X	m	Abscissa in a Cartesian plan
Y	m	Coordinate in a Cartesian plan
Y^*	/	Geometry factor for CCNBD test
Y_I; Y_{II}	/	Geometry factor for mode I and II (ASCB and SCB tests)
z_c		Complex number

Acronyms

ASCB	Asymetrical Semi-Circular Bending Test
BDT	Brazilian Test
BRGM	Bureau des Recherches Geologiques et Minieres
CB	Chevron Bend Specimen Method
CCBD	Central Crack Brazilian Test
CCNBD	Centra Crack Notched Brazilian Test
CCP	Central Cracked Panel
CERMES	Equipe des Geotechnique du Laboratoire Navier
CSC	CO_2 Capture, Transport and Storage
DIC	Digital Image Correlation
FBT	Flattaned Brazilian Disc
LMS-	Laboratoire de Mécanique des Solides de L'Ecole Polytechnique

Polytechnique		
LMT-Cachan		Laboratoire de Mécanique et Tecnologie
MR		Modified Ring Test
SCB		Semi-Circular Bending Test
SC3PB		Single edge straight through cracked rectangular plate in three-point bending test
SECB		Single Edge Cracked Beam under three-point bending test
SECRBB		Single Edge Cracked Round Bar in Bending
SENRBB		Single Edge Notched Round Bar in Bending
SIF	$Pa.\sqrt{m}$	Stress Intensity Factor
SR		Short Rod Specimen Method

Part I - Introduction

Contents

In this part, we give an introduction on the CO_2 storage context. Then, in section 1.2 more specific details of each type of reservoir. In section 1.3 the objectives of the thesis are exposed and in section 1.4 the structure of the document is explained.

1.1 General Aspects

The present thesis focuses on CO_2 storage. CO_2 capture and storage (CCS) is recognized as a promising solution to tackle greenhouse gas emissions. Key issues associated with CCS relate to the integrity of the reservoir and the containment effectiveness (IPCC, 2005). The CCS technique consists in capturing part of the CO_2 emitted from various industrial sources and in injecting it in saline aquifers, depleted hydrocarbons reservoirs or un-mineable coal seals in order to prevent larger climate effects associated to the greenhouse emissions.

For an efficient storage the reservoir rock should have a significant porosity, consisting in microstructural voids or fractures that can be occupied by the injected fluid. To avoid the contamination of the overlying rock formations, particularly the freshwater aquifers and the atmosphere, the reservoir rock must be under an impermeable rock layer (caprock), see e.g., (Bouc et al., 2009). The CO_2 injection pressure has to be high enough to introduce the fluid in the rock mass without any major change in the global underground structure. Nevertheless, the injection of a fluid in an underground reservoir can change the stress state and affect the rock mass behavior and properties (Jonny Rutqvist, 2012). It is thus essential to ensure the integrity of the reservoir-caprock system in order to avoid any possible leakage.

The rock is a heterogeneous porous material and the most fragile zones are around its cracks or defects. With a change in the stress state, cracks can propagate from these zones through the rock mass. Crack propagation may destabilize the reservoir and create zones from where the fluid can circulate, enhancing the injectivity, but also potentially increasing the risk of leakage if the crack propagates through the caprock-reservoir interface (Leguillon, et al. 2014). Therefore, the study of crack propagation in an underground CO_2 storage system is essential to ensure the integrity of the reservoir.

To study the crack propagation, we are interested in the fracture toughness parameter - K_{IC} called Fracture Toughness. The fracture toughness is an intrinsic parameter related to the ability of a material to resist the crack propagation (Whittaker, Singth, & Sum, 1992).

Furthermore, the CO_2 dissolved in water, forms an acid aqueous solution that is not inert for some reservoir rocks, especially the ones with calcite or dolomite in their composition (Fleury et al., 2011). This acidic water can chemically degrade the rock. The dissolution can alter the microstructure of the rock, affect its porosity and permeability, and modify its mechanical properties. The influence the acidic water has on rocks, especially on its fracture toughness is the key subject of this work.

1.1.1 CO_2 storage: characteristics and objectives

As shown in Figure 1. 1 (Geonet, 2008) a CCS system is composed of three parts:

– Capture

– Transport

– Injection into a deep geological target and storage over long term

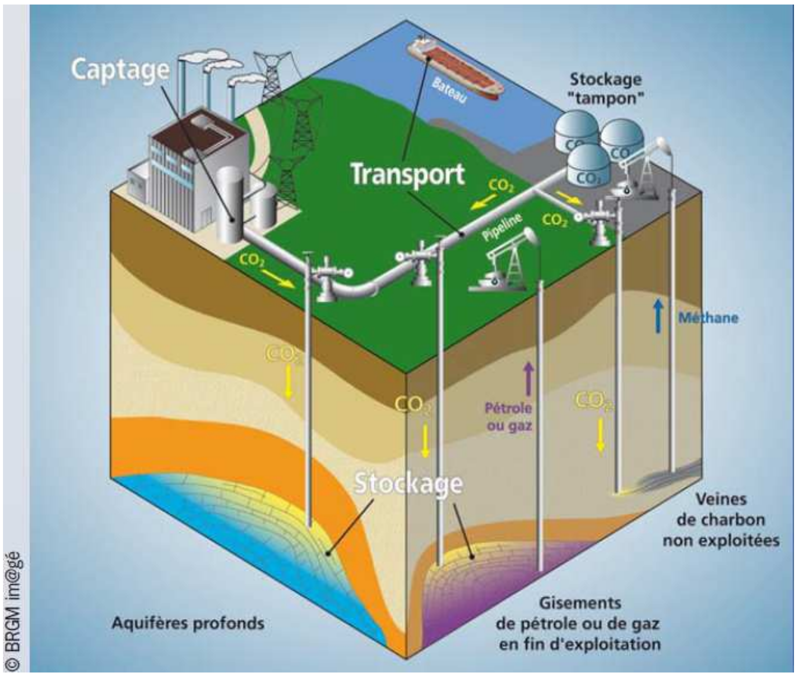

Figure 1. 1 - Storage complex - (Geonet, 2008)

The CO_2 **capture** starts with the separation of this gas from the combustion gas, followed by the dehydration, to avoid the corrosion of all the sets (transport canalizations and etc) and the hydrates formations that can obstruct the pipes, which facilitates its transport and storage.

The **transport** can be made by ship or pipes.

For the **injection phase**, the injection pressure is the key parameter. It has to be greater than the reservoir pressure, in order to move the internal fluid (deep saline aquifers and depleted hydrocarbons reservoirs), but must be controlled in order to avoid rock fracturing or faults reactivation. The complete study of the reservoir is essential to evaluate the maximum injection pressure. Another important aspect is the chemical interaction between the CO_2 and the reservoir rock or the caprock. Some chemical processes may change the fluid flow rate, due to dissolution/precipitation phenomena. The reservoir rock mass is a porous medium which allows CO_2 storage in the pores. Leakage should be prevented by the caprock which is an impermeable rock unit (structural trapping -Figure 1. 2).

In order to avoid leakage, there are several types of CO_2 trappings modes already exposed in the literature (Gaus et al, 2008), they are:

– The CO_2 mineralization – mineral trapping

– The capillary trapping – residual trapping

– The CO_2 dissolution (water) – Solubility trapping

– The structural trapping

Capillary trapping is related to a capillary pressure at the interface between a wetting fluid (here the pore water) by a non-wetting fluid (here supercritical CO_2). The mechanism that prevents the CO_2 from escaping by the capillarity trapping is related to the pore size of the material. What happens is that the pores are sufficiently small to capture the CO_2.

The trapping mode is also linked to the storage phases. During the injection phase, the structural trapping is the most important one. As the injection phase ends, other types of trapping gain in importance. We can see in Figure 1. 3 the evolution of different types of trapping with time. The dissolution and the mineralization trapping increase in importance after almost 1000 years after the injection period.

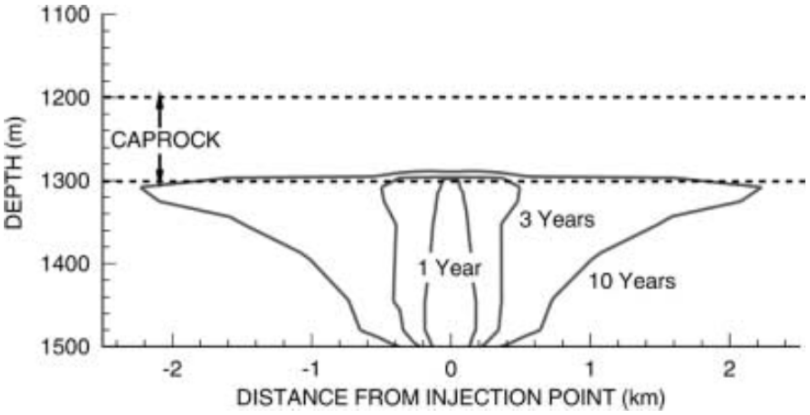

Figure 1. 2 – CO_2 plume after one, three and 10 years- Numerical simulation by (J Rutqvist & Tsang, 2002)

The dissolution of CO_2 in the water represents the major type of trapping in the long term. This trapping mode plays another important role (other than the trapping itself) in the storage process. Once the CO_2 is dissolved in water, the change in the chemical composition of pore water can play a role in the integrity reservoir evaluation. The acidic water with a low pH will induce minerals dissolution, which can change rock mechanical and physical properties like strength, fracture toughness, porosity and permeability. The changing of these parameters can provoke a loss of integrity which might potentially lead to uncontrolled fracturing from the reservoir to the caprock, hence inducing new leakage pathways. On one hand, once dissolved, the CO_2-rich fluid will have larger density than the resident reservoir fluid. Hence the natural tendency for gaseous CO_2 for upward migration will be inverted and the CO_2 aqueous will migrate downwards so that the leakage risk is expected to be decreased over time. On the other hand, once the CO_2 is dissolved in water, it will degrade the medium that can increase the potential of leakage over time.

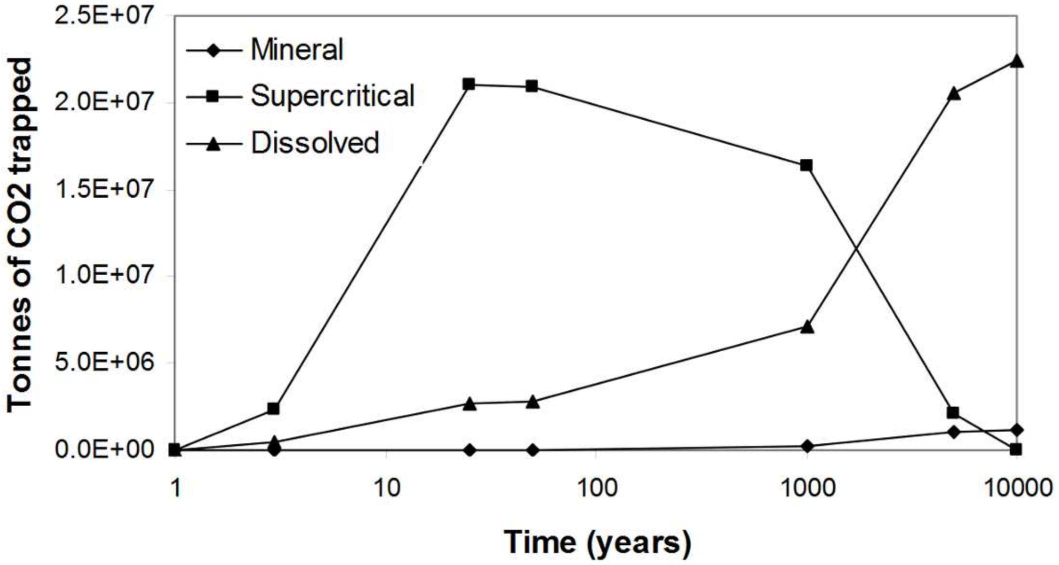

Figure 1. 3 – CO_2 trapping evolution at Sleipner, North Sea **(Audigane, et al, 2007)**

1.1.1.1 Zones of a Reservoir rock storage system

In reservoir rock storages, concerning the CO_2 concentration, we can divide the rock formation in three parts, as we can see in Figure 1. 4.

Close to the injection zone we can see the first region with almost only supercritical CO_2, then it can be observed the second zone, which is a biphasic one with a mixture of water and CO_2. Far from the injection zone it's the third one where it can be found a CO_2-saturated water region.

Interested phenomena can be seen in all zones. In the first zone, with a high concentration of CO_2 we can observe that the rock is dried by the CO_2, that alone is inert to the rock (in chemical terms). Depending of the rock formation this can stimulate the initiation of cracks. In the second zone the biphasic mixture provokes a heterogeneous dissolution of the rock, with the formation of what it can be called wormholes. While in the third zone, as the supercritical CO_2 has been completely dissolved in the aquifer's water the dissolution process is homogenous (André et al, 2007), as can be seen in Figure 1. 5. This third zone is the one studied in this work.

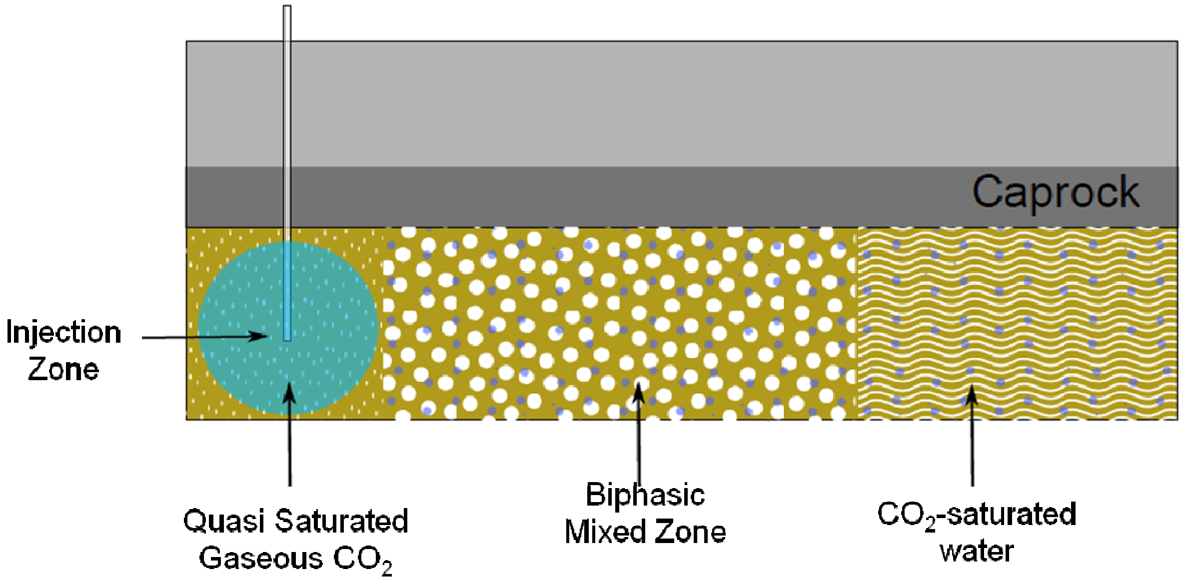

Figure 1. 4 - Zones of a reservoir rock

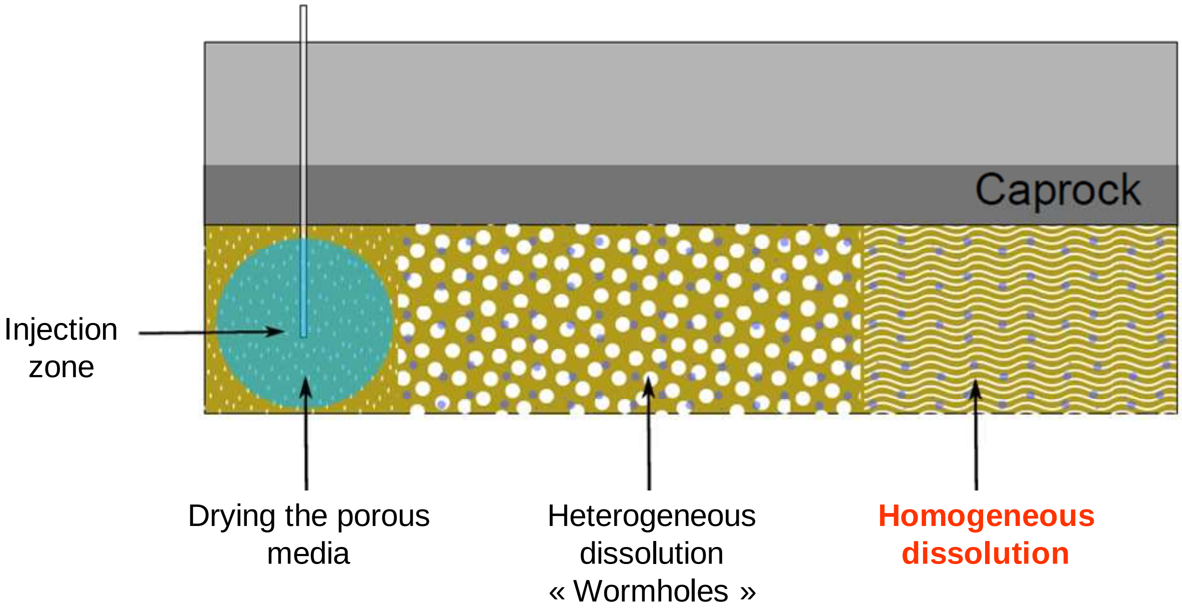

Figure 1. 5 - Difference of phenomena for different zones

1.1.1.2 Risks of CO_2 leakage

Concerning the risk of leakage, a prerequisite to CCS large scale industrial developments is the demonstration by the operators that the containment is effective and that the storage is safe (IEA Greenhouse Gas R&D Program (IEA-GHG), 2007).

One of the most important problems to analyze is: How to prevent the CO_2 leakage?

The lack of integrity on the reservoir-caprock system can affect several domains. Some of them are:

– Human impact: The CO_2 is dangerous at high concentrations (>5%)

– Environmental impacts:

- Vegetation: An increase to 30% concentration on the soil can be fatal to some vegetal species.
- Drinking water: The effect of the CO_2 leakage at freshwater is normally localized and should not affect other regions

– Rock integrity: Damage can occur under certain specific geological and hydrogeological conditions.

– CO_2-water-rock interaction: it plays an important role in the reservoir performance. The reservoir hydro-mechanical properties changes can:

- Affect the reservoir storage
- lead to an excessive pressure and affect the reservoir stability
- Provoke faults reactivation that potentially leads to a CO_2 leakage, and as a consequence alters the storage process

1.2 Deep underground storage

In this section we will describe the necessary elements to study deep underground CO_2 storages. In section 1.2.1 we talk about some of the particularities of the water-saturated chemical effects and in 1.2.2 we expose some generalities for the different types of reservoir.

1.2.1 Chemical effects

A major objective of this work is to investigate the role of chemical effects for the reservoir integrity.

Sites suitable for CO_2 geological storage are in sedimentary basins where the rock formation is typically: chalk, limestone and sandstone.

The CO_2 chemical effects of a storage site vary with (Le Guen et al., 2007, IPCC, 2005):

- type of reservoir – saline aquifer, depleted hydrocarbons or un-mineable coal seals
- reservoir rock mineralogy and cementation
- injection pressure that will affect the stress field
- temperature
- chemical reactions

The two most important parameters concerning the chemical effects on the rock are the pressure and the temperature in the reservoir.

The injection pressure affects the CO_2 storage in two different ways. First, it acts hydromechanically on the stress field and on the tendency for crack propagation, etc. Second, the overpressure increases the chemical reactions kinetics, provoking an increase of the minerals dissolution (Duan & Li, 2008).

The temperature has a fundamental role considering chemical, hydraulic and mechanical processes affecting the chemical equilibrium and the reaction kinetics, as well as the deformation and stresses in the rock formation. The temperature affects:

– The CO_2 concentration in water

– The minerals (e.g. $CaCO_3$) solubility in water + kinetics

Therefore, it is important to compare the influence of the pressure and the temperature in the dissolution processes of the specific mineral $CaCO_3$, knowing that the saturation concentration depends upon temperature and pressure.

Figure 1. 6 (data were taken from (Duan & Li, 2008)) shows the path followed by the $CaCO_3$ concentration in water passing from ambient conditions to reservoir condition (orange line). As we can see the temperature increase provokes a reduction of $CaCO_3$ solubility in water while the pressure increase induces a $CaCO_3$ solubility increase. However, as the calcite is a solid, the effect of temperature is more significant than the pressure.

The CO_2 solubility curve is shown in Figure 1. 7 based on the data from the work of (Duan & Sun, 2003). We can see here that, the influence of the pressure increase is more significant than the temperature for the considered range of temperature and pressure.

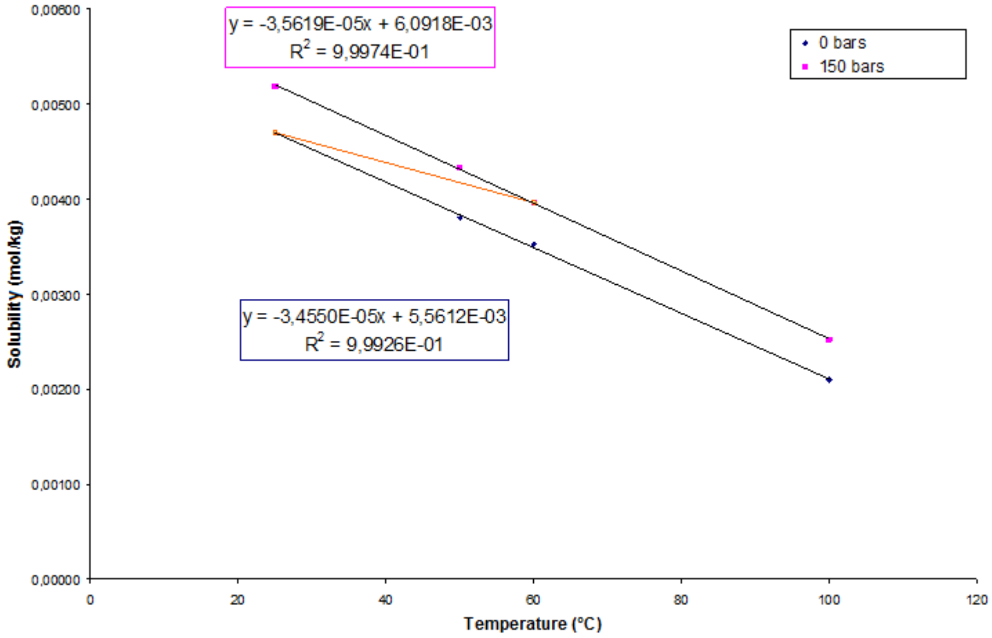

Figure 1. 6 - Influence of pressure and temperature on the $CaCO_3$ solubility [data from (Duan & Li, 2008)]

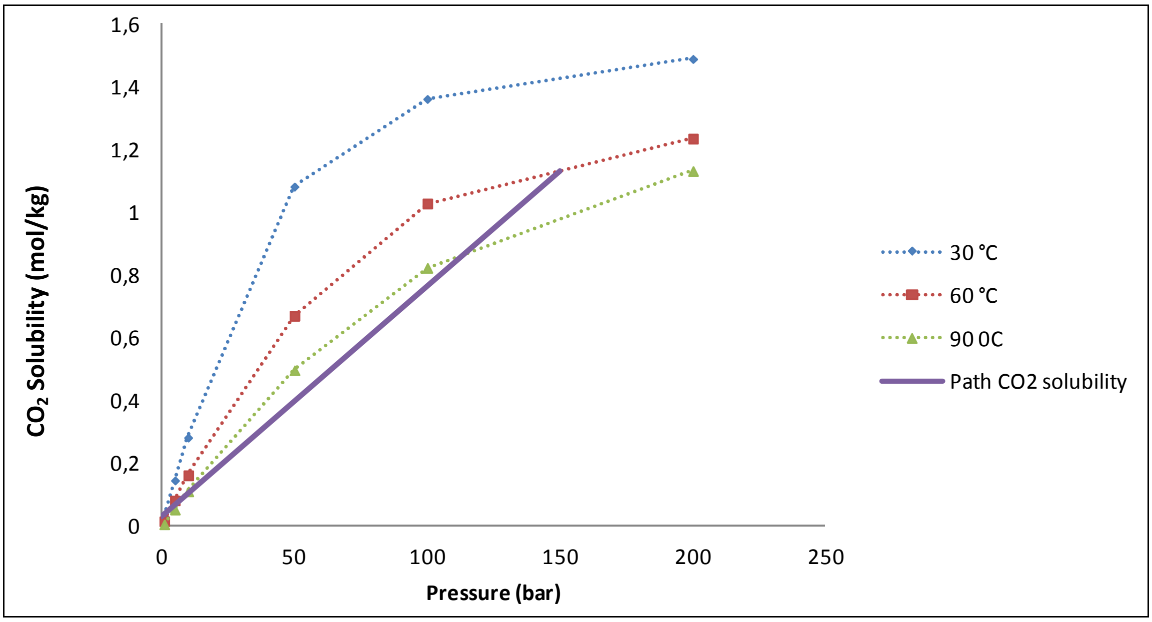

Figure 1. 7 – Effect of pressure and temperature on CO_2 solubility in water- [data from (Duan & Sun, 2003)]

1.2.2 Reservoirs

For each type of reservoir we can associate a particular chemical effect. They will be described below.

1.2.2.1 Type of reservoir

- *Saline aquifers*

The most intense CO_2 chemical reactions, that can impact a reservoir, occur when the CO_2 is dissolved in water. Though the presence of salts in the pore water has an important influence on the way the CO_2 is dissolved and on the way it reacts with the rock, we will not take them into account and consider just reaction with pure water. The approach is thus conservative, as CO_2 dissolves faster and to a larger concentration in pure water than in salted water (Figure 1. 8). First the CO_2 reacts with the water as follows:

$$CO_2(aq) + H_2O = [H_2CO_3] = H^+ + HCO_3^-$$

The water becomes acidic with the presence of the H^+ ions which affects the dissolution rate of the rock minerals. In carbonate rocks the dissolution follows the reaction:

$$H^+ + CaCO_3 = Ca_2^+ + HCO_3^-$$

Acidic water reacts stronger with some rock minerals as calcite. Even if we will give a general view of the storage possibilities with different types of reservoirs, we will only deal with chemical reactions derived from an aquifer reservoir in this work.

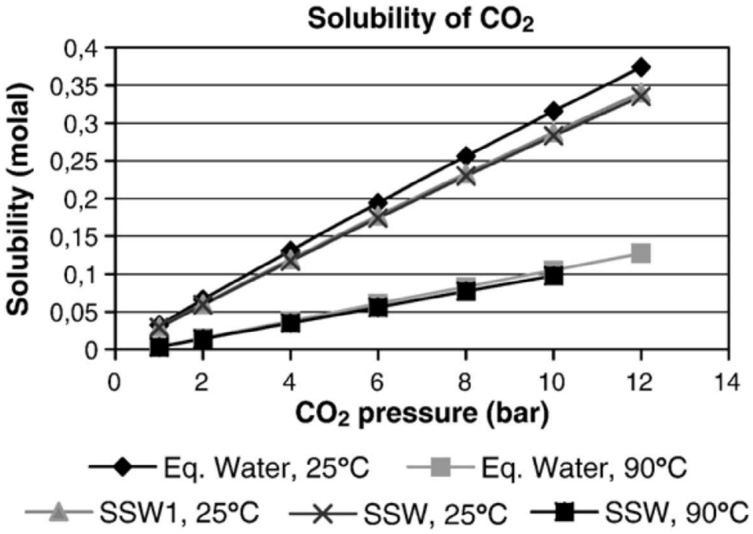

Figure 1. 8 – CO_2 solubility with temperature SSW Artificial salt water; SSW1 – artificial salt water modified (4 times the SO_4^{2-} concentration) Ekofisk site study (Madland, Finsnes, Alkafadgi, Risnes, & Austad, 2006)

- *Depleted oil reservoir and EOR (enhanced oil recovery)*

The CO_2 injected will react with the water and interact with the oil or gas within the rock formation allowing different phenomena to occur due to the CO_2 injection in an oil reservoir:

– The reservoir will have components of suction related to the water, oil and CO_2 that will vary with the CO_2 injection. The suction variability effect can reduce the rock resistance (Madland et al., 2006).

– The dissolution of some rock minerals is sensitive to acidic water.

- *Coal veins*

Carbon veins are rock structures with a radius that varies from 0.3 km to 1.3 km and a thickness from 1 to 30 m. Their permeability is generally very low and depends on the natural cracks and they are strongly compressible. The use of carbon veins to the CO_2 storage leads to completely different mechanisms from the salt aquifer or the oil reservoirs because the mineralogy of the rock and the CO_2 reactions are particular. The CO_2 storage in coal veins is used in the EBCM (Enhance coal bend methane recovery) technique, where CO_2 is injected to extract the methane.

This technique is possible due to the coal strong CO_2 adsorption which allows the enhancing of the methane production while storing the CO_2. In theory the CO_2 stays at the reservoir until the pressure reaches the CO_2 desorption pressure (Shukla, Ranjith, Haque, & Choi, 2010).

However, the CO_2 presence in the coal leads to a swelling phenomenon which is stronger than with the methane. This phenomenon leads to the reduction of the permeability once the cracks are closed. This can reduce the CO_2 injection performance. Nevertheless, the reservoir overpressure can reopen the cracks and increase the permeability again. The prediction of this permeability variation during the injection period is relevant to the injection planning and the project viability (Vandamme et al., 2010). Despite the importance of the study of this kind of reservoir, it will not be part of the present study.

1.2.2.2 Rock mineralogy

There are at least two types of rock formations that compose a storage site, the reservoir rock where the CO_2 is stored and the (impermeable) caprock which prevents the leakage. In reservoir rocks, the presence of calcite and dolomite can provoke strong reactions. We can say the presence of these minerals is one of the most important factors that can affect the integrity of the reservoir rocks (Hangx et al., 2013).

On other hand, the caprocks are mostly formed by rocks containing a significant quantity of clay minerals which do not react easily with CO_2 and which have a very low permeability. Therefore, we have to analyze the presence of:

– Carbonate minerals

– Clay minerals

– Sedimentary rocks cement – Calcite or dolomite;

We will analyze each of those below.

- *Carbonate minerals*

The carbonates, sulfates and evaporites have a fast kinetics reaction with CO_2-water (Kaufmann & Dreybrodt, 2007) and the reaction equilibrium is reached almost instantly (and considered as instantaneous in most numerical simulations). Therefore their presence indicates a strong dissolution potential, which when happens in a large scale can provoke a generalized pore collapse in the structure and will lead to significant reservoir subsidence (Stefanou & Sulem, 2014). This strong deformation of the reservoir affects the caprock and can induce the development of cracks which can be responsible for CO_2 leakage. However, (Sterpenich et al., 2009) points that most batch experiments tends to overestimate the dissolution rate.

- *Clay minerals*

The presence of clay minerals can involve two different phenomena. Concerning the clay minerals dissolution, the time scale to this phenomenon to occur is very large which we do not consider for short term behavior. Another, much more relevant phenomenon is the formation of cracks due to the drying of the water present in the rock in contact with supercritical CO_2 (I. Gaus, 2010).

The drying process happens because there is a percentage of the water that migrates from the rock to dissolve in the CO_2. This value is normally neglected, firstly because it is small and secondly because in sedimentary rocks they have a higher level of water, which means that the CO_2 will tend to dissolve in the water.

However, in the clay mineral formations, the presence of water is limited, so the tendency will invert, being the water that will be dissolved at the CO_2 and not the CO_2 that will be dissolved in water. This occurs mainly when the injected CO_2 in supercritical condition can reach the caprock with a considerable quantity of gas (Espinoza & Santamarina, 2012).

- *Sedimentary rocks cements*

The grains of a sedimentary rock are connected by cement and this component plays an important role in the chemical reaction scenario. As shown by Le Guen et al. (2007), the chemical reactions between a sandstones-CO_2-water are insignificant in short-term, so that the porosity and permeability changes are negligible. Nevertheless the importance of the cement is major when it is formed by calcite or dolomite, since these minerals are reactive with acidic water (Morse & Arvidson, 2002).

1.3 Objectives of the thesis

1.3.1 General description

In the present study, the following questions are addressed: what is the influence of CO_2-rock interactions on the mechanical behavior of reservoir rocks? More particularly does CO_2-induced dissolution affect the rock strength? And if so, can the effect have consequences on the storage integrity?

We will concentrate on the specific problem of the reservoir integrity, meaning we will not be looking for changes in properties that will not have an important impact on the reservoir safety.

Cracks propagation in the reservoir rock is the key issue of our study (Figure 1. 9), because crack propagation within the reservoir can have a strong influence on the fluid flow during injection, as can be seen in the example at In-Salah storage site (Morris et al., 2011), but may also play a role in the integrity loss of the reservoir-caprock system (Leguillon et al., 2014).

When we talk about the reservoir integrity one of the important questions is “which is the CO_2 limit pressure that can be injected at the reservoir?”

Mechanically speaking, when CO_2 is injected, it provokes an increase of the internal pressure that changes the stress field. If the pressure is high enough it can lead to crack propagation and the creation of preferential paths to the fluid flow. The creation of paths can be due to the evolution of the crack network.

However, the CO_2 presence on aquifer reservoirs has also chemical effects that can change the properties of the rock, and both consequences mechanical and chemical, can influence themselves reciprocally.

Several issues are then raised:

- the increase of pressure can accelerate the dissolution reactions
- the dissolution of the rock can facilitate the propagation of the cracks
- with the crack network development more reaction surface can be created, hence accelerating the dissolution process (Figure 1. 9).

To evaluate these questions we are interested in the analysis of:

- **Mechanical aspects** that are connected with the injection pressure with a focus on the fracture toughness
- **Chemical aspects** that are linked to the effect of minerals dissolution/precipitation on cracks development. This process can affect the mechanical and/or hydraulic properties.

These aspects are connected with the caprock integrity evaluation that is intimately linked with the storage integrity itself, therefore we should guarantee no crack propagation or damage through the isolating rock.

The mechanical parameter which controls cracks propagation is the fracture toughness of the rock. Therefore, an important aspect of this work is the experimental evaluation of the fracture toughness of rocks in modes I and II.

Different types of mechanical tests including indirect tractions tests such as the Brazilian disc test, the central crack notched Brazilian disc, the central crack Brazilian disc (BDT, CCNBD, CCBD); bending tests such as semi-circular Brazilian test and asymmetric semi-circular Brazilian test (SCB, ASCB) and shear tests such as the punch through shear test (PTST).

Moreover, SCB tests under water and CO_2-Saturated water were performed at low pressure (600 kPa). The effect of stress corrosion caused by the interaction between the fluid and the rock microstructure is evaluated.

We have performed mechanical tests with intact rocks and also with the same rock which has been chemically degraded in an autoclave at 60 °C and 15 MPa (typical reservoir conditions at which the CO_2 is in supercritical state). One of the objectives is, from a sufficient number of experimental results, to evaluate the Weibull parameters.

These parameters will be used for a probabilistic approach of crack initiation in an intact rock and for a chemically degraded one. The importance of this study is that for reservoir parameters analysis, as the fracture toughness, the evaluation may not be made only for a single medium value, but also for the determination of its probabilistic distribution, because the form of the distribution is essential to the integrity appraisal. More details about the Weibull statistical approach are given in the section 4 and the Appendix.

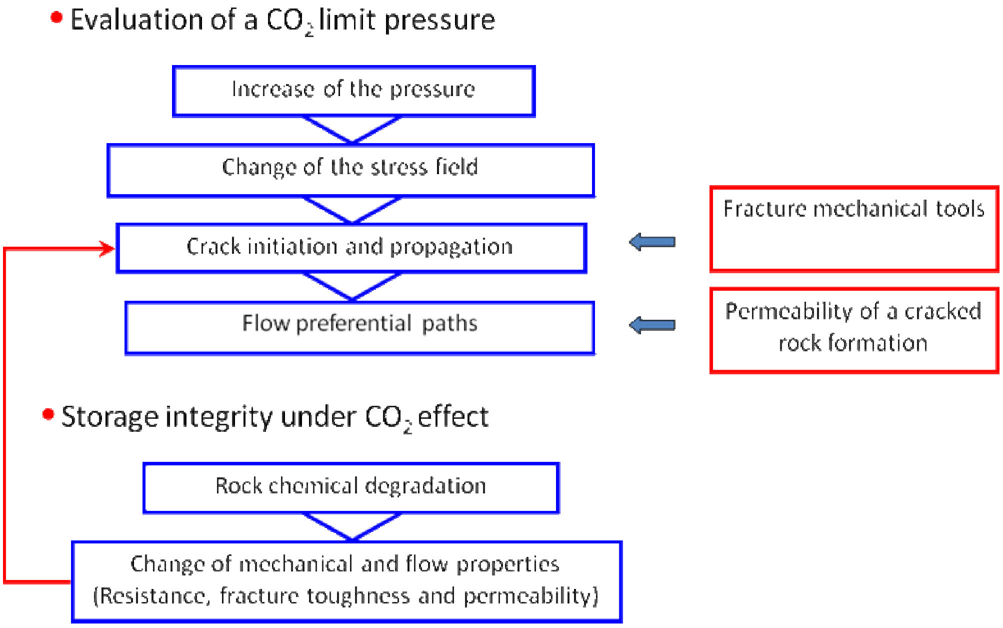

Figure 1. 9 – CO_2 sustainable injection pressure

1.3.2 General objectives

The general objectives are:

- Study the influence of chemical action of CO_2 on the fracture toughness of the reservoir rock
- Evaluate the performance assessment of the storage by the study of a crack network formation (performed with the finite element code Code_Aster@ and presented in the appendix)

1.3.3 Specific objectives

The specific objectives of the thesis are the:

- Performance of various fracture mechanical tests for the analysis of the influence of different aspects such as load and geometry
- Evaluation of fracture toughness for intact and degraded samples: Performance of the mechanical tests (intact samples and samples submitted to a four weeks period of CO_2 degradation in an autoclave – under reservoir conditions 15 MPa and 60 °C)
- Performance of mechanical tests submitted to water with CO_2 dissolved (acid water) under a pressure of 6 bars and ambient temperature (20 °C), to evaluate influence of the fluid on the fracture toughness of the rock

- Evaluation of Weibull parameters for the rock material, and the study of the probabilistic law for the intact and degraded rock, as the analysis of the influence of the Weibull modulus in a case study related to a deep reservoir.

1.4 Document structure

In the Part II (Fracture Toughness – Intact Rock) we describe some bases of the fracture mechanics theory, the methodology, the experiments set-ups for fracture tests, the results and the conclusions for the intact rock. We also describe the choice of rock material used in this work and we give a table of loading conditions for all fracture toughness methods.

In Part III (CO_2 effect on Fracture toughness) we describe some of the techniques used to degraded homogenously rocks with CO_2. The experimental set-ups for the chemical degradation in the autoclave, the SCB immerged test are also described, the characterization methods such as the mercury porosity and the SEM are also presented in this chapter. The results and the conclusions for the characterization of the degraded rock are also presented.

In the Part IV (Statistical Analysis of the limestone rock), we present the statistical analyze for the chosen rock.

In the General conclusions we discuss the results of the fracturing tests and their compatibility with the SEM and porosity analysis and we also summarize the main advances of this work and present some perspectives for future works.

1.5 Conclusion

The CO_2 storage raises several points of discussion that are interesting, in this chapter we tried to give an overview of them as we pointed the parts of the general discussion that will be relevant to this specific study, as we focus on integrity and CO_2 impact on intrinsic characteristics/properties (specially the fracture toughness of the rock) and parameters of the material.

Part II – Fracture Toughness Intact Rock

Contents

As discussed in the previous chapter, the integrity analysis in the CO_2 storage context in a reservoir rock has two different approaches that are connected with each other mechanical and chemical.

The first approach is to analyze the rock ability to resist crack propagation, this is what will be explained in this chapter. Therefore, we study in this part the elements of fracture mechanics that are essential to this study. We expose the mechanical tests chosen to characterize the chosen rock, the size choices concerning the sample, the notch and other geometry aspects.

Then, the results of the mechanical tests in intact samples are discussed, explaining which test has more repeatability and is easier to perform concerning the manufacturing of the samples and the test itself. A future comparison with the degraded samples will be made on the next chapter.

2.1 State of the art

In this section we will discuss the elements of the literature that give us the bases to the study we are performing here. We will give an overview of the fracture mechanic bases, the empirical relations existing between fracture toughness and other properties more commonly evaluated and the existing tests to evaluate rocks and more precisely the fracture toughness of the rock.

2.1.1 Fracture Mechanics bases

Fracture mechanics is the study of crack propagation. This implies the existence of an initial defect in the material. The defect can be a crack, a notch, or a fault depending on the scale. When the material, containing an initial defect, is submitted to a change in the stress field, the stress distribution will be affected by the presence of the defect.

In this work we are interested in brittle fracture of rock materials. Rocks are considered brittle materials, which means that they have a discontinuous behavior during the rupture process. The material will lose strength abruptly, and cracks will propagate through the material. Basic tools of fracture mechanics are recalled here.

2.1.1.1 A brief fracture mechanics history

In this sub-section, we will recall some of the earliest notions related with fracture mechanics that are still relevant today, like the works of Inglis, Griffith, Westergaard, Irwin and Rice.

(Inglis, 1913) analyzed the problem of a plate with an elliptical hole while (Griffith, 1921) studied the fracture thermodynamic criterion determining that the energy necessary to create a surface during a crack propagation was equivalent to the internal strain energy plus the external work, i.e. potential energy.

A few years later (Westergaard, 1939a) found the expression for the stress field around a crack. Following the work of Griffith, (Irwin, 1957a) developed the concepts of the energy release rate (G) and the stress intensity factor (SIF).

Another contribution of extreme importance was the J integral derived by (James R. Rice, 1968). The general concept is that the calculation of the energy variation rate is path-independent. These items will be discussed in the subsequent sub-sections.

2.1.1.2 Crack propagation modes

Before studying concepts as energy, stress field and etc, it is necessary to separate the types of crack propagation because the way and when each one will occur is relevant, and will be an important conclusion of this work.

As it is known, there are three different modes of crack propagation as shown in Figure 2. 1 :

- mode I – traction (opening mode),
- mode II – shear in the plane,
- mode III – shear out of the plane.

These propagation modes can happen isolated or mixed. Therefore a crack can propagate by:

- just one mode :
    - mode I
    - mode II
    - mode III
- a combination of two modes:
    - mode I and mode II
    - mode I and mode III
    - mode II and mode III
- a combination of the three modes : mode I, mode II and Mode III.

It is fundamental to understand the conditions for which they appear isolated or combined. These cracks propagate differently depending on the stress field configuration. It is important to notice that the direction propagation in mode I is not always collinear to the initial crack as shown in Figure 2. 2.

The Figure 2. 2, taken from the study performed by Cai (2012), shows the propagation of wing cracks and secondary cracks in a CCBD test with an inclined crack, the wing cracks as we can see in the literature are mode I cracks that are not collinear with the pre-existent crack, but propagates parallel to the higher principal stress direction (NMAB, 1983). It is important to be attentive with the literature expressions, once for the National Materials Advisory Board calls the wing cracks as secondary cracks.

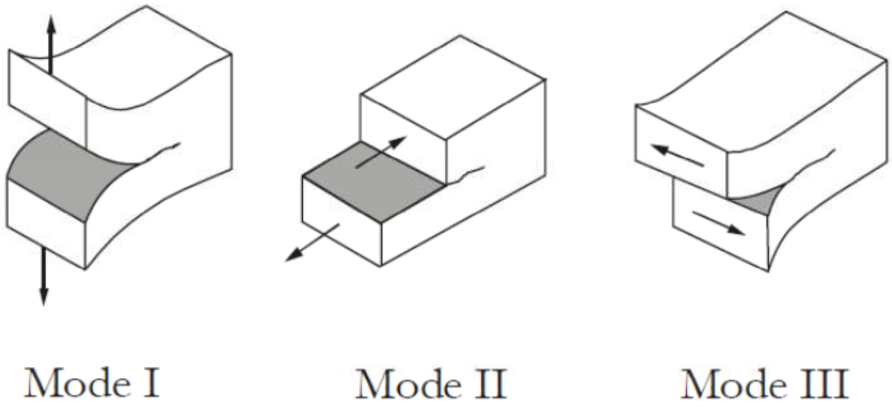

Figure 2. 1 - Crack propagation modes

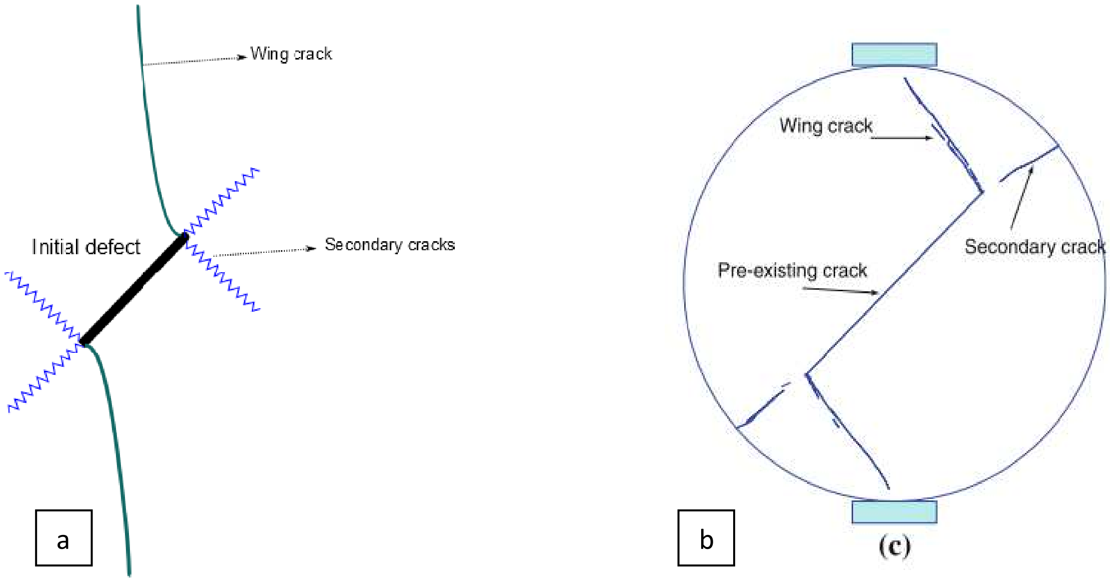

Figure 2. 2 - a) General scheme of a wing crack, b)simulation of a CCBD test (Cai, 2012)

2.1.1.3 Microcracks effects and Griffith criterion

The existence of microcracks reduces the capacity of a material to resist an external change of the stress field. This happens due to the surface reduction and stress redistribution as shown in Figure 2. 3.

As we can see in Figure 2. 3 when a crack appears there is a reduction of the internal surface from A to A_f. We can, then, expect stresses increase around the crack. The area of the sample A is higher than the effective surface that will support the load A- A_f, as $A > A - A_f$, consequently $\sigma < \sigma_f$. Under a higher stress the sample happens to be less resistant.

Griffith, having made several glass rods of different sizes, noticed that the resistance decreases when the size increase. This is possible, because in a larger specimen it is more probable to have an internal flaw that will lead to rupture. The effect is easily noticed when there is no confining pressure, because with confinement, the cracks can close, or even seal, adding resistance by friction and cohesion.

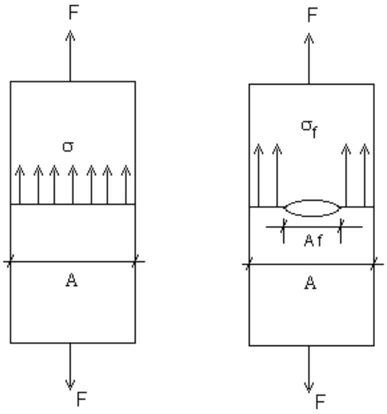

Figure 2. 3 - Stress concentration due the crack presence and stress configuration around the crack

2.1.1.3.1 Griffith released energy rate

Another important contribution to fracture mechanics is the Griffith criterion for crack propagation. It says that a new crack surface will be created (augmentation of the crack surface) when the internal energy and the external work are sufficient to create a new crack surface. So for a brittle material:

$$G \overset{\text{def}}{=} -\frac{\partial \Pi}{\partial a} = \frac{\partial W}{\partial a} - \frac{\partial U^e}{\partial a} = \frac{\partial \Gamma}{\partial a} = 2\gamma \tag{2.1}$$

where G is the energy release rate, W the external work, U the internal energy (plastic and elastic) and Γ surface energy, Π the total energy, γ the surface energy of the solid and a the crack length. And the propagation will occur when:

$$d\Pi \geq 2\gamma \mathrm{da} \tag{2.2}$$

Noting that the difference between $d\Pi$ and $2\gamma\mathrm{da}$ is the kinetic energy.

2.1.1.4 Westergaard solution and the stress intensity factor

Continuing the basis of the Inglis work in the elasticity theory, (Westergaard, 1939b) solved the problem of an infinite plate with a central crack submitted to a constant bi-axial stress σ_0 and found the following expressions for the stress tensor:

$$\sigma_{xx} = \sigma_0\sqrt{\frac{a}{2r}}cos\frac{\theta}{2}\left(1 + sin\frac{\theta}{2}sin\frac{3\theta}{2}\right) \tag{2.3}$$

$$\sigma_{yy} = \sigma_0\sqrt{\frac{a}{2r}}cos\frac{\theta}{2}\left(1 - sin\frac{\theta}{2}sin\frac{3\theta}{2}\right) \tag{2.4}$$

$$\sigma_{xy} = \sigma_0\sqrt{\frac{a}{2r}}cos\frac{\theta}{2}sin\frac{\theta}{2}sin\frac{3\theta}{2} \tag{2.5}$$

Then, (Irwin, 1957b) introduced the concept of Stress Intensity Factor (SIF) as:

$$\begin{Bmatrix} K_I \\ K_{II} \\ K_{III} \end{Bmatrix} = \lim_{r\to 0;\theta\to 0} \sqrt{2\pi r}\begin{Bmatrix} \sigma_{yy} \\ \sigma_{xy} \\ \sigma_{yz} \end{Bmatrix} \tag{2.6}$$

which is the correspondent measure of the strength at the crack tip. Applying this definition to the Westergaard problem we have for the mode I of crack propagation:

$$K_I = \sigma_0\sqrt{\pi a} \tag{2.7}$$

The SIF permits the study of the effects of the singularity of the stress at the crack tip as shown in Figure 2. 4.

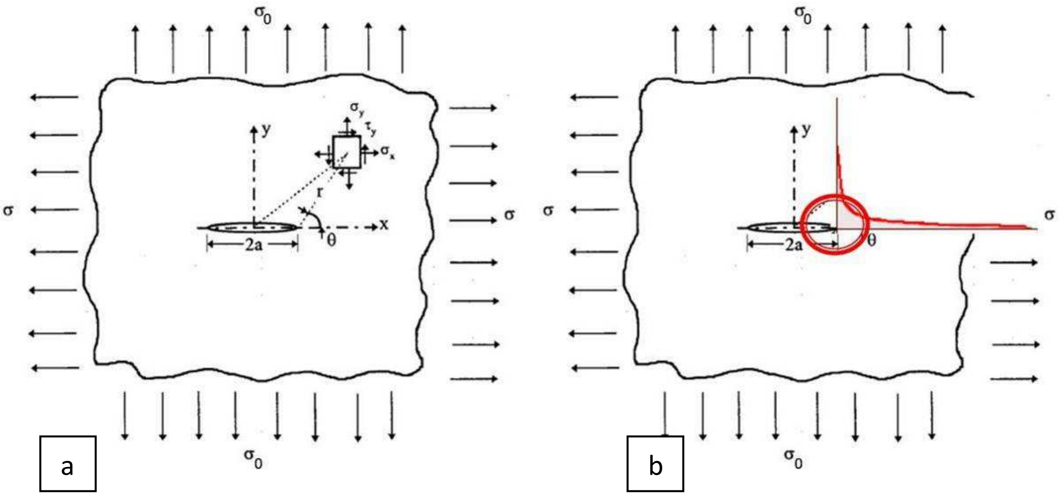

Figure 2. 4 - a) Infinite plate submitted to a bi-axial stress - b) Stress concentration zone around the crack tip

2.1.1.5 Variation from the Westergaard solution – How to calculate the SIF from the displacement field?

Another important and interesting method to calculate the SIF is based on the asymptotic crack lips displacement field (Westergaard, 1939).

Considering that:

$$K_I = \lim_{r\to 0} \sigma_{yy}\sqrt{2\pi r} \tag{2.8}$$

we can rewrite the equation in terms of the displacement of the crack lips (Figure 2. 5):

$$K_I = \frac{E\sqrt{2\pi}}{8\eta} \lim_{r\to 0} \frac{[u_n]}{\sqrt{r}} \tag{2.9}$$

where E is the Young modulus, η a term that depends of the type of analysis (for plane stress η=1 and for plane strain η=1-ν²), *r* the distance from the crack tip and u_n the normal displacement.

The $\lim\limits_{r\to 0}\dfrac{[u_y]}{\sqrt{r}}$ $\lim_{r\to 0}\frac{[u_y]}{\sqrt{r}}$ expression can be replaced by $\sqrt{\beta_I}$, knowing that β_I is the slope of the curve $u_n^2\, u_y{}^2$ *versus r*, we can see an example at the Figure 2. 6.

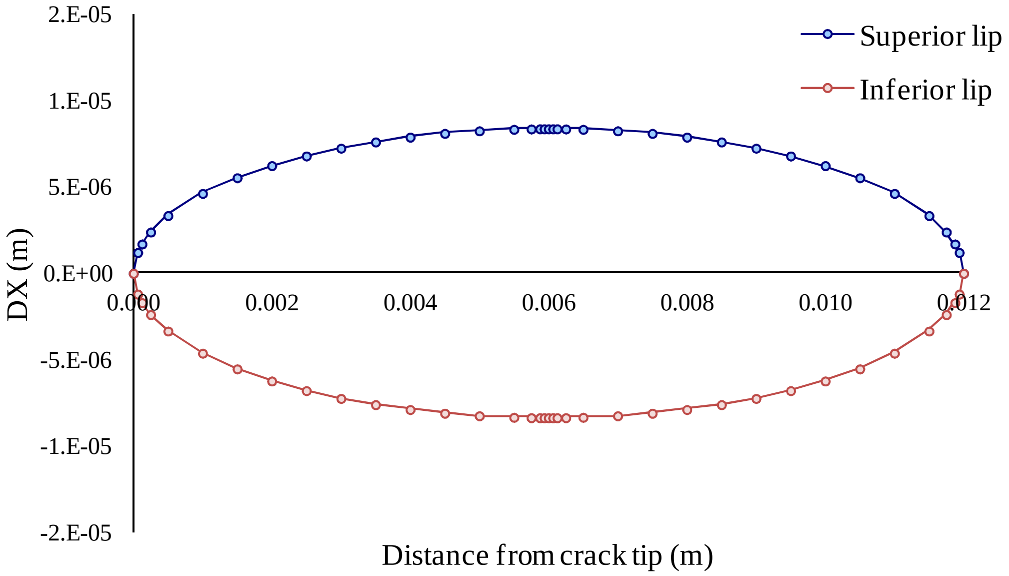

Figure 2. 5 - Displacement of the crack lips

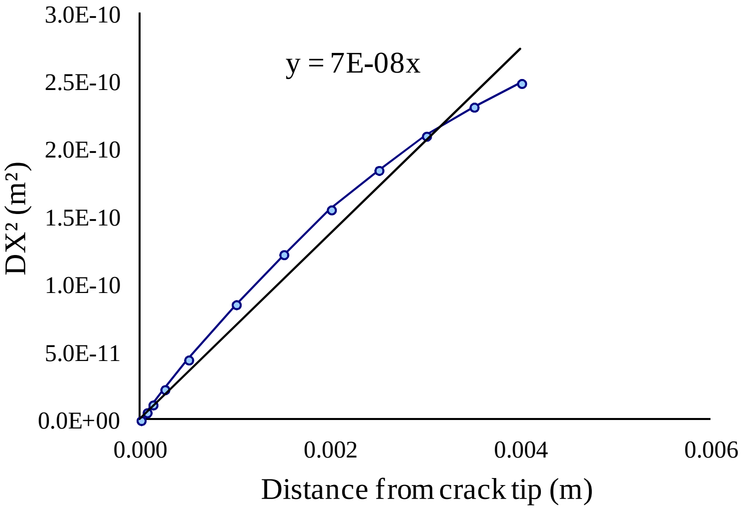

Figure 2. 6 – Example of curve for determination of β, β=7.10-8m

We have then:

$$K_I = \frac{E\sqrt{2\pi\beta_I}}{8\eta} \tag{2.10}$$

Similarly for mode II crack propagation we have:

$$K_{II} = \frac{E\sqrt{2\pi\beta_{II}}}{8\eta} \tag{2.11}$$

Where β_{II} is the slope of the curve $u_t^2 u_x{}^2$ *versus* r, where $u_t u_x$ is the tangential displacement. This analysis is useful in numerical simulations, because it can be applied to any configuration for a homogenous material.

2.1.1.6 Crack propagation criterion

At this point we can introduce a material property which is central in this work, the ***fracture toughness***. The fracture toughness or critical stress intensity factor K_{iC} (where i varies from I to III depending of the propagation mode), describes the capability of a material to resist a crack expansion. A crack propagates when the stress intensity factor is larger than the material fracture toughness.

$$K_{iC} \leq K_i \tag{2.12}$$

This relation expresses the limit that the SIF can go for each mode. However there are not only pure modes of crack expansion, but also mixed modes. The following expression shows the connection between the SIF for the three modes and the energy release rate (Irwin expression):

$$G = G_I + G_{II} + G_{III} = \frac{1}{E'}\left(K_I{}^2 + K_{II}{}^2 + \frac{K_{III}{}^2}{1-\upsilon} \right) \tag{2.13}$$

Where E’ differs from plane stress and plane strain, being E for plane strain and $E/1\text{-}v^2$ for plane stress. The critical energy release rate is given by:

$$G_I = \frac{{K_I}^2}{E'} \tag{2.14}$$

In theory, the Irwin expression as shown gives the coexistence between all modes. However, it supposes the collinear crack propagation, which means the crack propagation has to occur in the same direction as the initial crack (Leblond, 2003). This imposes that for a crack propagation a critical energy release will happen only for mode I, and when the crack is collinear (which is not true for wing cracks). However several experiments tried to define the critical energy release for mode II and III showing that they do not have necessarily the same value, as shown by (Vandello et al., 2012). Nevertheless for homogenous and isotropic materials the value for the critical energy release for the different modes is not significantly different.

2.1.1.7 Microstructure effect

The linear fracture mechanics derives from the elasticity theory that was derived from continuum mechanics (Guo et al. 1993). The macro scale observations are not more than the accumulation of micro scale effects that depends deeply of the rock microstructure (Kazerani, 2013).

A crack propagation model as the pore-emanated crack model developed by (Sammis & Ashby, 1986), clarifies the difference between the propagation by wing cracks (Figure 2. 7a) and the mechanism of pore-emanated crack on granular sedimentary rocks (Figure 2. 7b).

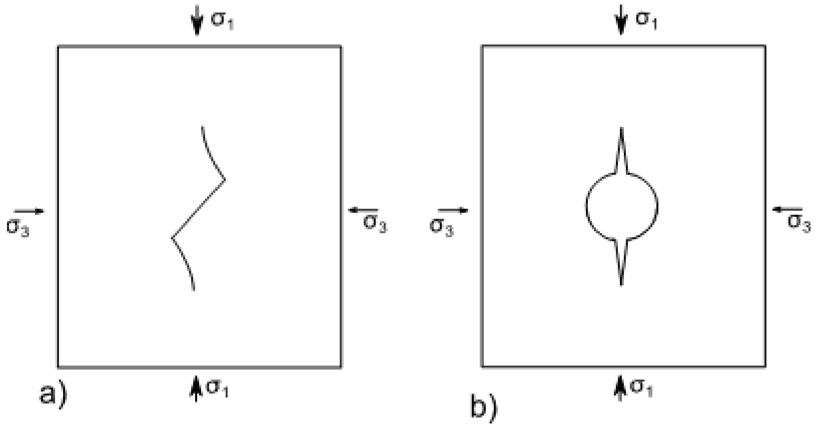

Figure 2. 7 - Crack propagation a) Wing cracks, b) Pore-emanated crack (after (Sammis & Ashby, 1986))

As shown by (Wolinskl et al., 1987) a crack generally propagates within a granular matrix around the grains. This happens because the energy required to contour the grain is lower than the energy to pass through it.

In Figure 2. 8a) we can see a damaged zone of a limestone sample, and in Figure 2. 8b) the cracks that propagates from the damaged zone around the grains.

Regarding the fatigue processes in classic fracture toughness tests, cracks that cannot propagate through grains are said to be stable, which means that the underlying crack growth process stems from subcritical propagation (Erarslan and Williams, 2012).

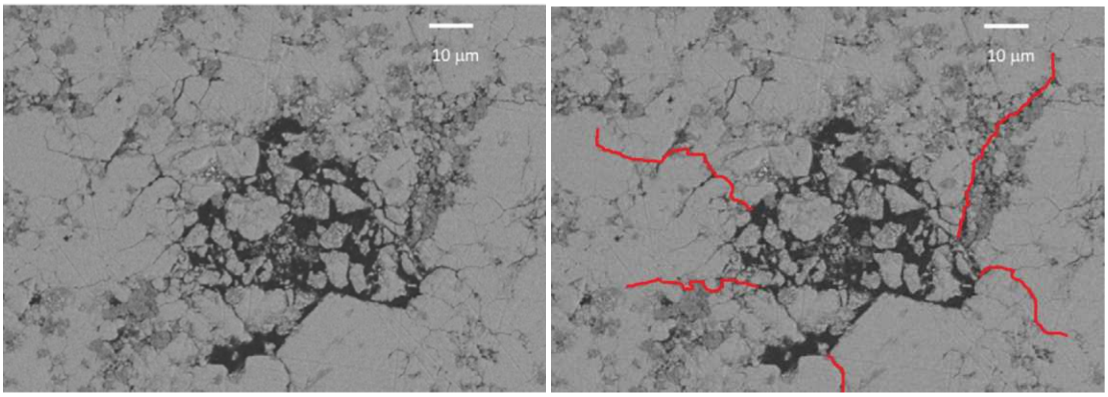

Figure 2. 8 - a) View of the damage zone b) Emphasis at the pore-emanated cracks that contour the grains during propagation (modified picture from (Wong & Baud, 2012)

2.1.1.8 Fluid effect

In order to study the mechanisms of crack propagation under geological condition, the analysis of the crack behavior submitted to a fluid contact is necessary.

It is known that a pressure increase in the fully saturated system increases the velocity of crack propagation Scholz (1992) and Atkinson (1984).

The hydro-mechanical and/or chemical effects of a fluid at a crack tip can induce crack propagation (Grgic & Giraud, 2014).

The chemical effect is a phenomenon that happens by the corrosion under stress in an aggressive environment. For some kind of rocks, especially limestone rocks, the water is a chemical agent that can dissolve the minerals. Rice (1978) showed that the stress corrosion effect, caused by the presence of a fluid on a rock material, reduces the surface energy needed to initiate the crack propagation.

In another study about the stress corrosion effect, more precisely, the study of the water effect in brittle fractures, was proposed by (Baud et al,. 2000) that was working in brittle faulting and cataclastic flow regimes for sandstones. They modified the sliding wing crack model proposed by (Ashby & Sammis, 1990) and the Hertzian fracture model of (Zhang et al., 1990) to include the chemical effects, specifically the reductions of fracture energy and toughness.

While (Lajtai et al., 1987), reproducing fracture toughness mechanical tests found for a granite that the presence of a fluid would produce a low decrease of the fracture toughness from 2.46 to 2.37 MPa.m$^{0.5}$.

2.1.2 Empirical correlations between the fracture toughness and other mechanical properties

In this section, we present some empirical relations that were proposed between the fracture toughness and other mechanical properties such as tensile resistance, brittleness, etc.

These relationships permit to estimate the fracture toughness of a rock material, without performing specific fracture toughness tests, or in the case of the Brazilian test without the determination of some internal parameter (initial maximum defect).

As these tests are more commonly performed, it can be very useful, in some occasions, to make an estimation using the results of these correlations.

2.1.2.1 Fracture toughness and tensile strength

Some authors have established empirical relations between the tensile strength and the fracture toughness as (Whittaker et al., 1992), (Zhixi, et al., 1997) and (Z. Zhang, 2002) .

The variety of rock materials tested by (Whittaker et al., 1992) was large including, limestone, granite, coal, marble etc. According to (Whittaker et al., 1992) this relation can be written as:

$$K_I = 0.27 + 0.107\sigma_t \tag{2.15}$$

For a coefficient of determination of 0,62 (R^2), knowing that (Zhixi, et al., 1997) found for shale and sandstone the following relation:

$$K_I = 0.27 + 0.085\sigma_t \tag{2.16}$$

with a coefficient of determination of 0,61. According to Zhang (2002) that used the data obtained by several authors to build its relation, the expression is with a 0.94 R^2:

$$K_I = 0.145\sigma_t \tag{2.17}$$

Knowing the values of K_I are expressed in MPa.$m^{0,5}$ and the σ_t in MPa.

In Table 2. 1 we can see the range of fracture toughness values observed by the authors.

Table 2. 1 - Some tensile strength values and the corresponding fracture toughness estimated values

Rock	Tensile Strength MPa	(Whittaker et al., 1992) K_I $MPa.m^{0.5}$	(Zhixi, et al., 1997) K_I $MPa.m^{0.5}$	(Z. Zhang, 2002) K_I $MPa.m^{0.5}$
Granite	7-25	1.019 – 2,70	-	1.015 – 3.625
Sandstone	4-25	0.698 – 2.70	0.25 – 1.1	0.58 – 3.625
Limestone	6-25	0.912 – 2.70	-	0.87 – 3.625
Marble	7-25	1.019 – 2.41	-	1.015 -2.90
Shale	3-8	-	0.51 – 0.65	-

2.1.2.2 Fracture toughness and acoustic emissions

The complexity of testing rocks coming from deep formations made (Zhixi et al., 1997) search for an alternative method to obtain the fracture toughness for rocks.

An interesting alternative to the traditional fracture toughness tests relied on geophysical data.

Performing tests with sedimentary rocks (SR - type reservoir rock) and shales (SH) and correlating with acoustic parameters like shear wave velocity V_s, compression wave velocity V_p and dynamic Young's modulus E_d, the following relations were found for the sedimentary rock and the shale respectively:

$$K_{IC_{SR}} = -0.332 + 3.6 \cdot 10^{-4} V_P \tag{2.18}$$

$$K_{IC_{SH}} = 0.388 + 5.4 \cdot 10^{-5} V_P \tag{2.19}$$

$$K_{IC_{SR}} = -0.552 + 6.1 \cdot 10^{-4} V_S \tag{2.20}$$

$$K_{IC_{SH}} = 0.349 + 1.4 \cdot 10^{-4} V_S \tag{2.21}$$

$$K_{IC_{SR}} = 0.2468 + 2.15 \cdot 10^{-2} E_d \tag{2.22}$$

$$K_{IC_{SH}} = 0.450 + 3.67 \cdot 10^{-2} E_d \tag{2.23}$$

With R^2 of 0.96, 0.75, 0.95, 0.80, 0.93, and 0.84 respectively.

2.1.2.3 Fracture toughness and Brittleness

There are two different brittleness indexes B_1 and B_2 and each one links itself with two other important mechanical properties, the compression strength σ_c and the tensile strength σ_t.

(Kahraman, 2004) have used the data given by (Bearman, 1999) to establish the following relations:

$$B_1 = \frac{\sigma_c \sigma_t}{2} \tag{2.24}$$

$$B_2 = \frac{\sigma_c - \sigma_t}{\sigma_c + \sigma_t} \tag{2.25}$$

Knowing that (Bearman, 1999) had obtained this relation having tested limestones, granites, sandstones, among others.

According to (Kahraman, 2004), we can link the fracture toughness and the brittlennes index through the follow empirical relation:

$$K_{IC} = 0.11 B_1^{0.42} \tag{2.26}$$

This relation has been obtained by compression and tensile tests and CB test (Chevron Bend specimen method).

Another relation using the SR method (Short rod specimen method) in a sandstone has been proposed by (Gunsallus & Kulhawy, 1984):

$$K_{IC} = 0.39 B_1^{0.22} \tag{2.27}$$

For a coefficient of determination of 0.60.

2.1.2.4 Fracture toughness and the point load strength

The point load test is a standard mechanical test for the strength analyzes of the rock. An invert cone applies a point load at the rock.

This test was also used by (Bearman, 1999) to create a correlation with the fracture toughness tests (CB method). The following relationship was found:

$$K_{IC} = 0.2 I_{s(50)} \tag{2.28}$$

Where $I_{s(50)}$ is the rock strength corrected by a diameter of 50 mm.

The relations for the SR test made by (Gunsallus & Kulhawy, 1984) gives the following relation:

$$K_{IC} = 0.0995 I_{s(50)} + 1.11 \tag{2.29}$$

2.1.3 Experimental techniques for the mechanical tests

As it was said previously, the main property analyzed in this work is the fracture toughness.

There are several mechanical tests that can be used to evaluate this property. The main differentiation between them is the method of loading, compression (or indirect traction), traction, bending, shear, torsion, etc and shape or type of crack (rectangular, circular, triangular, natural defect, pre-induced crack etc).

However in this work, as we don't study the third mode of crack propagation we will not discuss about the torsion mode, and we will not talk about several of the fracture toughness tests that will not be used in this work, as the SR method, CB method etc.

In most of the tests a created defect (that we call crack or notch) will be the initial point of weakness of the sample, but one test, the Brazilian Disc test discussed below, normally used to determine indirectly the tensile stress of the material, can also be used to determine the fracture toughness, if the size of the intrinsic characteristic defect can be known.

2.1.3.1 BDT – Brazilian disc test

The Brazilian disc test (Figure 2. 9) was developed in Rio de Janeiro – Brazil by professor Lobo Carneiro (Carneiro, 1953). It is a method to evaluate the tensile resistance in an indirect way. In other words, even if it is a compression stress that is applied at the sample and not a direct tensile effort, the rupture of the material is caused by a tensile stress field localized at the center of the sample.

In this work; we are particularly interested in another mechanical property, the fracture toughness, so by the work of (Guo et al., 1993) we can analyze the crack propagation of a rock by using the Brazilian test and determinate the fracture toughness of the rock.

For the technical details of a Brazilian test it is important to emphasize that there are different possible ways for the load application (Figure 2. 10), but (Erarslan & Williams, 2012) said these configurations were not able to guarantee the correct performance of the test.

This happens because the initial crack propagation would not start at the center of the sample (Figure 2. 11) as it should be to obtain the correspondent value of the fracture toughness (or tensile stress) of the material (Figure 2. 12). To avoid this complication we should use loading arcs, to prevent the rupture by shear stress (Figure 2. 13).

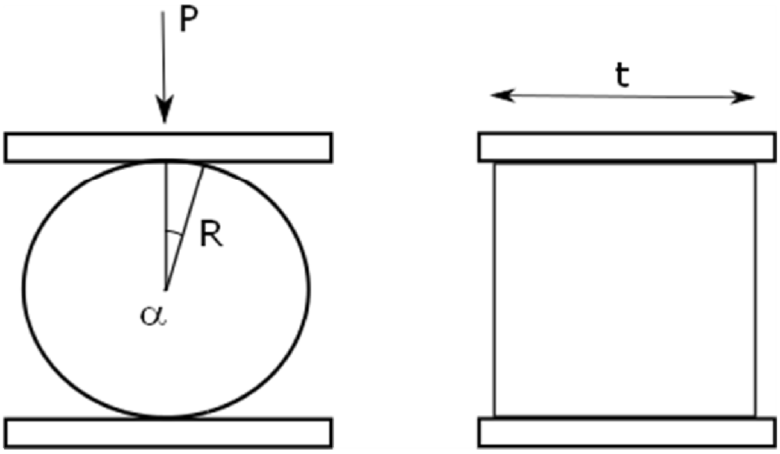

Figure 2. 9 - Brazilian test sketch

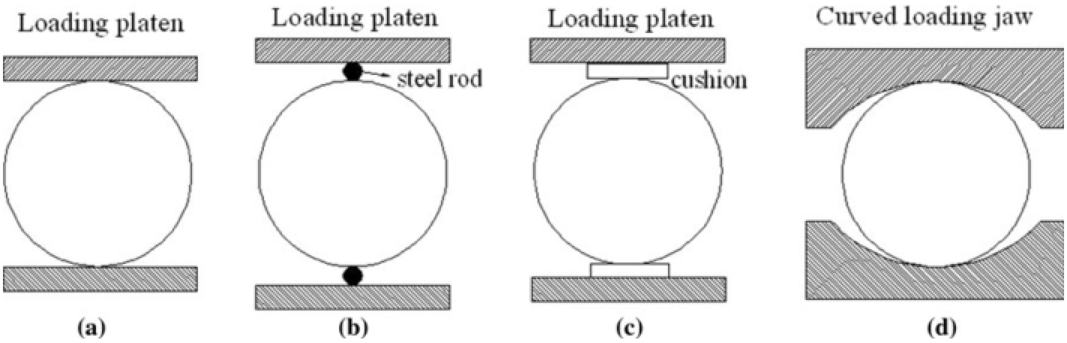

Figure 2. 10 - Different form of load application – Brazilian disc (Li & Wong, 2012)

In (Figure 2. 12) we can clearly see the crack initiation starting at the sample center, even if after the sample has been weakened we can see an initiation of a shear effort from the load support (Figure 2. 11). Therefore, in this work, we used two types of load support, the standard loading plate and the steel loading arc.

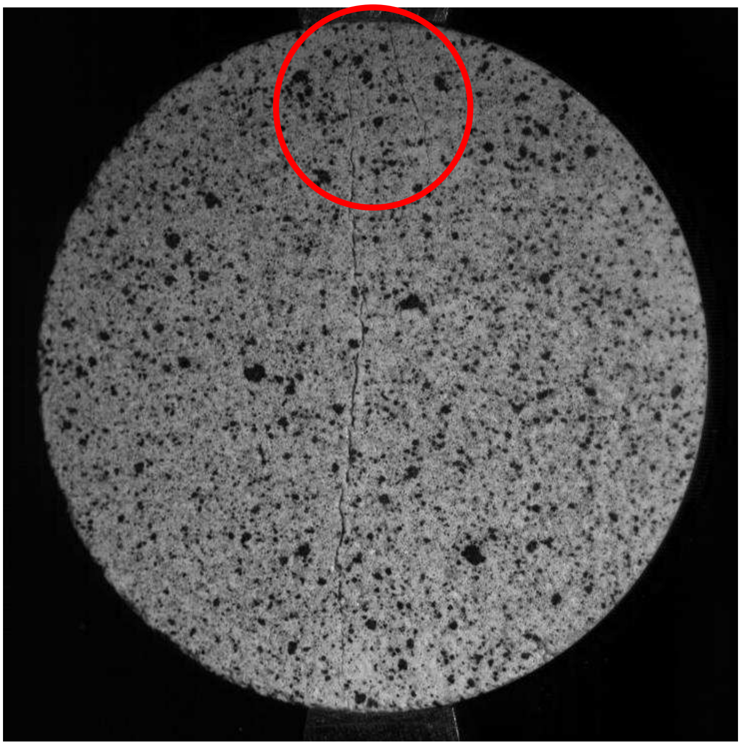

Figure 2. 11 - Photo of the sample after rupture - shear rupture initiation BDT15 sample

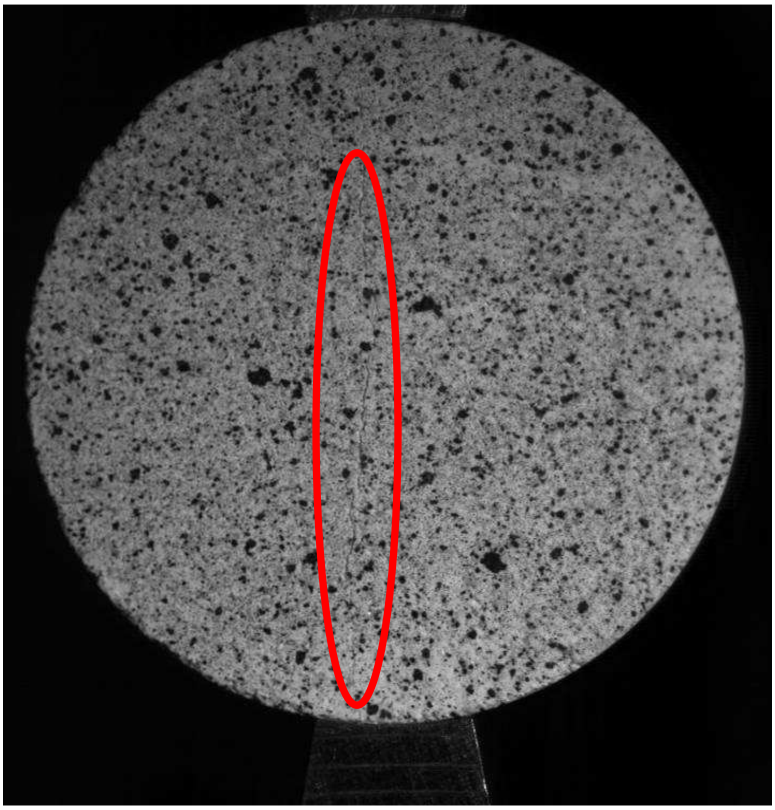

Figure 2. 12 - Sample submitted at a Brazilian test - crack initiation – diameter 40 mm – BDT15 sample

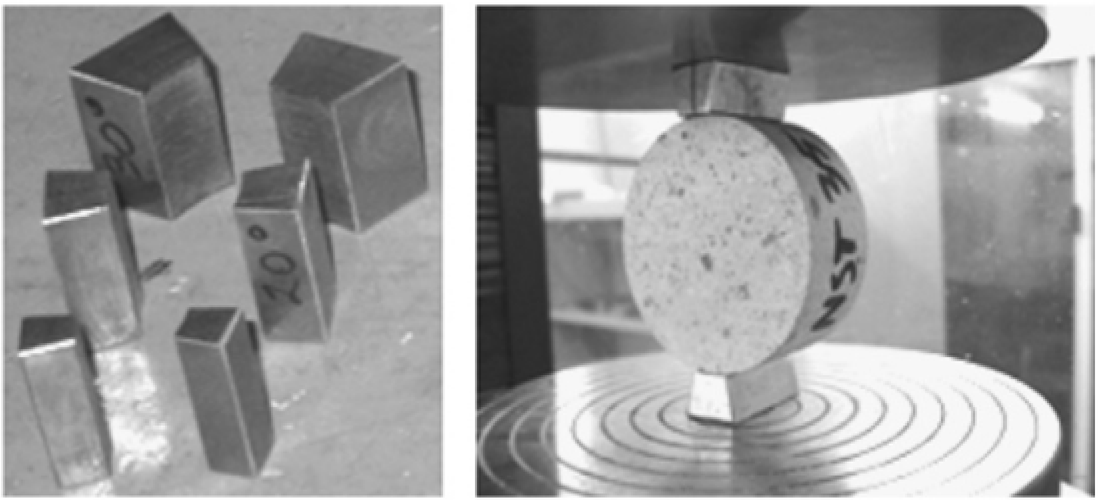

Figure 2. 13 – Steel loading arcs (Erarslan, et al., 2011)

It is important to emphasize that the stresses and the displacements fields are not the same as the boundary conditions are not identical (for the tests with and without an arc load "plate").

For the Brazilian test without the arc load plate (Figure 2. 9) the stress field is:

$$\sigma_{xx} = \frac{2P}{\pi L}\left\{\frac{(R-x)^3}{(R-x)^2+y^2} + \frac{(R+x)^3}{(R+x)^2+y^2} - \frac{1}{D}\right\} \tag{2.30}$$

$$\sigma_{yy} = \frac{2P}{\pi L}\left\{\frac{(R-x)\cdot y^2}{(R-x)^2+y^2} + \frac{(R+x)\cdot y^2}{(R+x)^2+y^2} - \frac{1}{D}\right\} \tag{2.31}$$

$$\sigma_{yy} = \frac{2P}{\pi L}\left\{\frac{(R-x)^2\cdot 2y}{(R-x)^2+y^2} + \frac{(R+x)^2\cdot 2y}{(R+x)^2+y^2} - \frac{1}{D}\right\} \tag{2.32}$$

Where *P* is the applied force, *R* the radius, l the thickness and *x* and *y* the geometrical positions we want calculate the stress field.

These relations are derivate from the complex potentials of Kolossov-Muskhelishvili described below by the equations (2.33) to (2.37).

$$\phi(z_c) = \frac{PR}{2L\pi}\left[\frac{z_c}{R} - \log\left(\frac{R+z_c}{R-z_c}\right)\right] \tag{2.33}$$

$$\Psi(z_c) = \frac{PR}{2L\pi}\left[\frac{R}{R-z_c} - \frac{R}{R+z_c} + \log\left(\frac{R+z_c}{R-z_c}\right)\right] \tag{2.34}$$

$$z_c = x + iy \tag{2.35}$$

$$\sigma_x + \sigma_y = 2\left[\phi'(z_c) + \overline{\phi'(z_c)}\right] \tag{2.36}$$

$$\sigma_x + \sigma_y + i\sigma_{xy} = -2\left[z_c\overline{\phi''(z_c)} + \overline{\Psi'(z_c)}\right] \tag{2.37}$$

For a Brazilian test where the load is applied in an arc section, the stress field change and the stress field for the coordinates along the load diameter are:

$$\sigma_\theta = \frac{P}{\pi RL\alpha}\left\{\frac{\left[1-\left(\frac{r}{R}\right)^2\right]\sin 2\alpha}{1-2\left(\frac{r}{R}\right)^2\cos 2\alpha+\left(\frac{r}{R}\right)^4} - \tan^{-1}\left[\frac{1+\left(\frac{r}{R}\right)^2}{1-\left(\frac{r}{R}\right)^2}\tan\alpha\right]\right\} \tag{2.38}$$

$$\sigma_r = \frac{P}{\pi RL\alpha}\left\{\frac{\left[1-\left(\frac{r}{R}\right)^2\right]\sin 2\alpha}{1-2\left(\frac{r}{R}\right)^2\cos 2\alpha+\left(\frac{r}{R}\right)^4} + \tan^{-1}\left[\frac{1+\left(\frac{r}{R}\right)^2}{1-\left(\frac{r}{R}\right)^2}\tan\alpha\right]\right\} \tag{2.39}$$

Where α is the semi-angle or the arc section (Figure 2. 14), and r the polar coordinate.

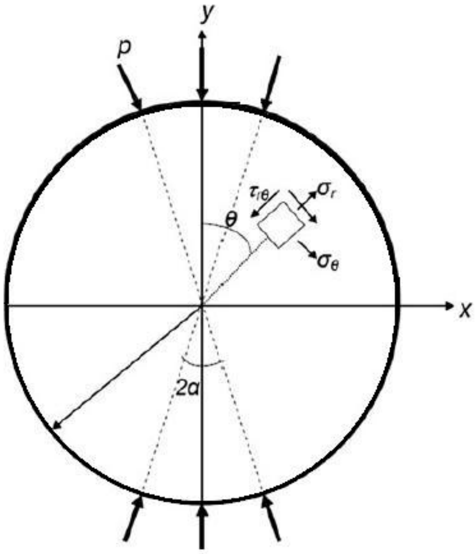

Figure 2. 14 – Brazilian disc submited to an arc loading (Erarslan et al., 2011)

(Guo et al., 1993) have established a method for the fracture toughness determination based on the results of the Brazilian test.

With different kinds of rocks he performed several mechanical tests with the Chevron Bend (CB) method, that is a classical ISRM method for evaluation of the fracture toughness for rocks (Ouchterlony, 1987) and the Brazilian test. (Guo et al., 1993), then correlate the CB results with the BDT results:

$$K_{IC} = \frac{2P}{L\alpha\pi^{3/2}R^{1/2}}\Phi\left(\frac{c}{R}\right) \tag{2.40}$$

Where P is the load, L the thickness of the sample, α the contact angle at the loading zone, R the radius of the sample and $\Phi\left(\frac{c}{R}\right)$ is:

$$\Phi\left(\frac{c}{R}\right)^{1/2} = \int_0^{c/R}\phi\left(\frac{r}{R}\right)\Big/\sqrt{\frac{c^2}{R}-\frac{r^2}{R}}\,d\left(\frac{r}{R}\right) \tag{2.41}$$

which can be estimated by the abacus of the Figure 2. 15.

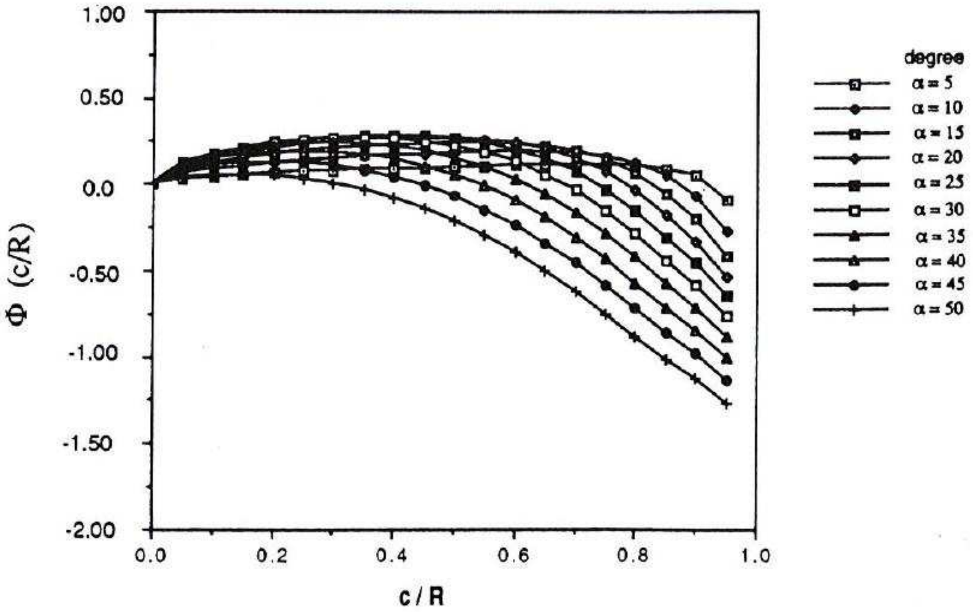

Figure 2. 15 - Abacus for the determination of □ by (Guo et al., 1993) – where c is the half notch crack

The expression for $\phi\left(\frac{r}{R}\right)$ can be found below:

$$\phi\left(\frac{r}{R}\right)=\left\{\frac{\left[1-\left(\frac{r}{R}\right)^2\right]\sin 2\alpha}{1-2\left(\frac{r}{R}\right)^2\cos 2\alpha+\left(\frac{r}{R}\right)^4}-\tan^{-1}\left[\frac{1+\left(\frac{r}{R}\right)^2}{1-\left(\frac{r}{R}\right)^2}\tan\alpha\right]\right\} \tag{2.42}$$

The expression (2.40) is derived from the fracture toughness expression (2.43) of a crack (2c length) submitted to a tensile stress in an infinite plate.

(Guo et al., 1993) assumed that the solution can be applied for a diametral crack on a disc.

$$KI=2\left(\frac{c}{R}\right)^{1/2}\int_0^c\left[\frac{\sigma(x)}{\left(c^2-x^2\right)^{1/2}}\right]dx \tag{2.43}$$

The biggest difficulty with this test is to choose the correct value for c. The value must represent the maximum defect present at the sample, and it should be located at the center of the sample.

2.1.3.2 *Fracture toughness tests for a loading mode type - Compression or indirect traction*

Other tests were created to improve the quality of the fracture toughness value. The BDT was not able to be enough accurate because of the difficulties imposed by the nature of the test. The imprecision of the value of the maximum defect and the difficulty of knowing where it is located were arguments to the development of other techniques.

Several tests use the indirect traction to measure the fracture toughness with several shapes.

However, maintaining the approximately same shape of the sample and the type of load the imprecision described above was perfected creating a defect at the center of the sample.

The two tests described in this sub-section are examples of this technique.

2.1.3.2.1 CCNBD - Central Crack Notch Brazilian Disc Test

The central crack notch Brazilian disc test is one of the tests proposed by the ISRM (Fowell, 1995) for the mode I fracture toughness evaluation on rock material.

The notch of the sample (Figure 2. 16) is made by a saw like in Figure 2. 17. We can see the general sketch can be seen in Figure 2. 18.

The expected dimensions, as it says the norm, have the following ratios:

$$\alpha_0 = \frac{a_0}{R} = suggested \quad 0.263 \rightarrow between \quad 0.2 - 0.3$$

$$\alpha_1 = \frac{a_1}{R} = suggested \quad 0.65 \rightarrow between \quad 0.4 - 0.8$$

$$\alpha_1 = \frac{a_1}{R} \geq \frac{\alpha_B}{2}$$

$$\alpha_B = \frac{B}{R} = suggested \quad 0.8$$

$$\alpha_s = \frac{D_s}{D} = suggested \quad 0.6933 \geq 0.44 \quad and \quad \geq 1.1729 \cdot \alpha_1^{7/6}$$

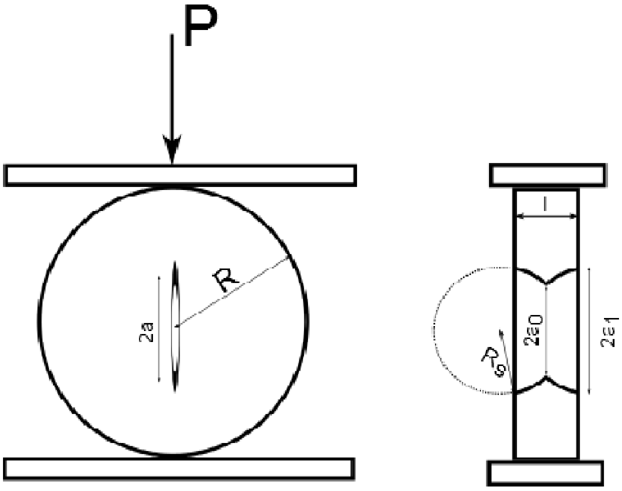

Figure 2. 16 – Sketch of the CCNBD test (Fowell, 1995)

where D_s is the saw diameter used to produce the notch, a_1 is the exterior notch size, a_0 the internal notch size, B is sample thickness, D the sample diameter.

The notch thickness must not be larger than 1.5 mm, to avoid changing the stress distribution. The diameter of the sample has to be larger than 10 times the maximum grain size. The notch has to be made by both disc faces as shown in Figure 2. 18.

The dimension of the saw disc that penetrates in the sample is h_c, and it is expressed by:

$$h_c = \left(\alpha_s - \sqrt{\alpha_s^2 - \alpha_0^2}\right)R + \frac{B}{2} \tag{2.44}$$

The sample has another condition to the diameter. The minimum value for it is called D_{min}, and it is important because it is the one that determine the minimum size of the sample for which we can find a constant value for the K_{IC} , that means, a value that will not change if we increase the diameter size.

The D_{min} can be estimated by the following equation (Fowell, 1995).

$$D_{\min} = 8.88 + 1.4744\left(\frac{K_{IC}}{\sigma_t}\right)^{-2} \tag{2.45}$$

For rocks the D_{min} is normally 75 mm, but it can be found in the literature different values as 20 or 35 mm (Iqbal & Mohanty, 2006) .

According to the ISRM recommendation the loading rate should not be greater than a value that would correspond to a stress intensity factor of 0.25 MPa.m^{0,5}/s and the rupture should not happen before 20 s.

Performing the test developed by (Fowell, 1995) the expression for the fracture toughness is:

$$K_{IC} = \frac{P_{max}}{B\sqrt{D}} Y^{*}{}_{min} \tag{2.46}$$

where $Y^{*}{}_{min}$ is a parameter that depends of the sample geometry and it is:

$$Y^{*}_{min} = u \cdot e^{v\,\alpha_1} \tag{2.47}$$

Where *u* and *v* can be found at the Table 2. 2.

Figure 2. 17 – Notch manufacturing method used in this work – saw of Navier laboratory

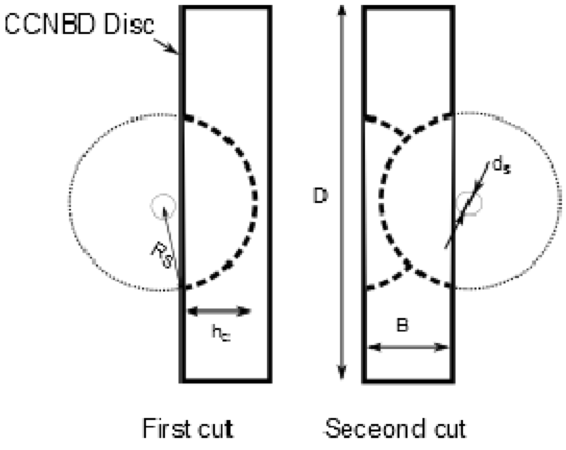

Figure 2. 18 – Notch manufacturing schema (Fowell, 1995)

Table 2. 2 - Values of *u* and *v*

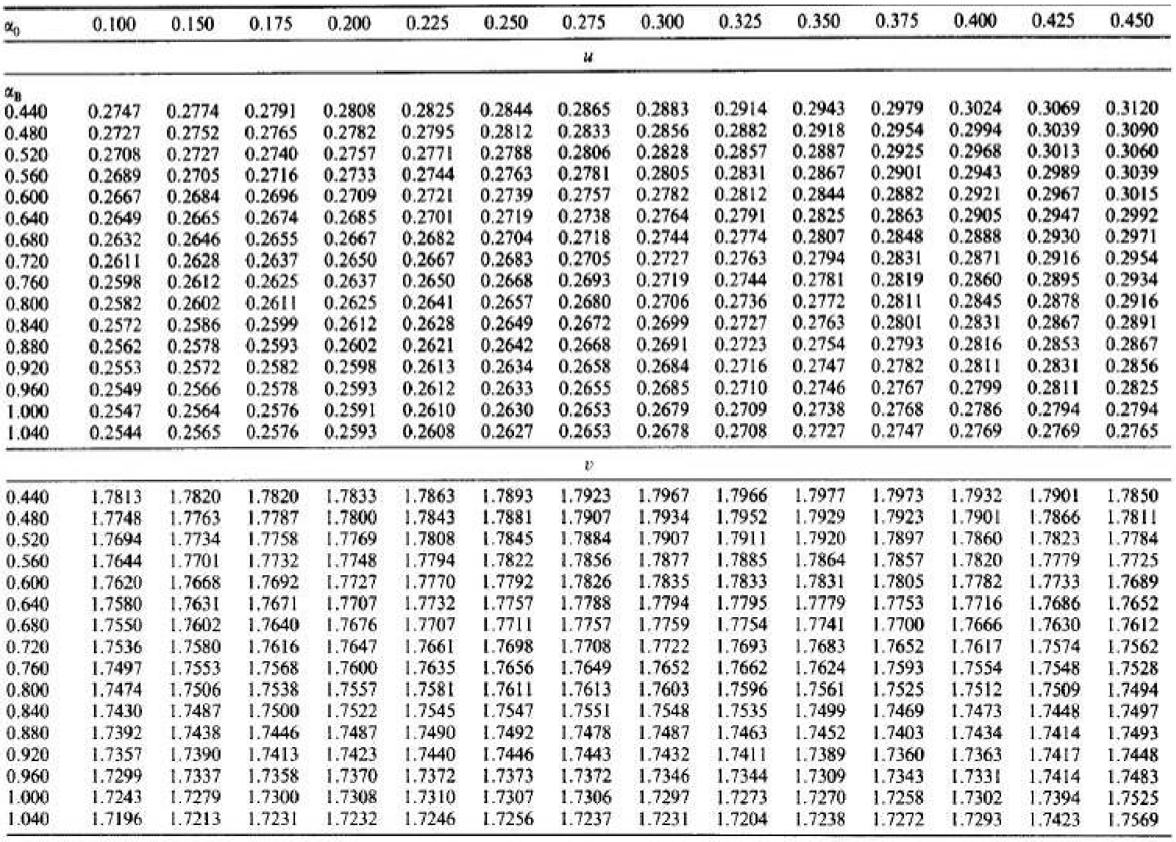

α_0	0.100	0.150	0.175	0.200	0.225	0.250	0.275	0.300	0.325	0.350	0.375	0.400	0.425	0.450
							u							
α_B														
0.440	0.2747	0.2774	0.2791	0.2808	0.2825	0.2844	0.2865	0.2883	0.2914	0.2943	0.2979	0.3024	0.3069	0.3120
0.480	0.2727	0.2752	0.2765	0.2782	0.2795	0.2812	0.2833	0.2856	0.2882	0.2918	0.2954	0.2994	0.3039	0.3090
0.520	0.2708	0.2727	0.2740	0.2757	0.2771	0.2788	0.2806	0.2828	0.2857	0.2887	0.2925	0.2968	0.3013	0.3060
0.560	0.2689	0.2705	0.2716	0.2733	0.2744	0.2763	0.2781	0.2805	0.2831	0.2867	0.2901	0.2943	0.2989	0.3039
0.600	0.2667	0.2684	0.2696	0.2709	0.2721	0.2739	0.2757	0.2782	0.2812	0.2844	0.2882	0.2921	0.2967	0.3015
0.640	0.2649	0.2665	0.2674	0.2685	0.2701	0.2719	0.2738	0.2764	0.2791	0.2825	0.2863	0.2905	0.2947	0.2992
0.680	0.2632	0.2646	0.2655	0.2667	0.2682	0.2704	0.2718	0.2744	0.2774	0.2807	0.2848	0.2888	0.2930	0.2971
0.720	0.2611	0.2628	0.2637	0.2650	0.2667	0.2683	0.2705	0.2727	0.2763	0.2794	0.2831	0.2871	0.2916	0.2954
0.760	0.2598	0.2612	0.2625	0.2637	0.2650	0.2668	0.2693	0.2719	0.2744	0.2781	0.2819	0.2860	0.2895	0.2934
0.800	0.2582	0.2602	0.2611	0.2625	0.2641	0.2657	0.2680	0.2706	0.2736	0.2772	0.2811	0.2845	0.2878	0.2916
0.840	0.2572	0.2586	0.2599	0.2612	0.2628	0.2649	0.2672	0.2699	0.2727	0.2763	0.2801	0.2831	0.2867	0.2891
0.880	0.2562	0.2578	0.2593	0.2602	0.2621	0.2642	0.2668	0.2691	0.2723	0.2754	0.2793	0.2816	0.2853	0.2867
0.920	0.2553	0.2572	0.2582	0.2598	0.2613	0.2634	0.2658	0.2684	0.2716	0.2747	0.2782	0.2811	0.2831	0.2856
0.960	0.2549	0.2566	0.2578	0.2593	0.2612	0.2633	0.2655	0.2685	0.2710	0.2746	0.2767	0.2799	0.2811	0.2825
1.000	0.2547	0.2564	0.2576	0.2591	0.2610	0.2630	0.2653	0.2679	0.2709	0.2738	0.2768	0.2786	0.2794	0.2794
1.040	0.2544	0.2565	0.2576	0.2593	0.2608	0.2627	0.2653	0.2678	0.2708	0.2727	0.2747	0.2769	0.2769	0.2765
							v							
0.440	1.7813	1.7820	1.7820	1.7833	1.7863	1.7893	1.7923	1.7967	1.7966	1.7977	1.7973	1.7932	1.7901	1.7850
0.480	1.7748	1.7763	1.7787	1.7800	1.7843	1.7881	1.7907	1.7934	1.7952	1.7929	1.7923	1.7901	1.7866	1.7811
0.520	1.7694	1.7734	1.7758	1.7769	1.7808	1.7845	1.7884	1.7907	1.7911	1.7920	1.7897	1.7860	1.7823	1.7784
0.560	1.7644	1.7701	1.7732	1.7748	1.7794	1.7822	1.7856	1.7877	1.7885	1.7864	1.7857	1.7820	1.7779	1.7725
0.600	1.7620	1.7668	1.7692	1.7727	1.7770	1.7792	1.7826	1.7835	1.7833	1.7831	1.7805	1.7782	1.7733	1.7689
0.640	1.7580	1.7631	1.7671	1.7707	1.7732	1.7757	1.7788	1.7794	1.7795	1.7779	1.7753	1.7716	1.7686	1.7652
0.680	1.7550	1.7602	1.7640	1.7676	1.7707	1.7711	1.7757	1.7759	1.7754	1.7741	1.7700	1.7666	1.7630	1.7612
0.720	1.7536	1.7580	1.7616	1.7647	1.7661	1.7698	1.7708	1.7722	1.7693	1.7683	1.7652	1.7617	1.7574	1.7562
0.760	1.7497	1.7553	1.7568	1.7600	1.7635	1.7656	1.7649	1.7652	1.7662	1.7624	1.7593	1.7554	1.7548	1.7528
0.800	1.7474	1.7506	1.7538	1.7557	1.7581	1.7611	1.7613	1.7603	1.7596	1.7561	1.7525	1.7512	1.7509	1.7494
0.840	1.7430	1.7487	1.7500	1.7522	1.7545	1.7547	1.7551	1.7548	1.7535	1.7499	1.7469	1.7473	1.7448	1.7497
0.880	1.7392	1.7438	1.7446	1.7487	1.7490	1.7492	1.7478	1.7487	1.7463	1.7452	1.7403	1.7434	1.7414	1.7493
0.920	1.7357	1.7390	1.7413	1.7423	1.7440	1.7446	1.7443	1.7432	1.7411	1.7389	1.7360	1.7363	1.7417	1.7448
0.960	1.7299	1.7337	1.7358	1.7370	1.7372	1.7373	1.7372	1.7346	1.7344	1.7309	1.7343	1.7331	1.7414	1.7483
1.000	1.7243	1.7279	1.7300	1.7308	1.7310	1.7307	1.7306	1.7297	1.7273	1.7270	1.7258	1.7302	1.7394	1.7525
1.040	1.7196	1.7213	1.7231	1.7232	1.7246	1.7256	1.7237	1.7231	1.7204	1.7238	1.7272	1.7293	1.7423	1.7569

However, (Chang, Lee, & Jeon, 2002) found the following expression by applying the STCA method (straight-through crack assumption) for the CCNBD test:

$$K_I = \frac{P}{\sqrt{\pi R B}}\sqrt{\alpha}\sqrt{\frac{\alpha_1-\alpha_0}{\alpha-\alpha_0}}N_I \tag{2.48}$$

$$K_{II} = \frac{P}{\sqrt{\pi R B}}\sqrt{\alpha}\sqrt{\frac{\alpha_1-\alpha_0}{\alpha-\alpha_0}}N_{II} \tag{2.49}$$

Where N_I et N_{II} are :

$$N_I = 1-4\sin^2\theta+4\sin^2\theta\left(1-4\cos^2\theta\right)\alpha^2 \tag{2.50}$$

$$N_{II} = \left[2+\left(8\cos^2\theta-5\right)\alpha^2\right]\sin 2\theta \tag{2.51}$$

This test has some problems, most of them related with the 3D notch geometry, but not only.

As the shaping of a simple rectangular notch is difficult, Fowell (1995) preferred to use a testing method from which it would be necessary to make a complicated analysis to the determination of the stress intensity factor (because the sample has a 3D shape not designable in a plane strain/stress analysis or an axisymmetric one), but that allowed a more reliable and reproducible notch.

This choice turned in a complicate numerical analyzes (3D) that is normally complementary to the experimental data. Another difficulty is the fact that the size of the crack depends of the sample thickness.

This happens because the notch is made from a saw in a sample of a thickness B.

The relation between a_0 and a_1 and the minimum value for the size a_1 are respectively:

$$a_1 = \sqrt{R_s^2-\left(\frac{\sqrt{R_s^2-a_0^2}-B}{2}\right)^2} \tag{2.52}$$

$$a_1 \geq \frac{\sqrt{4R_s-B^2}}{2} \tag{2.53}$$

Where Rs is the radium of the saw. If a_0 is equal to zero from the expression (2.54) we found the expression (2.55). Meaning no notch can be smaller than the value from the expression (2.56).

Another difficult concerns the reproducibility of the test, but this point will be discussed better in the results sub-section.

2.1.3.2.2 CCBD – Central Crack Brazilian Disc test

The central crack Brazilian disc test (Figure 2. 20) is an important fracture toughness test which allows, for any thickness of the sample, the shaping of a crack of any size (varying from 0 to the diameter of the sample). This happens because differently from the CCNBD samples, the size of the notch is independent from the sample thickness.

However, the sample preparation is more complicated, because a rectangular notch is not easily doable.

One of the tools for the shaping is a diamond saw machine (Figure 2. 19) (used in this work), but other methods are possible as the use of a laser to make the notch.

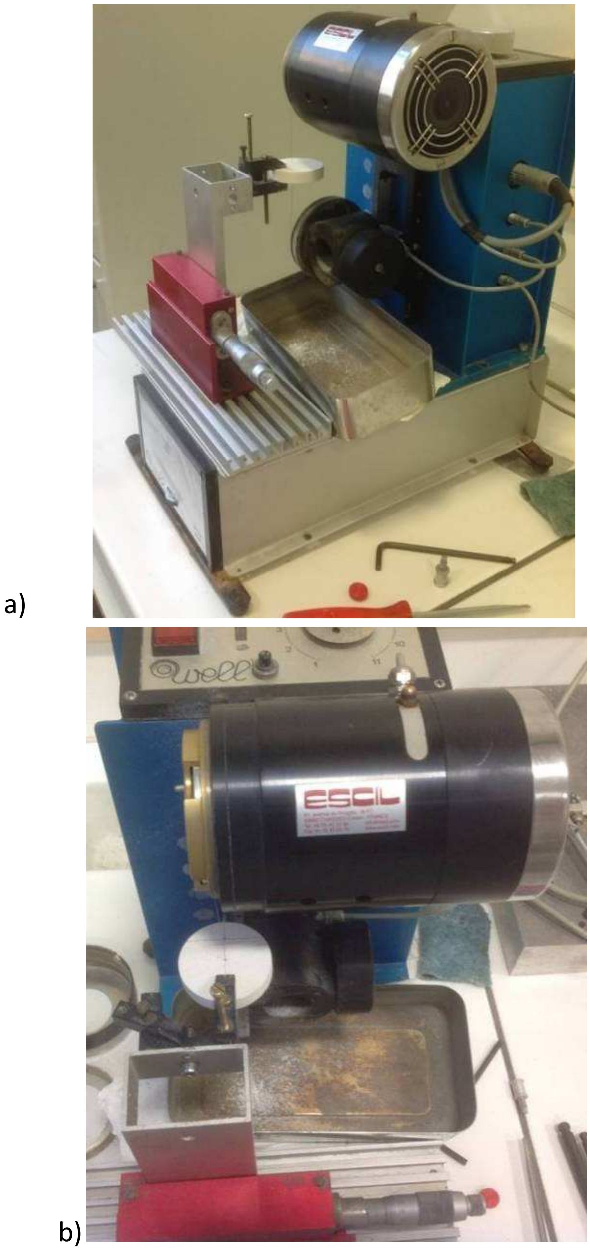

Figure 2. 19 - Diamond saw machine a) view of the inclined plan b) up view of the cutting system (LMS-Polytechnique)

For the CCBD test the fracture toughness for mode I and mode II are:

$$K_I = \frac{P\sqrt{2a}}{\sqrt{\pi}RL} N_I \quad (2.57)$$

$$K_{II} = \frac{P\sqrt{2a}}{\sqrt{\pi}RL} N_{II} \quad (2.58)$$

Where P is the load, *a* the semi-notch, *R* the radius of the sample and *L* the thickness.

The equations for N_I and N_{II} have the same expressions than the CCNBD test.

The parameter α is the ratio *a/R* (semi-notch/radius) and θ the angle of inclination of the central notch.

It is important to note that N_{II} is zero for θ=0 which characterizes a pure mode I and that N_I is equal to zero for pure mode II. The evolution of the K_I and K_{II} with θ can be seen in Figure 2. 21.

Here it can be seen that when N_I/K_I is close to zero the numerical simulation has a difficulty to converge, more than one point of calculation was made by (Dau Anh-Tuan, 2013), but even if the given results show an approximation close to zero, there is no angle where we can find $K_I=0$ numerically.

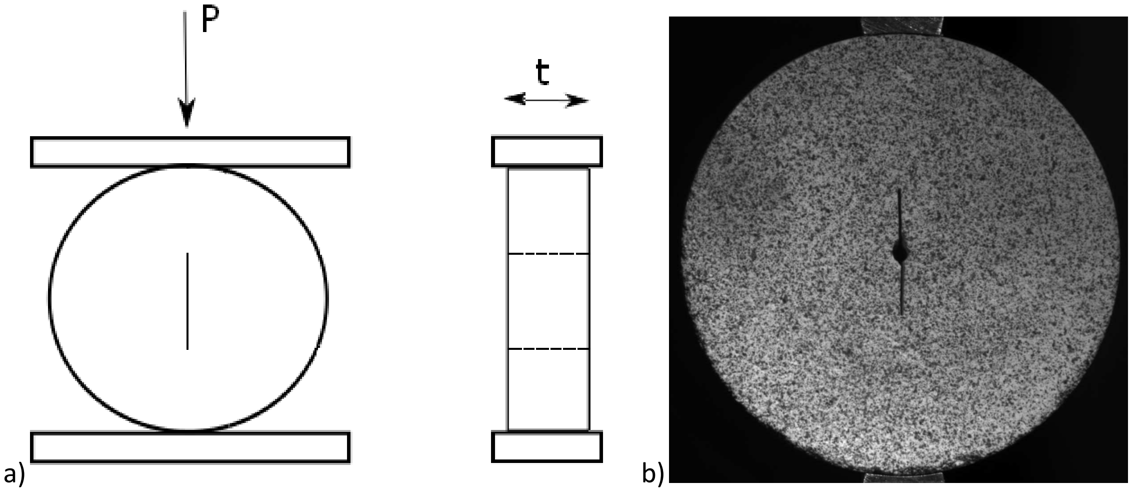

Figure 2. 20 – a)Sketch of the CCBD test, b)CCBD75 – example of test with a load arc

This information will be important to analyze critically the results for pure mode II in numerical simulations for any type of fracture toughness test, mainly the ones the crack rupture in inclined.

Of course, analyzing the N_I equation, we notice that the inclination angle that gives $N_I=0$, depends on the *a/R* ratio. In (Figure 2. 22) we can observe that there is just one ratio that theoretically produces a pure mode II (N_I=*0*) for a specific angle (28°), and in Figure 2. 23 we can see how θ varies with the ratio a/R for N_I =*0*.

So for the geometry of the samples here studied, the angle to reproduce a pure mode II is 28°.

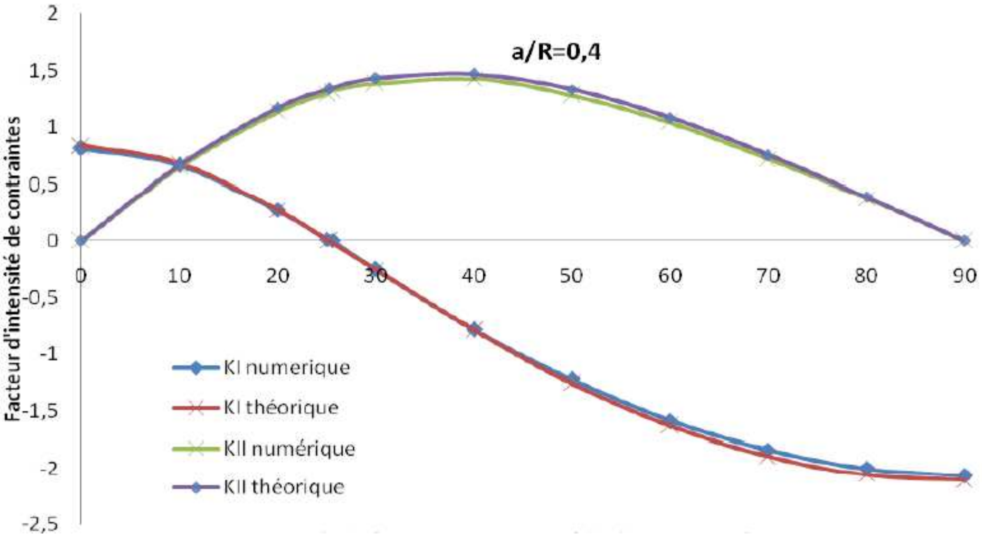

Figure 2. 21 - KI and KII variation with the angle change (Dau Anh-Tuan, 2013)

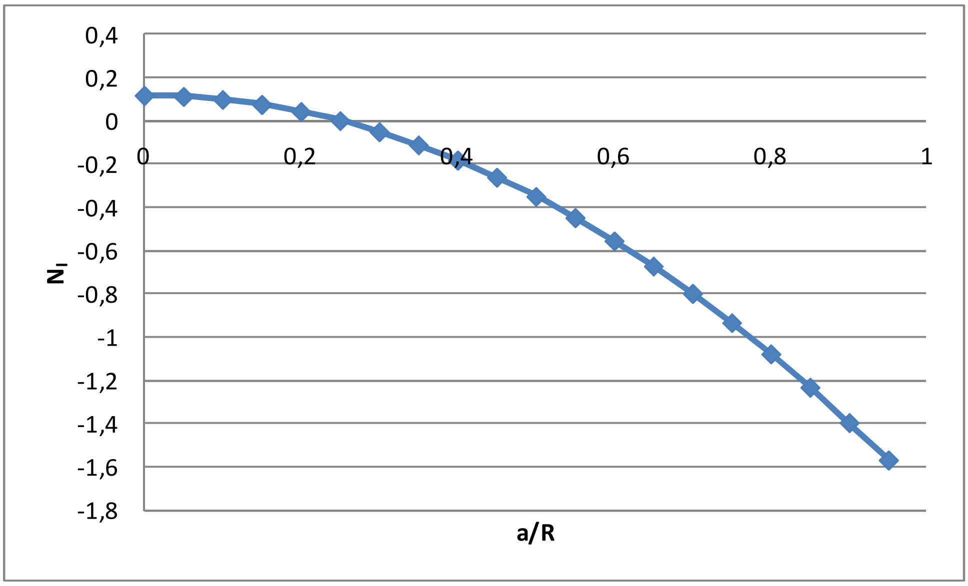

Figure 2. 22 - Variation of NI with α, for an angle = 28°

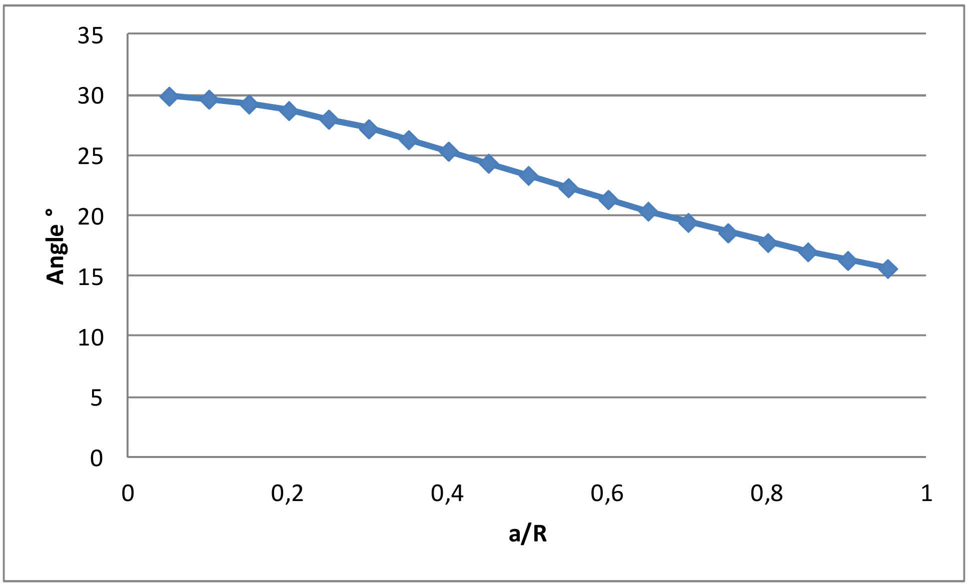

Figure 2. 23 - Angle variation in function of α for NI =0

2.1.3.3 Fracture toughness tests for a loading mode type - Bending

The tests described below, meaning, fracture toughness tests with a central crack have a particular difficulty, that is the complexity of performing a notch in the center of a sample that will be mostly representative of a natural defect. This requires more precision on the manufacturing of the sample and for a more accurate notch a more precise tool.

Not all labs will have a diamond saw machine, therefore searching to be precise and also the reproducibility of the results that would not require such specific equipment we performed tests also with a bending type of load.

However, as said above, the quality of the sample and the reproducibility are very important, and each one of its parameters comes with one common difficulty: the precision of the sample geometry.

For this reason, of several types of bending tests (the classical prismatic three-point bend test, SECB, SECRBB etc) we chose the SCB test, for its simplicity of manufacturing, symmetry of the sample and its 2D geometry.

2.1.3.3.1 SCB – Semi circular bending test

This test, which is also an ISRM suggested method (Kuruppu, Obara, Ayatollahi, Chong, & Funatsu, 2013) has some important advantages in comparison with the other three points bending tests to the determination of the fracture toughness.

The samples are easier to shape than for the traditional three point bending test with prismatic samples which require a more delicate process of manufacturing. This test also permits the fracture toughness evaluation for modes I, II and mixed.

The Figure 2. 24b shows the sample and test configuration for an ASCB in a general approach. We can see that varying the distance of one base, we can change from pure mode I (S_{II} =S_I) (Figure 2. 24a) passing to a mixed mode until for a certain value of S_{II} where K_I =0 and the pure mode II is presented (Figure 2. 24b). The stress intensity factor for modes I, and II are:

$$K_I = \frac{P\sqrt{\pi a}}{2RB} Y_I \left(a/R; S_I/R; S_{II}/R\right) \tag{2.59}$$

$$K_{II} = \frac{P\sqrt{\pi a}}{2RB} Y_{II} \left(a/R; S_I/R; S_{II}/R\right) \tag{2.60}$$

where P is the applied load, B the thickness, a the notch-size, R the radius, and S the support distance.

Y_I and Y_{II} are parameters dependents of the geometry, determined numerically and that can be taken from the Figure 2. 26 and Figure 2. 27 showing abacus computed by Ayatollahi et al. 2011.

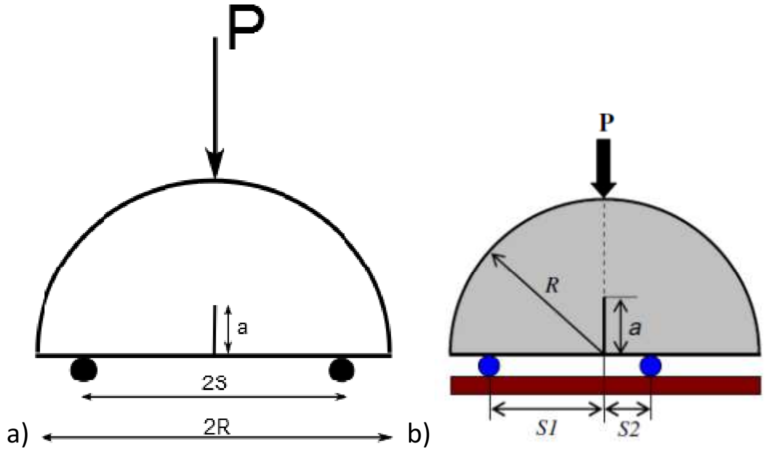

Figure 2. 24 - SCB configuration for a) mode I b) ASCB (Ayatollahi, Aliha, & Saghafi, 2011)

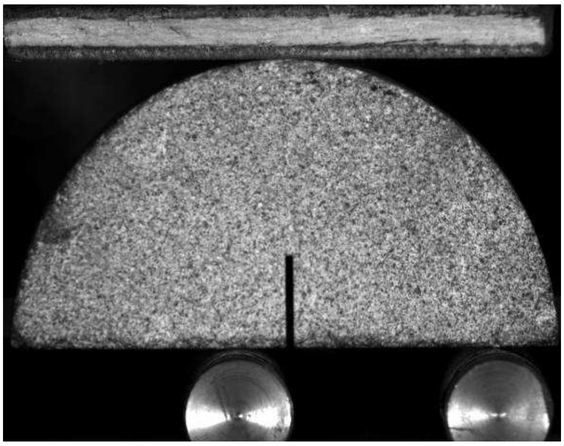

Figure 2. 25 - Mode II pure configuration ASCB – SCB13

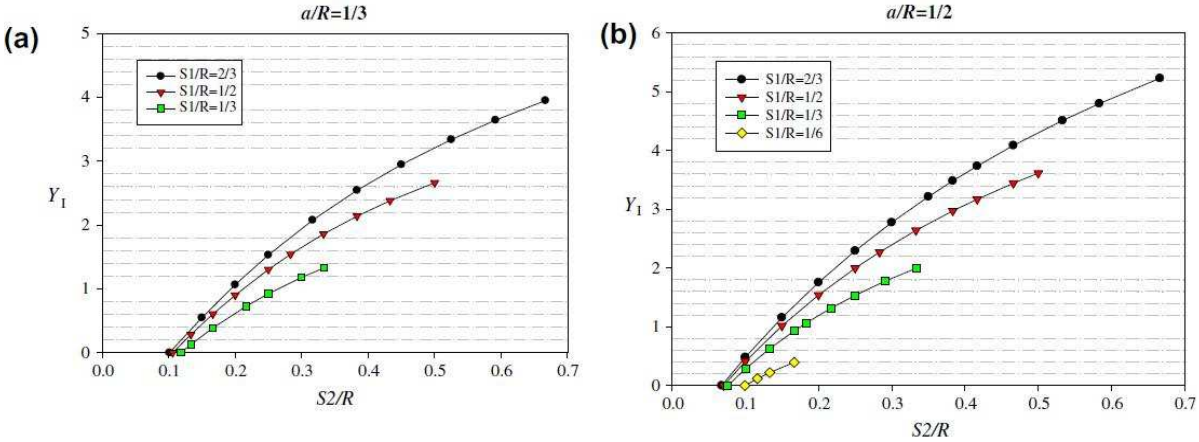

Figure 2. 26 – Abacus for the YI determination- ASCB (Asymetric semi-circular bending) (Ayatollahi et al., 2011)

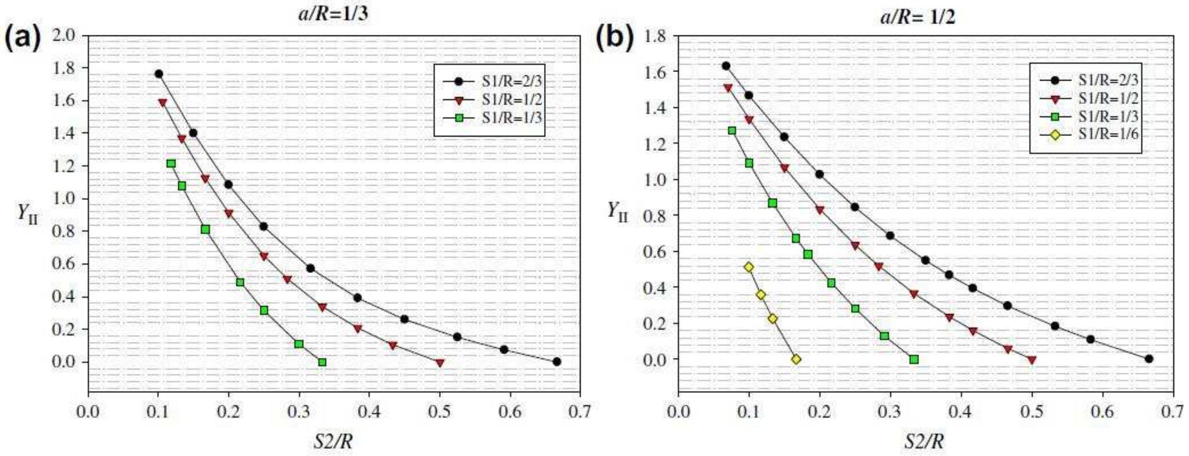

Figure 2. 27 - Abacus for the YII determination- ASCB (Asymmetric semi-circular bending) (Ayatollahi et al., 2011)

2.1.3.4 *Summary of Fracture toughness tests*

In the section 2.1.3 we talked mostly about the fracture toughness tests that can be used both to calculate the mode I/II or mixed of crack propagation, however, one test used just to determined the pure mode II will be described in section 2.7.

However, here we will show the summarized tables for testing both “pure” modes, including the PTST shown in section 2.7.

In Table 2. 3 and Table 2. 4 it can be seen the summary of the fracture toughness tests techniques used in this work.

Table 2. 3 - Summary mode I fracture toughness tests

Acronym	Name	Figure
CCBD	Central Crack Brazilian Test	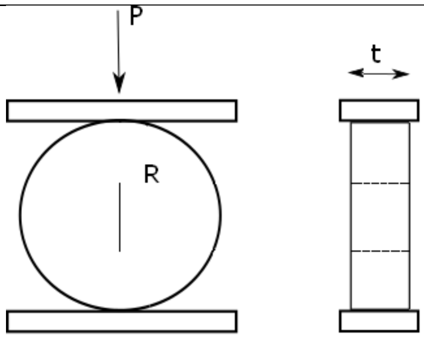
CCNBD	Central Crack Notched Brazilian Test	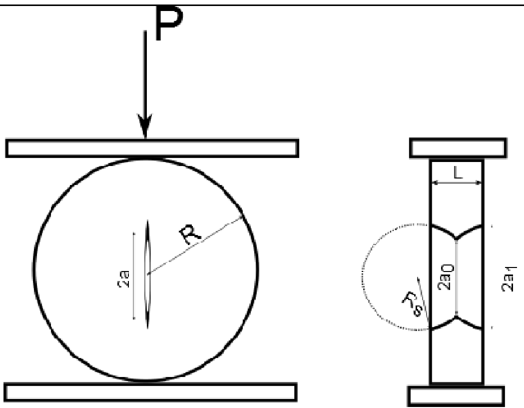
SCB	Semi- circular three point bending test	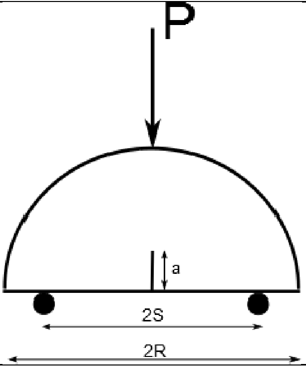

Table 2. 4 - Summary mode II fracture toughness tests

Acronym	Name	Figure
CCBD	Central Crack Brazilian Test	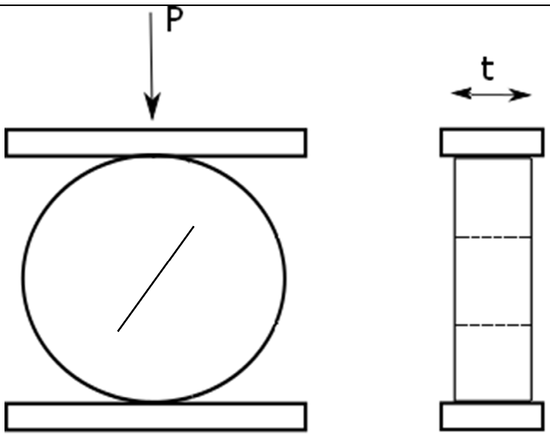
Punch Test	Central Crack Notched Brazilian Test	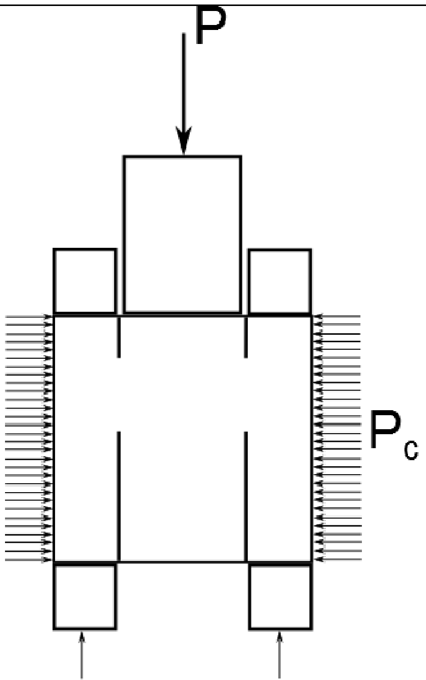
ASCB	Asymmetric Semi-circular three point bending test	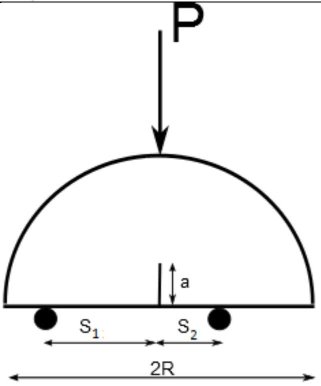

2.1.4 General results on fracture toughness of limestone from the literature

To finalize this sub-section we show, from the literature, values for the fracture toughness of various limestone rocks.

It can be seen that this parameter varies from 0.35 to 2.48 MPa.m$^{0.5}$ for the mode I (Table 2. 5) and from 0.75 to 4.53 MPa.m$^{0.5}$ to the mode II (Table 2. 6) for the limestone rocks studied and presented here.

The variability of this parameter for a same type of rock can attributed to many reasons. It can be due to the nature of the limestone because the variation of porosity and microstructure (micritic or oolitic limestone) can result in an important variation. But it can also come from the difficulty of shaping some types of samples.

It can be seen that from the studies performed by the same author, with the same geometry of the sample, the fracture toughness can have a variation as large as 34% (Gunsallus & Kulhawy, 1984).

The variability of this parameter as we can observe in the literature reinforces the necessity of a robust experimental technique for the fracture toughness determination of the studied rock.

Table 2. 5 – Fracture toughness values on mode I for different limestone rocks

Origin or type of limestone	Test (Diameter)	$K_{IC,}$(MPa.m^{0,5})	Source
Australia (Grey)	BDT	1.58	(Guo et al., 1993)
Australia (White)	BDT	1.38	(Guo et al., 1993)
Grey	BDT	1.58	(Whittaker et al., 1992)
White	BDT	1.38	(Whittaker et al., 1992)
Ashbourne, Derbyshire	CB	1.07	(Brown & Reddish, 1997)
Harrycroft	CB	0.82	(Bearman, 1999)
Middleton	CB	0.73	(Bearman, 1999)
Rüdersdorf	CB	1.12	(Tobias Backers, 2004)
Wredon	CB	1.7	(Bearman, 1999)
Central Province of Saudi Arabia	CCND (D=84mm)	0.35	(Khan & Al-Shayea, 2000)

Origin or type of limestone	Test (Diameter)	$K_{IC,}$(MPa.m^{0,5})	Source
Central Province of Saudi Arabia	CCND (D=98mm)	0.42	(Khan & Al-Shayea, 2000)
Central Province of Saudi Arabia	CCNBD	0.61 (D=80mm)	(Khan & Al-Shayea, 2000)
Arki	CCNBD	0.79	(Dwivedi, Sonia, Goela, & Dube, 2000)
Chamesson	CCNBD	0.64	(Saad, 2011)
Pierre de Lens	CCNBD	0.50	(Saad, 2011)
Chongqing	CCNBD	1.26	(Wang & Xing, 1999)
Indiana	CCP	0.97	(Sun & Ouchterlony, 1986)
Chongqing	FBT	1.25	(Wang & Xing, 1999)
Indiana	MR	1.2	(Lemiszki & Landes, 1996)
Oak Ridge	MR	0.8	(Lemiszki & Landes, 1996)
Indiana	SC3PB	0.99	(Whittaker et al., 1992)
Central Province of Saudi Arabia	SCB	0.68	(Khan & Al-Shayea, 2000)
Dolomitic	SCB	1.331	(Donovan & Karfakis, 2004)
Welsh	SCB	0.85	(Singh et Sun, 1990)
Indiana	SECB	0.97	(Ingraffea et Schmidt, 1979)
Fethiye	SECBD	2.177	(Altindag, 2000)
Fethiye	SECBD	2.18	(Altindag, 2000)
Isparta	SECBD	2.48	(Altindag, 2000)
Central Province of Saudi Arabia	SECRBB	0.55	(Khan & Al-Shayea, 2000)
Central Province of Saudi Arabia	SENRBB	0.39	(Khan & Al-Shayea, 2000)
Irondequoit	SR	1.36	(Gunsallus & Kulhawy, 1984)
Klinthagen	SR	1.87	(Oucterlony, 1989)

Origin or type of limestone	**Test (Diameter)**	**$K_{IC,}$(MPa.m^{0,5})**	**Source**
Reynales	SR	2.06	(Gunsallus & Kulhawy, 1984)
Shelly	SR	1.44	(Meredith, 1983)

Table 2. 6 – Fracture toughness values on mode II for different limestone rocks

Origin or type of limestone	**Test (Diameter)**	**$K_{IC,}$(MPa.m^{0,5})**	**Source**
Central Province of Saudi Arabia	CCND (for D=84mm)	0.75	(Khan & Al-Shayea, 2000)
Central Province of Saudi Arabia	CCND (for D=98mm)	0.92	(Khan & Al-Shayea, 2000)
Central Province of Saudi Arabia	CCNBD	0.86	(Khan & Al-Shayea, 2000)
Rüdersdorf	PTST	4.53	(Tobias Backers, 2004)

2.2 Methodology

In section 2.1.3 we gave the overview of the literature of the mechanical tests that can be performed to evaluate the fracture toughness of materials. In this section we will emphasize on the choice of the rock material to this study and the chosen dimension that were relevant to the selected material.

2.2.1 Rock material description

This work is focused on an oolitic limestone rock named *Pierre de Lens* (Figure 2. 28), from the Barremian age (130-125 Ma), composed of 99.9% calcite.

In terms of mineralogy composition, this rock can be considered as homogeneous.

The characteristics of the intact rock studied by (Saad, 2011) are:

- Sound speed: 4160 ± 180 m/s ;
- Resonant frequency: 24.9 ± 0.9 kHz ;
- Uniaxial compressive strength: 54 ± 11 MPa
- Pore mean radius: 0.62 µm
- Mean total porosity: 13.9 ± 0.9 % ;
- Water permeability: 409 ± 197 µD (1 µD = 10^{-18} m^2).

Figure 2. 28 and Figure 2. 29 respectively show some microscopic images and a simplified scheme of the microstructure of the Pierre de Lens limestone.

The oolitic limestone is composed of oolite grains with a diameter of about 0.5 mm surrounded by calcite cement. The major part of the porosity of the rock is concentrated around the oolites, as shown in Figure 2. 28.

- Variability of the samples

It should be emphasized that the fracture toughness is known to be a parameter that varies significantly (e.g., Tang, et al., 2000), which means that for the same rock and the same type of mechanical test, the dispersion of the values is known to be large.

One of the reasons is the difficulty of making identical samples (which can occur with natural materials). To minimize this effect, the shaping of the material is made in a way such that the samples are as similar as possible.

However, we are confronted with two difficulties:

- the methods used for manufacturing the samples, are not 100% accurate, since the size of the notches, the thickness of the samples are controlled by the operator and not by a machine;

- The second one is related to the fact that a rock is a natural material, inducing a variability of the tested samples. Even for a homogenous material random imperfections or defects are present in any sample.

These oolitic limestone was chosen to this study for being consistent with a sedimentary rock that could be potentially used in a CO_2 storage site.

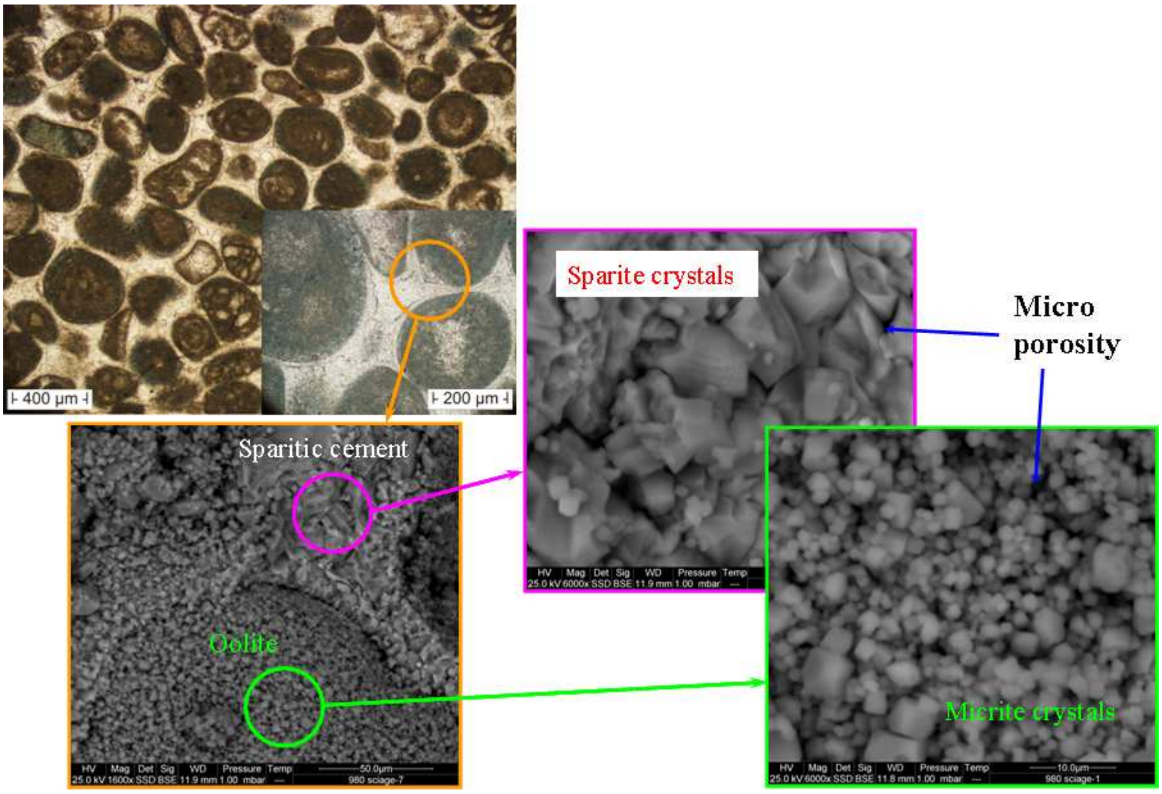

Figure 2. 28 – Pierre de Lens Microstructure (Ghabezloo et al., 2009)

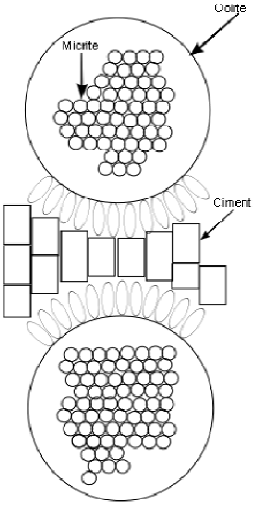

Figure 2. 29- Pierre de Lens microstructure schematic overview

2.2.2 Mechanical tests

Several mechanical tests were performed (as shown in Table 2. 7), to determine the fracture toughness of the rock on mode I and mode II.

We chose to perform tests with different types of loading, as compression or indirect traction (CCBD, CCNBD), bending (ASCB and SCB) and shear loading (PTST). As central in our study, further details on the BDT test are provided in section 2.2.2.3.

Table 2. 7- Number of each mechanical test

				Mechanical tests				
							Image correlation	
Type of test	**Mode**	**Saturation condition**	**Pressure**	**Degradation condition**	**CO2 presence**	**Number of samples**		**Fast Camera**
BDT				Intact		14	5	4
				Degraded		14	6	-
CCNBD	Mode I	Dry		Intact		13	7	-
				Degraded		3	-	-
	Mode II	Dry		Intact		18	-	-
				Degraded		1	-	-
CCBD	Mode I	Dry		Intact		11	5	4
				Degraded		4	3	2
	Mode II	Dry		Intact		2	2	-
SCB	Mode I	Dry		Intact		13	3	5
				Degraded		14	-	5
		Immerged	Atm		Pure water	4	-	-
			6 Bars		Pure water	3	-	-
					CO2-saturated water	3	-	-
ASCB	Mode II			Intact		4		
PTST		Dry	5 MPa	Intact		3	-	-
				Degraded		3	-	-
			10 MPa	Intact		3	-	-
				Degraded		3	-	-
			15 MPa	Intact		3	-	-
				Degraded		3	-	-

2.2.2.1 *Fracture toughness tests*

Several criteria were used for choosing the best combination of mechanical tests that would be made in this work. As mentioned in section 2.1.4, in the literature we can notice that for the same rock material the values for the fracture toughness can vary depending of the chosen set up.

(Khan & Al-Shayea, 2000) found values varying from 0.35 to 0.68 MPa.m$^{0.5}$ for the same limestone. This observation motivated us, first of all, to evaluate the *influence of the loading type* by testing the material in different loading configurations, namely compression, bending or shear loads.

In a second place it was essential that the sample preparation should be as simple as possible. For this reason all the samples have a cylindrical shape (no prismatic samples).

In third place, we would like to *compare and evaluate the ISRM proposed test CCNBD*, with a similar one with a simpler notch: so for the compression type of loading we chose two types of tests, the CCNBD and CCBD. Another reason, for these multiple analyses is the fact that we would like to evaluate the influence of the geometry of the fracture toughness, specially the 2D *versus* 3D geometry of the notch between both tests.

In fourth place, in the literature,(Chang et al., 2002) and (Ayatollahi et al., 2011) we can find that some authors describe the mode II for CCNBD, CCBD and ASCB as a possibility for the tests performed without confinement. These tests were performed and for a better analysis, *to evaluate the mode II toughness without confinement,* the DIC technique (described in section 2.6) was used together with numerical computations.

Complementary with the previous analysis would be the *evaluation of the mode II crack propagation with a quasi-confinement state*. To accomplish this objective, PTST tests have been performed.

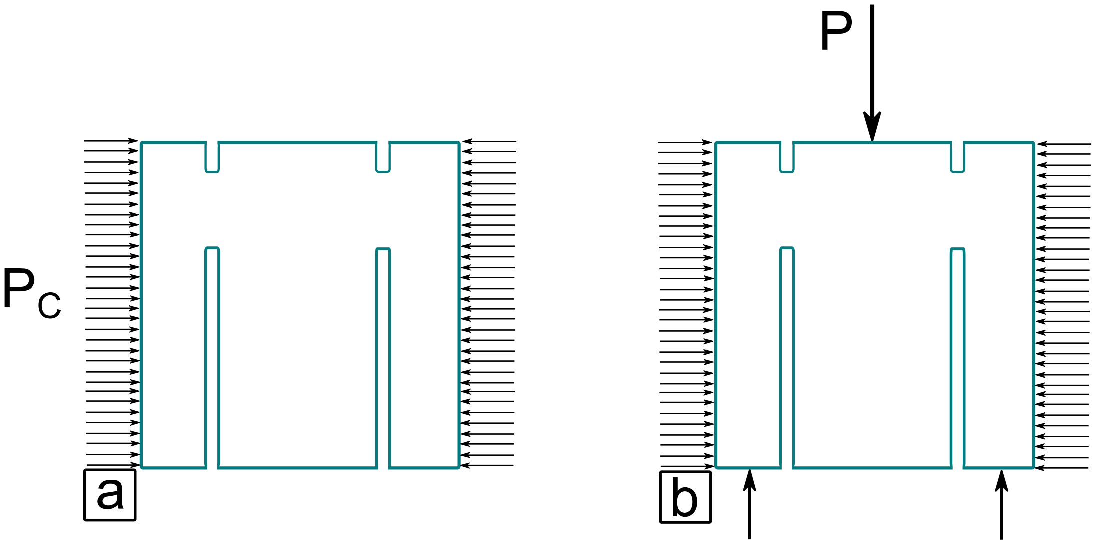

Figure 2. 30 - Steps of the loading application a) application of the confinement pressure b) application of the axial load

Concerning the loading conditions of the PTST test, as described in section 2.7, shown in first the confinement pressure is applied (a) and then the axial load increases until the rupture of the sample (Figure 2. 30). Three different confinement pressures have been applied (5, 10, and 15 MPa).

The general loading configuration of all fracture toughness tests and some aspects of the geometry of Figure 2. 30 the samples can be seen in Table 2. 8.

2.2.2.2 Samples shape

The SCB, CCNBD and the CCBD samples were drilled from a block with a drill of 50 mm of diameter and then, cut with a diamond saw to obtain a thickness of about 11.5 mm.

For the SCB sample, a wire saw is used to make a semi-circular cut, and then a notch of about 8 mm is made.

For the CCNBD, using a small saw of 32 mm of diameter, the notch was cut as shown in (Figure 2. 15).

For the CCBD sample, a small drill of 1 mm in the center of the sample was made to allow the passage of the diamond wire (Figure 2. 22). A notch was performed from the center of the sample until a distance of 8 mm, the result is a notch of 16 mm.

The PTST samples were drilled from a block with a 40 mm drill. Then, two more drills of 20 mm were made concentrically to the diameter: One from the top of the sample of about 4 mm and another from the bottom of the sample with a size of 24 mm.

Table 2. 8- Description of the samples and loading conditions for the fracture mechanic test

	PTST	SCB/CCND/CCBD
Description	**Values**	
Diameter (mm)	40	50
Thickness(mm)	40	11.5
Notch (a/R)	-	0.3
Speed load (mm/min)	0.02-0.025	0.06-0.08

2.2.2.3 BDT

According to the ISRM recommendations (Bieniawski & Hawkes, 1978) the suggested control is a force controlled test (loading rate in KN/s). However the tests performed in this work are displacement controlled. The first rate chosen from the literature was a displacement rate of 1 mm/min (Table 2. 9) as (Tavallali & Vervoort, 2010) that had used samples of 50 mm of diameter with a thickness of 25 mm.

However, for all the tests performed with the Digital Image Correlation (DIC) technique we noticed that this rate was too high, and we were unable to record enough photos for the general analysis. A new load rate was then set at 0.1 mm/min.

Table 2. 9- Brazilian test characteristics

Description	**Values**
Diameter (mm)	40
Thickness(mm)	20
Speed load (mm/min)	1/0.1

2.3 Mode I - Fracture Toughness Evaluation

The mode I is the most common studied crack propagation mode in the literature due to its facility (comparing to mode II and III).

However the imprecision of the values found in the literature lead us to perform a high range of mechanical tests to found a technique that will give us better results. In this section we will expose the results founds for the chosen limestone.

2.3.1 Evaluation of Mode I fracture toughness by SCB, CCBD and CCNBD tests

2.3.1.1 General results for the mode I fracture toughness tests

It has been performed 38 tests using three different methods (13 CCNBD, 11 CCBD and 14 SCB) to evaluate the mode I fracture toughness of the rock (see for example Figure 2. 31 for pictures of the experimental setup and samples of SCB experiments).

The results are presented for each type of tests in Table 2. 10, Table 2. 11 and Table 2. 12 and summarized in Table 2. 13.

The values obtained by the three types of fracture toughness tests show a good compatibility. The mean value of K_{IC} obtained from different experiments is 0.63 MPa.m$^{0.5}$ (Table 2. 12).

CCBD results show the smallest coefficient of variation (i.e. standard deviation per medium value) and CCNBD results show the highest one, but both mean values are close to the average of all experiments.

The force-displacement curves are shown in Figure 2. 32 for CCBD tests. It is important to mention that in these experiments the applied load was not a punctual load (Figure 2. 20b), but an arc load . Therefore a coefficient of 1.6 has to be applied for a ratio a/R of 0.3 (section 2.5.2.1).

The values of all CCBD tests can be found in Table 2. 10. We observe a very good repeatability of the tests. The slope of the load-displacement curve is similar for all the tests up to the first peak of the load. The first peak corresponds to the moment where the crack starts to propagate.

Table 2. 10 - Characteristics of CCBD tests on intact samples

Test name	Diameter (mm)	Thickness (mm)	Notch a (mm)	a/R	Load rate (mm/min)	First peak (kN)	K_{IC} MPa.m0.5
CCBD109	49.88	10.79	14.77	0.30	0.06	2.33	0.67
CCBD83	49.88	10.95	14.85	0.30	0.06	2.02	0.57
CCBD79	49.28	11.09	9.87	0.20	0.06	2.43	0.56
CCBD110	49.86	11.17	13.11	0.26	0.06	2.23	0.58
CCBD100	49.82	11.18	13.44	0.27	0.06	2.14	0.57
CCBD80	49.40	11.35	13.41	0.27	0.06	2.59	0.68
CCBD76	49.84	11.43	14.58	0.29	0.06	2.04	0.55
CCBD74	49.44	11.51	15.02	0.30	0.06	2.28	0.62
CCBD68	49.68	11.58	13.50	0.27	0.06	2.50	0.64
CCBD101	49.92	11.78	14.00	0.28	0.06	2.22	0.57
CCBD75	49.25	11.83	13.80	0.28	0.06	2.42	0.62

Table 2. 11 - General characteristics of the SCB tests on intact samples

Test name	Diameter (mm)	Thickness (mm)	Notch a (mm)	a/R	Y_I	Load rate (mm/min)	Maximum load (kN)	K_{IC} MPa.m0.5
SCB109	49.82	11.23	7.76	0.31	4.8	0.06	0.54	0.72
SCB107	49.85	11.23	7.84	0.31	4.8	0.02	0.48	0.64
SCB4	49.46	11.37	7.50	0.30	4.6	0.08	0.52	0.65
SCB6	49.49	11.54	8.00	0.32	4.9	0.08	0.45	0.61
SCB8	49.52	11.89	7.80	0.32	4.9	0.08	0.48	0.62
SCB48	49.87	12.00	7.02	0.28	4.1	0.06	0.69	0.70
SCB47	49.89	12.10	6.90	0.28	4.1	0.06	0.70	0.70
SCB7	49.57	12.12	7.80	0.31	4.8	0.08	0.53	0.66
SCB82	49.54	12.69	7.06	0.29	4.2	0.08	0.61	0.61
SCB81	49.58	13.00	8.40	0.34	5.3	0.08	0.53	0.71
SCB100	49.46	17.00	6.94	0.28	4.1	0.02	0.86	0.62
SCB10	49.49	19.25	7.64	0.31	4.8	0.06	0.82	0.63
SCB11	49.51	19.25	8.47	0.34	2.9	0.08	1.54	0.77
SCB9	49.5	19.86	7.48	0.30	4.6	0.06	0.86	0.62

*the difference of load rate is due to the use of different presses which were regulated by different mechanisms (some that would allow the use of our preferred load rate of 0.08)

Table 2. 12- General characteristics of the CCNBD tests on intact samples

Test name	Diameter (mm)	Thickness (mm)	a_1 (mm)	a_0 (mm)	Load rate (mm/min)	Maximun load (kN)	K_{IC} MPa.m0.5
CCNBD 02	49.55	12.04	29.00	17.55	0.08	1.91	0.70
CCNBD 03	49.56	12.28	29.50	17.50	0.08	1.97	0.71
CCNBD 09	49.49	11.85	29.47	20.38	0.08	1.23	0.47
CCNBD 10	49.55	11.87	28.99	20.80	0.08	1.26	0.48
CCNBD 16	49.55	10.78	29.55	21.73	0.08	1.32	0.56
CCNBD 18	49.45	11.94	29.36	20.53	0.08	1.50	0.57
CCNBD 19	49.53	11.64	29.78	21.12	0.08	1.46	0.57
CCNBD 21	49.44	15.90	31.24	17.77	0.08	1.86	0.53
CCNBD 23	49.46	11.04	30.54	24.00	0.08	2.01	0.86
CCNBD 43	49.52	11.44	30.50	24.00	0.08	1.74	0.71
CCNBD 74	49.82	11.69	26.30	10.93	0.06	1.72	0.59
CCNBD 75	49.88	11.25	25.32	7.25	0.06	1.92	0.66
CCNBD 76	49.88	11.82	25.21	6.075	0.06	2.04	0.66

For some samples, the rupture is abrupt while others have a more stable crack propagation. For the first type the force increases during the test is abruptly interrupted (Figure 2. 36), while for the second type the evolution of force during the test shows several peaks before the complete rupture of the sample (Figure 2. 37). In these tests, for the sake of simplicity, we chose to represent the CCBD curves only up to the first peak.

This is different from the SCB tests where the rupture is always abrupt. For the SCB tests, the tests performed on samples with the thickness varying from (11-13 mm) are represented on the Figure 2. 33. The values of K_{IC} and the curves in Figure 2. 33 show that the test has a good repeatability. However, we can see that the slopes of the SCB curves are less repeatable than the CCBD curves. The coefficient of variation is also less precise than the one obtained for CCBD tests.

Concerning the CCNBD test, it can be seen in Figure 2. 34 that the curves are not much repeatable, with a bigger variation on the slopes. This can possible be due to the higher variability of the notch in which the manufacturing is much less precise that the one on CCBD and SCB samples.

A typical aspect of the fracture surface as obtained in toughness tests (test CCNBD40) is shown in (Figure 2. 35). We observe that the oolites are not broken. Crack propagation starts from the void between the cement and the oolites and turn around the oolites during the propagation. In this picture, we can easily notice the texture of a surface after rupture. It can be seen the oolites that remain on this surface and the large voids representing the oolites that had been ripped out or that remained in the opposite surface (some of them are shown by the red arrows).

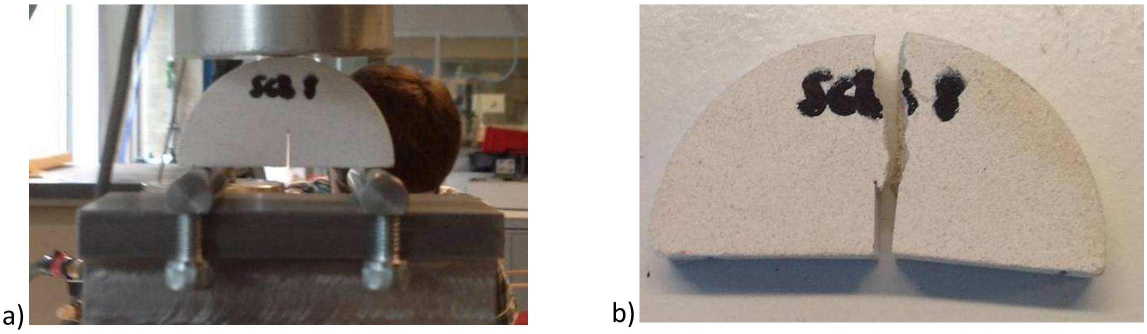

Figure 2. 31- Experimental setup and samples for SCB test (a and b)

Table 2. 13- Results of mode I fracture toughness experiments on intact samples

	Mode I-Intact samples			
Experiment	**SCB**	**CCBD**	**CCNBD**	**TOTAL**
Number of tests	14	11	13	**38**
Mean K_{IC} (MPa.m$^{0.5}$)	0.65	0.61	0.62	**0.63**
Coeff. of Variation	10%	7%	17%	**12%**
Min-Max	0.51-0.77	0.55-0.68	0.47-0.86	**0.47-0.86**

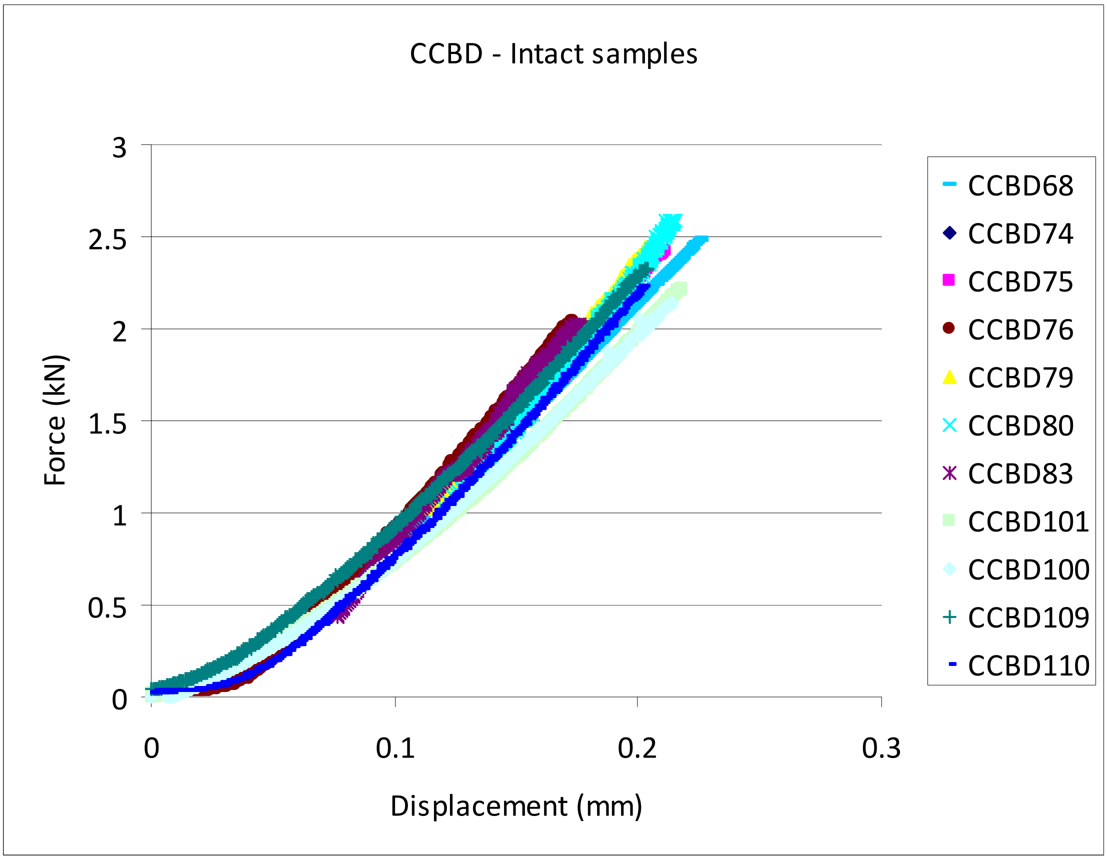

Figure 2. 32 - Force-displacement curves for CCBD experiments

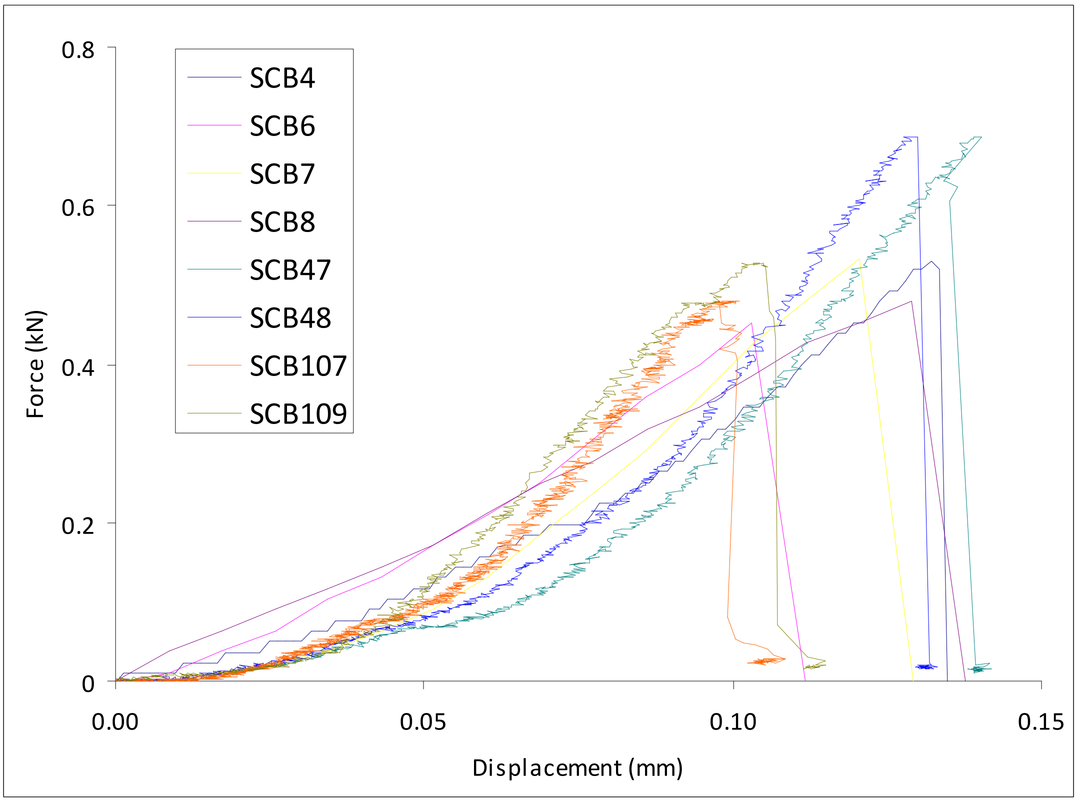

Figure 2. 33 - Force-displacement curves for SCB experiments

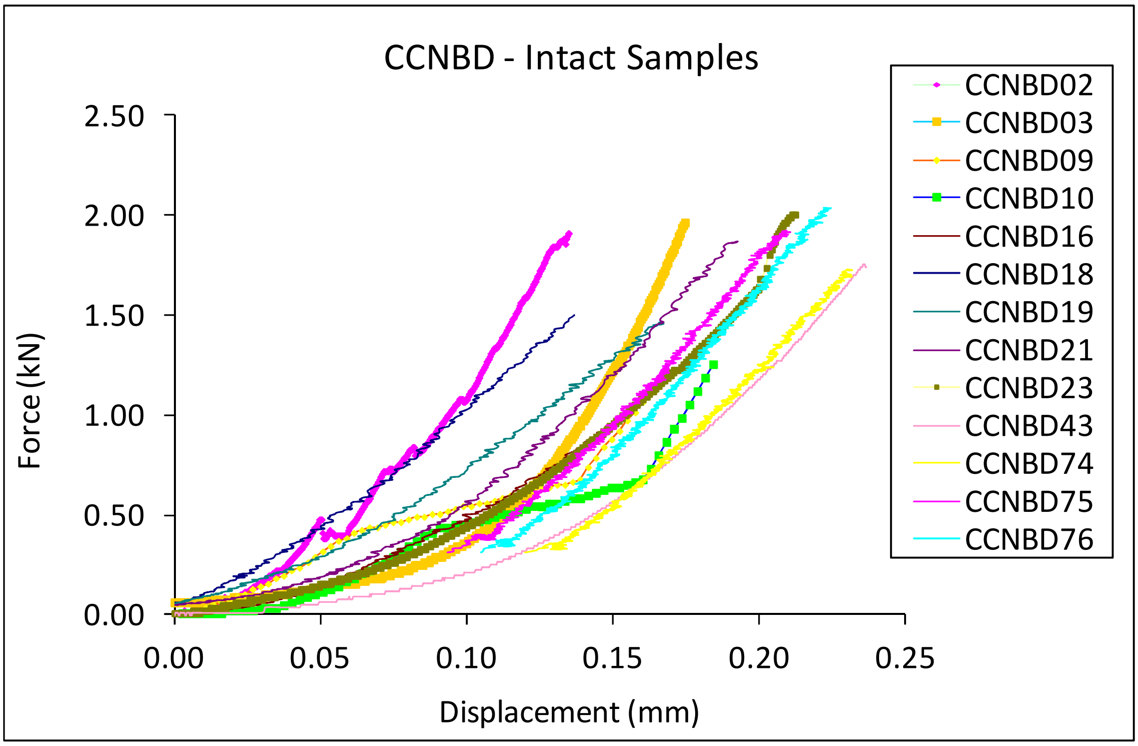

Figure 2. 34 - Force-displacement curves for CCNBD experiments

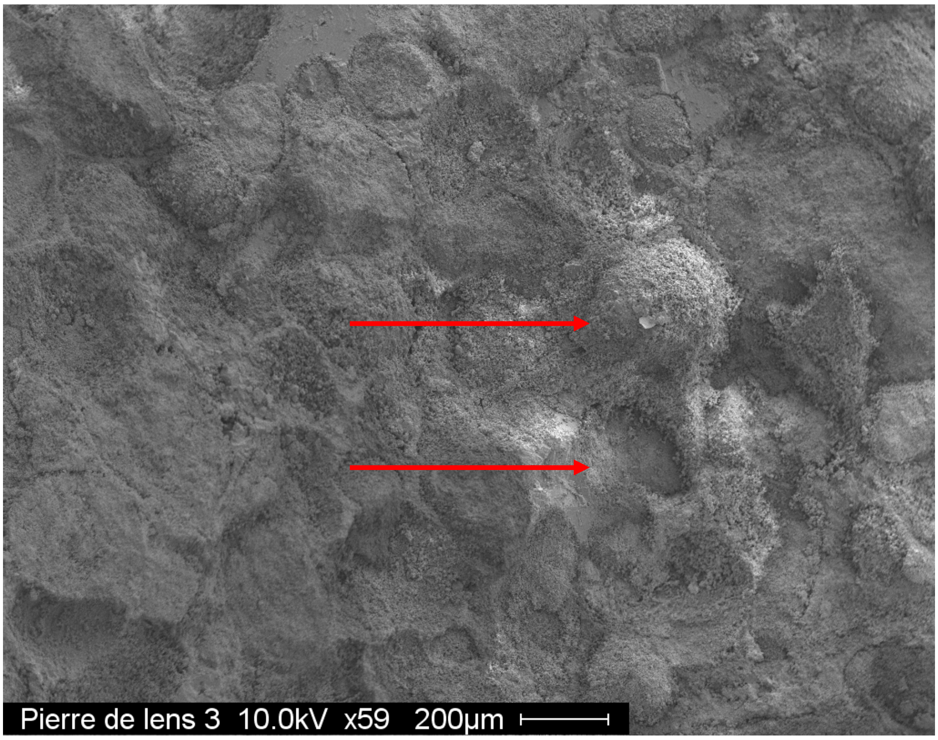

Figure 2. 35 - Detail of the fracture surface of the Pierre de Lens after a fracture toughness test CCNBD40

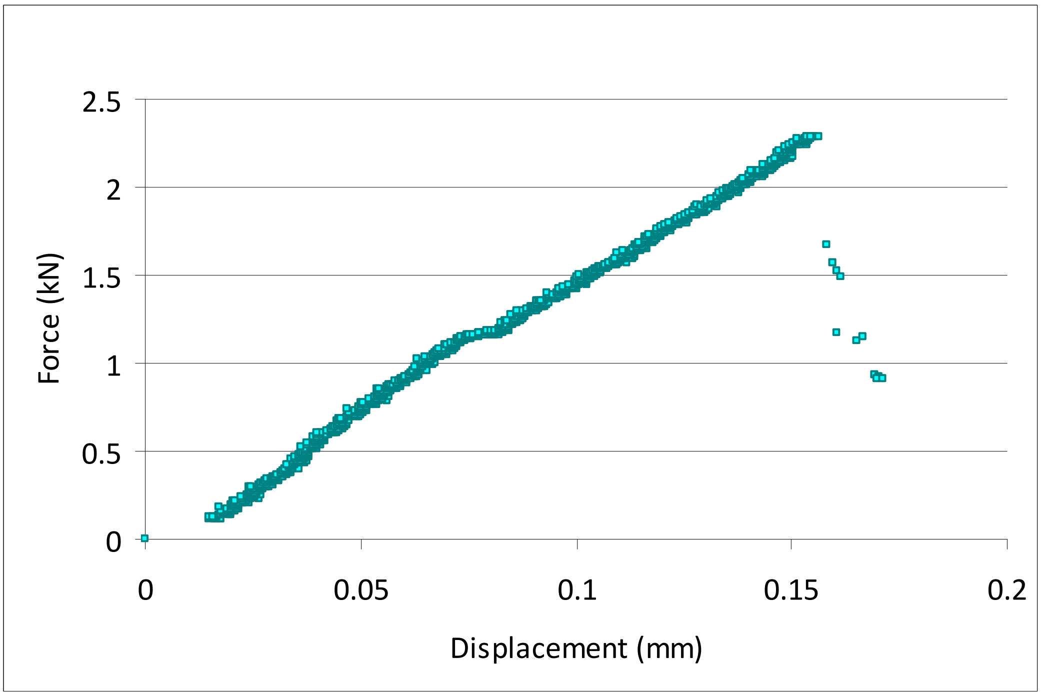

Figure 2. 36 - Force-displacement curve for the sample CCBD74

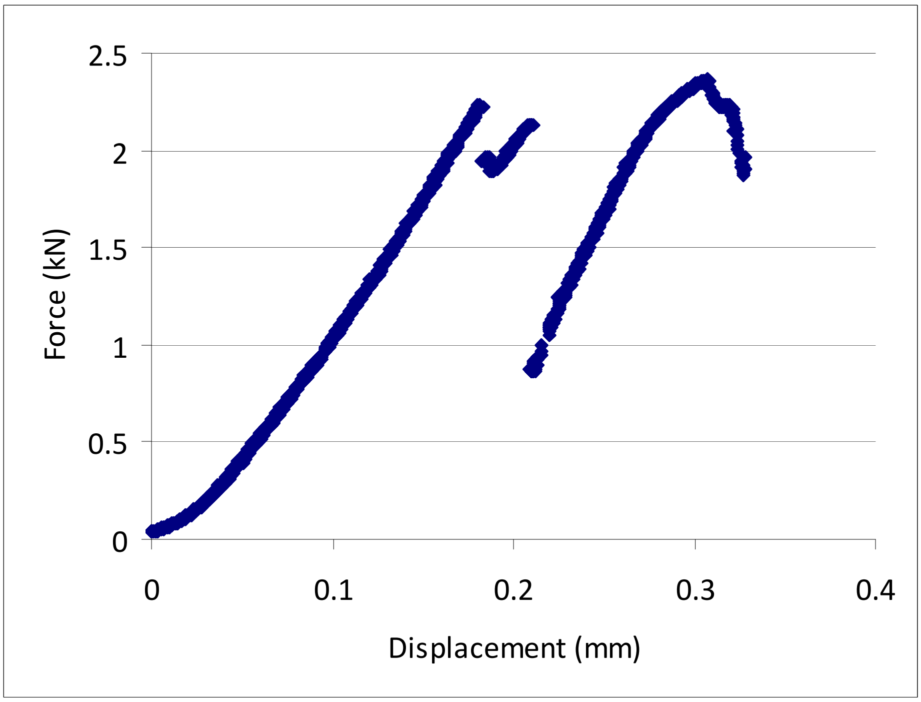

Figure 2. 37 - Force-displacement curve for the samples CCBD109

2.3.2 Comparison of Mode I fracture toughness obtained from CCNBD, CCBD and SCB with empirical relations

As shown in chapter 2, several empirical relationships exist in the literature for evaluating the fracture toughness as a function of the tensile and compressive strength of the rock (see equations 2.20, 2.21, 2.22, 2.30 and 2.31).

Brazilian tensile tests and uniaxial compression tests performed on Pierre de Lens limestone gave us values of 5.3 MPa and 50 MPa, respectively, for the tensile and compression strength of the rock. Using these values, the mode I fracture toughness KIC can be evaluated with these various expressions (Table 2. 14).

Table 2. 14 - Values of fracture toughness for the Pierre de Lens obtained by empirical expressions

Equation	(2.20)	(2.21)	(2.22)	(2.30)	(2.31)
K_I (MPa.m$^{0.5}$)	0.84	0.72	0.77	0.85	1.14

We notice that these empirical relationships lead to higher (and rather dispersed) values for fracture toughness. Note that different rocks have been used for establishing these relations and their validity is not always clearly stated in the corresponding papers.

However, we note that relation (2.21) from (Z. Zhang, 2002), based on tensile strength correlation (see section 2.1.2), gives a value compatible with our experimental results. Relations (2.30) and (2.31) are based in a correlation with the brittleness index of the rock. Nevertheless, Tiryaki (2006), who studied indirect methods to evaluate the brittleness, mentions that brittleness should not be considered as an intrinsic rock parameter. Therefore, such correlations should be used with caution.

2.4 Mode II - Fracture Toughness Evaluation

In an underground context is necessary to evaluate the fracture toughness in other types of modes for several aspects that can include the confinement pressure present in this situation.

Therefore, we develop a series of mechanical tests to estimate the fracture toughness in mode II with and without a confinement pressure.

However, in this section only the tests made without confinement pressure will be shown, letting the ones under confinement for a specific section 2.7.

2.4.1 Evaluation of Mode II fracture toughness by ASCB, CCBD and CCNBD tests

The results of the 23 mode II fracture toughness experiments using three different methods, (18 CCNBD, 2 CCBD and 4 ASCB), as presented Table 2. 15, Table 2. 16 and Table 2. 17. The expressions for the CCNBD, CCBD and SCB are respectively (2.48), (2.57) and (2.59). The results are summarized in Table 2. 18, showing a relatively good agreement.

We chose the CCNBD test to vary the thickness to see the impact of this parameter on the fracture toughness.

As it can be seen in Figure 2. 38, there is a little influence of the thickness in the fracture toughness, that goes in the direction that the literature exposes, as larger the sample is, it is more probable to the sample to be less resistant to crack propagation due the larger probability to the initial crack to find weak paths.

However we judge that this tendency in the size range found used in this study is not relevant enough.

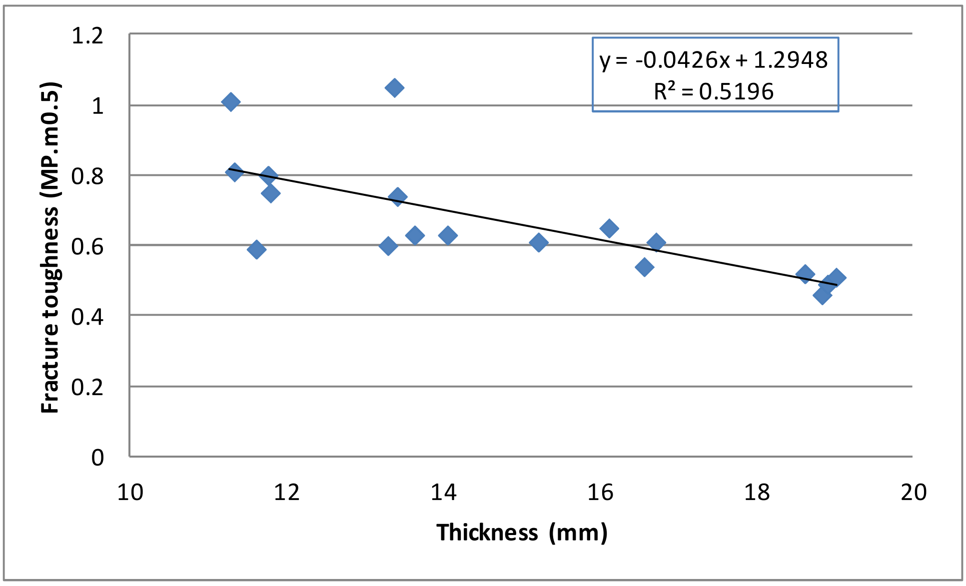

Figure 2. 38- Relation between thickness and Fracture toughness

The mean values of mode II fracture toughness vary between 0.70 and 0.73 MPa.m$^{0.5}$ for different methods. The variation coefficients for mode II experiments are generally higher than the ones obtained for mode I fracture toughness evaluation. The curves for the ASCB method Figure 2. 40 confirm the repeatability of the tests as it was already largely exposed for the mode I in the previous section.

In Figure 2. 39, the rupture of a sample after applying the asymmetric bending test can be seen. After failure, the sample presents a wing-shape crack, which is known to be related to mode I rupture (Ashby & Sammis, 1990). The same failure mode can be observed for the CCNBD and the CCBD tests.

These observations, a typical mode I crack for a supposedly mode II test raise some questions.

- Are these tests representatives of a real pure mode II crack propagation mode?
- Is it possible to obtain a pure mode II crack propagation in a non confined sample?

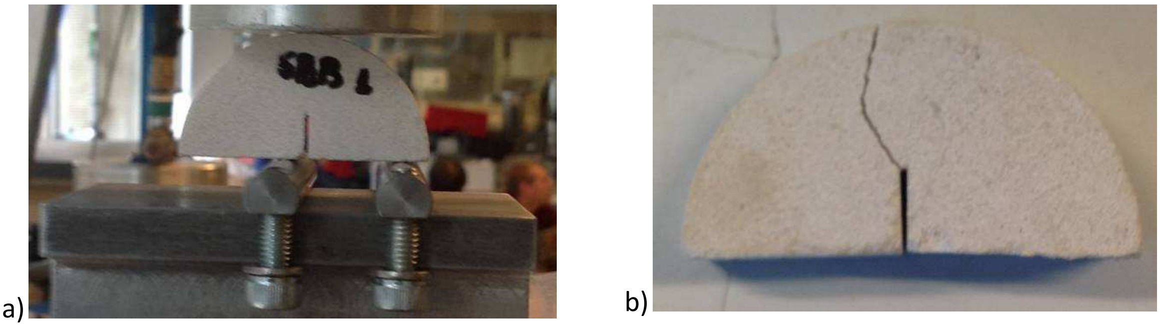

Figure 2. 39 - Experimental setup and samples for ASCB test (a and b)

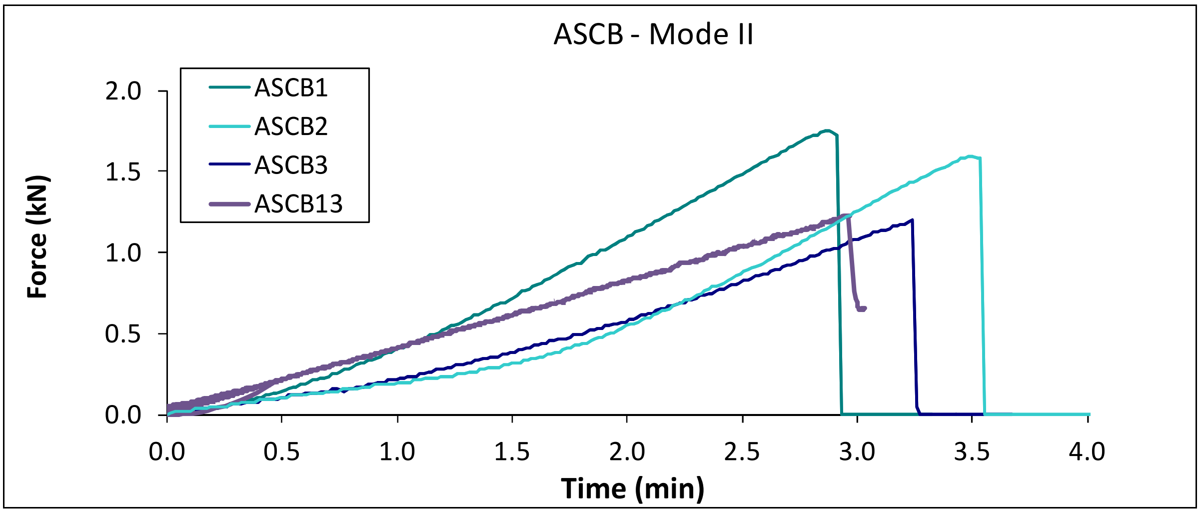

Figure 2. 40 - Displacement versus load for the ASCB samples.

Trying to answer these doubts and for a better understanding of the modes of propagation without confinement the Image correlation technique (FIC) is used and will be exposed in the section 2.6.5.

Table 2. 15 - Characteristics of al CCNBD tests

Test name	Diameter (mm)	Thickness (mm)	$2a_1$	$2a_0$	a (mm)	a/R	Beta °	N_1	N_2	Load rate (mm/min)	First Peak (kN)	K_{IIC} ($MPa.m^{0.5}$)
CCNBD04	49.45	13.37	28.75	15.55	24.35	0.49	23	0.04	2.39	0.08	1.91	1.05
CCNBD17	49.48	11.76	29.80	20.5	26.70	0.54	23	-0.04	2.33	0.08	1.25	0.80
CCNBD07	49.69	11.61	29.39	20.5	26.42	0.53	23	-0.02	2.32	0.08	0.93	0.59
CCNBD05	49.48	13.29	28.80	16.56	24.72	0.50	23	0.03	2.27	0.08	1.14	0.60
CCNBD06	49.45	13.63	29.38	16.54	25.10	0.51	23	0.01	2.28	0.8	1.21	0.63
CCNBD17	49.51	14.05	28.85	18.5	25.40	0.51	23	0.01	2.41	0.08	1.17	0.63
CCNBD02	49.6	16.71	28.98	16.5	24.82	0.50	23	0.02	2.45	0.08	1.35	0.61
CCNBD09	49.49	18.83	29.89	10	23.26	0.47	23	0.07	2.39	0.08	1.19	0.46
CCNBD10	49.49	16.56	29.83	14.5	24.72	0.50	23	0.03	2.44	0.08	1.17	0.54
CCNBD01	49.51	18.61	30.32	12.5	24.38	0.49	23	0.04	2.43	0.08	1.29	0.52
CCNBD03	49.53	16.11	30.41	16.5	25.77	0.52	23	-0.01	2.39	0.08	1.39	0.65
CCNBD08	49.49	11.79	29.76	20.5	26.67	0.54	23	-0.03	2.33	0.08	1.17	0.75
CCNBD15	49.53	13.41	29.38	18	25.58	0.52	23	0.00	2.40	0.08	1.31	0.74
CCNBD13	49.53	18.9	30.29	12.5	24.36	0.49	23	0.04	2.43	0.08	1.25	0.49
CCNBD14	49.51	19.01	30.26	11.5	24.01	0.48	23	0.05	2.42	0.08	1.31	0.51
CCNBD16	49.56	15.21	29.92	18.8	26.21	0.53	23	-0.02	2.38	0.08	1.23	0.61
CCNBD11	45.51	11.28	30.34	22.4	27.69	0.61	20	0.09	2.56	0.08	1.24	1.01
CCNBD12	49.52	11.33	29.78	21.3	26.95	0.54	23	-0.04	2.31	0.08	1.23	0.81

Table 2. 16 - Characteristics of al CCBD tests

Test name	Diameter (mm)	Thickness (mm)	a (mm)	a/R	Beta °	N_1	N_2	Load rate (mm/min)	First Peak (kN)	K_{IIC} ($MPa.m^{0.5}$)
CCBD77	49.92	11.5	14.64	0.30	28	-0.04	1.75	0.08	1.44	0.60
CCBD82	49.9	11.51	15	0.30	28	-0.05	1.75	0.08	1.9	0.80

Table 2. 17 - Characteristics of al ASCB tests

Test name	Diameter (mm)	Thickness (mm)	Notch a (mm)	a/R	S_1/R	S_2/R	Y_{II}	Load rate (mm/min)	Maximum load (kN)	K_{IIC} $MPa.m^{0.5}$
ASCB1	49.62	12.10	7.80	0.31	0.81	0.10	1.91	0.08	1.75	0.87
ASCB2	49.88	11.87	9.00	0.36	0.80	0.10	1.86	0.08	1.59	0.84
ASCB3	49.49	12.44	8.00	0.32	0.81	0.10	1.90	0.08	1.20	0.59
ASCB13	49.33	11.5	7.55	0.31	0.8	0.10	1.91	0.08	1.23	0.64

Table 2. 18- Results of mode II fracture toughness experiments on intact samples

	Mode II-Intact samples		
Experiment	**CCNBD**	**CCBD**	**ASCB**
Number	18	2	4
Mean K_{IIC} ($MPa.m^{0.5}$)	0.67	0.70	0.73
Coeff. of Variation	27%	20%	19%
Min-Max	0.4-1.05	0.60-0.80	0.59-0.87

2.5 Numerical Analysis of BDT, CCBD and SCB tests

The experimental evaluations for mode I and mode II were complemented with a numerical analysis of the performed tests.

For this we chose a Finite Element software to characterize this material that due its homogeneity we consider as a continuum material.

2.5.1 Numerical Model

2.5.1.1 Code_Aster®

The Finite Element (FEM) software used in this work is Code_Aster® which is a free and open source software.

Aster is an acronym for "*Analyses des Structures et Thermo-mécanique pour des Études et des Recherches*". The software development started in 1989 at the research and development unit at EDF (Electricité de France). The programming language used in this code is Fortran. The Code_Aster allows, among others, the calculation of non-linear phenomena in mechanics.

2.5.1.2 Mesh optimization – BDT test

We use the classical Brazilian disc test to validate the size of the general mesh applied for all fracture toughness numerical tests.

We assume here a 2D plane stress model. The model diameter is the same as the one of the Brazilian test samples (40 mm).

The mesh used for the reference analysis, the displacement and the stress fields are shown in the Figure 2. 41.

We analyze then the analytical solutions of the stress field (equations 2.34-2.36) with two cuts of the numerical model, one vertical and another horizontal both passing by the center of the geometry (Figure 2. 42).

The results of the stress field for the numerical analysis (reference mesh size) and the analytical solution can be seen on Figure 2. 43. This was made for different mesh sizes.

The relative error was calculated to choose the reference mesh that will be used for the CCBD and the SCB tests. The error is calculated between the numerical and analytical solutions. The reference mesh was chosen when the increase in mesh elements did not have a significant impact on the stress field calculation (Figure 2. 44).

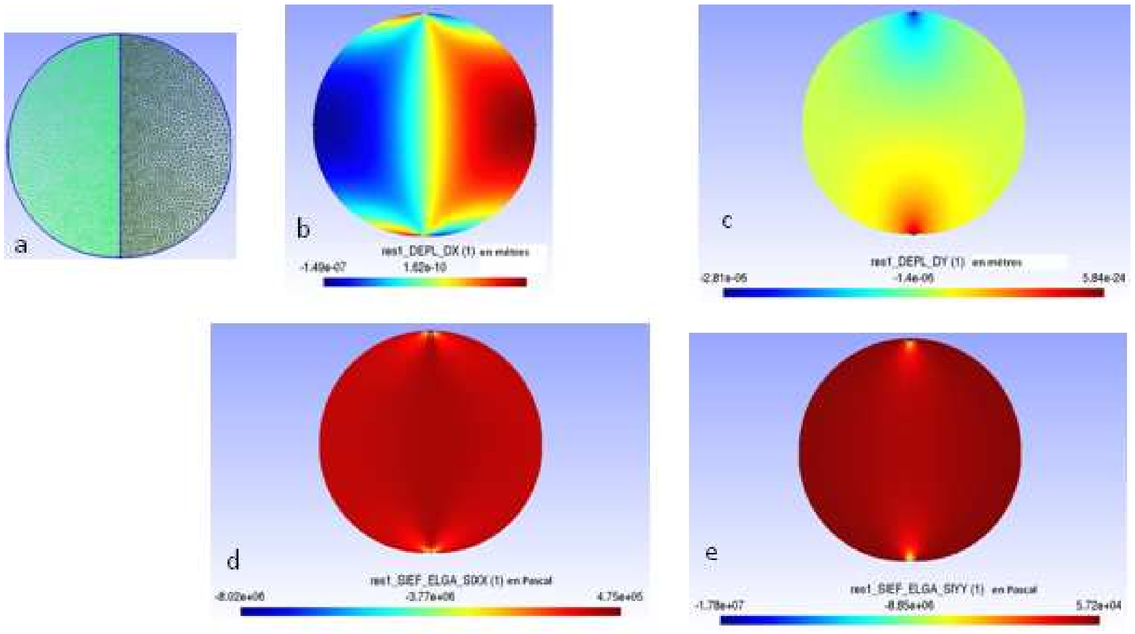

Figure 2. 41- a) Mesh b) Horizontal displacement field c) Vertical displacement field d) Horizontal stress field e) Vertical Stress field

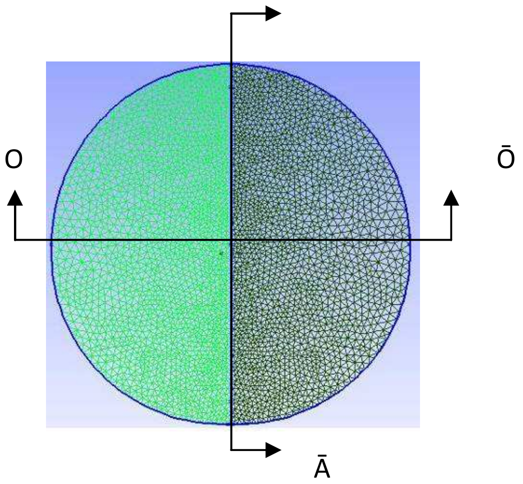

Figure 2. 42 - Cuts from where we take the displacement and stress information to compare with the analytical solution

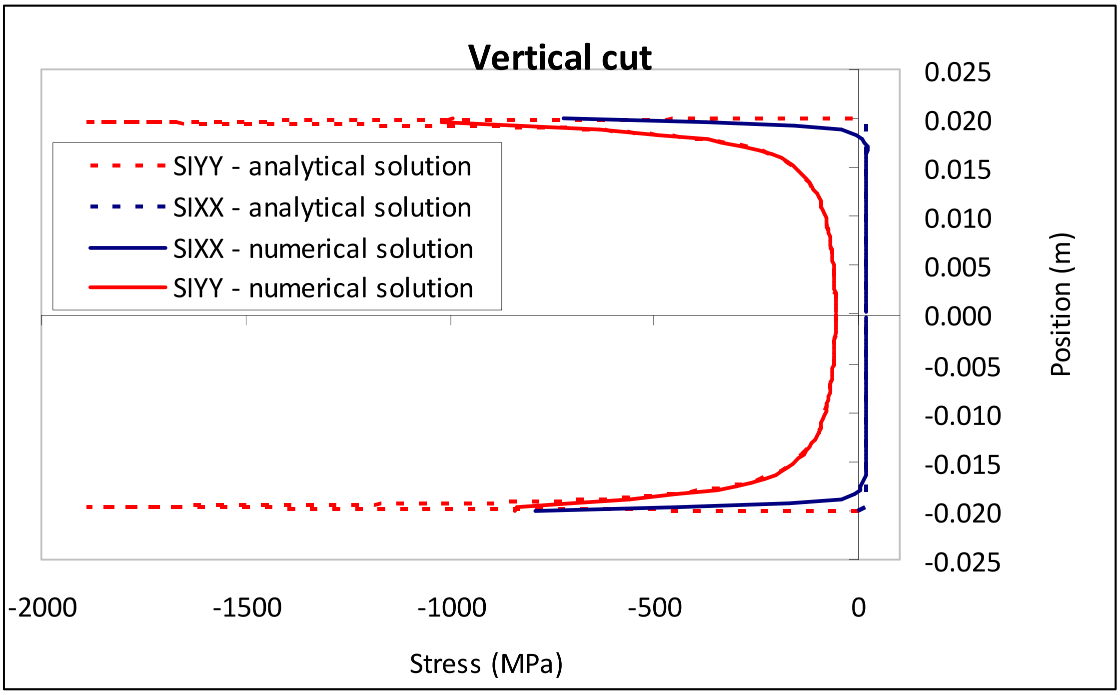

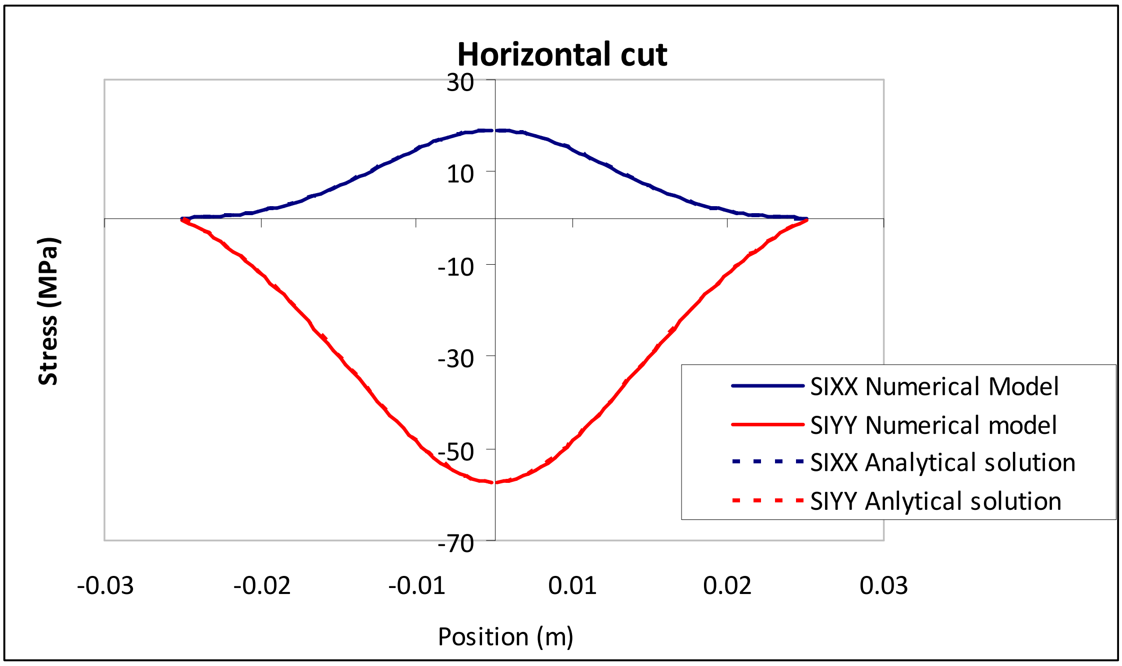

Figure 2. 43– Comparison between the analytical and the numerical stress field at the vertical and horizontal cuts

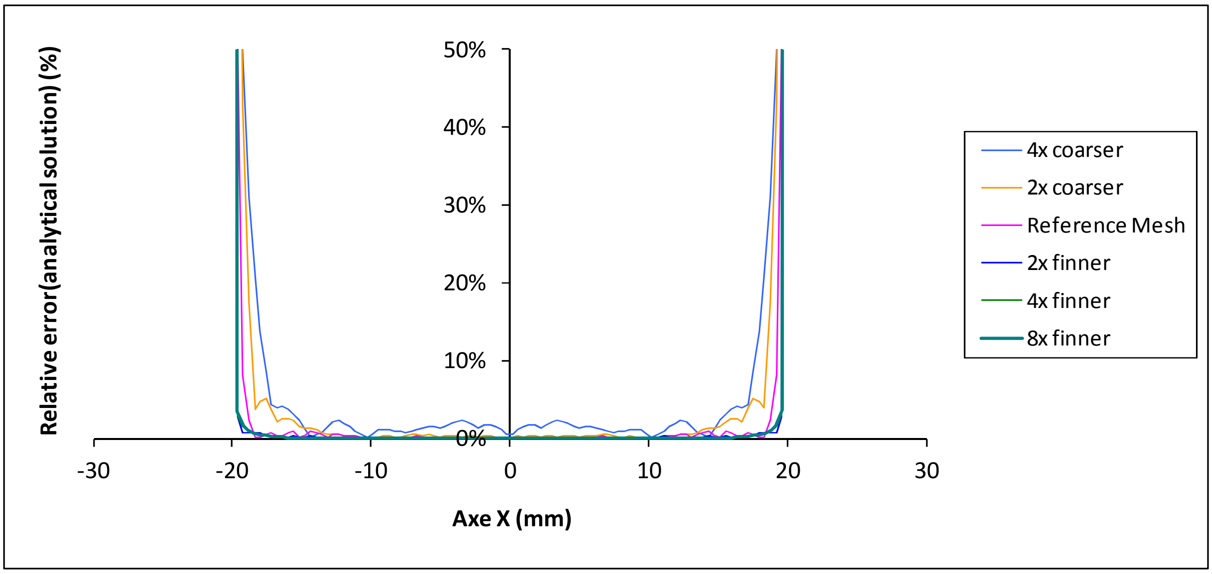

Figure 2. 44- Comparison between several mesh sizes*

* the multiplication size correspond to the reference mesh.

2.5.2 Numerical Application to CCBD ad SCB tests

We performed as for the Brazilian test, simulation of the CCBD and the SCB test, for mode I and Mode II.

2.5.2.1 CCBD Mode I

We can see in Figure 2. 45 the finite element mesh and the simulation results for mode I CCBD test. A zero-thickness crack was used in the model in a geometry with 50 mm diameter and a ratio a/R of 0.3.

The load is applied by an arc distribution (20 °). The displacements are symmetric and are in agreement with the theoretical results. Using the method of the extrapolation of the displacement field presented in section (2.1.1.5), we were able to calculate the fracture toughness for a sample submitted at a CCBD test.

We used the rupture (first peak) force applied on the tested sample CCBD74 in order to compute the corresponding stress intensity factor for this load.

In Figure 2. 46 we can see the curves that derive the β_I parameter for the equation 2.10, being the slope of the curve Dx^2 *versus* the distance from the crack tip (for mode I).

The fracture toughness test derived from the numerical analysis and the one measured at the laboratory, by the relation (2.57) and the peak force, for CCBD test are in very good agreement, respectively reaching 0.54 and 0.55 MPa.m$^{0.5}$.

The CCBD tests are performed with an arc load support, however the equation 2.57 is for a diametric load. A numerical test with the same dimensions of the CCBD74 test was performed with a diametrical load to evaluate the ratio between the equivalent load and the real load. The ratio is of 1.6.

2.5.2.2 CCBD Mode II

As for the CCBD mode I, the analysis was made using the same geometry for the mechanical tests and the inclination to obtain the pure mode II (28°) (CCBD77 test).

In Figure 2. 47, we can see the mesh, the displacement fields and the tensile (positive stress) and compressive zones of the stress fields. The displacements are not symmetric, since the notch is inclined.

The numerical analysis of the CCBD77 test provides for mode II a fracture toughness value of 0.6 MPa.m$^{0.5}$ (using equation 2.11) and for the mode I of 0.1 MPa.m$^{0.5}$. This numerical analysis shows that the mode II should be almost pure. However, to a deeper knowledge of the phenomenon that occurs in this mode and verification of this statement in section 2.6.5 we will show the results of the image correlation which demonstrate that pure mode II is not achieved for this test.

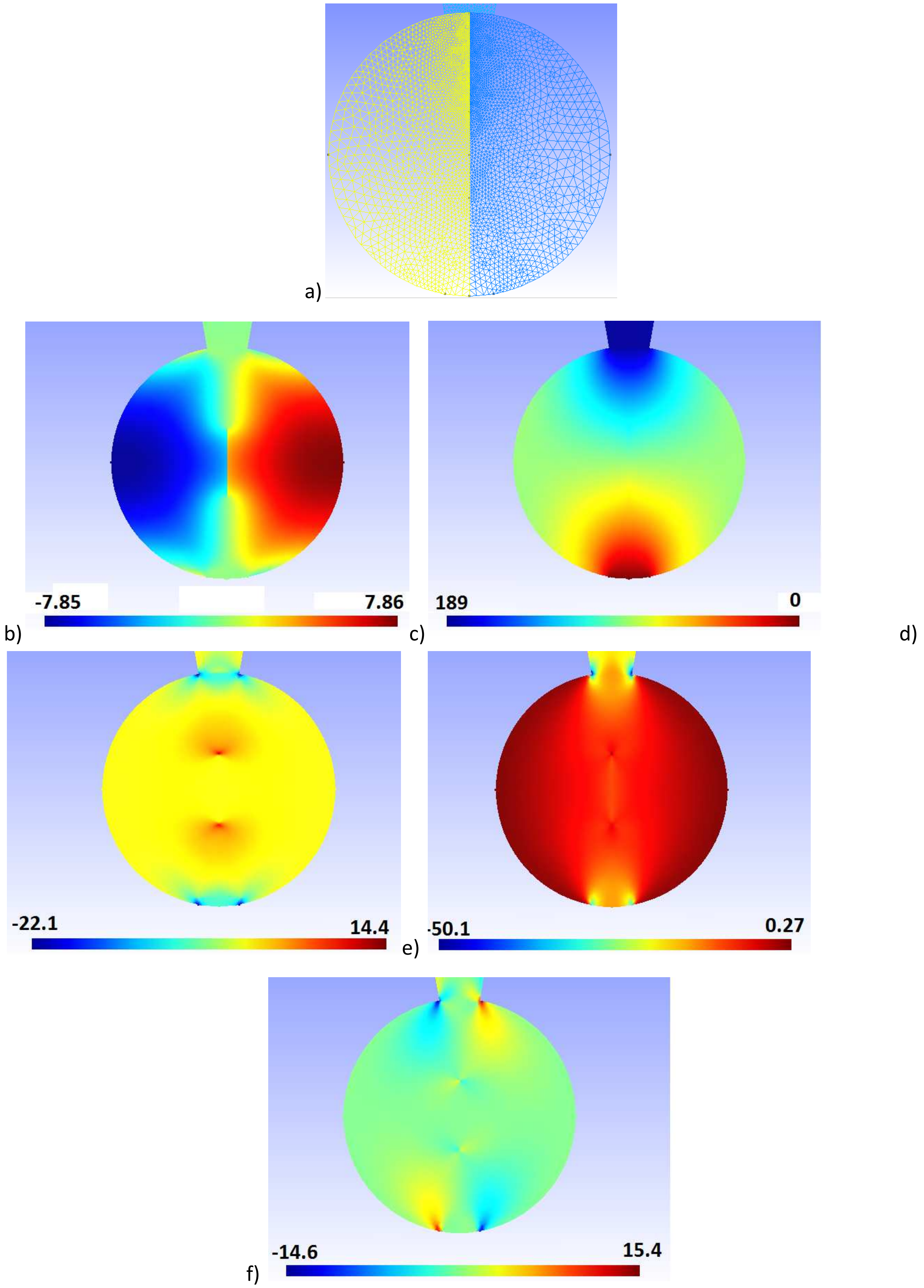

Figure 2. 45- Mesh(a), displacements DX(b), DY (c) in (µm) and stress σ_{xx} (d), σ_{Yy} (e) and σ_{xy} (c) fields (in MPa) - CCBD test

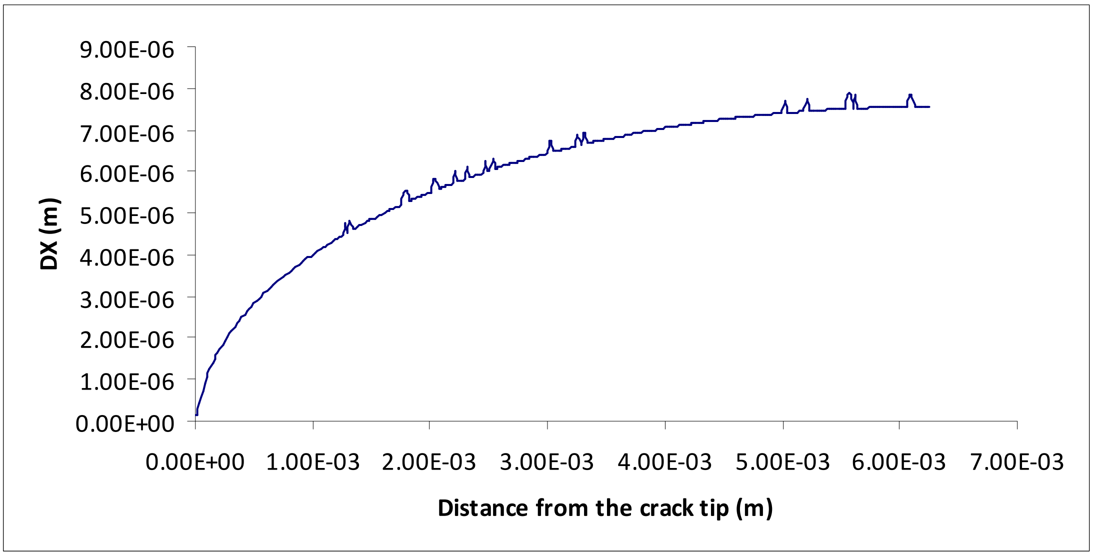

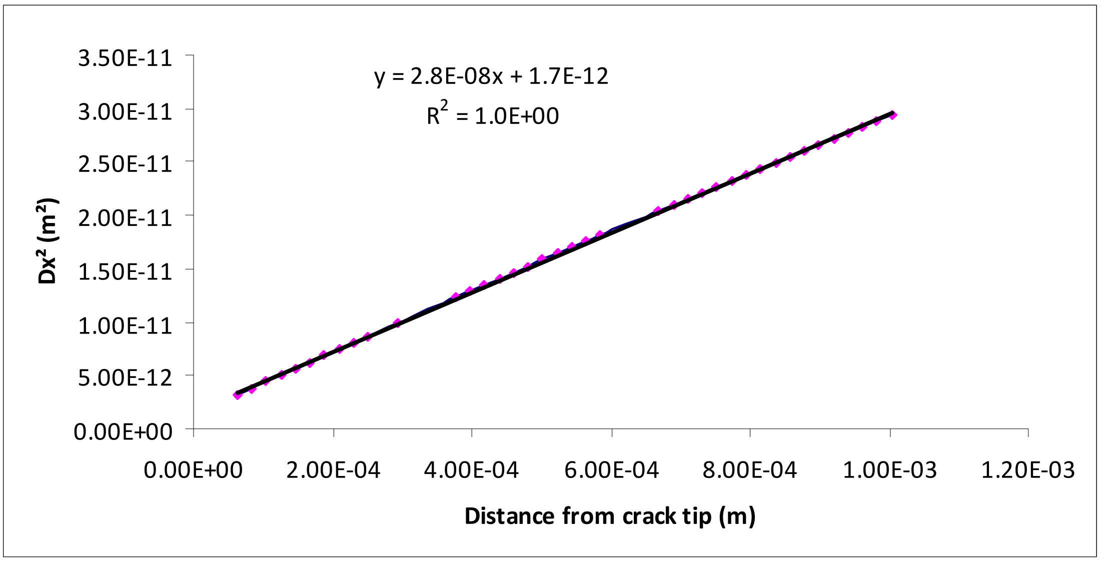

Figure 2. 46- Differential displacements (DX) and DX² at the crack

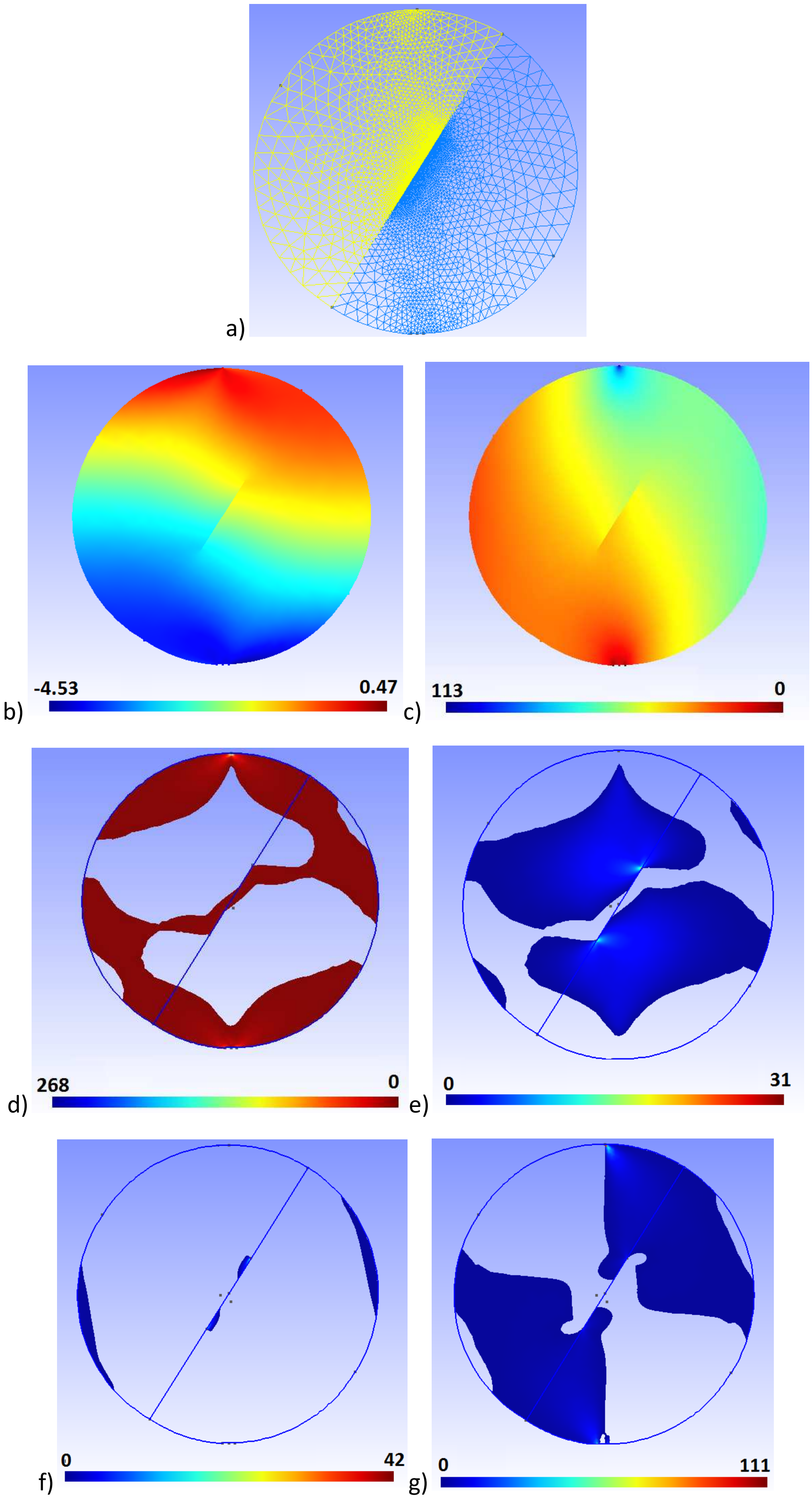

Figure 2. 47- Mesh and displacement field b) DX (µm), c) DY (µm) d) Compression and e) Tensile zone for the stress field σ_{xx}. f) σ_{Yy} and g) σ_{xy} Traction zone (MPa) test CCBD mode II

2.5.2.3 SCB

Figure 2. 48 shows the mesh used in the SCB simulation and the symmetric displacement fields along axis X and Y. The fracture toughness in mode I calculated from the numerical model simulation results is of 0.70 MPa.m$^{0.5}$ and by the equation 2.10 is 0.76 MPa.m$^{0.5}$.

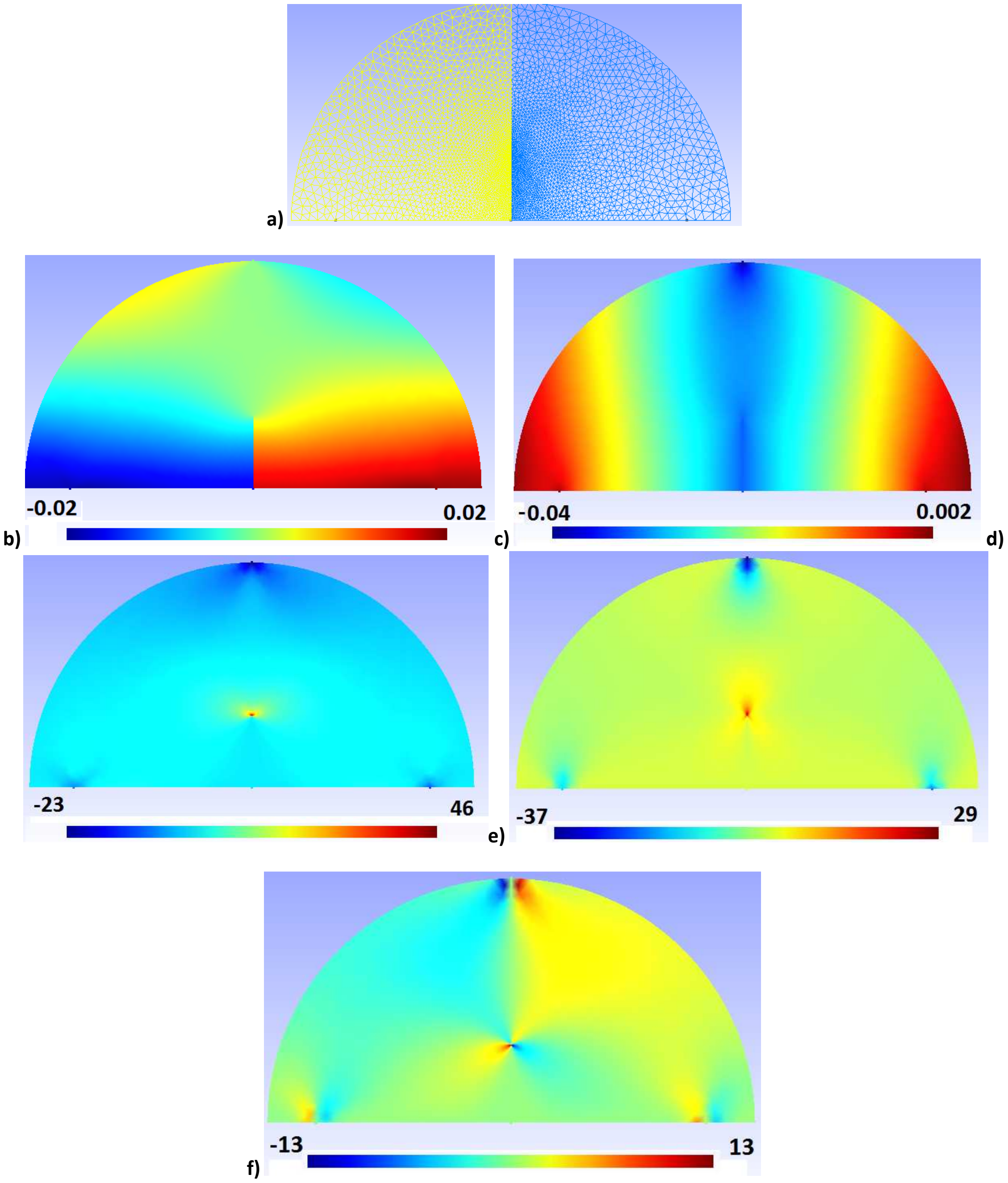

Figure 2. 48 – a)Mesh , displacement fields on mm b)DX c) DYS, stress fields (MPa) d)σxx e) σyy and f) σxy SCB test

2.6 Image correlation technique

In this work, we used the Digital Image Correlation (DIC) as a comparative method for estimating the rock mechanical properties like elastic modulus, Poisson's ratio and fracture toughness. The use of three different programs were needed – CORELIS, BRAZIL and FIC (Hild & Roux, 2006).

In order to record the images we used in a first place a "simple" camera that can record with a maximum frequency of 0.7 images/s, and in a second step, we used a fast camera, which can reach more than 10,000 images/s.

In the first case we collected data during all the experimental procedure, and in the second case, we had just information corresponding to 0.7 seconds that will be taken during the crack propagation.

This means that between two photos made by the "simple" camera, we have a period of time equivalent or larger than the whole information collected by the speed camera.

Knowing this is important for preparation of the test that allows us the fracture toughness determination.

The use of the fast camera in this work is really important, because the material (oolitic limestone) is very brittle, and just with the "simple" camera we were not able to capture the onset of the crack propagation. The equipment can record definitively the images in three different ways. As we press the button to record it can record the 0.7 seconds before we press the button, the 0.7 after we press or 0.35 before and 0.35 after.

To record the crack propagation we chose the set that allows us to record the images 0.7 seconds before we press the button.

We will need the images of the crack propagation to evaluate the fracture toughness using the software FIC (as it will be shown in the section 2.6.4).

2.6.1 Brief description of the DIC method

The process of image correlation is based on the analysis of the displacement field (François Hild & Roux, 2006). The displacement field can be measured because we create a special texture on the surface of the sample. This texture can be applied by a distant spray paint that will form small circles with different levels of grey as it can be seen in Figure 2. 49.

Each image can be considered as a scalar function f(x) - the reference image and g(x) the deformed image. So, for each deformed image there is a relationship defined by the following equation:

$$g_i(x) = f\left[x + u_i(x)\right] \tag{3.61}$$

and we are able to find the $u_i(x)$ corresponding to each deformation (displacement and rotation). More about the DIC will be explained in the CORELIS section.

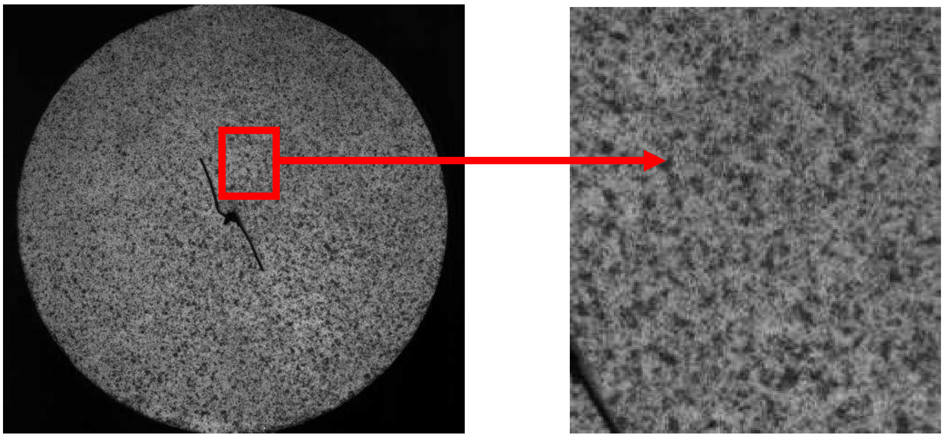

Figure 2. 49 - Grey level in a sample for CCBD Mode II tests

2.6.2 CORELIS

Corelis is a computer code developed by (F. Hild & Roux, 2006) which allows us analyzing qualitatively the deformation and the crack propagation. The output of this code is used as an input for the other programs that will be used to determine the elastic properties (BRAZIL) of the rock and the fracture toughness (FIC).

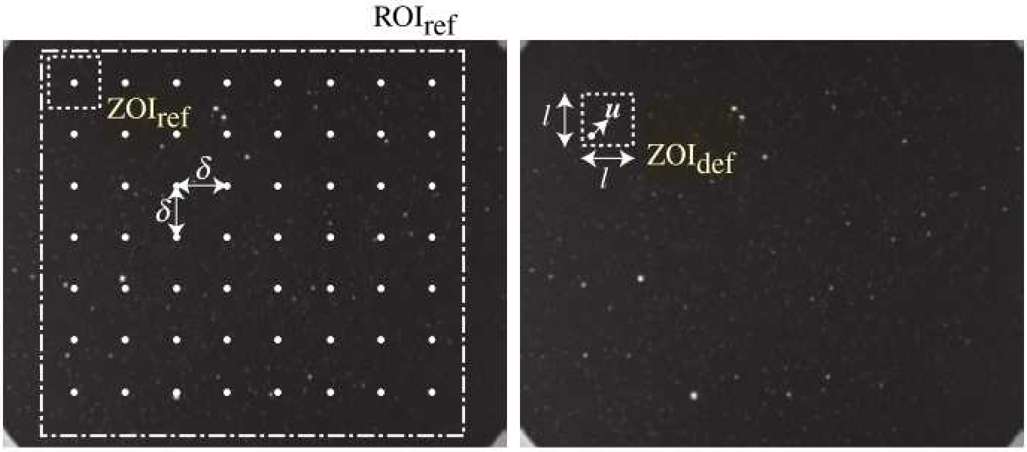

Figure 2. 50 - ROI and ZOI of a image (F. Hild & Roux, 2006)

The analysis starts with the selection of the ROI (Region of Interest). Then, when the ZOI (Zone of Interest, see Figure 2. 50) has to be chosen we can select a range of 4, 8, or 16 pixels.

The ZOI is the block of pixels at which the displacement/deformation will be applied, this means the equation 3.62 will not be solved pixel by pixel, but with a region of *n* pixels and for the resolution of the problem, the following equation will have to be maximized for the ZOI.

$$(f * g)(\underline{v}) = \int f(\underline{x}) g(\underline{x} + \underline{v}) d\underline{x} \tag{3.62}$$

We will be able to determine the displacement field when on the process of iterations we find the best optimization of the previous equation for the whole region.

2.6.3 BRAZIL

In this program we use as input, the output of the CORELIS program. In addition to this information we have to give the real dimensions of the sample and the load for each picture. For this reason, this method can only be used (as we can do with the material we have) if the test were recorded by a camera (not the fast camera), because even if we were able to record the load, the precision is not accurate enough, so we would not extract a valid information.

Based on the (Hondros, 1959) analytical solution for the stress field for a Brazilian test, derived by the Kolossov-Muskhelishvili complex potential, we are able to compare the analytical displacement field with the measured displacement field. The comparison between the two analyses permits to obtain the elastic properties of the material.

The stress field can be formulated following the complex potentials of Kolossov-Muskhelishvili expression where the stress field is described by the expressions described in section 2.1.1.

To found the properties of the rock the program has to minimize the error between the analytical solution and the solution given globally from the data of each pixel.

2.6.4 FIC

The FIC program is used to find the fracture toughness of the rock. For that we use, as mentioned previously, the output of CORELIS as an input. In addition, we also have to give the following information: elastic properties, the rate meters/pixel (indicates the dimension in meter that each pixel corresponds – example the sample has 50 mm and 990 pixels of diameter, then the rate meters/pixel is: 5.05E-5) and the location of the initial crack.

The FIC program can determine the SIF based on the Williams approach (Yates, Zanganeh, & Tai, 2010) of the stress field around the crack. By this approach we can write the displacement field for the different propagation modes I and II as:

$$Mode\ I\left\{\begin{array}{l} u_I=\sum_{n=1}^{\infty}\frac{r^{n/2}}{2\mu}a_n\frac{\frac{\left[\kappa+\frac{n}{2}+(-1)^n\right]\cos n\theta}{2}-\frac{n}{2}\cos(n-4\theta)}{2} \\ v_I=\sum_{n=1}^{\infty}\frac{r^{n/2}}{2\mu}a_n\frac{\frac{\left[\kappa-\frac{n}{2}-(-1)^n\right]\sin n\theta}{2}-\frac{n}{2}\sin(n-4\theta)}{2} \end{array}\right\} \tag{3.63}$$

$$Mode\ II\left\{\begin{array}{l} u_{II}=\sum_{n=1}^{\infty}\frac{r^{n/2}}{2\mu}b_n\frac{\frac{\left[\kappa+\frac{n}{2}+(-1)^n\right]\sin n\theta}{2}-\frac{n}{2}\cos(n-4\theta)}{2} \\ v_{II}=\sum_{n=1}^{\infty}\frac{r^{n/2}}{2\mu}b_n\frac{\frac{\left[\kappa-\frac{n}{2}-(-1)^n\right]\cos n\theta}{2}-\frac{n}{2}\sin(n-4\theta)}{2} \end{array}\right\} \tag{3.64}$$

Where μ and κ are the Lamé parameters; r and θ the radial distances and n the coefficient of the series. To ease the computation of the SIF by the DIC, we have to explicit the scalar functions (reference and deformed) for the modes I (f and g functions) and II (h and l functions), that will be used to find the displacement field, concerning the digital image correlation as follows:

$$f_{n,m}=\frac{r_m^{n/2}}{2\mu}\left\{\frac{\frac{\left[\kappa+\frac{n}{2}+(-1)^n\right]\cos n\theta_m}{2}-\frac{n}{2}\cos(n-4\theta_m)}{2}\right\} \tag{3.65}$$

$$g_{n,m}=-\frac{r_m^{n/2}}{2\mu}\left\{\frac{\frac{\left[\kappa+\frac{n}{2}+(-1)^n\right]\sin n\theta_m}{2}-\frac{n}{2}\sin(n-4\theta_m)}{2}\right\} \tag{3.66}$$

$$h_{n,m} = \frac{r_m^{n/2}}{2\mu}\left\{\frac{\dfrac{\left[\kappa - \dfrac{n}{2} - (-1)^n\right]\sin n\theta_m}{2} + \dfrac{n}{2}\sin(n - 4\theta_m)}{2}\right\} \tag{3.67}$$

$$l_{n,m} = \frac{r_m^{n/2}}{2\mu}\left\{\frac{\dfrac{\left[\kappa - \dfrac{n}{2} - (-1)^n\right]\cos n\theta_m}{2} + \dfrac{n}{2}\cos(n - 4\theta_m)}{2}\right\} \tag{3.68}$$

Where m is the data point index and n is the series term (stopping at 3 or terms up to $r^{3/2}$) . The displacement field can be expressed by the following matrix:

$$\begin{Bmatrix} \ddot{u}_1 \\ \vdots \\ u_m \\ v_1 \\ \vdots \\ v_m \end{Bmatrix} = \begin{bmatrix} f_{1,1} & \cdots & f_{n,1} & g_{1,1} & \cdots & g_{n,1} \\ & \vdots & & & \vdots & \\ f_{1,m} & \cdots & h_{n,m} & g_{1,m} & \cdots & g_{n,m} \\ h_{1,1} & \cdots & h_{n,1} & l_{1,1} & \cdots & l_{n,1} \\ & \vdots & & & \vdots & \\ h_{1,m} & \cdots & h_{n,m} & l_{1,m} & \cdots & l_{n,m} \end{bmatrix} \begin{Bmatrix} a_1 \\ \vdots \\ a_n \\ b_1 \\ \vdots \\ b_n \end{Bmatrix} \tag{3.69}$$

Where a_i and b_i are the coefficients to resolve the equations.

If we want to express this matrix in a more common notation, we can choose the SIF. So we will have:

$$K_I = a_1\sqrt{2\pi} \tag{3.70}$$

$$K_{II} = -b_1\sqrt{2\pi} \tag{3.71}$$

$$T = 4a_2 \tag{3.72}$$

Those are respectively the SIF for the mode I, mode II and the T-stress. However it is simple to observe, that no rigid body motion is considered in the previous matrix. To a more complete analysis this can be corrected by adding a few terms that can be identified on the matrix (3.73).

This is useful because in most of the Brazilian experiments there is an important body rotation, and this allows us to identify the real coefficients a_1 and b_1 to the K_I determination and where a_0 and b_0 compensates the rigid body motion and R the rigid body rotation.

$$\begin{Bmatrix} \ddot{u}_1 \\ \vdots \\ u_m \\ v_1 \\ \vdots \\ v_m \end{Bmatrix} = \begin{bmatrix} 1 & f_{1,1} & \cdots & f_{n,1} & 0 & g_{1,1} & \cdots & g_{n,1} & -r_1 \sin\theta_1 \\ & & \vdots & & & & \vdots & & \\ 1 & f_{1,m} & \cdots & h_{n,m} & 0 & g_{1,m} & \cdots & g_{n,m} & -r_m \sin\theta_m \\ 0 & h_{1,1} & \cdots & h_{n,1} & 1 & l_{1,1} & \cdots & l_{n,1} & r_1 \sin\theta_1 \\ & & \vdots & & & & \vdots & & \\ 0 & h_{1,m} & \cdots & h_{n,m} & 1 & l_{1,m} & \cdots & l_{n,m} & r_m \cos\theta_m \end{bmatrix} \begin{Bmatrix} a_0 \\ a_1 \\ \vdots \\ a_n \\ b_0 \\ b_1 \\ \vdots \\ b_n \\ R \end{Bmatrix} \tag{3.73}$$

2.6.5 Digital image correlation results

A part of these fracture toughness experiments, have been combined with the Digital Image Correlation (DIC) technique. The images of the sample during the experiments have been recorded using a high-speed camera with a rate of 1 image per second to 10.000 images per second.

Recording images with these rates permits to follow with a great precision the initiation and propagation of the cracks during the experiments. Of great interest is also to check the validity of the performed experiments by verifying where the crack propagation initiates and how it propagates. The method consists in taking an initial photograph and measuring the displacement field from the following photographs by comparison with the initial one (Figure 2. 51).

For example a given mode I CCBD experiment, the classical load analysis of the mechanical test gives a K_{IC} value of 0.62 MPa.m$^{0.5}$ (CCBD74). For the CCBD77 a sample in mode II, as presented in (Table 2. 19), for the same experiment the digital image correlation gives a K_{IC} value of 0.60 MPa.m$^{0.5}$, which confirms the validity and good quality of the mechanical test for the mode I fracture toughness.

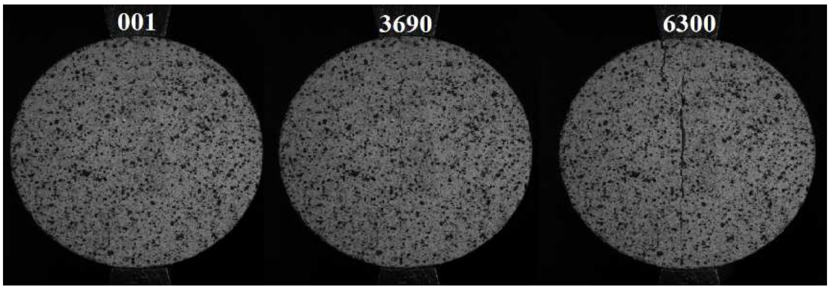

Figure 2. 51- Images and photo numbers from DIC of a Brazilian disk experiment

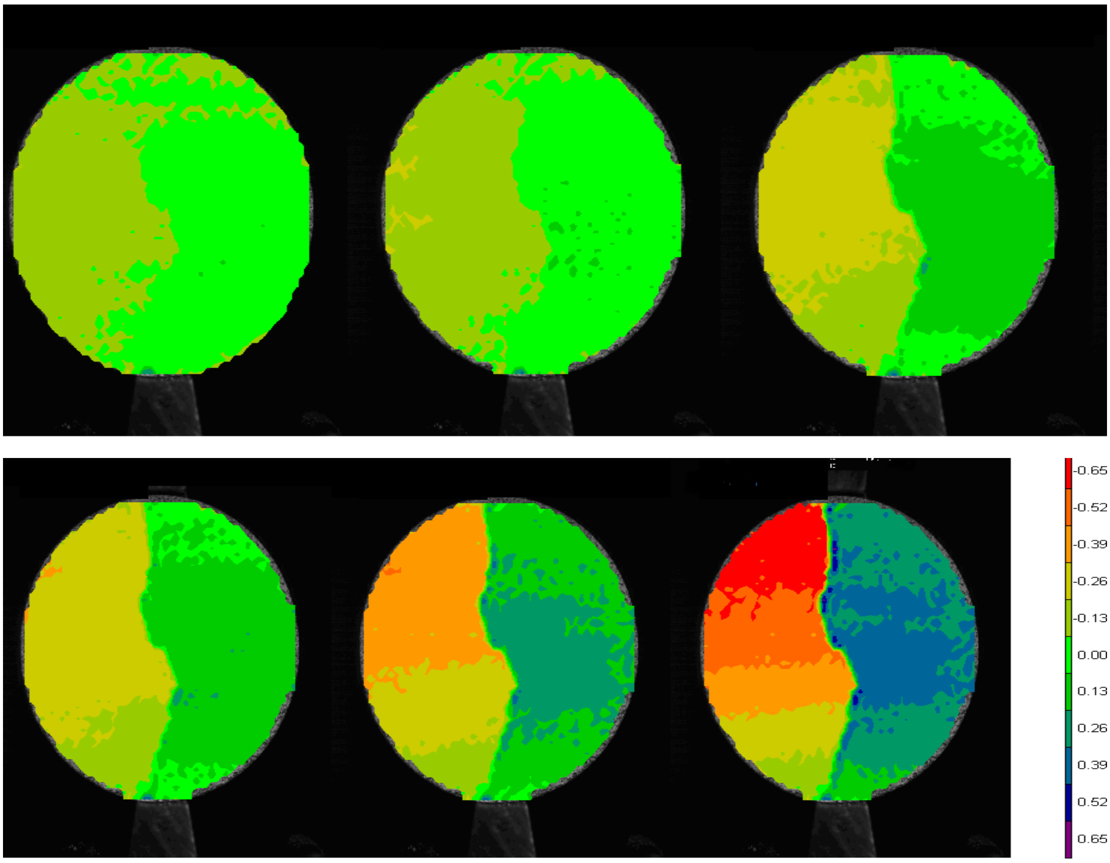

Figure 2. 52 - Evolution of the lateral displacement for a CCBD mode II test

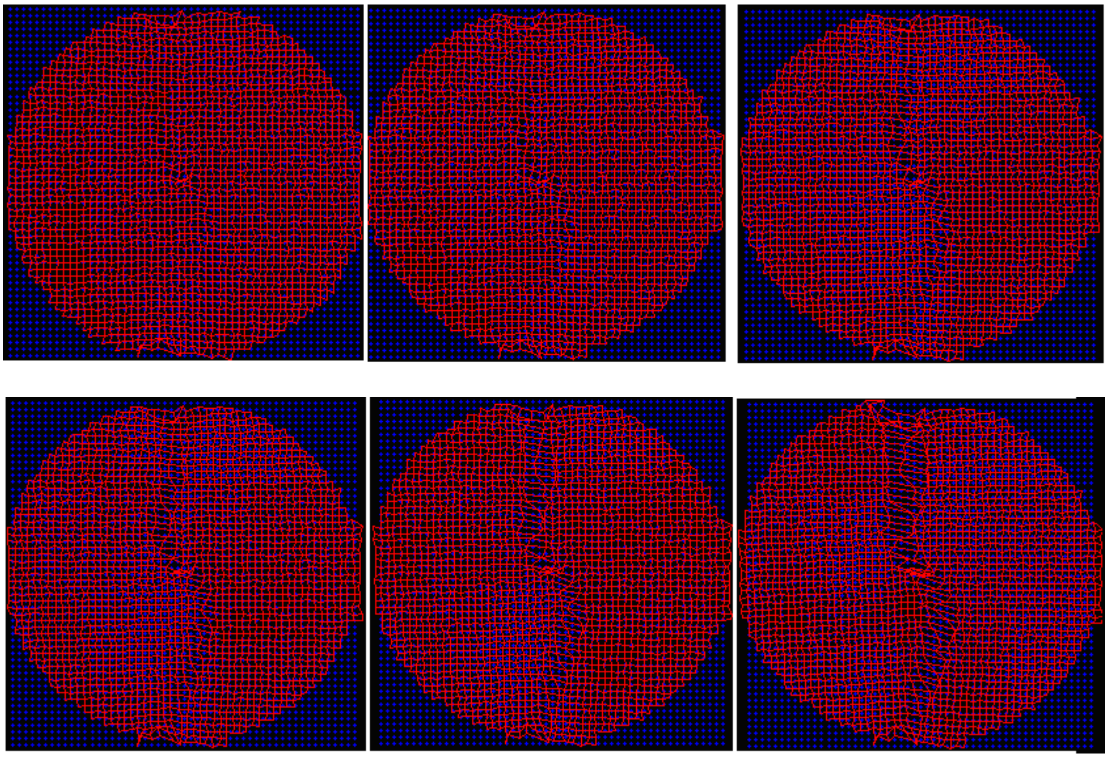

Figure 2. 53 - Evolution of the displacement mesh given by Correlis

Table 2. 19- Comparison of the results of mechanical tests and the digital image analysis experiments for evaluation of mode I and mode II fracture toughness

CCBD	***Mode I***	***Mode II/Mixed***	
Method	**K_{IC} (MPa.m$^{0.5}$)**	**K_{IC} (MPa.m$^{0.5}$)**	**K_{IIC} (MPa.m$^{0.5}$)**
Mechanical test	0.62	0.00	0.60
DIC	0.60	0.51	0.64

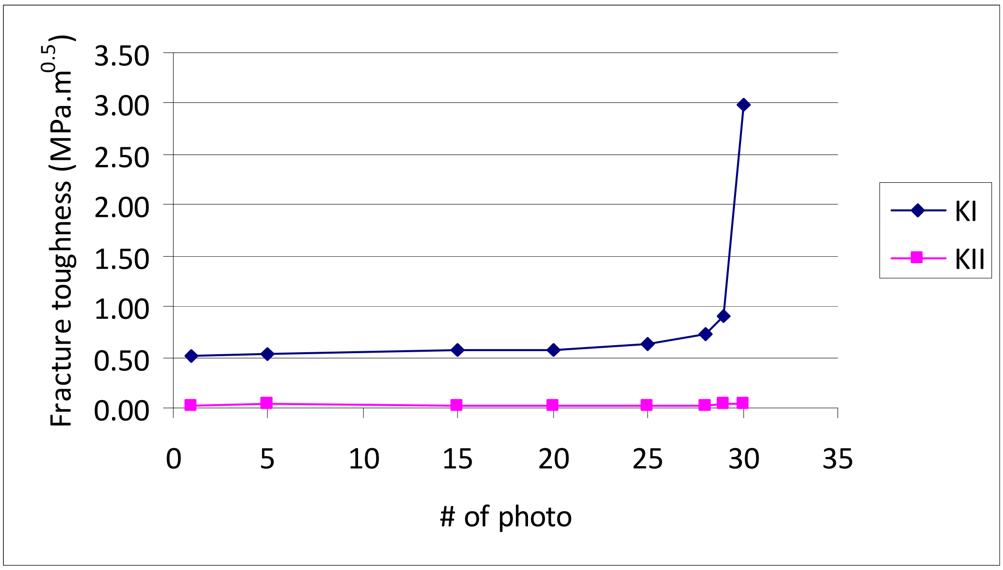

Figure 2. 54- Fracture toughness analysis by image DIC

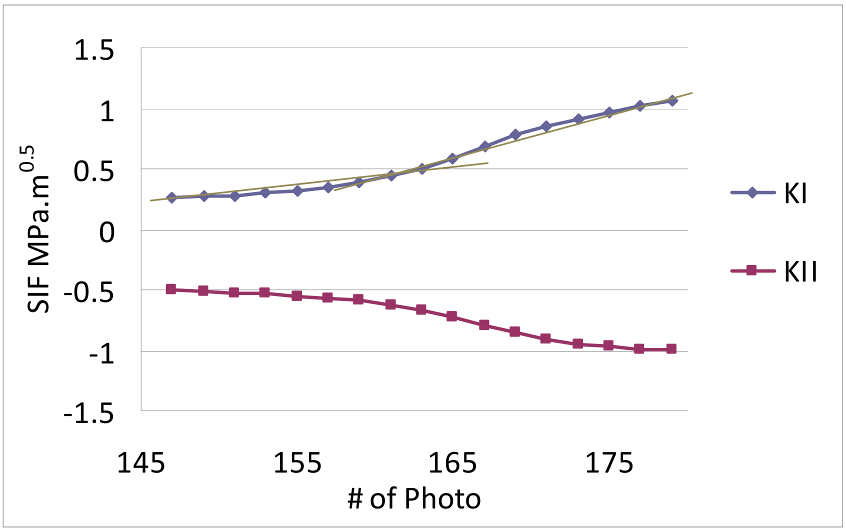

Figure 2. 55- Evolution of SIF with loading stage for a CCBD in mixed mode

For the SCB test the Figure 2. 54 shows the evolution of the stress intensity factor during the final phase of the test. We observe that the stress intensity factor for mode II remains negligible during the test. The value of fracture toughness from the DIC method is of 0.73 MPa.m$^{0.5}$ and the experimental value is of 0.76 MPa.m$^{0.5}$ for the SCB37 test. These tests were performed using a degraded sample that stayed a month in the autoclave without water change.

A very interesting result of the DIC experiments concerns the mode II fracture toughness evaluation, because of the questions raised in section 2.4.1.

The Figure 2. 52 and Figure 2. 53 show the evolution of the displacement field for a CCBD sample submitted to a “pure” mode II obtained by the CORRELIS program developed by LMT-Cachan.

The evolution of the displacement gives us an indicator of which sequence of photos should be analyzed by the FIC program (F. Hild & Roux, 2006) to determine the fracture toughness at the very moment of crack propagation. We analyze the data given by the FIC program together with the CORRELIS analysis to evaluate the fracture toughness.

In CCBD experiment, the angle of inclination of the pre-existing crack with respect to the direction of the load application can be calculated as a function of the sample and crack dimensions in order to achieve a pure mode II fracture propagation. This is done by solving equation (2.54) to find the angle θ resulting in N_I=0. The result of this experiment gives a value of K_{IIC} equal to 0.60 MPa.m$^{0.5}$ (Table 2. 19).

For the same experiment the evolution of the stress intensity factor during several loading stages using the digital image correlation technique is shown in Figure 2. 55 (SIF vs the photo number).

The fracture toughness corresponds to the change in the slope of the curve: the change will correspond to an image *n* given by the CORRELIS program so that the next image *n+1* will present a significant increase in the displacement field, showing that the sample reaches its rupture.

Such an analysis was also conducted for other mechanical tests (including the CCBD in mode II). As shown in Figure 2. 55, although the notch inclination is positioned so that the rupture should theoretically be in pure mode II (the negative value for the mode II is due to the direction of crack propagation), the displacement field evaluated from DIC shows that the SIF in mode I remains significant. **The crack propagation in this experiment occurred therefore in mixed-mode.**

Chang et al., 2002 tried to use this technique to find the pure mode II for granite and marble. The values, around 1.3 MPa.m$^{0.5}$, are close to the mode I values, 1.3 MPa.m$^{0.5}$ for the granite and 1.1 MPa.m$^{0.5}$ for the marble.

Backers (2002), found for a marble a value of K_{IC} = 1.1 MPa.m$^{0.5}$, and a value of K_{IIC} using the PTST test of 11 MPa.m$^{0.5}$ for a confining pressure of 25 MPa.

2.7 PTST – Punch Through Shear Test

- Fracture toughness tests with a loading mode type - SHEAR

The section 2.6.5 and the results of the digital image correlation tests showed us the difficult of obtaining the pure mode II of crack propagation in an unconfined sample. This obliged us to search for a more reliable method to evaluate the fracture toughness for the mode II.

The PTST - Punch through shear test (Figure 2. 56) is the ISRM test for the fracture toughness in mode II evaluation. In this test, an external pressure is applied to the sample that will induce more easily a mode II mode of crack propagation. As the sample is confined, and the confinement pressure increases the crack can't open avoiding the appearance of mode I that would provoke a mixed mode.

This last consideration is important, because, even with a shear loading mode, it is possible to propagate a crack in mixed mode (Figure 2. 57), and this phenomenon is attenuated with confined samples with a high confinement pressure (Backers, 2002).

The calculation of the fracture toughness for this sample is done numerically, that will be described in the next section.

Some of the samples used in this study can be seen in Figure 2. 58 and the apparatus for the fracture mechanical test can be seen in Figure 2. 59.

In Figure 2. 60 we can see the whole set up for the PTST experiment, the press, the cell position and the GDS.

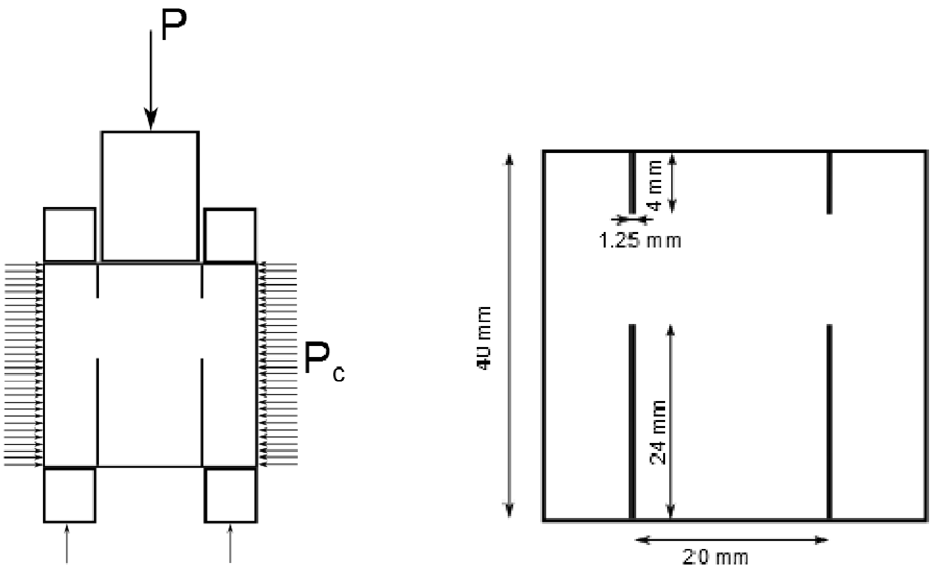

Figure 2. 56 - Set-up of PTST and dimensions

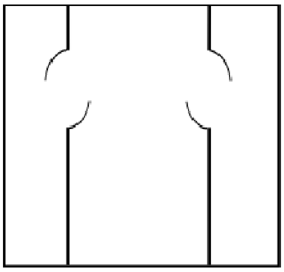

Figure 2. 57 - Propagation mode - wing crack

Figure 2. 58 - PTST samples

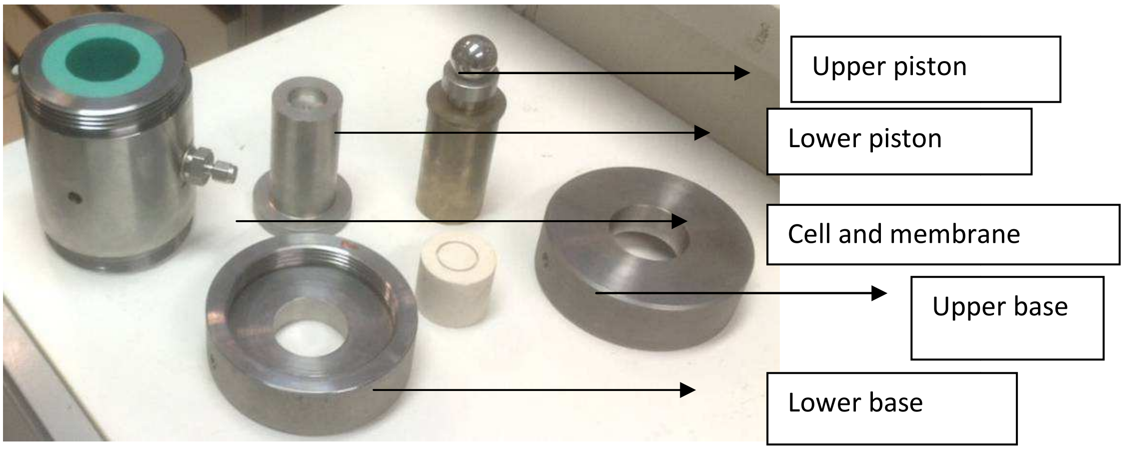

Figure 2. 59 - Hooke cell and a sample

Figure 2. 60 - Cell installed at the press – GDS – dispositive at CERMES

2.7.1 PTST numerical simulation

To analyze the fracture toughness on a PTST sample, we have to perform a numerical simulation of the test. As the sample is cylindrical we can perform an axisymmetric simulation as shown in Figure 2. 61 .

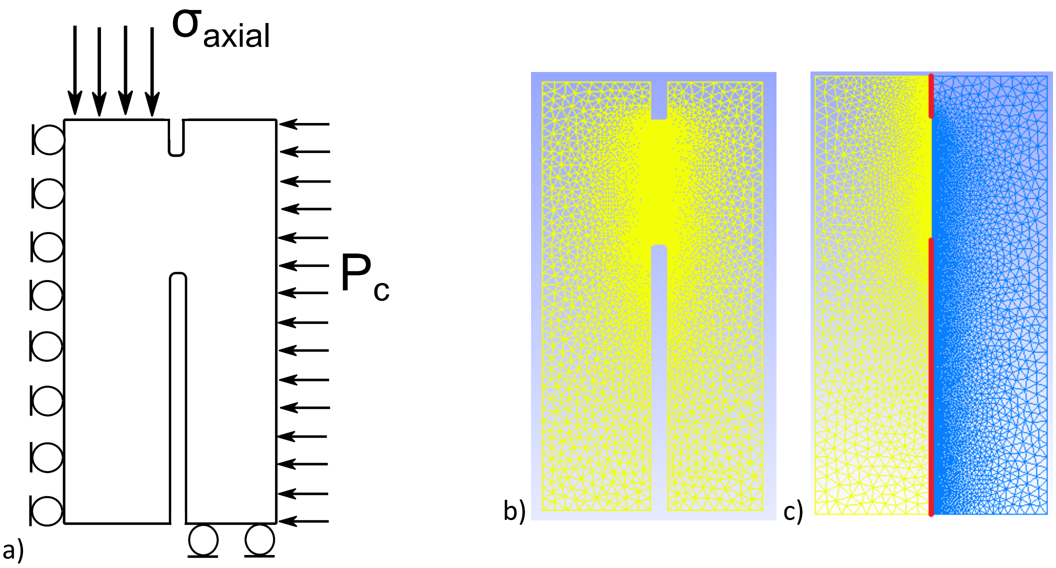

Figure 2. 61- Numerical model for the PTST a) schema of loading b) mesh for the PTST test, and c) mesh for the PTST without thickness

The analysis performed in this section aims at investigating the influence of the thickness of the sample notch. This analysis is important once a crack in an underground condition will not have a thickness. As the PTST sample has notches with thickness, the impact this detail could provoke on the K_{IIC} calculation should be measured.

The PTST is used to measure the pure mode II, which is more likely to happen in a confined environment. We present three figures (Figure 2. 62 to Figure 2. 64) to illustrate the change in the mode I or II when the thickness of the notch changes. The numerical model is performed on the real load conditions and geometry shown in Figure 2. 61.

We take the example of the PTST01 test to illustrate the process, mode details about the general results for the PTST samples will be given in the next section.

The Figure 2. 62 shows the calculations for the PTST with the notch thickness in the tested sample (1.25 mm): the measured K_I and K_{II} measured are respectively 0.46 and 1.6 MPa.m$^{0.5}$ (intersection of the trend lines mode I and mode II for the bottom notch). The Bottom crack is the notch in the bottom part of the sample, while the Top crack, the notch in the upper part of the sample.

However, to verify the potential impact of the change in the thickness, we performed tests with a thickness of 0.6 mm. The Figure 2. 62 shows the results and we can see the K_I and K_{II} are respectively 0.25 and 1.93 MPa.m$^{0.5}$.

We can see that the mixed mode continue to exist, even with a thickness twice smaller. Pushing the analysis further, we performed the analysis with a zero-thickness notch (Figure 2. 61). In this case, the results show that the K_I is negative, showing the existence of a pure mode II (Figure 2. 64).

The PTST01 test has a confining pressure of 5 MPa : we could expect the influence of the notch thickness will be even larger for a higher confining pressure. In this view, we made the same analysis for the PTST18 test.

We can see that reducing the thickness from 1.55 mm to 0.60 mm the mode I is inexistent. The values of K_I and K_{II} decrease from 0.33 and 3.21 to 0 and 4.34 MPa.m$^{0.5}$ as we can see in Figure 2. 65 and Figure 2. 66.

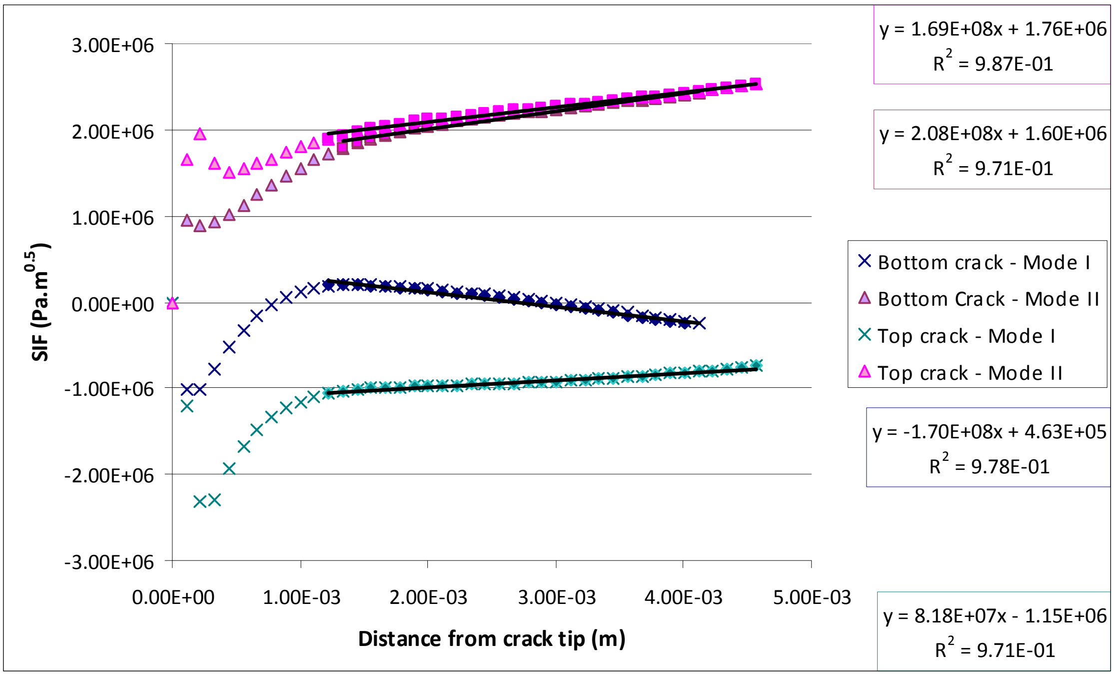

Figure 2. 62- Fracture toughness evaluation by the stress state around the top and bottom of the crack tip – sample PTST01 – Confining pressure 05 MPa

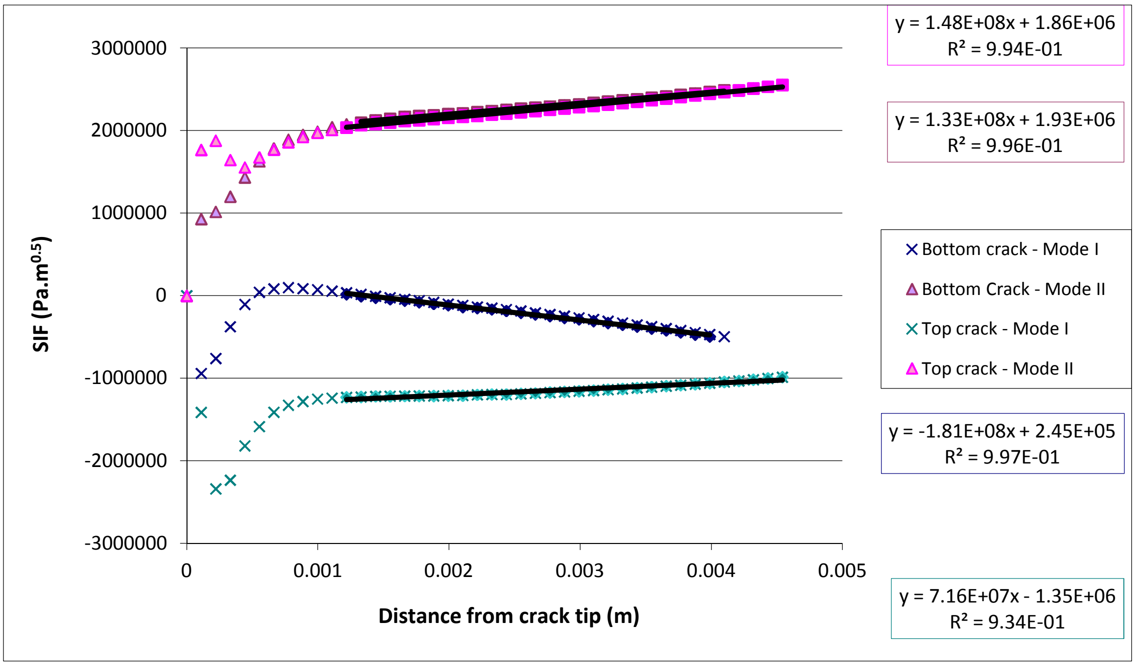

Figure 2. 63- Fracture toughness evaluation by the stress state around the top and bottom of the crack tip – sample PTST01 – Confining pressure 05 MPa – changed thickness 0.6 mm

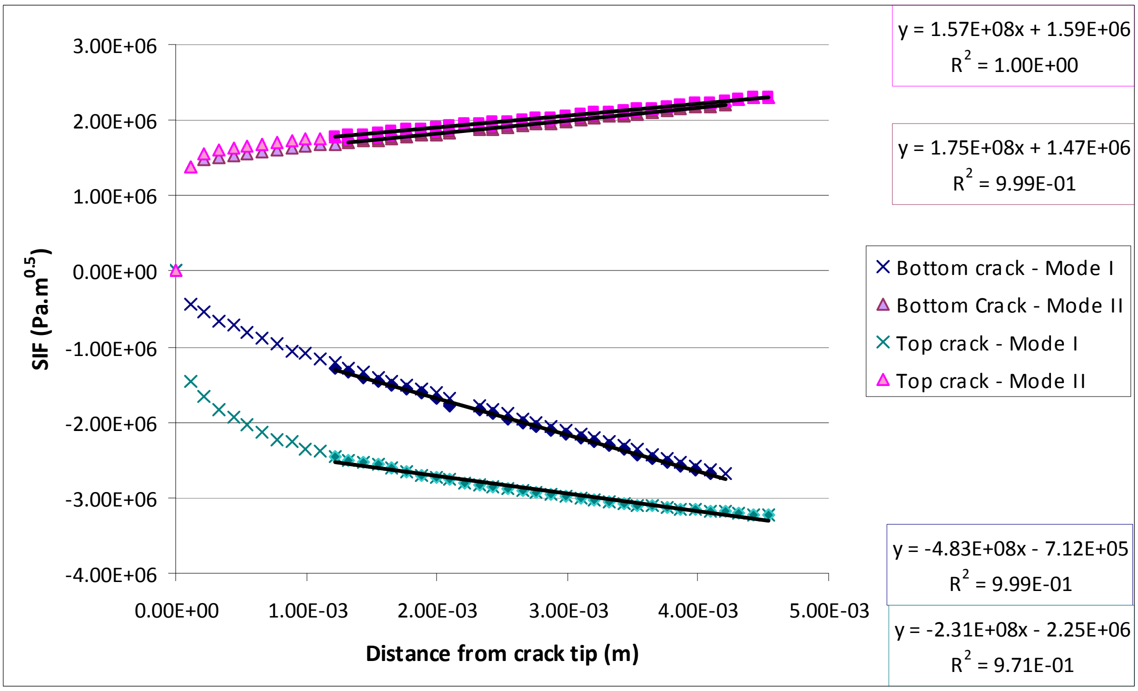

Figure 2. 64- Fracture toughness evaluation by the stress state around the top and bottom of the crack tip – sample PTST01 – Confining pressure 05 MPa – without thickness

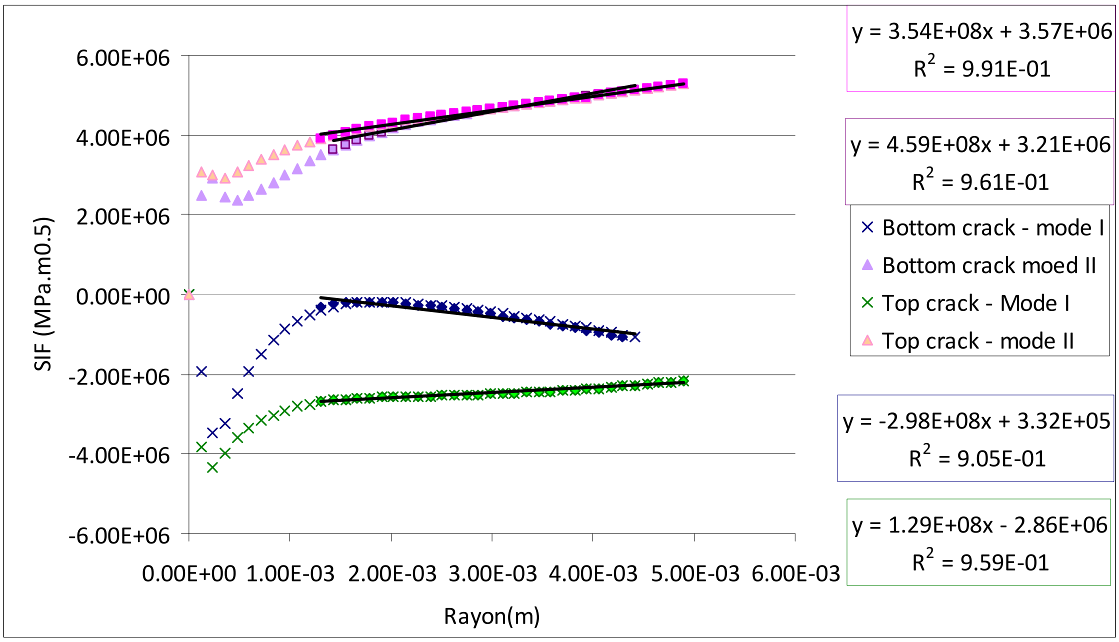

Figure 2. 65 - Fracture toughness evaluation by the stress around the top and bottom of the crack tip - sample PTST18 - Confining pressure 15 MPa – thickness 1.55 mm

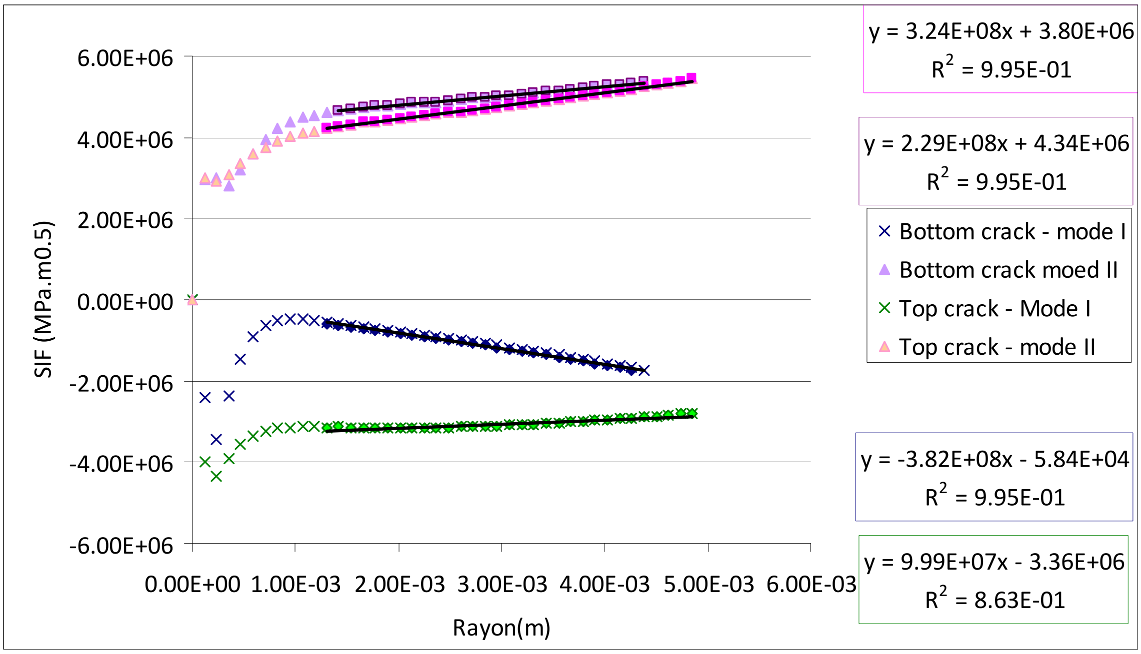

Figure 2. 66 - Fracture toughness evaluation by the stress around the top and bottom of the crack tip - sample PTST18 - Confining pressure 15 MPa – thickness 0.6 mm

2.7.2 Results - Evaluation of the fracture toughness on mode II by the punch-through shear test (PTST)

As discussed above, the evaluation of K_{IIC} with CCBD is not accurate, because a mixed mode actually it developed during the test. However, the mode II fracture toughness is important because the shear mode of failure has been demonstrated to be the most critical one for deep exploitation of aquifers and in particular for CO_2 storage, e.g., (Rutqvist et al., 2007); (Rohmer & Bouc, 2010).

Yet, up to now, we have conducted standard mechanical tests without confinement and these tests have shown that K_{IIC} cannot be determined in an unconfined environment (Figure 2. 55).

An experimental set-up similar to Backers (2002) has been developed in CERMES as shown in Figure 2. 59 and Figure 2. 60. The experimental load-displacement curves for confinement pressures of 5, 10 and 15 MPa can be seen in Figure 2. 67

We observe that the maximum load, and thus the fracture toughness increases with the confining pressure. The numerical analysis was developed in Code_Aster under axisymmetric conditions.

In Figure 2. 61 we can see a typical example of the loading sketch and of the mesh. All the meshes used for the various simulations have 10175 nodes and 20128 elements.

As we can see in Figure 2. 69 the crack propagates through the line that connects point B in the upper notch to point A in the lower one. In Figure 2. 69b it can be seen the geometry used for numerical simulation and the line AB from where the stress state is evaluated.

Backers (2002) has shown that the point B has the maximum normalized K_{II}, so we chose to evaluate the parameter assuming that the crack will propagate in mode II from the point B to the point A.

The evaluation of the fracture toughness had to be done numerically, using the real sample dimensions and loading conditions

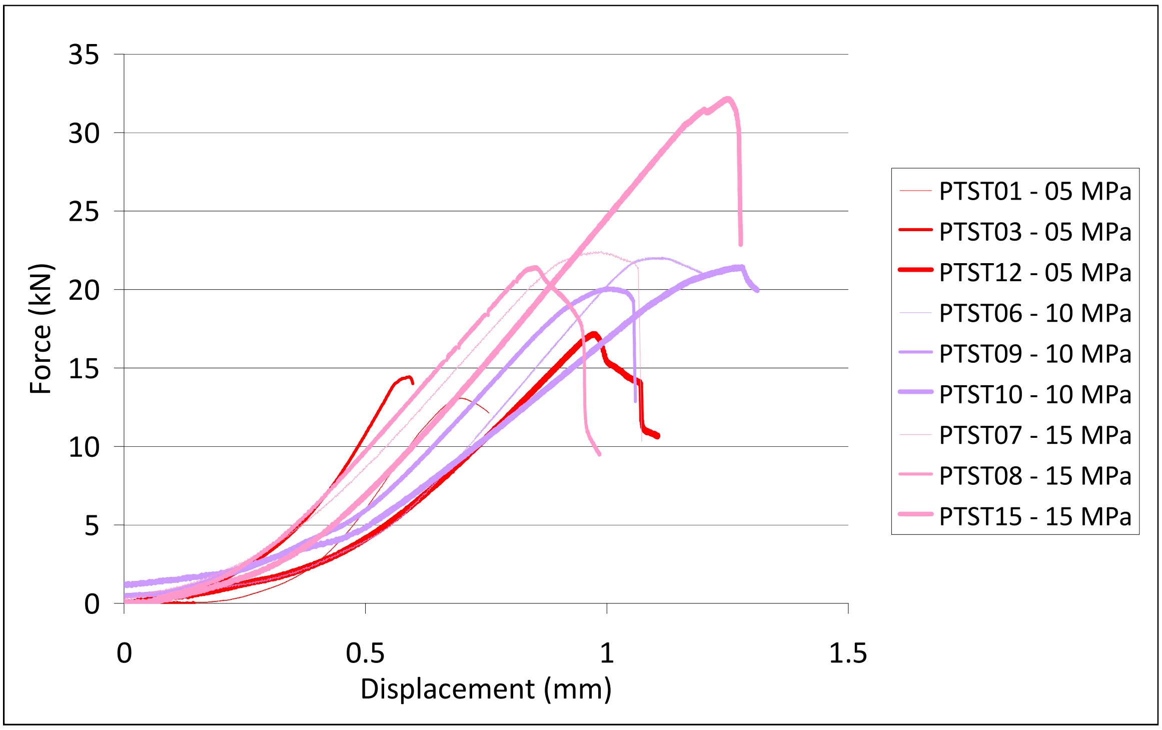

Figure 2. 67 - PTST intact samples curves for confinement of 05, 10 and 15 MPa

As we can see in Figure 2. 69, the crack tip has a quasi-rectangular form, with a round edge. For this reason, a similar form of crack tip was chosen in the numerical model. (Dau Anh-Tuan, 2013) discussed the choice of the crack tip shape for a problem of a horizontal crack in traction. He modelled different crack tip forms, either straight (quasi-rectangular), triangle or circular. For the PTST test, he used the form of a crack tip with rounded edges. The choice was made based of this analysis and the post-mortem SEM imagine (Figure 2. 69). Figure 2. 70 shows a closer view of the crack tip used in the numerical model.

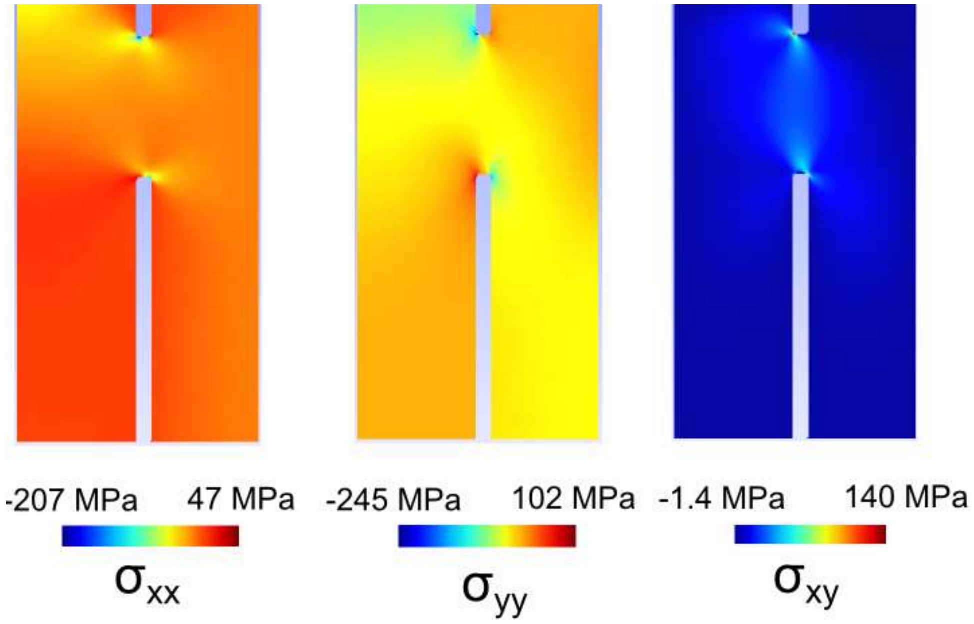

Figure 2. 68 - Stress field for a PTST08 test – 15 MPa confinement pressure and 70 MPa axial pressure

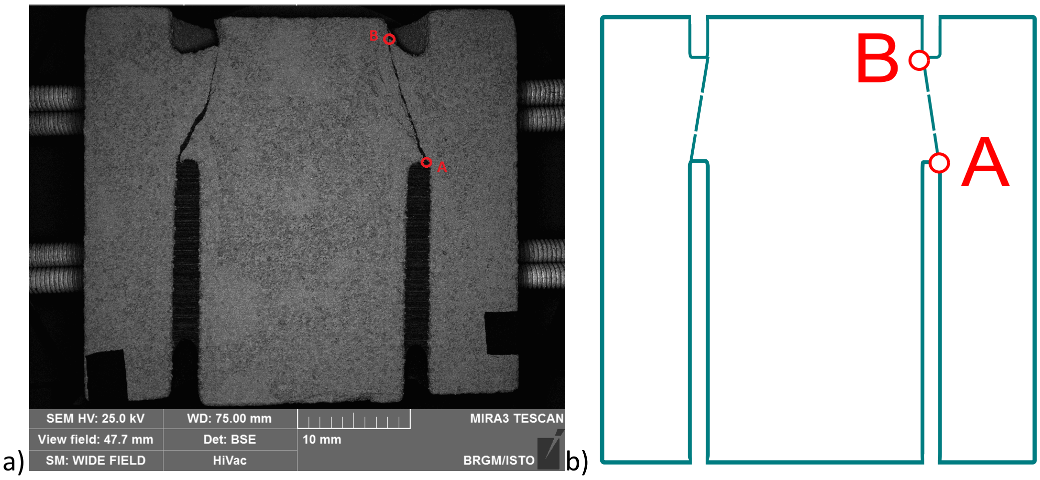

Figure 2. 69- a)SEM image of a longitudinal section passing at the sample's centre – PTST02, b) Sketch of the PTST sample after test – base for numerical simulation

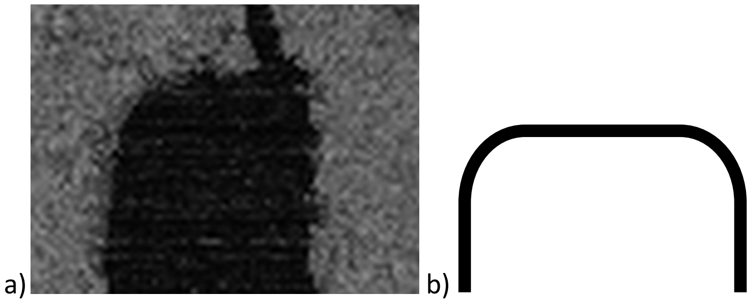

Figure 2. 70– a) View of the crack tip SEM post-mortem image, b) View of the edge rounding of the crack tip

The evaluation of mode I and II stress intensity factor is done by plotting the relation between $\sqrt{2\pi}\sigma_{\theta\theta}$ (for the mode I) or $\sqrt{2\pi}\sigma_{r\theta}$ (for the mode II) and the distance from the crack tip (Figure 2. 71). As the stress tends to infinity around the crack tip, the stress intensity factor is calculated by the intersection between the straight line interpolated on the data and the vertical axis. In the example shown in this figure, K_I has a negative value, showing that the mode I is inexistent and K_{II} is 2.37 MPa.m$^{0.5}$. The results for all samples can be seen in Table 2. 20

However, two elements in Figure 2. 69 raise questions on this analysis.

First: the top notch, after the mechanical test, is larger than the bottom one, showing that the region has been locally submitted to a very high compressive stress that damaged the area (Figure 2. 69a). As a consequence, the exact position of point B in the failed sample is unknown.

Table 2. 20 - Characteristics of PTST intact samples

Test name	Diameter (mm)	Internal diameter (mm)	Thickness (mm)	Notch thickness (mm)	Up notch (mm)	Bottom notch (mm)	Load rate (mm/min)	First peak (kN)	Confining pressure (MPa)	Axial pressure (MPa)	K_{IC} (MPa.m$^{0.5}$)	K_{IIC} (Ma.m$^{0.5}$)
PTST01	40.02	19.62	38.19	1.25	3.8	24.0	0.02	13.1	5	43.28	0.48	1.57
PTST03	40.02	19.62	41.50	1.25	4.2	21.1	0.02	14.0	5	46.39	0.88	1.79
PTST12	39.82	19.74	38.83	1.25	3.5	23.0	0.025	17.3	5	56.46	0.66	1.93
PTST06	40.04	19.68	36.64	1.25	3.0	22.0	0.025	21.9	10	72.00	0.41	2.61
PTST09	40.07	19.63	36.34	1.25	3.0	21.0	0.025	19.4	10	63.97	0.11	2.22
PTST10	40.02	19.68	39.97	1.25	4.0	24.0	0.025	21.4	10	70.35	0.32	2.43
PTST07	40.03	19.73	36.47	1.25	3.0	22.0	0.025	22.4	15	73.33	0.00	2.72
PTST08	40.05	19.8	36.56	1.25	3.0	22.0	0.025	21.3	15	69.18	0.00	2.57
PTST15	40.06	19.84	39.98	1.25	4.0	24.0	0.025	31.5	15	101.73	0.40	3.60

Second: by observing the SEM image (Figure 2. 69a) and the calculation of K_I and K_{II} shown in the Figure 2. 71 for 5 MPa of confining pressure, Figure 2. 72 for 10 MPa and Figure 2. 65 for 15 MPa, we can see the crack propagation from the bottom does not seem to have propagated through shear mode, but opening mode.

The crack in Figure 2. 69a and the existence of a significant K_I, that is clearly shown by the numerical model, outlined the difficulty in reproducing at laboratory scale a shear mode of rupture that is more likely to happen in underground conditions.

This happens because the crack of the samples has some thickness, contrary to underground crack/fractures, which are more likely characterized by zero thickness crack, with a contact between the two lips, or are likely to be filled with some rock material.

The emptiness of the thickness allows the exterior inferior zone of the crack to bend provoking an opening of the crack during propagation. However, this is more a hypothesis than an observation. Other complementary tests and/or analysis should be performed to confirm or deny this point.

These remarks let us conclude that the crack has most probably begun at the point A; and the propagation seems to be on a mixed mode. Therefore the stress intensity factors in modes I and II and recalculated at point A (Table 2. 22)

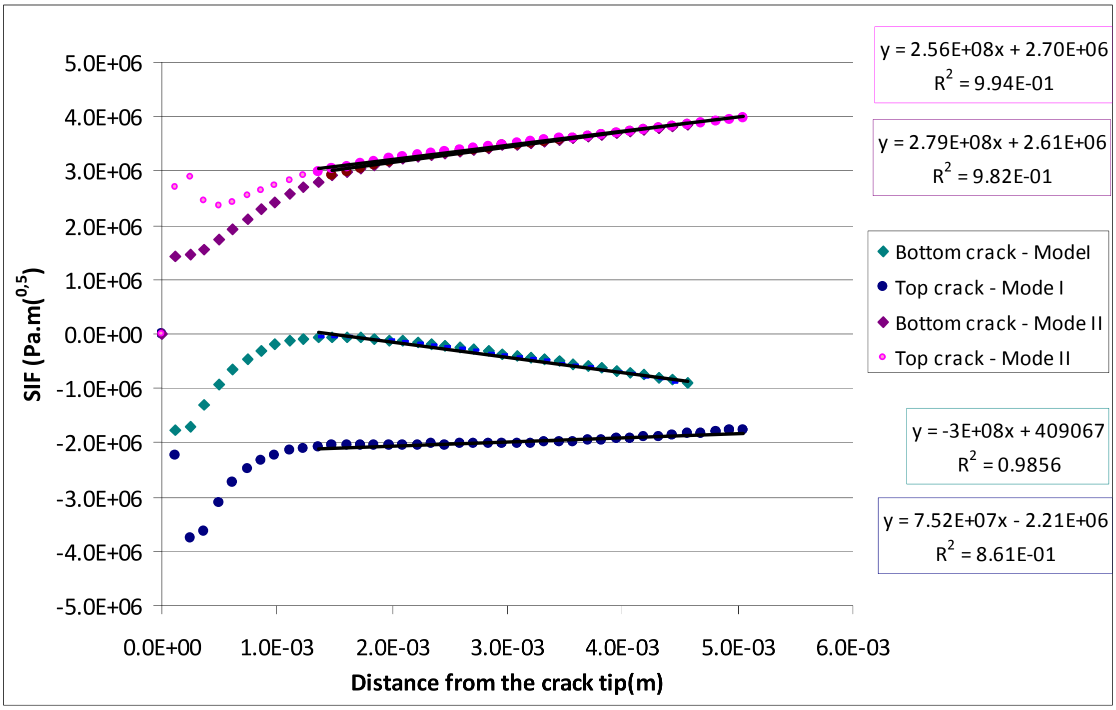

Figure 2. 71- Fracture toughness evaluation by the stress state around the top and bottom of the crack tip – sample PTST02 – Confining pressure 05 MPa

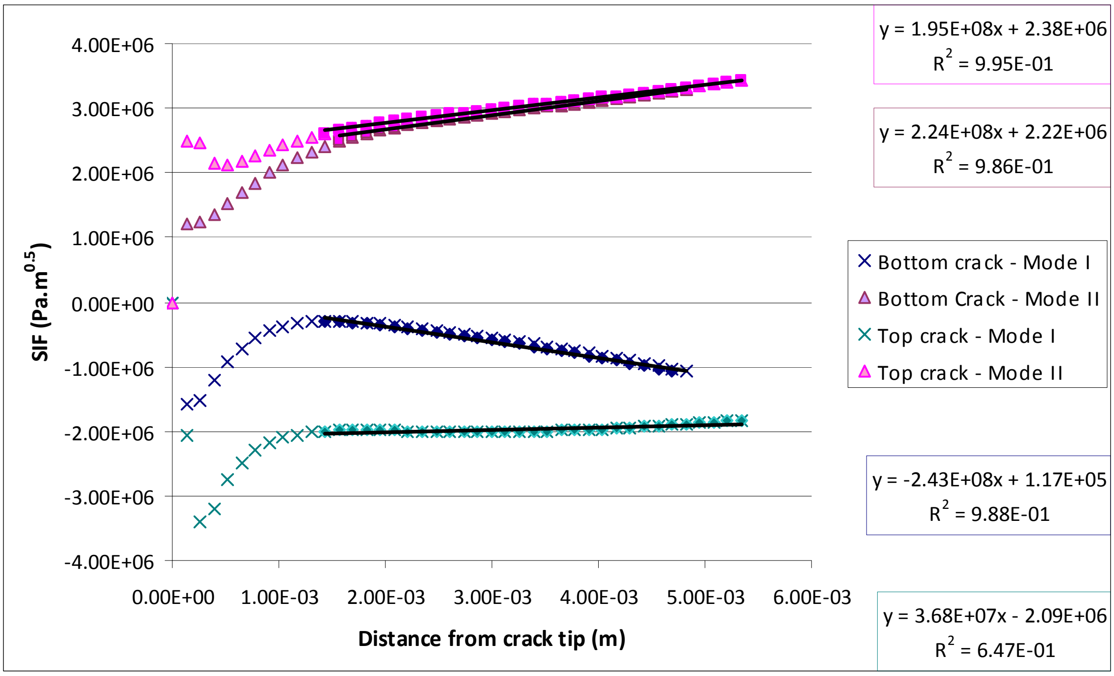

Figure 2. 72 - Fracture toughness evaluation by the stress around the top and bottom of the crack tip - sample PTST09 - Confining pressure 10 MPa

Table 2. 21 - Fracture toughness on mode II by the analysis of the stress state around the tip of the top crack

	Intact		
Confinement	**5 MPa**	**10 MPa**	**15 MPa**
Nombre	3	3	3
Moyenne (MPa.m$^{0.5}$)	2.01	2.65	3.10
CV	10%	9%	25%
Min – Max (MPa.m$^{0.5}$)	1.81-1.99	2.38-2.87	2.58-3.99

Table 2. 22- Fracture toughness on mode II by the analysis of the stress state around the tip of the bottom crack

	Intact					
Confinement pressure	**5 MPa**		**10 MPa**		**15 MPa**	
Mode	K_I	K_{II}	K_I	K_{II}	K_I	K_{II}
Number	3		3		3	
Mean value (MPa.m$^{0.5}$)	0.45	1.61	0.28	2.42	0.13	2.96
CV	52%	18%	55%	8%	27%	19%
Min – Max (MPa.m$^{0.5}$)	0.20-0.66	1.34-1.93	0.11-0.41	2.22-2.61	0.00-0.40	2.57-3.60

Evaluating the sample PTST02 as the crack propagates from the bottom to top, we can find that the mode I exists at this point (Figure 2. 71) and even if it is less important than mode II, the mixed mode here presented at the point A may be more likely to happen than the pure mode II at the point B. Table 2. 21 shows the results of these analysis for all samples. We can see that, similarly as for the Figure 2. 67, the fracture toughness increases with the increase of the confinement pressure.

Table 2. 23 - Confining pressure influence on the K_{II}/K_I ratio

Confining pressure	Atm	5 MPa	10 MPa	15 MPa
K_I (MPa.m$^{0.5}$)	0.51	0.45	0.28	0.13
K_{II} (MPa.m$^{0.5}$)	0.64	1.61	2.42	2.96
K_{II}/K_I	**1.3**	**3.6**	**8.64**	**22.77**
K_I/K_{II}	**0.8**	**0.28**	**0.11**	**0.04**

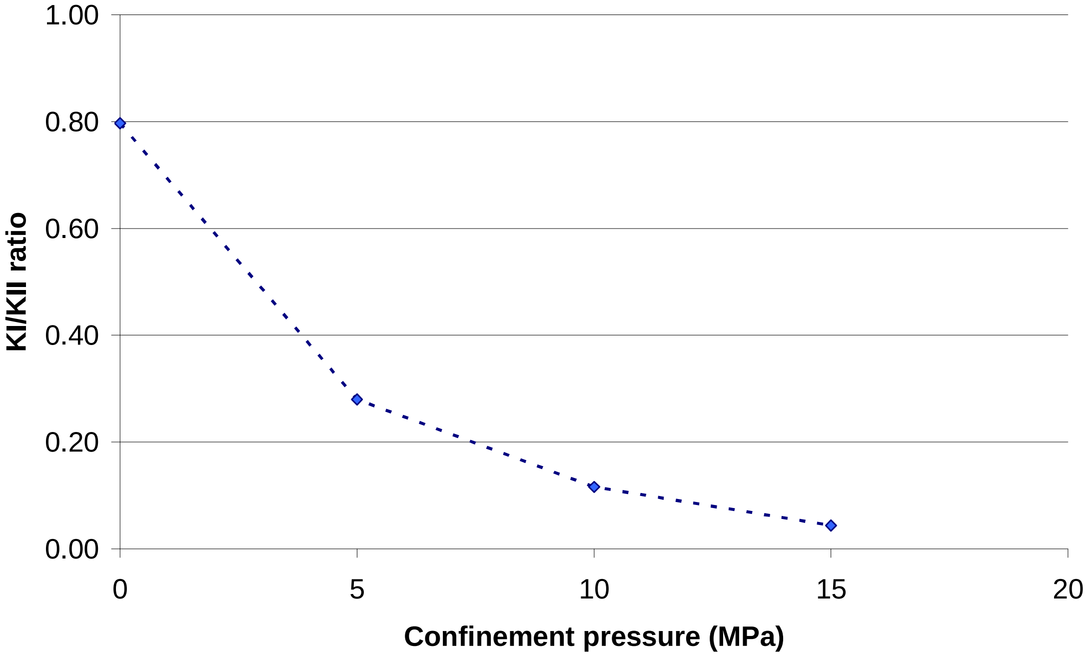

Figure 2. 73- Ration of K_I /K_{II} at the rupture for different confinement pressures

Nevertheless, other tests were performed with a higher confinement pressure and the relation between K_{II}/K_I decreases as the confinement pressure increases (Table 2. 23). It can be seen in Figure 2. 73 that the relation between K_I/K_{II} tends to zero after 15 MPa of confinement pressure. However even if the ratio K_I/K_{II} is close to zero, the mode I is still present, even at high confinement pressure.

2.8 Conclusion of Part II

This chapter was used to give to the reader an overview of the main mechanical tests used to evaluate a rock property called fracture toughness.

We evaluate for the chosen rock, the *Pierre de Lens* limestone, the fracture toughness in modes I and II. But, besides the mechanical tests, other analyzes, as numerical simulations and the use of digital correlation techniques were used to determine this parameter.

We could establish that some mechanical tests are easier to perform than others and have more reliable/repeatable results. The SCB and the CCBD test are both very repeatable, however the SCB test is simpler to realize.

The use of other techniques to verify the results (numerical simulation and DIC) were essential to a better understanding of the mode II of crack propagation and the differences of conditions that will allow each one to happen.

Part III – CO_2 Effect on Fracture Toughness

Contents

While in the previous chapter we focused just in the mechanical aspect of the CO_2 injection on reservoir rocks, we neglected the changes that could occur in the rock due the presence of a fluid that in water could provoke chemical reaction in certain minerals present in rocks.

In this part of the study we will then analyze the effect that a chemical dissolution on the limestone rock used in this work could have on the fracture toughness of the rock.

For this analysis the fracture toughness tests performed in the previous chapter will be analyzed now for degraded samples.

Techniques of degradation described in the literature will be exposed and the chosen technique used in this work.

The ways to characterize the rock as a porous material will also be related in this section, as the differences between the porous distribution between a intact and a degraded sample.

Another important aspect of this chapter will be the effect of the presence of a fluid during a mechanical test to determine the fracture toughness of the rock.

3.1 State of the art

In this section we will describe some of the observable effects of CO_2 in limestone rocks as some of the methods to degrade the samples.

The effect that other acid solutions have on a porous material will also be comment.

3.1.1 Chemical effects on rock properties

The CO_2 effect on rocks properties has been studied by several authors (e.g. (Le Guen et al., 2007), (I. et. al Gaus, 2008) and etc). The influence of CO_2-saturated water on several reservoir rocks has been described briefly in chapter I. However, a more complete view of the CO_2 chemical effects on limestone is needed to this work and will be exposed in section 3.1.1.1. Others chemical effects provoked by other acid solutions will be exposed in section 3.1.2.

3.1.1.1 CO_2 effects on limestone

The CO_2 injection in a reservoir rock has different impacts depending on the reservoir zone (André et al., 2007).

Within an aquifer, in the zone near the injection point, the rock mass tends to dry the rock by three mechanisms. One is the fluid (internal water) displacement, the second is the water vaporization due to the injection of CO_2 and the third one is provoked by the saturation of the supercritical CO_2 by the internal water, however this third component is negligible compared with the other two.

The influence of wet CO_2 can be reproduced in an autoclave in reservoir conditions where the supercritical CO_2 is present without another fluid. In this zone, no CO_2 influence can be observed on the microstructure or on the mechanical properties (Rimmele et al., 2009).

However, in a zone far from the wellbore, the CO_2 is present in a CO_2-saturated water form. In this study we are interested in this second zone.

Nevertheless, to study each one of these zones, two principal approaches exist.

The first one is the batch degradation process. This is a static process where there is no fluid flow through the sample, some studies that use this procedure are for example (Rimmele et al., 2009), (Renard et al., 2011), (Montes-Hernandez et al., 2006) and (Morse & Arvidson, 2002).

However, several authors intended to study the hydraulic conditions in a reservoir used experiments with the percolation of fluids as for example the CO_2-saturated water (Luquot & Gouze, 2009), (Zuo et al., 2011), (Osselin, 2013) and (Smith et al., 2013).

When we chose to submit a rock to the same conditions that would be found in a zone far from the wellbore in reservoir underground, and we try to reproduce these conditions in an autoclave, the rock has to be in the presence of the water.

The injected CO_2 will dissolve in water creating a low pH environment. The acidic water will attack the rock promoting changes within the microstructure and porosity, especially at the border (Figure 3. 1). However, experiments performed in a oolitic limestone at 28 MPa and 90 °C by (Rimmele et al., 2009) did not show a change on mechanical properties of the rock after a month in a batch cell.

Both situations described above characterize a situation where the degradation environment is static, which means, no fluid percolation.

To simulate a condition where the acidic fluid passes through the sample (Luquot & Gouze, 2009) designed percolation cells as shown in Figure 3. 2 - Percolation test - (Luquot & Gouze, 2009)

The samples used by (Luquot & Gouze, 2009) have 9 x 18 mm (diameter and length respectively).

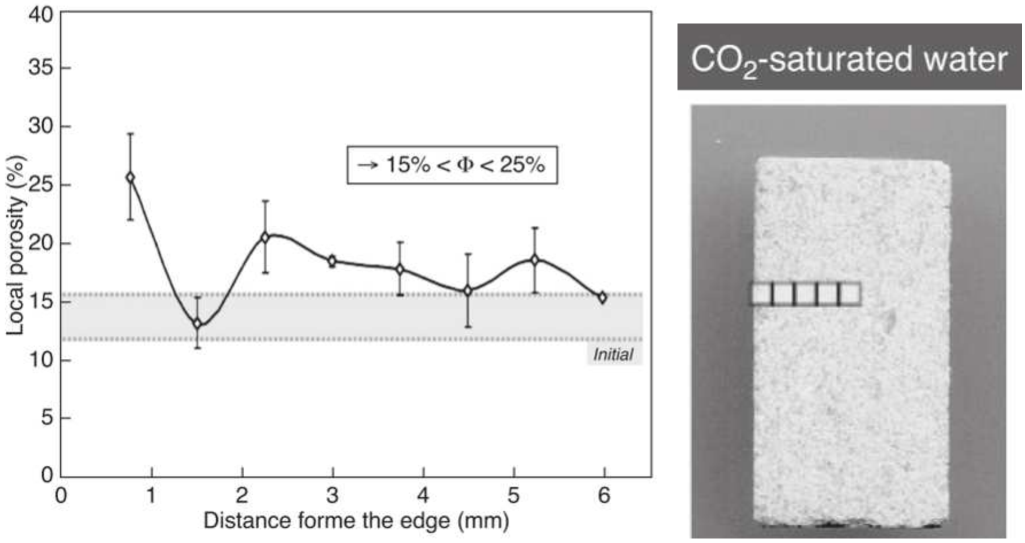

Figure 3. 1 - Porosity variation of a sample on CO2-saturated water conditions (Rimmele, 2009)

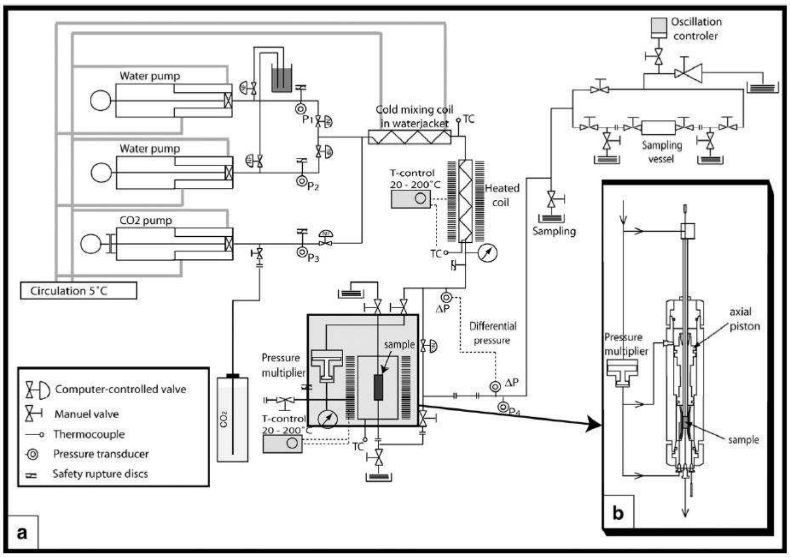

Figure 3. 2 - Percolation test - (Luquot & Gouze, 2009)

The D1 experiment performed by (Luquot & Gouze, 2009) simulated the conditions at vicinity of the injection well condition, with a high flow rate of Q=$1.9\times10^{-8} m^3 s^{-1}$, a pressure of 120 bars and a temperature of 70 °C. The influence of the CO_2 + water percolation was analyzed in a percolation test that can be seen in Figure 3. 2 - Percolation test - (Luquot & Gouze, 2009)

The set-up consists of several pumps that will inject a mixture between water and supercritical CO_2. This solution will pass through a heating system. A pressure multiplier allows the injection of the fluid in the desired pressure conditions. The solution will flow at the sample at a precise flow rate. The fluids are collected to measure the mineral concentrations.

The samples after and before the percolation process, can be seen in Figure 3. 3a and the change in porosity in Figure 3. 4b. We can see that the porosity variation is important for samples conditions in a zone close to the injection point.

To analyze the importance of the microstructure in the degradation process, (Smith et al., 2013) have studied the change on mineralogy of heterogenic limestone and dolomite cores provoked by the CO_2-saturated brine water in reservoir conditions (60 °C and 24 MPa).

They have shown that rocks with high heterogeneous microstructure form paths of dissolution called wormholes, while homogenous rocks can have a steady-state carbonate mass transfer. We also know that the presence of wormholes are associated with a biphasic solution of CO2 and water, as exposed in section 1.1.1.1.

In Figure 3. 4 the effect of CO_2 percolation on heterogeneous samples can be seen and the presence of wormholes are clear. The fluid flow in this sample was of 0.05 ml/min.

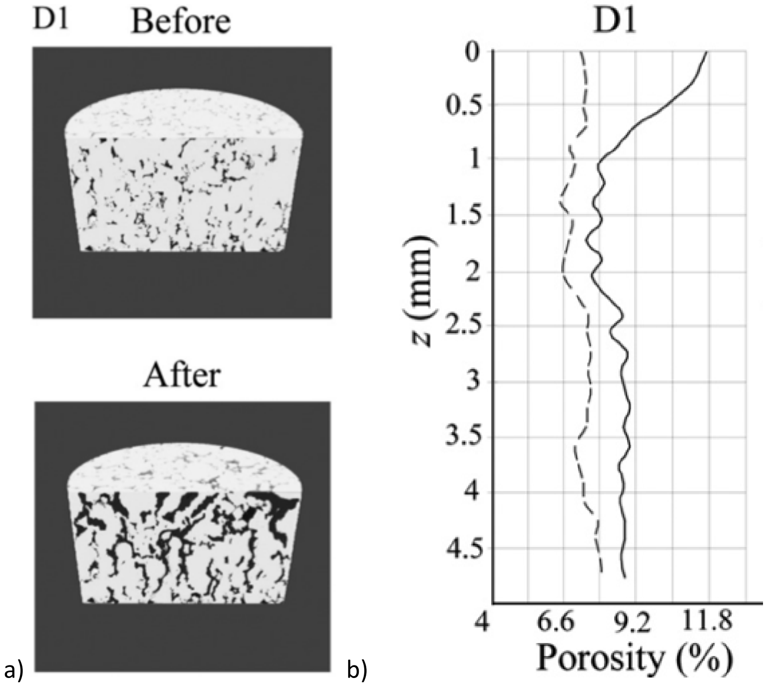

Figure 3. 3 - a) Limestone degradation analysis (Contour oolites – weaker permeability zone) b) Porosity change through the sample (before – dotted; plain – after)) (Luquot & Gouze, 2009)

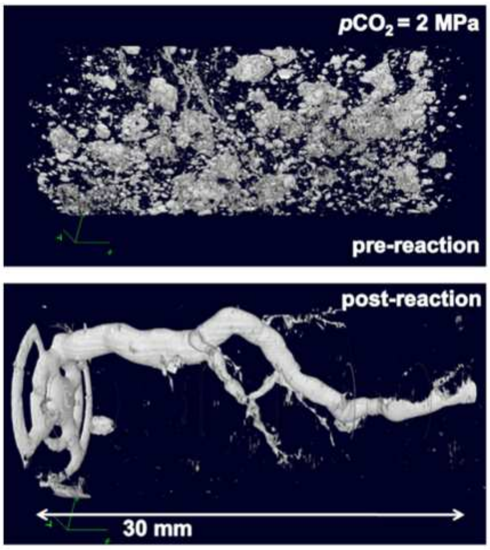

Figure 3. 4 – XCMT (X-ray computed microtomography) images and profiles of calcite, dolomite for Vuggy samples reacted with pCO2. Pore space has been filtered to show only newly produced porosity as gray in XCMT images (reactive flow from left to right) (Smith et al., 2013)

3.1.2 Chemical effects of acid solutions

After CO_2 injection, different zones are created (André, et al., 2007), (Bemer & Lombard, 2009), and each zone is characterized by a particular chemical reaction. Close to the injection point, the zone is almost saturated with supercritical CO_2, and the phenomenon observed is the drying of the rock. In an intermediary zone there is a presence of a biphasic mixture of supercritical CO_2 and brine water causing dissolution in wormholes patterns. However, in a zone far from the injection point, the CO_2 is completely dissolved in the pore water and the dissolution is expected to be homogenous (Figure 3. 5) from André et al. 2007), this third zone is the one chosen to our work.

When we are studying about chemical reactions caused by acidic water in this zone, one of the principal difficulties of the chemical influence of water saturated CO_2 on rocks is to reproduce homogeneous degradation in the laboratory, especially for large samples (more than 15 mm of diameter/thickness).

When we have larger samples the degradation is more likely to be heterogeneous, varying from the exterior and the interior part of the sample. To avoid this heterogeneous degradation, (Egermann et al., 2006) used a retarded acid that starts the dissolution of the material just when activated at a temperature of (60-70°C). This allows the complete saturation of the sample before the degradation initiation, and by consequence this technique allows to reproduce a homogeneous pattern of dissolution.

(Bemer & Lombard, 2009) used samples of 40 mm of diameter and 80 mm of length. They could provoke a 2% variation of porosity which results in a decrease of bulk and shear elastic moduli as shown in Figure 3. 6.

(Zinsmeister, 2013) studying the evolution of hydromechanics properties of a Lavoux limestone after degradation by the use of the retard acid found that there is a significant decrease of the mechanical moduli and a transition of the rupture mode from a fragile to a more ductile mode.

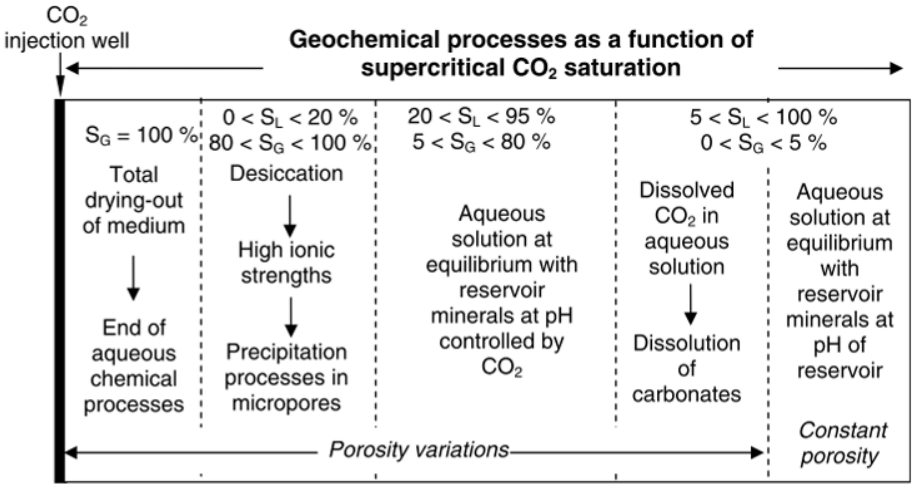

Figure 3. 5 - Vertical cross-section representation of geochemical processes believed to occur during CO2 injection in an aquifer. The chemical processes are highly dependent on the CO2 content in the water. The overall evolution of reservoir porosity is affected by two opposite processes: carbonate dissolution by acid aqueous solution and mineral scaling due to desiccation of the medium(André et al., 2007)**.**

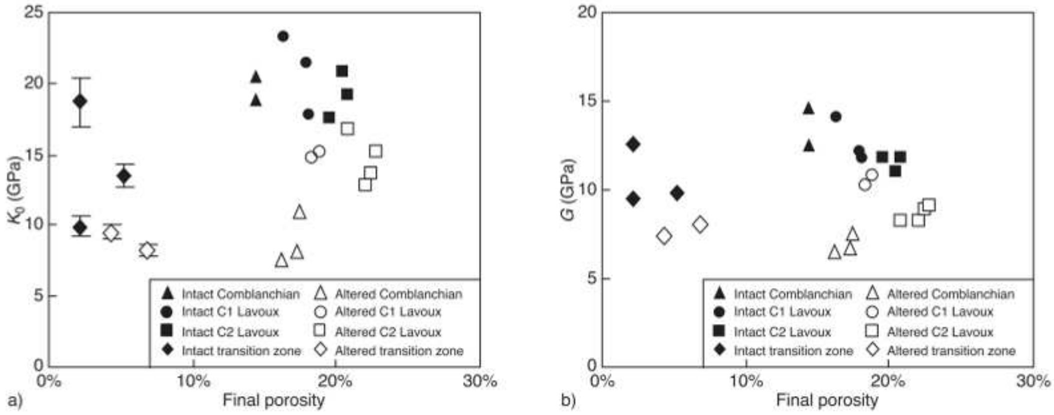

Figure 3. 6 - Drained elastic moduli of intact and altered samples.

In the study of the influence of acid solutions in porous materials in the fracture toughness (Reis, 2010) tested different acid solutions effects on the fracture toughness for a concrete.

Even if we, here study another type of material (a limestone rock), it is important to search in the literature the influence of chemical degradations on the property that we are studying – the fracture toughness.

Knowing that, the work of (Reis, 2010) provides us a start in this matter. Studying fracture toughness in concrete, samples were submerged in different acid solutions diluted at 5% (the type of acids can be found in Table 3. 1) for seven days and then tested the samples by three point bending tests.

The samples used were 30 x 60 x 240 mm. The results on the fracture toughness can be seen in (Table 3. 1).

All acid solutions induced an important decrease on the fracture toughness of the rock. It can be seen that the pH of the solution has an important influence on the fracture toughness of rocks. The CO_2-saturated water at reservoir conditions is known for having a pH of 4 (André et al., 2007), that present an acidity close to the acid lactic.

However, the conditions of saturation of the minerals from the concrete and from a limestone rock in the different solutions are not the same. So it is not possible to compare the fracture toughness effects between the two solutions.

Table 3. 1- Different acid solutions and their pH (Reis, 2010) (corrected)

Solution Type	pH
Sulfuric acid	1.2
Acetic acid	2.5
Lactic acid	3.9

Table 3. 2 – Fracture toughness variation for the different acid solutions (Reis, 2010)

Solution type	**K_{IC} MPa.m$^{0.5}$**
Reference	1.58
Sulfuric acid	0.59
Acetic acid	0.77
Lactic acid	0.94

3.2 Methodology

The mechanical tests performed for the degraded samples follow, in most cases, were already described in section 2.1.3 and 2.2. So, in this section we will treat only about the chosen chemical protocol to degrade the samples and the SCB test under a fluid presence and confinement.

3.2.1 Chemical degradation protocol

It is known that the CO_2 attacks rocks in different ways (3.1.1), and so, the form of the CO_2 (gaseous or dissolved) will change the mechanism of degradation. Here, we focus on dissolved-CO_2 induced chemical degradation.

The processes underlying chemical degradation are mainly influenced by the mineralogy of the rock. Here, a fast dissolution of the calcite minerals is expected, the reaction being controlled by the degree of calcite saturation in the water. So, for a degradation process improvement we should minimized the chances of the calcite saturation on the autoclave water, for the amount of time we would like to let the dissolution occur.

According to a study made by the BRGM (Trémosa, 2014) the water will be saturated within a time period of one week, given our autoclave size (4 liters) with 10 CCBD or BDT samples.

In the study of (Trémosa, 2014), using the geochemistry code PhreeqC v2.18 (Parkhurst & Appelo, 1999) based into the thermodynamic data base from the Thermoddem v2011 (Blanc et al., 2012) it was calculated the water composition in equilibrium with the Pierre the Lens limestone.

The model simulates the dissolution process of the calcite at water in reservoir conditions (60 °C and 15 MPa) in a 1D configuration, but with a proportion of water and rock similar to the existent at the batch experiments. The samples used at the simulation have 20 mm of thickness.

The autoclave used in this work is presented in Figure 3. 7. The samples will be placed in reservoir conditions of 60 °C and 150 bars, in an autoclave with a capacity of four liters. Three liters are occupied by the water and one liter by the samples and the supercritical CO_2 as can be seen in Figure 3. 8.

Unfortunately, we have a limited amount of water and time, but a large number of samples to degrade, and only 10 samples to be degraded per time, which means we are limited by the autoclave's size and its operation mode that don't allow the percolation of fluid (in this case water), but allow the dissolution of CO_2 only on the three liters it was put on it (per time).

In this case, to achieve a stronger dissolution, we must put the samples for more than one week (for CCND and BDT samples). Yet as suggested by the geochemical simulations of BRGM, the water is expected to be saturated after one week: this forces us to renew the water after one week (for each week). The samples will stay in the autoclave for a month, and the water will be renewed four times. Details with the different times per kind of samples can be seen in Table 3. 3.

Figure 3. 7- Autoclave IFSTTAR – rock diameter 50 mm

A similar procedure it was performed for the PTST samples. The degraded samples that will be tested will stay individually in the autoclave for six days. The quantity of samples of PTST and CCBD to be put on the autoclave changes because the PTST the sample is larger than the CCBD sample, demanding more time to obtain the same degradation ratio. However, to simplify the procedure it was chosen to reduce the number of samples to one (a single sample was put on the autoclave) for a period of six days providing the same degradation effect obtained by the other samples.

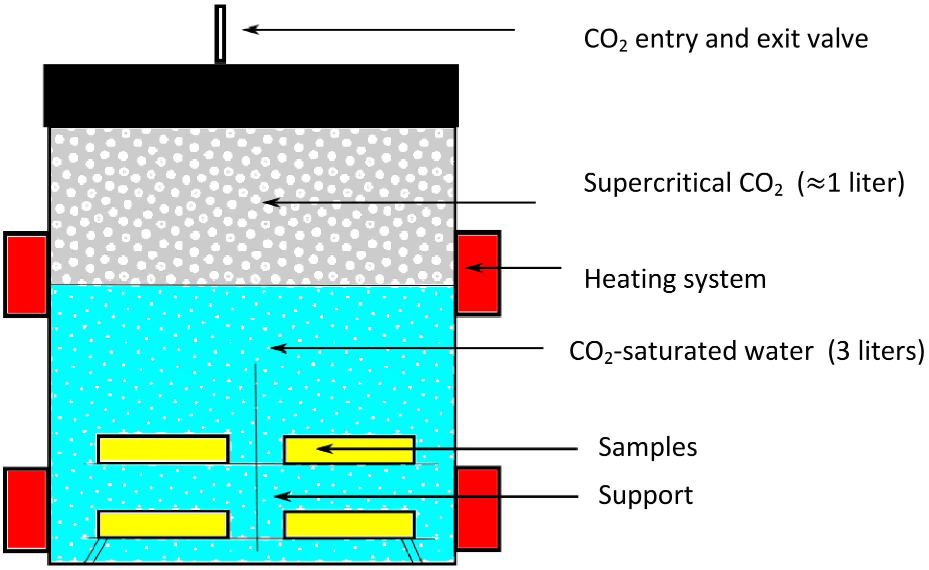

Figure 3. 8– Overview of the interior of the autoclave - sketch

Table 3. 3 - Quantity and time of samples at the autoclave

Type of test	Number of samples in the autoclave	Time in the autoclave (week)	Water change period (week)*
BDT	10	4	1
CCBD/CCNBD/SCB/ASCB	10	4	1
PTST	1	1	1

*period of time that the sample will remain in the autoclave without changing the water

The choice of degradation time, pressure and temperature are based on the necessity of reaching similar reservoir conditions. The study is based on CO_2 injection scenario far from the wellbore. In this condition CO_2 is dissolved in water forming an acid solution that can attack carbonate rocks. Nevertheless, some differences exist between a degradation process in a batch recipient and the degradation process in a reservoir.

There are two mean differences that are:

1- in a batch there is no fluid flow through the rock: Thus of chemical degradation in the batch experiment is reduced as compared to reservoir conditions

2- The ratio of the mass of water over mass of rock is much lower in the reservoir than in batch conditions: Thus a higher dissolution can be achieved as more calcite can be dissolved up to reaching the concentration saturation of the fluid.

It is known that the change of porosity due to CO_2 injection on a limestone reservoir for a period of 10 years is about 0.25-0.5% (André, et al., 2007) and as we can see in the section 3.2.3, the change of porosity with this degradation procedure is 0.4 %, showing that the procedure adopted here is representative of this scenario.

The porosity of the sample was measured by the mercury intrusion porosimetry analysis. The porosity was measure after being dry at a constant temperature of 55 °C for a week. We prefer to dry in a low temperature to avoid the creation of cracks in the interior of the sample cause by temperature variation.

3.2.2 SCB under water

An important part of this work is the evaluation of water/CO_2-saturated water on the fracture toughness parameter.

Three SCB experiments have been performed on samples filled with water and three other experiments with CO_2-saturated water at pressure of 6 bars. For this latter the samples remained in CO_2-saturated water during two days before starting the experiment.

Another four samples under water at atmospheric pressure were tested. The set-up can be seen in Figure 3. 9. The loading and the samples geometry can be seen in Table 3. 4.

Table 3. 4– SCB under water characteristics

Description	Values
Diameter (mm)	50
Thickness(mm)	11.5
Notch (a/R)	0.30
Load speed (mm/min)	0.02

Figure 3. 9- Experimental setup for SCB experiments under confinement in presence of water and CO_2-saturated water

3.2.3 Characterization of the degraded samples

The chemical degradation has an impact on the microstructure and the porosity of the rock samples. The use of the electron microscope (SEM) analysis together with the mercury intrusion porosimetry can help to clarify the impact the CO_2-saturated water on the studied limestone. These techniques are described below.

3.2.3.1 SEM – Scanning electron microscope

The analysis of the Pierre de Lens using the electronic microscope is made by means of the back-scattered electros technique (BSE). This is sensitive to the atomic number and it is more appropriate to identify the microstructure of a material (Ghabezloo et al., 2009). The secondary electrons are a good method to analyze properties such as the roughness of the material surface.

Rock samples used for CCBD, SCB and PTST tests were analysed. The images were taken following the Figure 3. 10, Figure 3. 11 and Figure 3. 12. For the sample PTST, a full panoramic view was made.

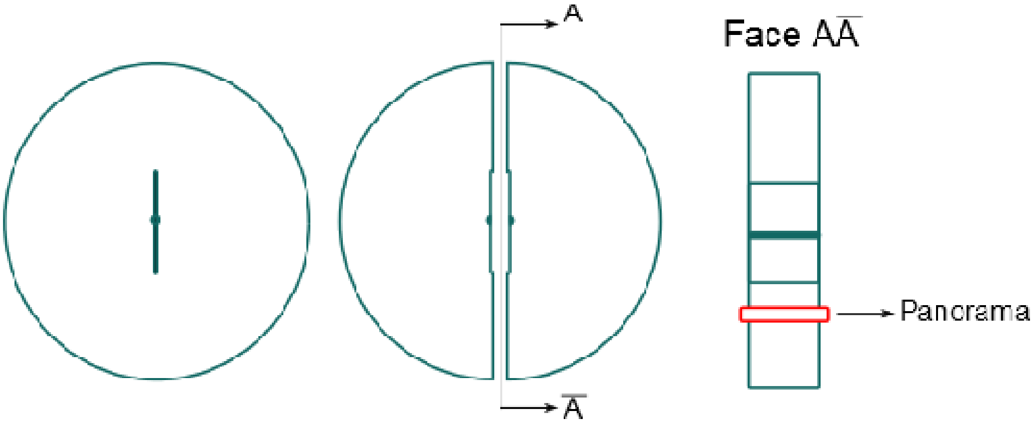

Figure 3. 10- Localization of the panorama for the CCBD sample

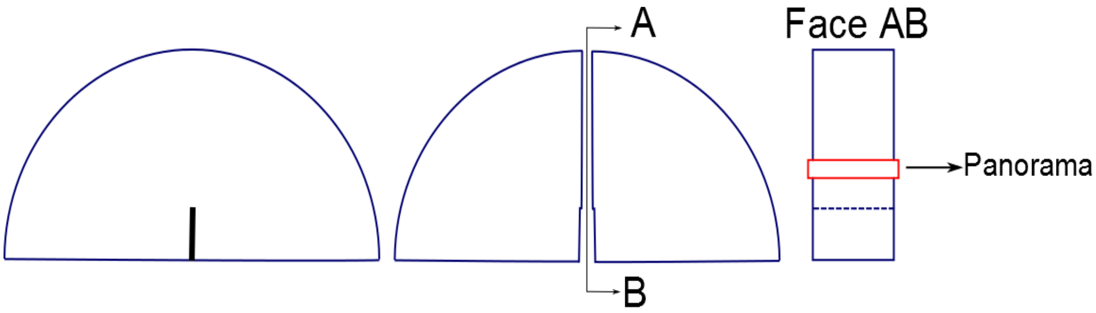

Figure 3. 11- Localization of the panorama for the SCB sample

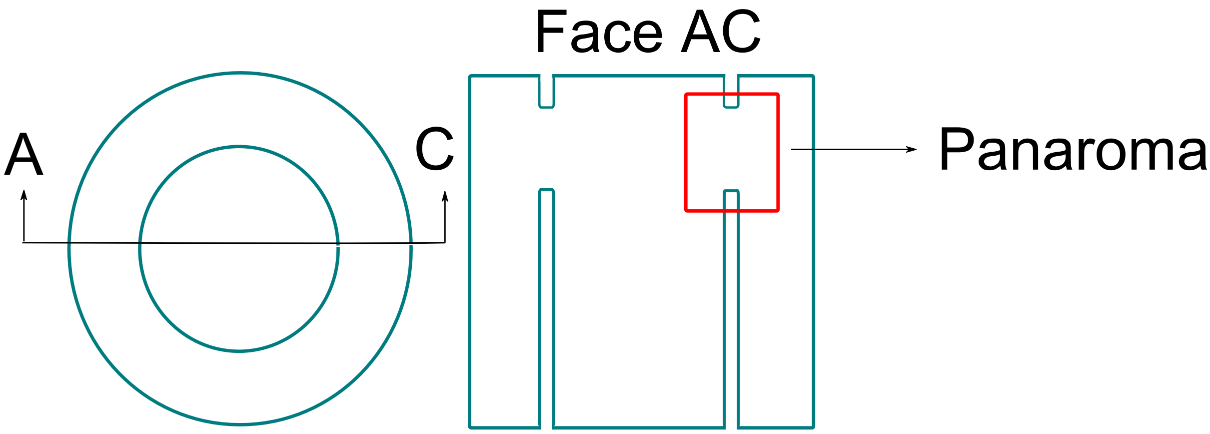

Figure 3. 12- Localization of the partial panorama of the sample PTST

3.2.3.2 Mercury intrusion porosimetry

The mercury porosimetry is a technique to analyze the microstructure of the porous materials. With this method it is possible to determinate the apparent density, the size distribution and pore volume.

The pore size determination is possible because the necessary pressure to penetrate is inversely proportional to the pore-size (Jurin's law, Jurin, 1728).

$$D = \frac{4T\cos\theta}{P} \tag{3.74}$$

where D is the pore diameter size, P the injection mercury pressure and T the superficial tension, that for the mercury is equal to 485 dyne/cm, and θ the contact angle that depends of the material and can vary from 112° to 146°: for the calcite is equal to 146° (Robert, 2004); Figure 3. 13. .

The process consists in making two injections, one at low pressure (0 – 0.2 MPa) and one at high pressure (0.2 to 27 MPa). The sequence of cumulative volume of mercury that can enter the sample indicates the different pores diameters and total porosity of the sample.

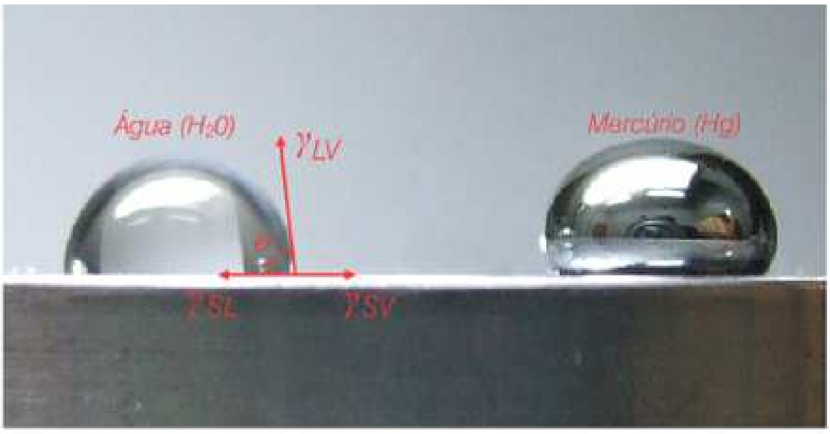

Figure 3. 13- Difference between a water contact angle and the mercury contact angle

3.3 Results

The chemical effects due to the CO_2 degradation in the rock are divided in three. First the effects on the microstructure of the rock, second the effect of the fracture toughness due to the chemical degradation at the batch process and the third the effect of the CO_2 at the crack tip in a confined test under water with CO_2 dissolved.

Each one of these aspects brings important answers to the study case.

In this section we will expose the results of the tests and characterizations of the samples.

3.3.1 CO_2 effects on the microstructure

To evaluate the effect of CO_2 on the rock fracture toughness, a series of limestone samples prepared for the experiments have been immerged in CO_2 saturated water in an autoclave.

Mercury intrusion porosimetry experiments have been performed to evaluate the influence of this chemical degradation on the pore volume of the sample.

The results of the mercury porosity analysis are presented in Figure 3. 14 and show a slight increase of the porosity from 14.5% to 14.9%.

The pore size distribution of the intact samples and degraded samples moved from a quasi-bimodal distribution to a quasi-unimodal one with a reduction of the mean pore entry radius from 1.6 µm to 1.0 µm.

For the intact sample the quasi-bimodal mode presents two characteristics pore sizes, one of 0.6 µm and another of 1.6 µm. For the degraded samples we can see or a bimodal distribution or a unimodal with characteristics pore sizes of 0.5 and 1.3 µm or 1 µm.

Figure 3. 15 shows panoramic SEM observations along the width of intact and degraded samples. On the image of the intact sample the oolites with semi-circular geometry with the porous zone around them can be clearly observed. These oolites are less clearly observable on the degraded samples with less contrast between the oolites and the zone around them.

These observations are compatible with the mercury intrusion porosimetry results in Figure 3. 14 showing the reduction of the intensity of the peak corresponding to bigger pores in the microstructure.

The images of the degraded samples show also the relative homogeneity of the microstructure. In order to improve the homogeneity of degraded samples, relatively thin samples (around 11 mm here) are used in this study, as it was already discussed.

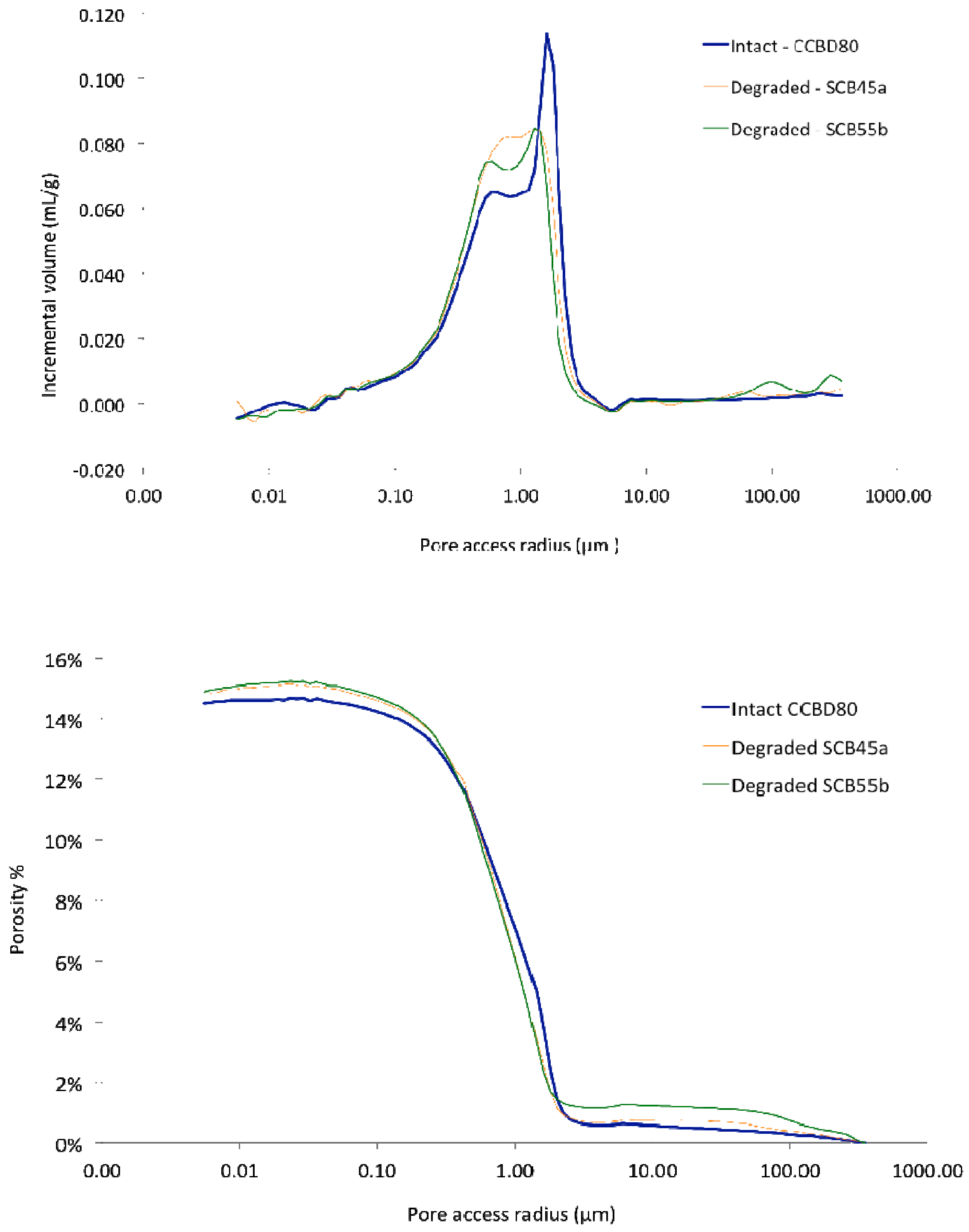

Figure 3. 14- Mercury intrusion porosimetry results: (top) incremental curve (bottom) cumulative curve

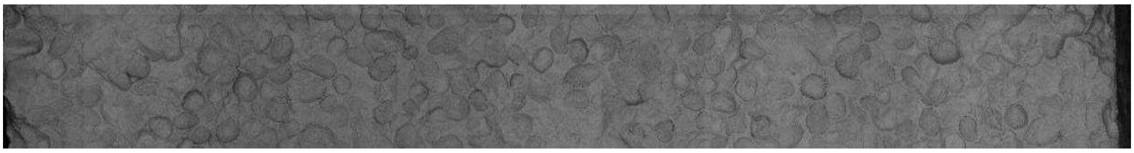

Intact sample, SCB, K_{IC}=0.71

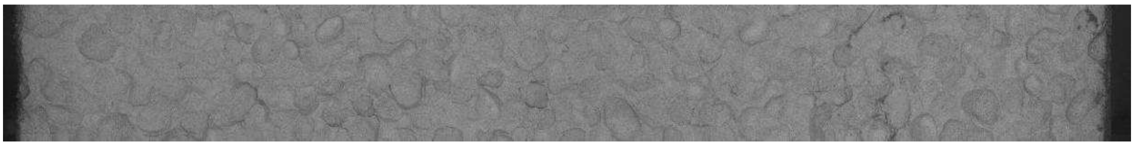

Degraded sample, SCB, K_{IC}=0.58

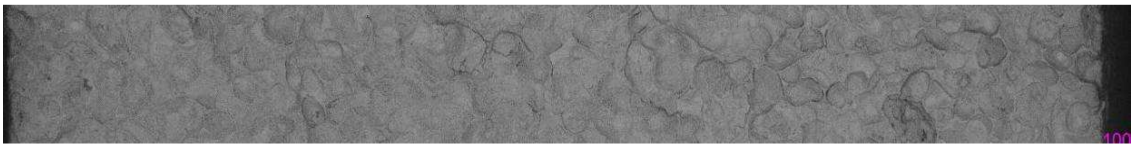

Degraded sample, SCB, K_{IC}=0.58

Figure 3. 15 - Panoramic SEM observation along the width of intact and degraded samples used for semi-circular bend experiments

3.3.2 Effect of CO_2 degradation at the fracture toughness of the rock

In order to understand how the chemical degradation can affect the fracture toughness of the rock for both modes, mode I and mode II, mechanical tests were performed and the results are here exposed.

3.3.2.1 Mode I Fracture toughness evaluation for degraded samples

The results of mode I fracture toughness evaluation for chemically degraded samples are presented in Table 3. 5, Table 3. 8 and Table 3. 7.

The mean value of mode I fracture toughness of degraded rock equals 0.58 $MPa.m^{0.5}$ using 18 experiments with SCB and CCBD methods. The mean values obtained for intact samples are respectively 0.65 and 0.61 $MPa.m^{0.5}$ for SCB and CCBD experiments, showing a very slight decrease of the rock fracture toughness due to chemical degradation.

Other studies as (Sterpenich et al., 2009) and (Rimmele et al., 2009) showed no significant variation for mechanical properties (uniaxial strength and Young's modulus) on limestone samples that stayed a month on reservoir conditions.

In Figure 3. 16, Figure 3. 17 and Figure 3. 18, it can be seen curves of the tests on degraded samples exposing the influence of CO_2-saturated water in reservoir condition at the Pierre de Lens limestone don't affect the homogeneity of the results.

The low decrease in the fracture toughness (summarized in Table 3. 8 and Table 3. 9) can be supposed to be due the low increase of porosity of the rock, and not only due its natural variability. The number of tests for each intact and degraded samples, as the low variability of the parameter (coefficient of variation around 10%) eliminates the possibility of error on the measurements.

Table 3. 5 - Characteristics of CCBD degraded samples – Mode I

Test Name	Diameter (mm)	Thickness (mm)	Notch a (mm)	a/R	Load rate (mm/min)	First peak (kN)	K_{IC} $MPa.m^{0.5}$
CCBD50	49.82	10.70	14.30	0.29	0.06	1.92	0.55
CCBD54	49.79	11.69	15.09	0.30	0.06	2.00	0.54
CCBD60	49.76	11.83	13.08	0.26	0.06	2.43	0.60
CCBD93	49.87	12.73	12.48	0.25	0.06	2.94	0.66

Table 3. 6 - Characteristics of CCNBD degraded samples – Mode I

Test Name	Diameter (mm)	Thickness (mm)	a_1 (mm)	a_0 (mm)	Load rate (mm/min)	Maximun load (kN)	K_{IC} MPa.m0.5
CCNBD 39	49.40	11.67	30.26	22.50	0.08	1.59	0.65
CCNBD 40	49.44	11.53	30.22	22.00	0.08	1.50	0.60
CCNBD 41	49.39	11.44	30.20	23.00	0.80	1.40	0.57

Table 3. 7- Characteristics of SCB degraded samples

Test name	Diameter (mm)	Thickness (mm)	Notch a (mm)	a/R	Y_I	Load rate (mm/min)	Maximum load (kN)	K_{IC} $MPa.m^{0.5}$
SCB14	49.33	11.05	7.31	0.30	4.6	0.06	0.52	0.66
SCB15	49.33	11.08	7.39	0.30	4.6	0.06	0.48	0.61
SCB45	46.66	11.27	8.41	0.34	5.3	0.08	0.38	0.58
SCB46	49.66	11.26	7.28	0.29	4.2	0.06	0.55	0.62
SCB56	49.52	11.08	8.04	0.32	4.9	0.06	0.41	0.58
SCB72	49.64	11.25	7.8	0.31	4.8	0.06	0.48	0.64
SCB73	49.7	11.68	7.38	0.30	4.6	0.06	0.57	0.69
SCB66	49.57	11.34	7.77	0.31	4.8	0.08	0.36	0.48
SCB71	49.57	11.5	8.48	0.34	5.3	0.08	0.40	0.61
SCB108	49.73	11.22	7.76	0.31	4.8	0.06	0.46	0.62
SCB110	49.72	11.18	7.06	0.28	4.1	0.06	0.48	0.52
SBD55	49.5	11.22	8.14	0.33	5.1	0.06	0.40	0.59
SCB70	49.5	11.35	7.47	0.30	4.6	0.08	0.37	0.46
SCB67	49.47	11.37	8.49	0.34	5.3	0.08	0.32	0.49

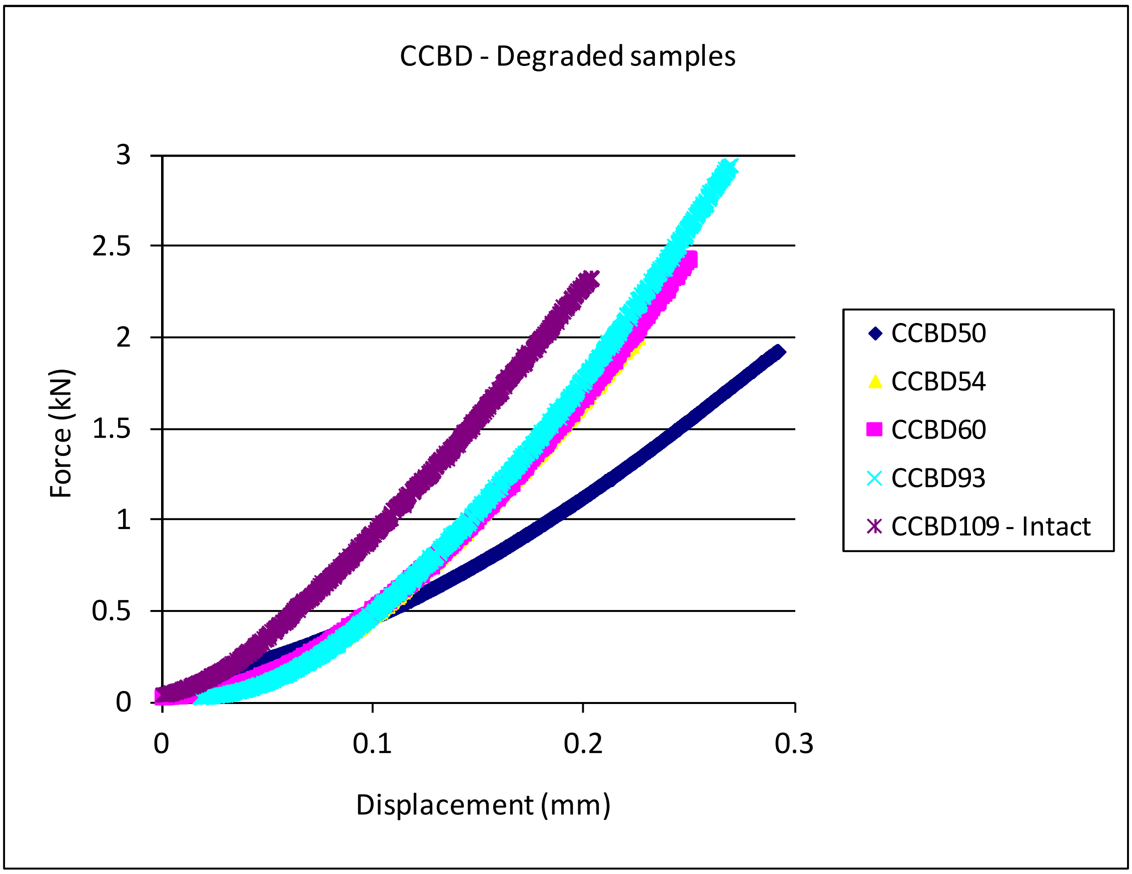

Figure 3. 16 - CCBD on degraded samples : Force - displacement response

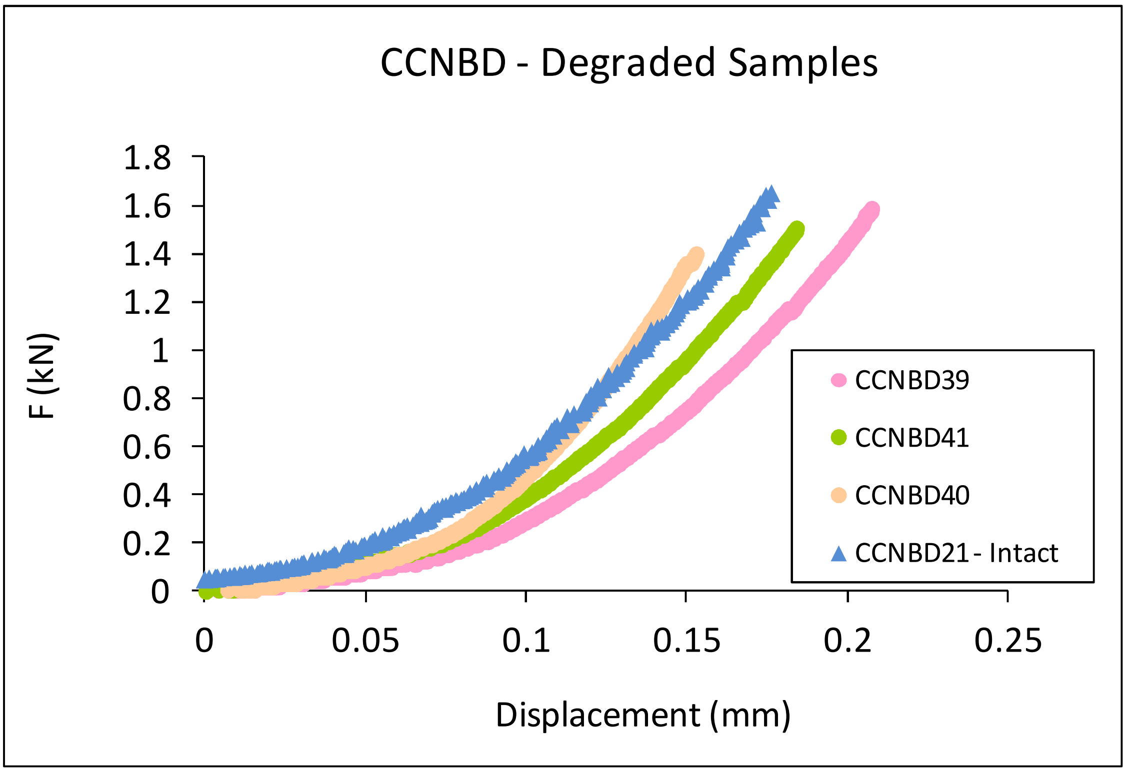

Figure 3. 17 - CCNBD on degraded samples : Force - displacement response

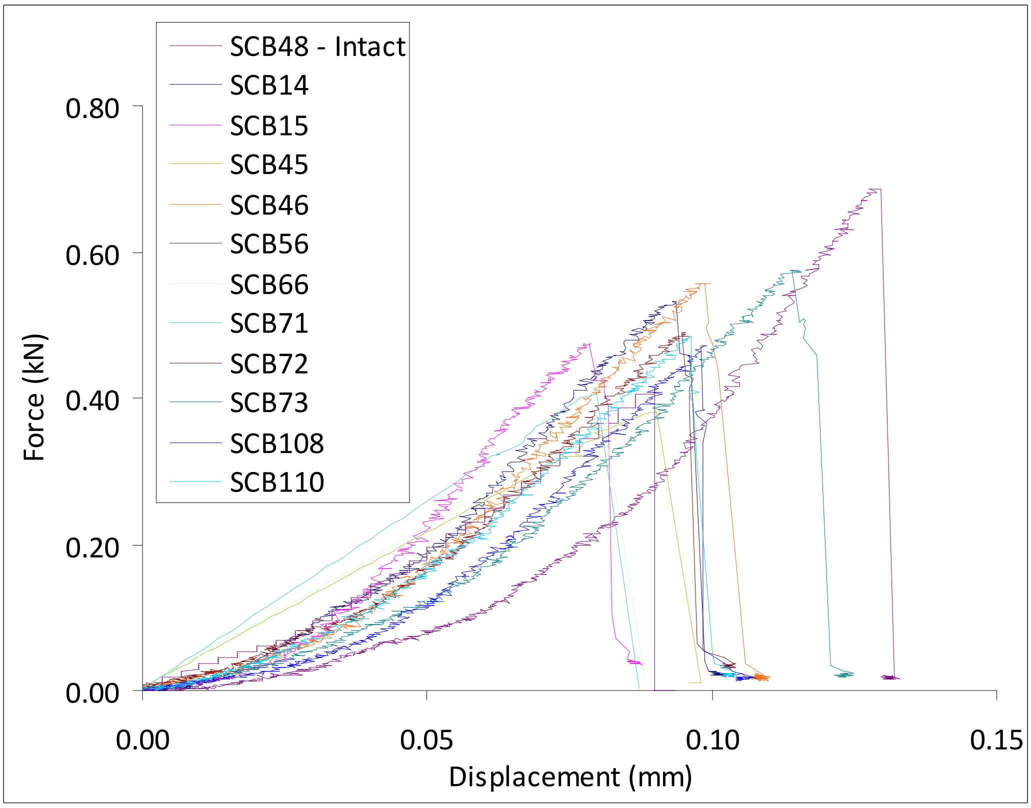

Figure 3. 18 - SCB degraded curves - displacement x force

Table 3. 8 - Results of mode I fracture toughness experiments on intact samples

	Model I-Degraded samples			
Experiment	**SCB**	**CCBD**	**CCNBD**	**TOTAL**
Number	14	4	3	**21**
Mean K_{IC} (MPa.m$^{0.5}$)	0.58	0.58	0.61	**0.58**
Variation coeff.	12%	9%	11%	**11%**
Min-Max	0.46-0.69	0.54-0.66	0.53-0.65	**0.46-0.69**

Table 3. 9 - Total results for intact and degraded samples

	Mode I	
Experiment	**Intact**	**Degraded**
Number	38	21
Mean K_{IC} (MPa.m$^{0.5}$)	0.63	0.6
Variation coeff.	12%	16%
Min-Max	0.47-0.86	0.46-0.92

3.3.2.2 Mode II - Fracture toughness evaluation for degraded samples

As in the analysis of the mode II in unconfined samples showed us the difficult on finding a pure mode II for this kind of test, here we will analyze only the samples of the PTST for the pure mode II.

The same observations that were made for the mode I can be made for PTST tests (Table 3. 12, Table 3. 11 and Table 3. 12) can be made for the results here presented. Low variation on the fracture toughness was found between the intact and degraded samples.

Comparing the Figure 3. 19 (PTST – degraded samples) with the Figure 2. 67 (PTST – Intact samples) we can see that the general behaviour of the curves didn't change when we put side by side the degraded and intact samples.

This is compatible with the very slight variations of the sample porosity after chemical degradation as presented in the previous section.

Table 3. 10- Characteristics of PTST degraded test

Test name	Diameter (mm)	Internal Diameter (mm)	Thickness (mm)	Notch Thickness (mm)	Up notch (mm)	Bottom Notch (mm)	Load rate (mm/min)	First peak (kN)	Confining Pressure (MPa)	Axial Pressure (MPa)	K_{IC} (MPa.m$^{0.5}$)	K_{IIC} (MPa.m$^{0.5}$)
PTST02	39.34	18.8	35.1	1.55	4.08	21.04	0.02	16.50	5	59.44	0.90	1.79
PTST04	39.92	19.2	41.24	1.55	4.12	24.74	0.02	13.58	5	46.90	0.32	1.53
PTST05	39.57	19.37	38.71	1.55	3.87	23.23	0.025	17.18	10	58.30	0.07	1.95
PTST11	39.94	18.6	38.58	1.55	3.00	23.00	0.025	15.27	5	56.20	0.62	1.65
PTST13	39.74	19.8	38.88	1.55	3.50	23.00	0.025	20.72	10	67.29	0.31	2.34
PTST14	39.69	19.49	38.43	1.55	3.50	23.00	0.025	19.43	10	65.13	0.38	2.10
PTST17	39.95	19.49	38.54	1.55	3.50	24.00	0.025	22.69	15	76.05	0.00	2.67
PTST18	39.92	19.58	39.21	1.55	4.00	24.00	0.025	28.40	15	94.32	0.33	3.21
PTST19	39.75	19.48	38.67	1.55	4.00	23.00	0.025	20.60	15	69.12	0.00	2.44

Table 3. 11 - Comparative values of PTST results for intact and degraded samples (top crack calculation)

	Intact			**Degraded**		
Confinement	**5 MPa**	**10 MPa**	**15 MPa**	**5 MPa**	**10 MPa**	**15 MPa**
Number of tests	3	3	3	3	3	3
Mean value of K_{II} (MPa.m$^{0.5}$)	2.01	2.65	3.10	2.1	2.57	3.06
CV	10%	9%	25%	12%	14%	14%
Min - Max	1.81-1.99	2.38-2.87	2.58-3.99	1.91-2.37	2.22-2.54	2.79-3.57

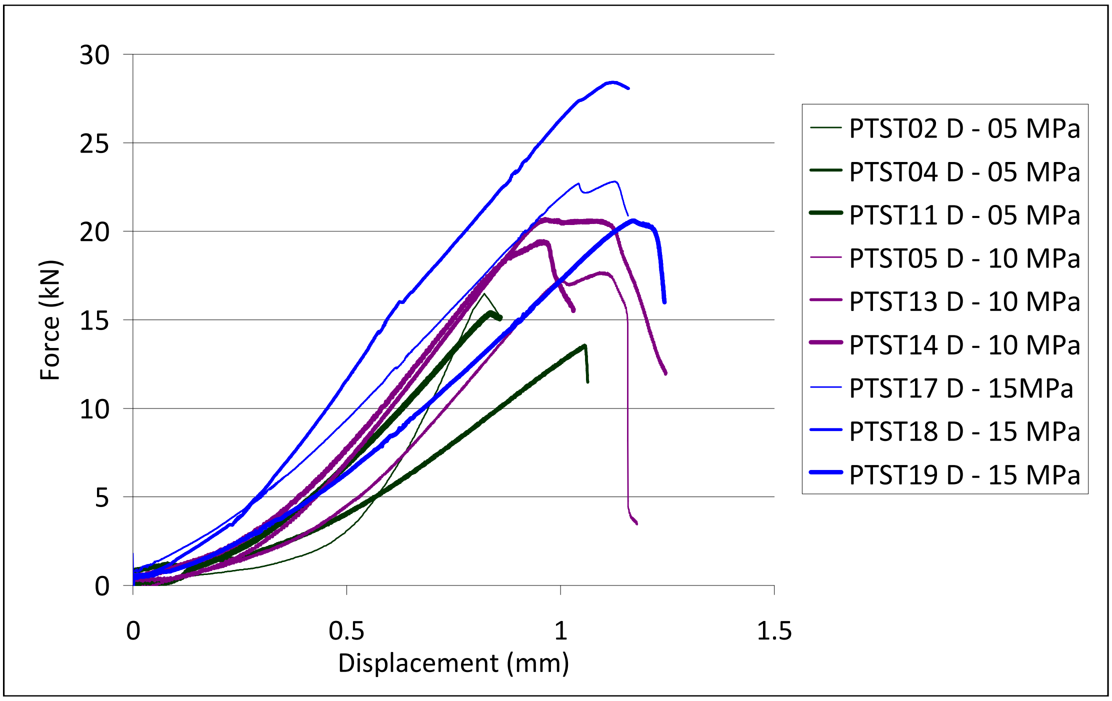

Figure 3. 19 - PTST degraded samples curves

Table 3. 12 - Comparative values of PTST results for intact and degraded samples (bottom crack calculation)

	Intact						**Degraded**					
Confinement pressure	**5 MPa**		**10 MPa**		**15 MPa**		**5 MPa**		**10 MPa**		**15 MPa**	
Mode	K_I	K_{II}	K_I	K_{II}	K_I	K_{II}	K_I	K_{II}	K_I	K_{II}	K_I	K_{II}
Number of tests	3		3		3		3		3		3	
Mean value ($MPa,m^{0.5}$)	0.45	1.61	0.28	2.42	0.13	2.96	0.61	1.66	0.25	2.10	0.11	2.77
CV	52%	18%	55%	8%	27%	19%	47%	8%	64%	7%	41%	14%
Min - Max	0.2-0.66	1.34-1.93	0.11-0.41	2.22-2.61	0-0.4	2.57-3.6	0.32-0.62	1.53-1.79	0.07-0.31	1.95-2.34	0-0.33	2.44-3.21

3.3.3 Effect of fluid saturation (water and CO_2-saturated water) on rock fracture toughness under confining pressure

Previously presented experiments have been all performed on dry samples. However in a reservoir the rock pore space is filled with a fluid and is under a confining pressure.

In order to see the influence of these conditions on the evaluated rock fracture toughness, some SCB experiments have been performed inside a cell under confining pressure on samples with presence of water or CO_2-saturated water. The experimental setup has been designed and a new base has been fabricated to perform this experiment inside a triaxial cell. The experiments were performed under a relatively low confining pressure of 600 kPa.

Three SCB experiments have been performed on samples saturated with water and three other experiments with CO_2-saturated water. For this latter the samples remained in CO_2-saturated water during two days before starting the experiment. The experimental results are presented in Table 3. 13 and show a reduction of mode I fracture toughness from 0.65 MPa.m$^{0.5}$ for dry samples to 0.47 MPa.m$^{0.5}$ for water saturated samples. This reduction can be mostly attributed to a physical effect of the presence of water, which can affect the strength of the rock.

The mode I fracture toughness measured on samples in presence of CO_2-saturated water results in a value, equal to 0.50 MPa.m$^{0.5}$, which is very close to the value measured on water saturated samples. This result shows that the chemical degradation during three days before starting the experiment, and the presence of CO_2 in water have not a significant influence on the rock fracture toughness. This is compatible with the overall weak influence of the degradation by CO_2, even after a period of one month, on the fracture toughness, as presented before. A synthesis of the evaluated mode I fracture toughness using SCB experiments under different conditions are presented in Table 3. 14.

The results show there is no significant impact of the CO_2 presence on a confined test. The presence of water can play an important role, as an important decrease of the fracture toughness is observed on the sample in the presence of water. The decrease of the fracture toughness in the presence of a fluid is due to the stress corrosion as explained in section 2.1.1.8.

Table 3. 13- Results of mode I fracture toughness evaluation under confining pressure in presence of water and CO_2-saturated water

	Model I - SCB under confining pressure	
	Water	CO_2 saturated water
Mean K_{IC} (MPa.m$^{0.5}$)	0.47	0.50
Number	3	3
Variation coeff,	18%	11%
Min-Max	0.42-0.57	0.44-0.55
Loading rate (mm/min)	0.02	
Confining pressure (KPa)	600	

Table 3. 14- Comparison of the evaluated mode I fracture toughness using SCB experiments under different conditions

Conditions	Intact sample, dry	Degraded sample, dry	Intact sample, in water, no confinement	Intact sample, in water, under confinement	Intact sample, in CO_2-saturated water, under confinement
Mean K_{IC} (MPa.m$^{0.5}$)	0.65	0.58	0.37	0.47	0.50
Number	14	14	3	3	3
Coeff, of Variation	10%	12%	17%	18%	11%
Min-Max	0.51-0.77	0.46-0.69	0.30-0.42	0.42-0.57	0.44-0.55

3.4 Conclusions of Part III

The fracture toughness for the mode I had varied from 0.63 to 0.6 $MPa.m^{0.5}$ for the intact and degraded samples respectively, while for a 15 MPa the fracture toughness in mode II has changed from 2.96 to 2.77 $MPa.m^{0.5}$. A variation that is compatible with change in porosity.

(André et al., 2007) showed that for a period of 10 years the expected porosity change is ranging between 0.25 and 0.5% for reservoir conditions of 75 °C and 20 MPa. From the mercury porosity analysis we can see a porosity that varies from 14.9 % to 14.5 % a change of 0.4%.

Based on this, we can assume that the values of the chemical degradation process here studied may be of the same order of magnitude than the one expected considering a period of 10 years of injection (CO2 injection rate of 1 kg/s) into a reservoir scale composed of Pierre de Lens limestone (using the site conditions as described in André et al., (2007), see details of the reactive transport modelling carried out in BRGM report (Trémosa, 2014).

Part IV – Statistical analyses of the experimental results

Contents

In geotechnical studies we can have two different approaches when dealing with a problem. We can considerer the material homogeneous or heterogeneous. As the rock materials are heterogeneous when we chose to treat them as homogeneous we are normally making a mean of the values or taking the most probable value to the study.

Nevertheless, we can resolve the situation by another point of view, which is based in the distribution that this value (elastic modulus, Poison coefficient, fracture toughness etc) has. When we deal with distribution, we deal with the frequency of each possible value and its associated probability.

In the study of crack propagation a probabilistic approach is an interesting method to evaluate the phenomenon. In this section we will expose the model proposed by (Guy, 2010) to determine the parameters that would compose the Weibull distribution to the chosen rock. The chosen model (Weibull) is commonly used to describe the probabilistic failure of quasi-brittle materials.

4.1 Modelling damage in rocks

Damage in rocks strongly depends of the nature of the rock and as discussed above rocks are by nature heterogeneous materials.

A probabilistic approach of fracture based on Weibull model is a useful tool for studying the random nature of the failure of rocks. A preliminary study shown in the appendix section exposes the difference between the fracturing and the network of cracks that are formed in an underground rock layer submitted to a specific load when some parameters of the probabilistic model are varied.

The Weibull parameters are the Weibull modulus m and the scale parameter σ_0^m/λ_0. The parameter m represents the heterogeneity of the material, meaning, m =1 corresponds to a high level of heterogeneity while $m=\infty$ corresponds to a homogeneous case, and the approach is deterministic.

For the scale parameter σ_0^m/λ_0, σ_0 (Wong, Wong, Chau, & Tang, 2006) is a parameter inversely proportional to the minimum crack length (Wong, Wong, Chau, & Tang, 2006), meaning that lower the crack length is, higher will be the σ_0 parameter. While λ_0 is the density of defects.

4.2 Weibull parameters for crack propagation in intact and degraded rocks

Using the results of the Brazilian tests we can evaluate the corresponding Weibull distribution as shown in Figure 4. 1.

By successive interpolations, using the method described in the appendix (as described by Guy (2010): chapter 3), and changing the values of σ_0 and m until the minimization of the error between the experimental values and the trend curve, we could find the values of m and σ_0 as given in Table 4. 1.

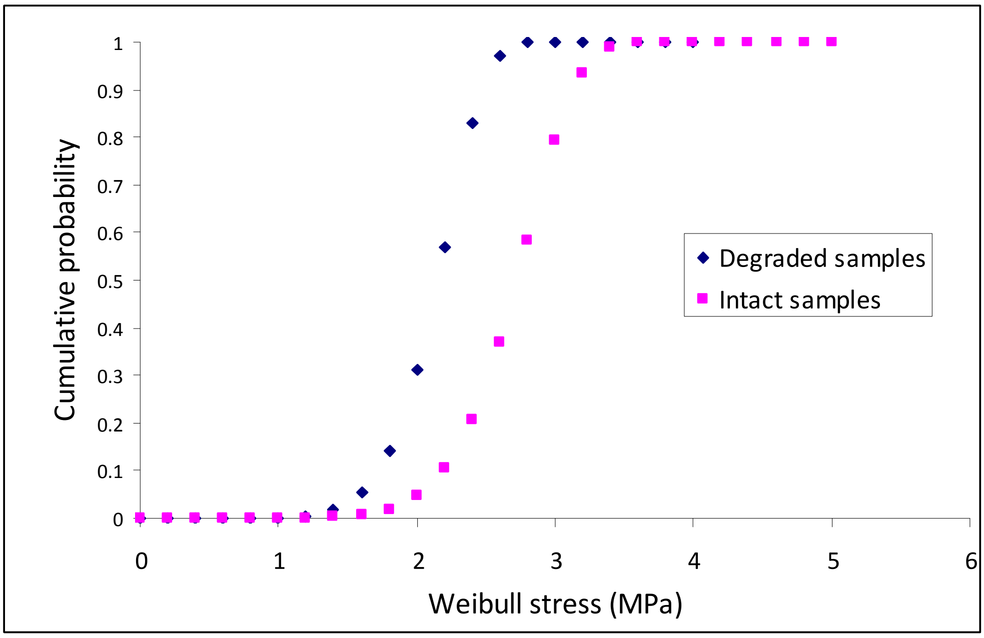

Figure 4. 1 - Weibull distributions for the degraded and the intact samples.

We can obtain the Weibull parameters by the intersection of the curve of Figure 4. 4 and the slope of the curve.

As we can see the axis of the curve represent each side of the follow equation:

$$\ln(-\ln(1-P_{Fi}) = m[\ln(\sigma_{wi}) - ln(\sigma_0)] \quad \textbf{(4. 1)}$$

Where P_F is the probability of rupture and σ_w the Weibull stress obtained from the follow expression:

$$\sigma_w = \sigma_f(HZ\lambda_0)^{1/m} \quad \textbf{(4. 2)}$$

Where H is the heterogeneity factor H, of the stress field, for the Brazilian test, Z the sample volume, and σ_f the principal stress at the rupture (that for the Brazilian test is in the centre of the sample.

The heterogeneity factor H is determined using the empirical relationship, which has been derived by Guy (2010) using Brazilian tests:

$$H = \frac{\alpha}{(1+m)^{\beta}} \tag{4. 3}$$

where α and β are respectively 0.41 and 0.67.

With the data of the Brazilian samples (Figure 4. 2 and Figure 4. 3), and the geometry of the samples we were able to build the data for the expression 4.1 and in consequence the Figure 4. 4.

The Table 4. 1 shows the values of the Weibull parameters that could be extracted of the Figure 4. 4.

While the m parameter changed from 8.55 to 8.52 from an intact sample to a degraded sample, the σ_0 parameter changed from 2.8 to 2.2 MPa.

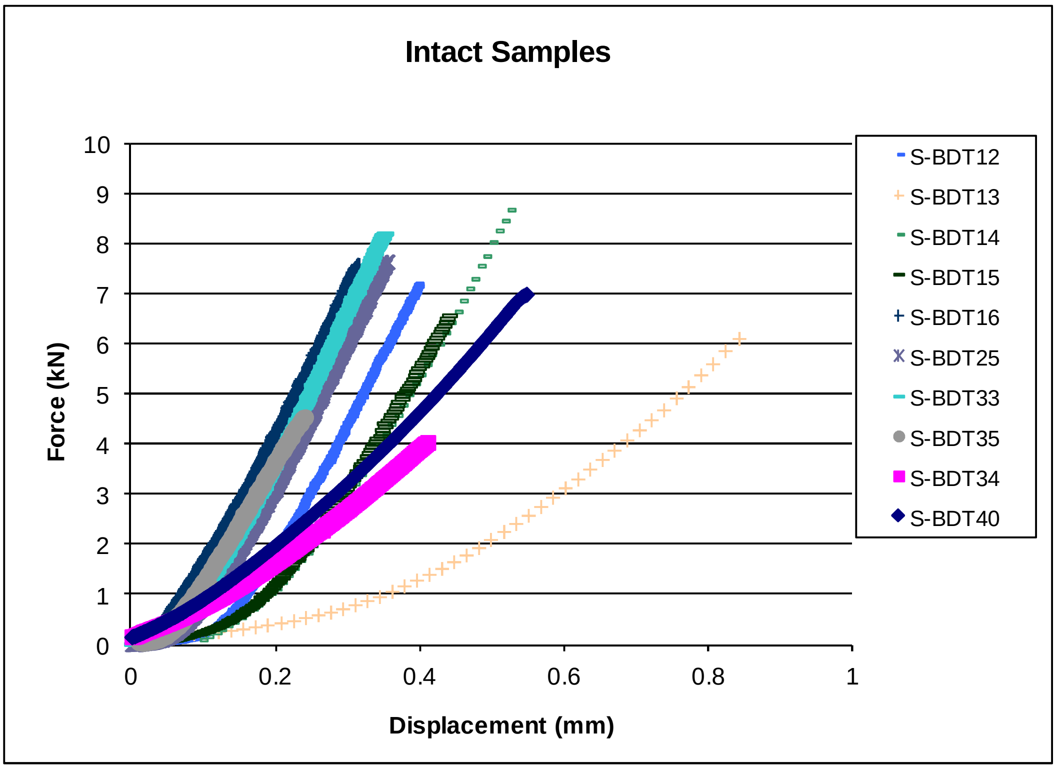

Figure 4. 2 - Curve Displacement x Force for intact samples (BDT tests)

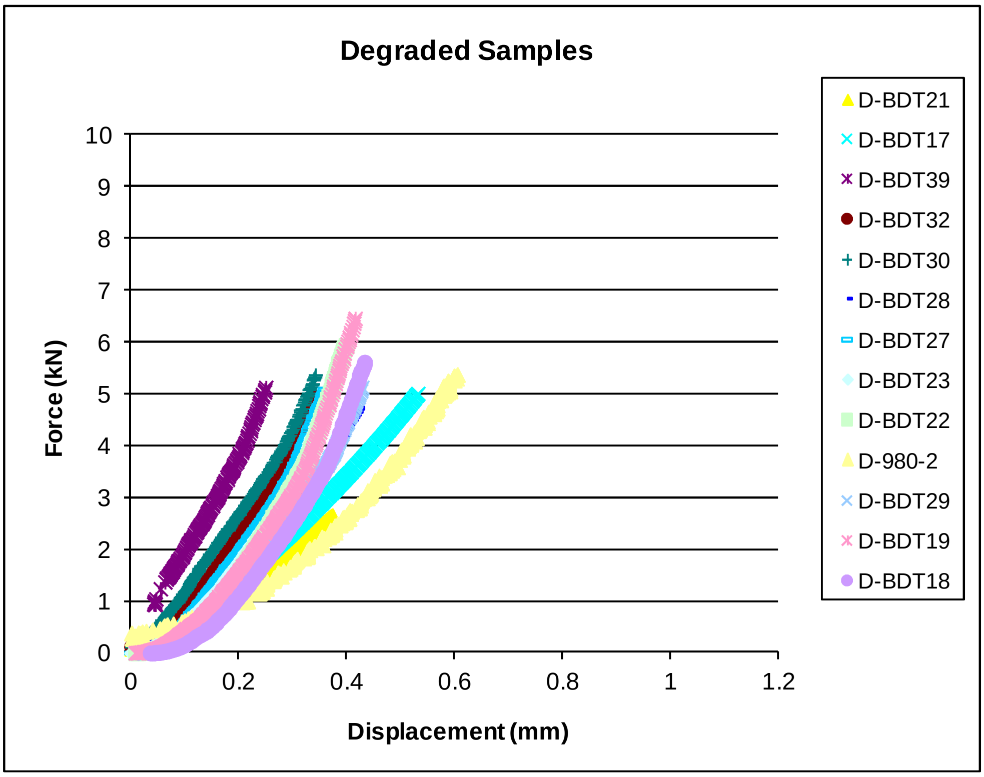

Figure 4. 3 - Curve Displacement versus Force for degraded samples (BDT tests)

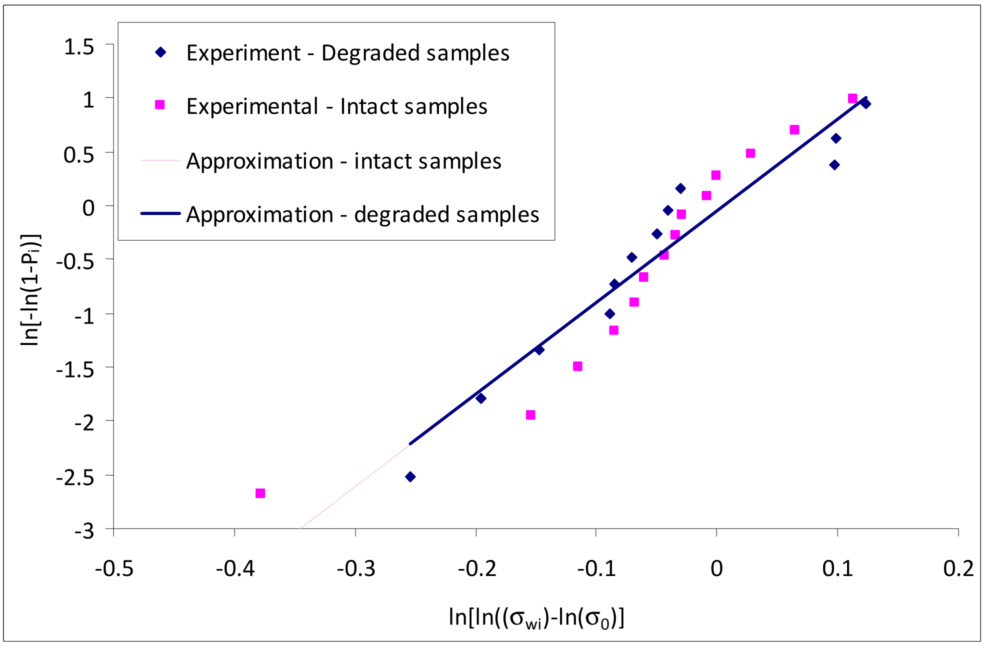

Figure 4. 4- Weibull diagram

Table 4. 1- Values of the Weibull parameters for the intact and dedraded limestone

	Intact	Degraded
m (Weibull moduls)	8.55	8.52
σ_0 (MPa)	2.8	2.2

4.3 Impact of the probabilistic approach

As it could be seen the difference between the intact and degraded parameters is not significant, neither the behaviour of the curves of Figure 4. 4.

This means that for a limestone reservoir that was submitted to a degradation of the same order of magnitude of the samples here studied (0.4 % of porosity change), there would be no significant difference in the development of cracks (probability of crack initiation) between the degraded reservoir and the intact one. It should be recalled here, that the degradation conditions represented here are similar to the reservoir zone far from the injection point, for a period of 10 years.

PART V - GENERAL CONCLUSIONS

Contents

The results described in the previous chapter show different important points to be discussed, as the consistence of the values for the fracture toughness for the mode I and mode II for the intact rock and the influence of the CO_2 on these values.

In sections 5.1 and 5.2 we will recall the main conclusions of the results for the intact rock, and concerning the influence of the CO_2. In section 5.3 we will expose some implications of this study for CO_2 storage.

Finally in section 5.4 we present some research perspectives and make some recommendations.

5.1 Conclusions on the fracture toughness results of the intact rock

First, the mode I fracture toughness of the intact material (Pierre de Lens limestone) could be determined by different types of mechanical tests with a good agreement between all the experimental results.

The mode II fracture toughness of the intact value could not be determined by the standard CCBD or the ASCB test (without confinement). Even if the theory indicates that the pure mode II exists for a given inclination angle of the initial crack for the CCBD test, the Digital Image Correlation technique showed (Figure 2. 55) that the rupture took place in a mixed mode configuration. This phenomenon exists because the pure mode II cannot actually occur in an unconfined environment. Under this condition, the notch will propagate provoking an opening of the crack.

Trying to simulate the conditions of a pure mode II, PTST tests were performed. In this test, a confining pressure is applied to the sample to prevent an important opening of the crack during rupture. Tests were performed under different confining pressures of 5, 10 and 15 MPa.

Figure 2. 62, Figure 2. 65, Figure 2. 71 and Figure 2. 72 show that, as opposed to (T Backers, 2002), the crack does not propagate from the top crack where we can see a pure mode II developing, but from the bottom crack where a mixed mode exists. The values were obtained by numerical simulation and show that the pure mode II did not happen but the K_I/K_{II} ratio at rupture decreases up to a constant value of 0.1 for confining pressures higher than 10MPa (Figure 2. 73).

We can see that a condition close to the pure mode II can be obtained at a confining pressure larger than 10 MPa. Interestingly, this corresponds to confinement pressure of the order of the ones of CO_2 storage reservoirs. This result was obtained by a numerical analysis. This analysis is a great tool to explore the existence of a mixed mode of crack propagation for experimental test.

However, contrary to the CCBD test, we were not able to use digital image correlation to verify from the real displacement field the actual fracture mode of the sample in the PTST test. Other techniques such as acoustic emission could be used in the future.

5.2 Conclusions on the influence of on the fracture toughness

5.2.1 Results that could be used to a deterministic approach

After the establishment of different protocols for the determination of the fracture toughness of all tests, with particular attention given to the correct shaping of all samples, we can say that the variation of the experimental values obtained for the fracture toughness between the intact and degraded samples, can be indeed attributed to the effect of CO_2.

All mechanical tests showed that the CO_2 has very little impact on the fracture toughness of the rock. The impact observed on the fracture toughness is comparable to a storage condition of 20 MPa and 75 °C for a period of storage of 10 years, in a zone far from the injection point (CO2 injection rate of 1 kg/s), where the flow rate is low and the CO_2 is dissolved in water.

The porosity analysis (Figure 3. 14) shows that the internal porosity distribution changes with the CO_2-induced degradation. The difference between the intact and degraded distribution is more visible than the changing of the total porosity values.

The SEM images (Figure 3. 15) corroborate this affirmation: the oolite's contour of the intact sample is more evident than the one of a degraded sample, we can clearly see the oolites on the intact samples while the distinction between the oolites and the cement is not so visible on the degraded samples.

This zone of porosity is represented by the first peak showed by the mercury porosity analysis. Recall that the porosity of an intact sample is concentrated around the oolites.

When the degradation process occurs, the characteristic pores initially of 1.6 µm tends to reduce to 1 µm, provoking a homogenization of the pore size distribution.

However, these changes have a very small impact on the fracture toughness values for modes I and II, as showed in Table 3. 9 to Table 3. 12: for the mode I, the mean value reaches 0.63 $MPa.m^{0.5}$ for the intact rock and 0.58 $MPa.m^{0.5}$ for the degraded rock, while for the mode II, a value of 2.96 $MPa.m^{0.5}$ for the intact rock and 2.77 $MPa.m^{0.5}$ for the degraded rock were found.

It can be concluded that there is no significant impact of the CO_2 chemical degradation on the fracture toughness of a limestone submitted to the process here presented, even if a change on microstructure was observed when the samples are submitted to a batch degradation process.

Another important point is outlined in Table 3. 14. We can notice the influence of stress corrosion on the fracture toughness is more pronounced than CO_2 influence itself. So for the design of a CO_2 storage site, the impact of this phenomenon should be taken in account: there is a reduction of 17% in the fracture toughness from an intact rock at dry conditions and saturated at 600 KPa. The design of an injection site, should take into account the fracture toughness of a saturated sample, because it is the most disadvantage case.

5.2.2 Results that could be used to a probabilistic approach of rock fracture

It is known that a series of values can have the same mean value, even having a complete different distribution. For this reason the stress of crack initiation is evaluated in a probabilistic view, complementary to the deterministic evaluation of the fracture toughness.

In a probabilistic approach, it would be necessary to evaluate the distribution parameter to evaluate the impact of CO_2 in the crack propagation process. Here, the distribution is studied as following a Weibull distribution and the parameters to be determined were *m* (Weibull modulus) and σ_0 (the scale parameter).

In Table 4. 1 we can see there is no significant variation in these parameters, showing the CO_2 has no significant impact on the Weibull distribution of the crack initiation process.

5.3 Implications on the CO_2 storage

The experimental and the numerical analysis carried out, have raised important conclusions related the CO_2 impact on the rock reservoir.

First, it is important to notice that the porosity variation found here (0.4%) can be assimilated to a 10 year period in a zone far from the injection zone. It means that this zone will have a small change in the rock microstructure. The change will not cause an increase in the probability of fracture initiation in the reservoir rock under those conditions (i.e. without percolation).

To the design of a CO_2 storage site, the characterization of the fracture toughness on pure mode II is essential, since the crack propagation in a high confining pressure is more likely to happen in a pure mode II. The more I is an opening mode of crack propagation and is not easy to reproduce when a confining pressure exists provoking the closing of the cracks. To evaluate the mode II in a confinement pressure situation we used here the PTST test.

The PTST analysis shows that there is an important relation between the thicknesses of the notch on samples submitted to a "pure mode II" test in confining conditions and the existence or not of a mixed mode. However, this importance decreases by increasing the confining pressure.

For some PTST's tests performed here, considering a confining pressure of 15 MPa, a pure mode II is achieved. We can conclude the PTST is an important test to evaluate the conditions needed to the design of a storage site that is more likely to have cracks propagating in a pure mode II, nevertheless, this analysis must have be taken cautiously: mode I was not detected even if it was existent as shown by the DIC analysis.

It is important to conclude that in the beginning of this study one of the objectives was to include a chemical code coupled to the mechanical code at the ENDO-HETEROGENE model (as described in Appendix).

In this view, a relation between the variation in porosity and the fracture toughness of the rock was expected to be established. The results presented here show that this implementation is not necessary for a limestone rock which was submitted to a change in porosity of the order of 0.4 %.

An important recall is that a change of this order of magnitude is representative of a zone far from the injection point after a injection period of 10 years.

5.4 Perspectives and recommendations

This thesis gave better insight in the behaviour of a limestone reservoir rock in presence of CO_2-saturated water, showing that the CO_2 has no significant impact on fracture toughness properties under batch conditions (without percolation).

However, similar studies should be performed with samples coming from the caprock. The caprock sample has a lower permeability than the reservoir rock. Therefore, the degradation process, that depends of the permeability and porosity of the rock, will be more difficult to achieve in the laboratory. However, the mineral composition of the caprock material is a major factor for the study of the impact of CO_2-saturated water. Dissolution of minerals could create heterogeneous paths of degradation, and the increase of potential defects, this could happens for examples some caprocks with high percentage of calcite, like Opalinus clay or Weyburn anhydrite (around 15%).

We also outline some recommendations concerning the laboratory test.

The use of SCB tests to the determination of mode I fracture toughness is recommended. The shaping of the sample being much simpler than the CCBD tests, one can manufacture larger amount of samples in a short time. We also recommend the use of diamond saw to the cut of the semi-circular samples and the notch as it gives a better precision and a thinner notch. SCB tests can also be performed in a cell for saturated samples.

Concerning the study of mode II of crack propagation, we have shown the difficulties for inducing a pure mode II crack propagation in the tested samples. However, the Punch-Through Shear test (PTST) seems to be a good solution as the sample can be put under confinement. However, to verify that the mode II is actually happening, the present device could be improved with the use of acoustic emissions that can track the initiation of the crack, and the propagation mode (Stanchits et al, 2003).

It is important to say that one of the difficulties of reproducing the mode II in a lab configuration is related to the thickness of the notch and its influence on the development of a mixed propagation mode.

APPENDIX

Preliminary results of the impact of Weibull parameters on the reservoir integrity

Contents

A.1 Evaluation of crack propagation in a study case

A.1.1 Identification of the Weibull parameters.

In this section, we will explain the method used for the evaluation of the Weibull parameters. This section is essential for the numerical analyses and its contribution for the elements described in section A.1.3, which deals with the numerical model to describe fracture initiation and propagation.

A Weibull distribution is used to represent the heterogeneous nature of rock brittle failure. This means that initiation of crack threshold, the parameter for the crack initiation criteria, is not constant in each location, but it varies. This variation is made taking in account a Weibull distribution.

The Weibull model is used to model the probability of failure:

$$P_f = \exp\left[-\int_{\Omega} \sum_{i=1}^{n} \left(\frac{\langle E\overline{\varepsilon}_i(x) - \sigma_u \rangle}{\sigma_0} \right)^m \frac{d\Omega(x)}{\Omega_r} \right] \tag{A. 1}$$

where P_f represents the probability of failure, n is the number of spatial dimensions, E the Young modulus, $\overline{\varepsilon}_i(x)$ the nonlocal strain and σ_u, σ_0 and m the Weibull parameters. Ω_r is the reference volume.

The Weibull model is commonly used to describe the probabilistic failure of quasi-brittle materials.

While the Weibull model describes the crack initiation, there is still another random quantity that has to be handled, the distribution of defects that might initiate a crack. The critical defects follow the Poison distribution (Guy, Seyedi, & Hild, 2012).

We consider that the fracture propagation of quasi-brittle materials can be described by the hypothesis of the weakest link, which means that once a crack has started. This will lead the material to failure according to the following expression:

$$P_i(|\Omega|, \sigma_1) = P_{N_d \geq 1}(\Omega, \sigma_1) = P_{N_d = 0}(\Omega, \sigma_1) = 1 - \exp\left[\ddot{} - |\Omega| \lambda_t(\sigma_1) \right] \tag{A. 2}$$

Where $P_{N_d=0}(\Omega, \sigma_1)$ is the probability of finding no critical defects on the domain size $|\Omega|$, λ_t the density of defects that exists in a crack and σ_1 the maximum principal stress.

This formulation implicates a uniform load distribution, while mechanical tests we had performed do not have a uniform stress distribution.

However, we can use the Weibull model for our mechanical tests using the concept of an effective volume, $\Omega_{eff}(\sigma_1)$ (Guy et al., 2012).

$$\Omega_{eff}(\sigma_1) = \int_{\Omega} \left[\frac{\sigma(P)}{\sigma_{MAX}} \right]^m d\Omega = H(\sigma_1) \cdot \Omega \tag{A. 3}$$

where H is the stress heterogeneity factor, P the chosen point.

Using the effective volume we have:

$$P(\sigma_1) = 1 - \exp\left[-\Omega_{eff}(\sigma_1) \lambda_t(\sigma_1) \right] \tag{A. 4}$$

Knowing that the stress heterogeneity factor can be written (Guy, 2010) by:

$$H = \frac{1}{S} \int_{\Omega} \left[\frac{\sigma(P)}{\sigma_{MAX}} \right]^m d\Omega \tag{A. 5}$$

where S_s is the sample frontal surface (πr^2- for the Brazilian disc), Ω_s the domain (the frontal surface area), $\sigma_{ws}(P)\sigma_S(\mathrm{P})$ the stress at each point of the domain, σ_{1s} the maximum stress in the domain.

Therefore, to determine the Weibull parameters we have to find the Weibull stress for each mechanical test.

$$\sigma_w = \sigma_f \left(HZ\lambda_0 \right)^{1/m} \tag{A. 6}$$

Where σ_w is the Weibull stress, σ_0^m / λ_0 σ_0^m/λ_0 is the scale parameter. We can find then:

$$P_{fi} = 1 - \exp\left[-\left(\frac{\sigma_{wi}}{\sigma_0} \right)^m \right] \tag{A. 7}$$

Reformulation of the expression gives:

$$\ln\left[-\ln\left(1-P_i\right)\right]=m\left[\ln\left(\sigma_{wi}\right)-\ln\left(\sigma_0\right)\right] \tag{A. 8}$$

which means that for each σ_{wi} we will find a rupture probability that will correspond to it. Then we identify the Weibull parameters by the minimization of the error from the curve obtained by the expression (A. 8) (as we did in section 4.2).

As proposed by (Guy, 2010), for each stress at failure it is attribute the follow probability:

$$P_{Fi}=\frac{i}{n+1} \tag{A. 9}$$

where *n* is the total number of tests and *i* the number of the test.

A.1.2 The ENDO-HETEROGENE model

In rock material defects, cracks and/or fractures are expected to exist following a certain distribution.

In the ENDO-HETEROGENE model developed by (Guy, 2010) microcracks are distributed randomly within the material. The potentially initiated defect density (λ_t), follows the Poisson point process given by the equation (A. 10).

$$\lambda_t(\sigma)=\lambda_0\left(\frac{\sigma}{\sigma_0}\right)^m \tag{A. 10}$$

The probabilistic model for the crack initiation follows the theory of the weakest link as:

$$P_F=1-\exp\left[-Z_{eff}\lambda_t(\sigma)\right] \tag{A. 11}$$

As the stress intensity factor for a crack of size *a* is

$$K_I=\sigma\sqrt{a} \tag{A. 12}$$

And the threshold of crack propagation relates the stress intensity factor and the fracture toughness, the initiation stress level is:

$$\sigma_{th} = \frac{K_I}{\sqrt{a}} \qquad \textbf{(A. 13)}$$

For the model, there are some characteristics that must be taken in account, as the lengths of cracks and rock heterogeneity.

The probabilistic model has then two thresholds, one random for crack initiation (Weibull model) and another for the crack initiation (fracture mechanics) that is deterministic. The model is based on stress regularization which means is mesh independent.

The operator for the stress regularization are:

$$\overline{\underline{\sigma}} - l_c \overline{\underline{\sigma}} = \underline{\sigma} \qquad \textbf{(A. 14)}$$

$$\left(\vec{\nabla}\overline{\underline{\sigma}}\right) \cdot \vec{n} = \vec{0} \qquad \textbf{(A. 15)}$$

Where $\overline{\underline{\sigma}}$ is the regularized stress tensor.

This is based on the fact that for some materials we consider that the behaviour in a point depends of the state around it.

The use of a regularized deformation tensor was not appropriate in the case of heterogeneous materials, because with this type of model we cannot avoid the mesh dependence problem.

The first problem is that the response doesn't correspond to a fragile material and the second one is the dependence on the mesh element size. A lot of tests were made by (Guy, 2010), to verify the follow criteria:

- The correct response to a fragile material behaviour
- The independence of the mesh element size
- The independence of the mesh element direction

To resolve the problem two equation are assembled to formulate a single solution: The Westergaard asymptotic solution for the crack tip and the of regularisation equation (Helmholtz equation) given that the stress in a certain point *p* is:

$$\underline{\underline{\overline{\sigma_p}}}(K_I, K_{II}) = \frac{\Gamma^2\left(\frac{3}{4}\right)}{5\pi}\frac{1}{\sqrt{\pi l_c}}\begin{bmatrix} 4K_I & 4K_{II} & 0 \\ 4K_{II} & 6K_I & 0 \\ 0 & 0 & 0 \end{bmatrix} + \overline{\sigma_{33p}}\vec{e}_3 \otimes \vec{e}_3 \qquad \text{(A. 16)}$$

where l_c is the characteristic length, Γ the gamma function (Guy et al., 2012).

So the following crack growth threshold is compared to the principal maximum stress:

$$Sg = \frac{6\Gamma^2\left(\frac{3}{4}\right)}{5\pi}\frac{K_I}{\sqrt{\pi l_c}} \qquad \text{(A. 17)}$$

It is important to say that the initial defects must be modelled as microcracks, this leads to the size of the characteristic length and elements sizes of the model that must be larger than the microcracks (Figure A. 1).

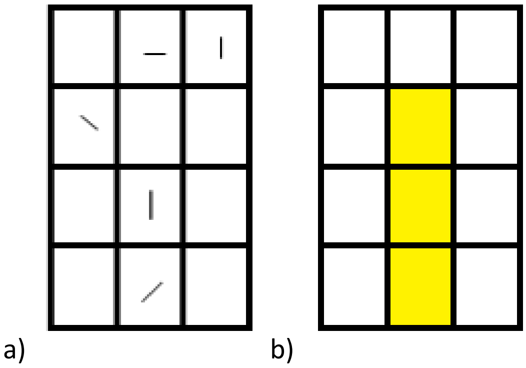

Figure A. 1- model of a a) microcrack b) crack

A.1.3 Weibull parameter for the intact and degraded rock

The parameters found by the evaluation of the Brazilian test show us that the m parameter is about 8.5 and σ_0 around 2.8 MPa. The fracture toughness of the rock is 0.6 MPa, and the Young modulus is 10 GPa and the Poisson ratio is 0.3.

Several simulations were performed with Code_Aster© as shown in Figure A. 2 using the ENDO_HETEROGENE model described at the previous section and implemented in the Code_Aster©, which is a finite-element multiphysics simulator developed by EdF and distributed under GPL license.

The heterogeneity of the rock is represented via a micro-defects' distribution following the Poisson-Weibull approach as previously described.

Hence, the threshold necessary for a crack to initiate, varies from one element to another one of the mesh, as it can be seen in Figure A. 3.

The interest of the analysis performed here is to evaluate the fracturing of a reservoir layer due the variation of the Weibull parameters (m and σ_0), i.e. due to changes in the spatial distribution of the defects. In these simulations we chose to keep σ_0 constant, and to vary m (1, 3, 6 and 9).

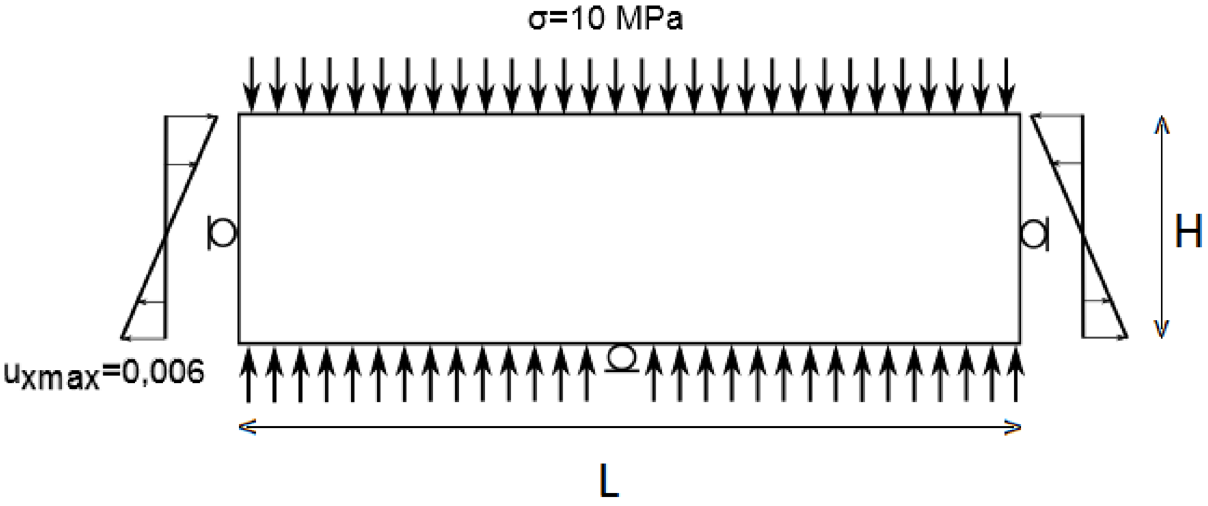

Figure A. 2 – Sketch of the reservoir case, L= 4 m and H = 1 m.

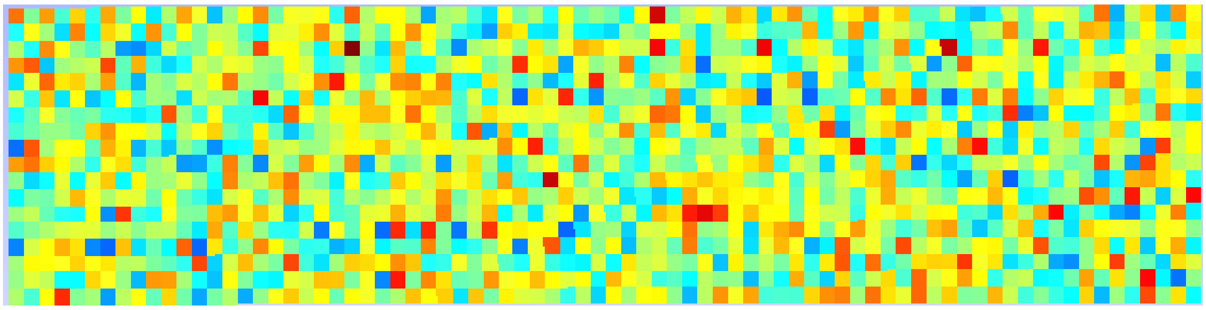

Figure A. 3 - Variation of the crack initiation parameter - Dark blue - 0, Dark red 3,5 MPa

For each simulation, the number of cracks developed and the number of broken elements were reported. The size (in element mesh unit) of the larger one was also evaluated. In Figure A. 6 and Figure A. 7, we can see the more heterogeneous the rock is (m=1 – heterogeneous, m = ∞ - homogenous rock), the larger cracks are developed. However, Figure A. 8 shows us that the size of the larger crack does not change with the change of m.

The difference between the crack distributions can be seen in Figure A. 4 and Figure A. 5.

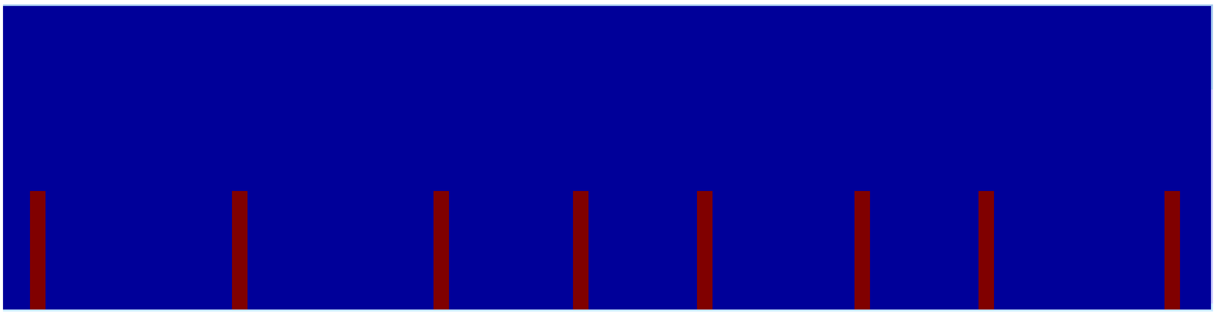

Figure A. 4 - Crack network developed in an homogenous media.

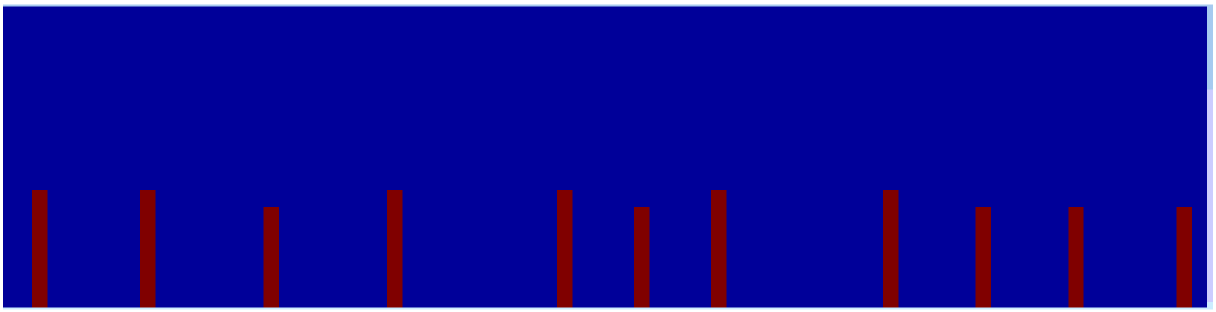

Figure A. 5 - Crack network developed in an heterogeneous media

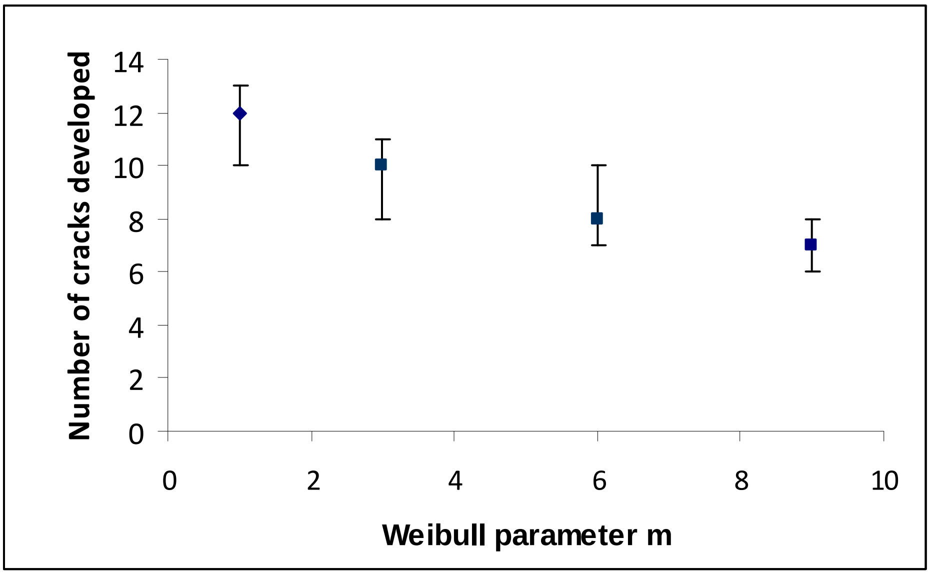

Figure A. 6 - Variation of the number of cracks developed for various Weibull modulus.

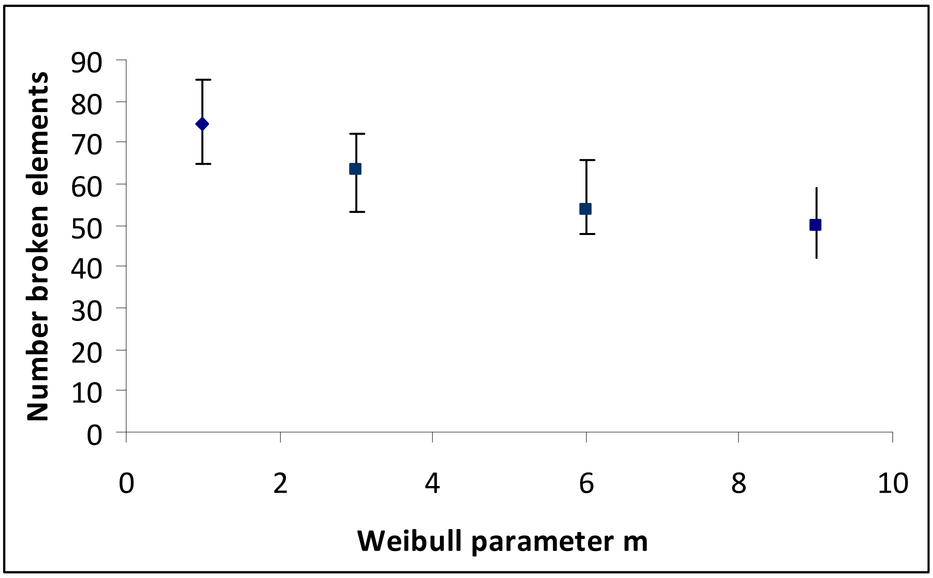

Figure A. 7- Variation of the number of broken elements for various Weibull modulus.

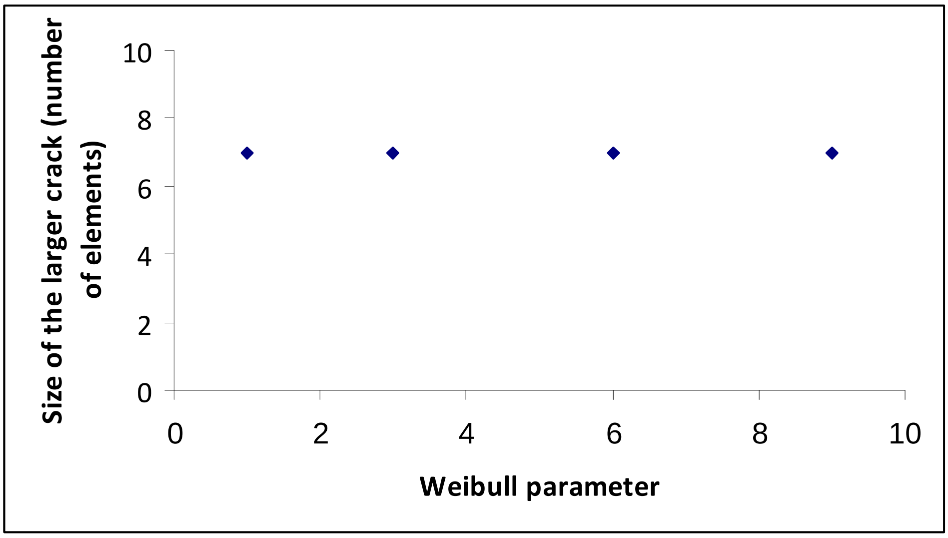

Figure A. 8 - Size of the larger crack (element unit)

This allows us to conclude that, the fracture network of a reservoir changes with *m*, however the cracks maximum size do not change with *m*. This is important for crack propagation through the complete layer, which can result in making easier for the fluid to flow from a layer to another.

It is important to notice here, that (Guy, 2010) had observed in his simulations on Code_Aster© that once a crack had started to propagate it created a barrier preventing other cracks to develop around it, creating a preferential path of crack propagation in the first elements to crack. The same patter was not found in this study and in the simulations here performed.

We can see in Figure A. 4 and Figure A. 5 the development of several cracks. This difference happens because the fracture toughness value for the material tested by (Guy, 2010) is smaller than the material here studied, facilitating the crack propagation when it starts rather than provoking the initiation of the fractures around due to the increase the stress tension in the vicinity.

BIBLIOGRAPHY

Altindag, R. (2000). The relationships between fracture toughness and other mechancical properties rocks. *Journal of Science Engineering*, *2*(2), 39–47.

André, L., Audigane, P., Azaroual, M., & Menjoz, A. (2007). Numerical modeling of fluid–rock chemical interactions at the supercritical CO2–liquid interface during CO2 injection into a carbonate reservoir, the Dogger aquifer (Paris Basin, France). *Energy Conversion and Management*, *48*(6), 1782–1797. doi:10.1016/j.enconman.2007.01.006

Ashby, M., & Sammis, C. (1990). The damage mechanics of brittle solids in compression. *Pure and Applied Geophysics*, *133*(3).

Atkinson, B. K. (1984). Subcritical crack growth in geological materials. *Journal of Geophysical Research*, *89*(B6), 4077–4114. doi:10.1029/JB089iB06p04077

Audigane, P., Gaus, I., Czernichowski-Lauriol, I., Pruess, K., & Xu, T. (2007). Two-dimensional reactive transport modeling of CO2 injection in a saline aquifer at the Sleipner site, North Sea. *American Journal of Science*, *307*(7), 974–1008. doi:10.2475/07.2007.02

Backers, T. (2002). Rock fracture toughness testing in Mode II—punch-through shear test. *International Journal of Rock Mechanics and Mining Sciences*, *39*(6), 755–769. doi:10.1016/S1365-1609(02)00066-7

Backers, T. (2004). *Fracture Toughness Determination and Micromechanics of Rock Under Mode I and Mode II Loading*.

Baud, P., Zhu, W., & Wong, T. (2000). Failure mode and weaking effect of water on sanstone. *Journal of Geophysical Research*, *105*(7), 371–389.

Bearman, R. . (1999). The use of the point load test for the rapid estimation of Mode I fracture toughness. *International Journal of Rock Mechanics and Mining Sciences*, *36*(2), 257–263. doi:10.1016/S0148-9062(99)00015-7

Bemer, E., & Lombard, J. (2009). From Injectivity to Integrity Studies of CO2 Geological Storage. *Oil & Gas Science and Technology – Revue de l'Institut Français Du Pétrole*, *65*(3), 445–459. doi:10.2516/ogst/2009028

Bieniawski, Z. T., & Hawkes, I. (1978). Suggested methods for determining tensile strength of rock materials. *International Journal of Rock Mechanics and Mining Sciences & Geomechanics Abstracts*, *15*(3), 99–103. doi:10.1016/0148-9062(78)91494-8

Bouc, O., Audigane, P., Bellenfant, G., Fabriol, H., Gastine, M., Rohmer, J., & Seyedi, D. (2009). Determining safety criteria for CO2 geological storage. *Energy Procedia*, *1*(1), 2439–2446. doi:10.1016/j.egypro.2009.02.005

Brown, G., & Reddish, D. (1997). Experimental relations between rock fracture toughness and density. *International Journal of Rock Mechanics and Mining Sciences*, *34*(1), 153–155. doi:10.1016/S1365-1609(97)80042-1

Cai, M. (2012). Fracture Initiation and Propagation in a Brazilian Disc with a Plane Interface: a Numerical Study. *Rock Mechanics and Rock Engineering*, *46*(2), 289–302. doi:10.1007/s00603-012-0331-1

Carneiro, F. L. L. (1953). Une nouvelle méthode pour la détermination de la résistence à la traction des bétons. *Bulletin RILEM*, *13*, 103–108.

Chang, S., Lee, C.-I., & Jeon, S. (2002). Measurement of rock fracture toughness under modes I and II and mixed-mode conditions by using disc-type specimens. *Engineering Geology*, *66*(1-2), 79–97. doi:10.1016/S0013-7952(02)00033-9

Dau Anh-Tuan. (2013). *« Modélisation numérique et étude expérimentale de la ténacité des roches en mode II » Résumé*. Paris.

Donovan, J., & Karfakis, M. G. (2004). Adaptation of a simple wedge test for the rapid determination of mode I fracture toughness and the assessment of relative fracture resistance. *International Journal of Rock Mechanics and Mining Sciences*, *41*(4), 695–701. doi:10.1016/j.ijrmms.2004.01.001

Dwivedi, R., Sonia, A. K., Goela, R. K., & Dube, A. K. (2000). Fracture toughness of rocks under sub-zero temperature conditions. *International Journal of Rock Mechanics and Mining Sciences*, *37*(8), 1267–1275. doi:10.1016/S1365-1609(00)00051-4

Egermann, P., Bemer, E., & Zinszner, B. (2006). An experimental investigation of the rock properties evolution associated to different levels of CO2 injection like alteration processes. In *International Symposium of the Society of Core Analysts* (pp. 1–15). Trondheim.

Erarslan, N., & Williams, D. J. (2012). Experimental, numerical and analytical studies on tensile strength of rocks. *International Journal of Rock Mechanics and Mining Sciences*, *49*, 21–30. doi:10.1016/j.ijrmms.2011.11.007

Espinoza, D. N., & Santamarina, J. C. (2012). Clay interaction with liquid and supercritical CO2: The relevance of electrical and capillary forces. *International Journal of Greenhouse Gas Control*, *10*, 351–362. doi:10.1016/j.ijggc.2012.06.020

Fleury, M., Pironon, J., Nindre, Y. M. Le, Bildstein, O., Berne, P., Langeau, V., … Vidal, O. (2011). Evaluating sealing efficiency of caprocks for CO2 storage: An overviewof the Geocarbone Integrity program and results. *Energy Procedia*, *4*, 5227–5235. doi:https://doi.org/10.1016/j.egypro.2011.02.501

Fowell, R. J. (1995). Suggested Method for Determining mode I fracutre Toughncess Using Cracked Chevron Notched Brazilian Disc (CCNBD) Specimens. *International Journal of Rock Mechanics and Mining Sciences and Geomechanics*, *32*(I), 57–64.

Gaus, I. et. al. (2008). Geochemical and solute transport modelling for CO2 storage, what to expect from it? *International Journal of Greenhouse Gas Control*, *2*(4), 605–625.

Gaus, I. (2010). Role and impact of CO2–rock interactions during CO2 storage in sedimentary rocks. *International Journal of Greenhouse Gas Control*, *4*(1), 73–89. doi:10.1016/j.ijggc.2009.09.015

Geonet. (2008). Que signifie vraiment le stockage géologique du CO2? Arts, Rob Beaubien, Stanley Benedictus, Tjirk Czernichowski-lauriol, Isabelle Fabriol, H. Gastine, Marie Gundogan, Ozgur Kirby, Gary Lombardi, Salvatore May, Franz Pearce, Jonathan Persoglia, Sergio Remmelts, Gijs Riley, Nick Sohrabi, Mehran Stead, Rowena: GeoNet.

Ghabezloo, S., Sulem, J., Guédon, S., & Martineau, F. (2009). Effective stress law for the permeability of a limestone. *International Journal of Rock Mechanics and Mining Sciences*, *46*(2), 297–306. doi:10.1016/j.ijrmms.2008.05.006

Grgic, D., & Giraud, A. (2014). Mechanics of Materials The influence of different fluids on the static fatigue of a porous rock : Poro-mechanical coupling versus chemical effects. *Mechanics of Materials*, *71*, 34–51. doi:10.1016/j.mechmat.2013.06.011

Griffith, A. A. (1921). The phenomena of rupture and flow in solids. *Philosophical Transactions of the Royal Society of London*, *221*(1921), 163–198. Retrieved from http://www.jstor.org/stable/91192

Gunsallus, K. ., & Kulhawy, F. H. (1984). A comparative evaluation of rock strength measures. *International Journal of Rock Mechanics and Mining Sciences*, *21*(5), 233–248.

Guo, H., Aziz, N. I., & Schmidt, L. C. (1993). Rock fracture-toughness determination by the Brazilian test. *Engineering Geology*, *33*(3), 177–188. doi:10.1016/0013-7952(93)90056-I

Guy, N. (2010). *Modélisation probabiliste de l'endommagement des roches : application au stockage géologique du CO2*. ENS Cachan.

Guy, N., Seyedi, D. M., & Hild, F. (2012). A probabilistic nonlocal model for crack initiation and propagation in heterogeneous brittle materials. *International Journal for Numerical Methods in Engineering*, n/a–n/a.

Hangx, S., van der Linden, A., Marcelis, F., & Bauer, A. (2013). The effect of CO2 on the mechanical properties of the Captain Sandstone: Geological storage of CO2 at the Goldeneye field (UK). *International Journal of Greenhouse Gas Control*. doi:10.1016/j.ijggc.2012.12.016

Hild, F., & Roux, S. (2006). Digital Image Correlation: from Displacement Measurement to Identification of Elastic Properties - a Review. *Strain*, *42*(2), 69–80. doi:10.1111/j.1475-1305.2006.00258.x

Hild, F., & Roux, S. (2006). Measuring stress intensity factors with a camera: Integrated digital image correlation (I-DIC). *Comptes Rendus Mécanique*, *334*(1), 8–12. doi:10.1016/j.crme.2005.11.002

Hondros, G. (1959). The evaluation of poisson's ratio and the modulus of materials of a low tensile resistence by the brazilian (indirect tensile) test with particular reference to concrete. *Australian Journal of Applied Science*, *10*, 243–268.

Inglis, C. (1913). Streses in a plate due to the presence of cracks and sharp corners. *Transactions of the Royal Institute of Naval Archictects*, *55*(213-241).

IPCC. (2005). *Carbon Dioxide Capture from the Air Using a Polyamine Based Regenerable Solid Adsorbent. Journal of the American Chemical Society*. doi:10.1021/ja2100005

Iqbal, M. J., & Mohanty, B. (2006). Experimental Calibration of ISRM Suggested Fracture Toughness Measurement Techniques in Selected Brittle Rocks. *Rock Mechanics and Rock Engineering*, *40*(5), 453–475. doi:10.1007/s00603-006-0107-6

Irwin, G. (1957a). Analysis of stress and strain near the en of a crack traversing a plate. *Journal of Applied Mechanics*, *24*, 361–364.

Irwin, G. (1957b). Analysis of stress and strain near the en of a crack traversing a plate. *Journal of Applied Mechanics*, *24*, 361–364.

Jurin, J. (1728). Disquisitio Physicae de Tubulis capillaribus. *Commentarii Academiae Scientiarum Imperialis Petropolitana*, *3*, 281–292.

Kahraman, S. (2004). A brittleness index to estimate fracture toughness. *International Journal of Rock Mechanics and Mining Sciences*, *41*(2), 343–348. doi:10.1016/j.ijrmms.2003.07.010

Kaufmann, G., & Dreybrodt, W. (2007). Calcite dissolution kinetics in the system CaCO3–H2O–CO2 at high undersaturation. *Geochimica et Cosmochimica Acta*, *71*(6), 1398–1410. doi:10.1016/j.gca.2006.10.024

Kazerani, T. (2013). Effect of micromechanical parameters of microstructure on compressive and tensile failure process of rock. *International Journal of Rock Mechanics and Mining Sciences*, *64*, 44–55. doi:10.1016/j.ijrmms.2013.08.016

Khan, K., & Al-Shayea, N. A. (2000). Effect of Specimen Geometry and Testing Method on Mixed Mode I-II Fracture Toughness of a Limestone Rock from Saudi Arabia. *Rock Mechanics and Rock Engineering*, *33*(3), 179–206. doi:10.1007/s006030070006

Kuruppu, M. D., Obara, Y., Ayatollahi, M. R., Chong, K. P., & Funatsu, T. (2013). ISRM-Suggested Method for Determining the Mode I Static Fracture Toughness Using Semi-Circular Bend Specimen. *Rock Mechanics and Rock Engineering*. doi:10.1007/s00603-013-0422-7

Lajtai, E. Z., Schmidtke, R. H., & Bielus, L. P. (1987). The effect of water on the time-dependent deformation and fracture of a granite. *International Journal of Rock Mechanics and Mining Sciences & Geomechanics Abstracts*, *24*(4), 247–255. doi:10.1016/0148-9062(87)90179-3

Le Guen, Y., Renard, F., Hellmann, R., Brosse, E., Collombet, M., Tisserand, D., & Gratier, J.-P. (2007). Enhanced deformation of limestone and sandstone in the presence of high Pco2 fluids. *Journal of Geophysical Research*, *112*(B5). doi:10.1029/2006JB004637

Leguillon, D., Karnaeva, E., Baroni, A., & Putot, C. (2014). Tight sedimentary covers for CO2 sequestration. *Fracture Phenomena in Nature and Technology*, 113–122.

Lemiszki, P. J., & Landes, J. D. (1996). Fracture toughness testing of core from the Cambro-Ordovician section on the Oak Ridge Reservation. In *Proceedings of the 2nd North American Rock Mechanical Symposium, Montréal, Québec, Canada.* (pp. 1627–1634).

Luquot, L., & Gouze, P. (2009). Experimental determination of porosity and permeability changes induced by injection of CO2 into carbonate rocks. *Chemical Geology*, *265*(1-2), 148–159. doi:10.1016/j.chemgeo.2009.03.028

Madland, M. V., Finsnes, a, Alkafadgi, a, Risnes, R., & Austad, T. (2006). The influence of CO2 gas and carbonate water on the mechanical stability of chalk. *Journal of Petroleum Science and Engineering*, *51*(3-4), 149–168. doi:10.1016/j.petrol.2006.01.002

Montes-Hernandez, G., Pironon, J., & Villieras, F. (2006). Synthesis of a red iron oxide/montmorillonite pigment in a CO2-rich brine solution. *Journal of Colloid and Interface Science*, *303*(2), 472–6. doi:10.1016/j.jcis.2006.07.064

Morris, J. P., Detwiler, R. L., Friedmann, S. J., Vorobiev, O. Y., & Hao, Y. (2011). The large-scale geomechanical and hydrogeological effects of multiple CO2 injection sites on formation stability. *International Journal of Greenhouse Gas Control*, *5*(1), 69–74. doi:10.1016/j.ijggc.2010.07.006

Morse, J. W., & Arvidson, R. S. (2002). The dissolution kinetics of major sedimentary carbonate minerals. *Earth-Science Reviews*, *58*(1-2), 51–84. doi:10.1016/S0012-8252(01)00083-6

NMAB. (1983). *Fracture in Compression of Brittle Solids* (National M.). National Academy Press.

Osselin, F. (2013). *Thermochemical-based poroelastic modell...ontext of CO2 storage in deep aquifers.pdf*. Université Paris-Est.

Ouchterlony, F. (1987). A presentation of the ISRM suggested methods for determining the fracture toughness of rock material. In *6. International Congress on Rock Mechanics* (pp. 1181–1186). Montreal: Balkema Publishers, A.A. / Taylor & Francis The Netherlands.

Oucterlony, F. (1989). Fracture toughness testing of rock with core based specimens, the development of an ISRM standard. In *Procedings 6th International Congr.res of Rock Mechanics, Balkema, Rotterdam,* (pp. 231–251).

Reis, J. M. L. (2010). Fracture assessment of polymer concrete in chemical degradation solutions. *Construction and Building Materials*, *24*(9), 1708–1712. doi:10.1016/j.conbuildmat.2010.02.020

Renard, S., Sterpenich, J., Pironon, J., Chiquet, P., Lescanne, M., & Randi, A. (2011). Geochemical study of the reactivity of a carbonate rock in a geological storage of CO2 : Implications of co-injected gases. *Energy Procedia*, *4*, 5364–5369. doi:10.1016/j.egypro.2011.02.519

Rice, J. R. (1968). Mathematical Analysis in the Mechanics of Fracture. In H. Liebowitz (Ed.), *Fracture: An Advanced Treatise (Vol. 2, Mathematical Fundamentals)* (Vol. 2, pp. 191–311). N.Y.: Academic Press.

Rice, J. R. (1978). Thermodynamics of the quasi-static of grifith cracks. *Journal of the Mechanics and Physics of Solids*, *26*(1974), 61–78.

Rimmele, G., Barlet-Gouédard, V., & Renard, F. (2009). Evolution of the Petrophysical and Mineralogical Properties of Two Reservoir Rocks Under Thermodynamic Conditions Relevant for CO2 Geological Storage at 3 km Depth. *Oil & Gas Science and Technology – Revue de l'Institut Français Du Pétrole*, *65*(4), 565–580. doi:10.2516/ogst/2009071

Rohmer, J., & Bouc, O. (2010). A response surface methodology to address uncertainties in cap rock failure assessment for CO2 geological storage in deep aquifers. *International Journal of Greenhouse Gas Control*, *4*(2), 198–208. doi:10.1016/j.ijggc.2009.12.001

Rutqvist, J. (2012). The Geomechanics of CO2 Storage in Deep Sedimentary Formations. *Geotechnical and Geological Engineering*, *30*(3), 525–551. doi:10.1007/s10706-011-9491-0

Rutqvist, J., Birkholzer, J., Cappa, F., & Tsang, C. (2007). Estimating maximum sustainable injection pressure during geological sequestration of CO2 using coupled fluid flow and geomechanical fault-slip analysis. *Energy Conversion and Management*, *48*(6), 1798–1807. doi:10.1016/j.enconman.2007.01.021

Rutqvist, J., & Tsang, C.-F. (2002). A study of caprock hydromechanical changes associated with CO2 -injection into a brine formation. *Environmental Geology*, *42*(2-3), 296–305. doi:10.1007/s00254-001-0499-2

Saad, A. (2011). *Influence du changement climatique et des conditions extrêmes sur les massifs fractures. rôle des fluides dans leur processus d'altération*. UNIVERSITÉ PARIS-EST.

Sammis, C. G., & Ashby, M. F. (1986). The failluire of brittle porous solids under compressive stress states. *Acta Metallurgica*, *34*(3), 511–526.

Smith, M. M., Sholokhova, Y., Hao, Y., & Carroll, S. A. (2013). CO2 -induced dissolution of low permeability carbonates . Part I : Characterization and experiments. *Advances in Water Resources*, *62*, 370–387. doi:10.1016/j.advwatres.2013.09.008

Stanchits, S., Dresen, G. (2003). Separation of Tensile and Shear Cracks Based on Acoustic Emission Analysis of Rock Fracture. In *International Symposium Non-Destructive Testing in Civil Engineering (NDT-CE) (Berlin 2003).*

Stefanou, I., & Sulem, J. (2014). Chemically induced compaction bands: Triggering conditions and band thickness. *Journal of Geophysical Research: Solid Earth*, *119*(2), 880–899. doi:10.1002/2013JB010342

Sterpenich, J., Sausse, J., Pironon, J., Géhin, a., Hubert, G., Perfetti, E., & Grgic, D. (2009). Experimental ageing of oolitic limestones under CO2 storage conditions. *Chemical Geology*, *265*(1-2), 99–112. doi:10.1016/j.chemgeo.2009.04.011

Sun, Z., & Ouchterlony, F. (1986). Fracture toughness of stripa granite cores. *International Journal of Rock Mechanics and Mining Sciences & Geomechanics Abstracts*, *23*(6), 399–409. doi:10.1016/0148-9062(86)92305-3

Tang, C. A., Liu, H., Lee, P. K. ., Tsui, Y., & Tham, L. G. (2000). Numerical studies of the influence of microstructure on rock failure in uniaxial compression — Part I: effect of heterogeneity,. *International Journal of Rock Mechanics and Mining Sciences*, *37*(4), 555–569.

Tavallali, A., & Vervoort, A. (2010). Effect of layer orientation on the failure of layered sandstone under Brazilian test conditions. *International Journal of Rock Mechanics and Mining Sciences*, *47*(2), 313–322. doi:10.1016/j.ijrmms.2010.01.001

Tiryaki, B. (2006). Evaluation of the indirect measures of rock brittleness and fracture toughness in rock cutting. *The Journal of The South African Institute of Mining and Metallurgy*, *106*(June), 407–424.

Trémosa, J. (2014). *Simulations géochimiques en appui à la thèse de Gisèle Suhett-Helmer* (Vol. d).

Wang, Q., & Xing, L. (1999). Determination of fracture toughness K IC by using the ¯ attened Brazilian disk specimen for rocks. *Engineering Fracture Mechanics*, *64*, 193–201.

Westergaard, H. (1939a). Bearing pressure and cracks. *Journal of Applied Mechanics*.

Westergaard, H. (1939b). Bearing pressure and cracks. *Journal of Applied Mechanics*.

Whittaker, B. N., Singth, R. N., & Sum, G. (1992). *Rock fracture mechanics - principles, design and applications*. Amsterdam.

Wolinskl, S., Hordijk, D. A., Reinhardt, H. W., & Cornelissen, H. A. W. (1987). Influence of aggregate size on fracture mechanics parameters of concrete. *International Journal of Cement Composites and Lightweight Concrete,*, *9*(2), 95–103. doi:10.1016/0262-5075(87)90025-X

Wong, T., Wong, R. H. C., Chau, K. T., & Tang, C. a. (2006). Microcrack statistics, Weibull distribution and micromechanical modeling of compressive failure in rock. *Mechanics of Materials*, *38*(7), 664–681. doi:10.1016/j.mechmat.2005.12.002

Yates, J. R., Zanganeh, M., & Tai, Y. H. (2010). Quantifying crack tip displacement fields with DIC. *Engineering Fracture Mechanics*, *77*(11), 2063–2076. doi:10.1016/j.engfracmech.2010.03.025

Zhang, J., Wong, T.-F., & Davis, D. M. (1990). Micromechanics of pressure-induced grain crushing in porous rocks. *Journal of Geophysical Research*, *95*(B1), 341. doi:10.1029/JB095iB01p00341

Zhang, Z. (2002). An empirical relation between mode I fracture toughness and the tensile strength of rock. *International Journal of Rock Mechanics and Mining Sciences*, *39*(3), 401–406. doi:10.1016/S1365-1609(02)00032-1

Zhixi, C., Mian, C., Yan, J., & Rongzun, H. (1997). Determination of rock fracture toughness and its relationship with acoustic velocity. *International Journal of Rock Mechanics and Mining Sciencies*, *34*, 3–4.

Zinsmeister, L. (2013). *Etude de l’évolution hydromécanique d'un carbonate après altération chimique - Application des méthodes de mesure des champs multi-échelles par correlation d'images 2D - 3D*. Ecole Polythecnique.

Zuo, L., Krevor, S., Falta, R. W., & Benson, S. (2011). An Experimental Study of CO2 Exsolution and Relative Permeability Measurements During CO2 Saturated Water Depressurization. *Transport in Porous Media*, *91*(2), 459–478. doi:10.1007/s11242-011-9854-2